UNIVERSITY
OF SUSSEX

Doctoral Thesis

Search for scalar bottom quarks in compressed final states with b-jets and missing transverse momentum with the ATLAS detector

A thesis submitted in fulfilment of the requirements
for the degree of Doctor of Philosophy

in the

Department of Physics and Astronomy
School of Mathematical and Physical Sciences

Author:
Mario Spina

Supervisor:
Prof. Iacopo Vivarelli

17th March 2022

STATEMENT

I, Mario Spina, hereby declare that this thesis has not been and will not be, submitted in whole or in part to another university for the award of any other degree.

Brighton,
17th March 2022

Mario Spina

A mio papà

University of Sussex
School of Mathematical and Physical Sciences
Department of Physics and Astronomy

Doctoral Thesis

Search for scalar bottom quarks in compressed final states with b-jets and missing transverse momentum with the ATLAS detector

by Mario Spina

Abstract

A search for the direct production of bottom squark pairs according to R-parity conserving supersymmetric models is presented in this thesis. The search targets final states with b-jets and missing transverse momentum. The analysis is based on 139 fb^{-1} of proton-proton data collected by the ATLAS detector at the LHC at a centre-of-mass energy $\sqrt{s} = 13$ TeV. Simplified models where the bottom squark decays into a bottom quark and the lightest, stable neutralino are targeted, and scenarios where the two supersymmetric particles are almost mass-degenerate are considered by this analysis. The compressed final states originating from these simplified models are reconstructed by exploiting a novel secondary-vertex identification technique to detect low momentum b-hadrons using tracks from the ATLAS inner detector. The performance and calibration of this algorithm are presented in this thesis. The analysis shows no significant deviations from Standard Model predictions and stringent exclusion limits are placed on the bottom squark masses for the examined simplified model. Bottom squark masses up to 660 GeV for mass splittings between the squark and the neutralino of 10 GeV are excluded at 95 % CL.

Preface

The content of this thesis reflects the work done by the Author during his PhD at the University of Sussex, as a member of the ATLAS Collaboration at CERN, Geneva.
A vast physics programme, including precise measurement of Standard Model processes and the searches for new phenomena beyond the Standard Model, is addressed by the ATLAS Collaboration. The results presented in this thesis are obtained by exploiting collaborative tools and resources available to all ATLAS members. In such collaborative environment the individual contribution is often part of a larger collective effort which includes contributions from other authors. It is the policy of the Collaboration to publish the results of any search or measurement on behalf of the full ATLAS Collaboration. In the following, a list of contributions and publications which saw the Author playing a more central role is given.

To gain ATLAS authorship, the Author of this thesis performed the measurement of the electron trigger efficiency for the Run 2 data from 2015 to 2017. The Author of this work also provided the official scale factors to correct the simulated electron trigger efficiencies, as it is detailed in Appendix A. These measurements are important for the whole Collaboration, and are directly applied to any analysis exploiting an electron trigger. This effort resulted in the publication of the paper *Performance of electron and photon triggers in ATLAS during LHC Run 2* [1].

To improve the reconstruction of b-hadrons with low transverse momentum by the ATLAS detector, dedicated algorithms have been developed by a smaller research team. The Author's work within this team is described in Chapter 4 and is documented in the public note *Soft b-hadron tagging for compressed SUSY scenarios* [2].

The Author's main contributions to the ATLAS Collaboration physics programme is the search for pair-produced bottom squarks in final states with b-jets and missing transverse energy. The analysis is performed using 139 fb^{-1} of proton-proton data collected by the ATLAS detector at a centre-of-mass energy of $\sqrt{s} = 13$ TeV. This analysis is presented in detail in Chapter 5 and Chapter 6, and the main Author's contribution involves the development and realisation of a search strategy for the compressed final states, involving the presence of low-transverse-momentum b-hadrons. This work is published in the paper *Search for new phenomena in final states with b-jets and missing transverse momentum in* $\sqrt{s} = 13$ *TeV pp collisions with the ATLAS detector* [3].

Acknowledgements

The end of a PhD is always an emotional moment for anyone, as an important chapter of someone's life ends and hopefully a new one is starting. And it is no exception for myself. Once on the top of the mountain, looking back at the path walked, the obstacles and successes met, and the huge experiences gained makes quite an emotion. And for sure, this is a path I could have never walked alone, so I am truly grateful to each and every person who crossed their paths with mine.

An enormous thanks goes to Iacopo, my supervisor. His unmatched charisma and limitless knowledge of nearly any topic about particle physics was a constant beacon during the past four years of my life. You are the only one who could have seen me to the end of this PhD, and if I am a little more confident in presenting and discussing any of my work it is only because of your guidance. I should also thank Fabrizio, my second supervisor, for his presence and infinite kindness. Your positive presence always improves anyone's mood in the office. A special thanks goes also to Alex, for being a fair and extremely competent reviewer over the years; and to Antonella, who created and keeps wisely leading this EPP Sussex group. Without you I would literally never have been here. I would also say a big thank you to Lily, Kate and Josh for making each meeting more interesting with your insights and thoughts.

A very special thanks is for Kerim, whose incredibly vast knowledge of particle physics and unmatched expertise in programming had a huge impact on my PhD. I hope my coding is no longer as bugged as it used to be. I also am grateful for having met Batool, Benedict, Mark and Tom. Your hard work is inspiring, and the guidance you offer to us students is invaluable.

I was lucky enough to meet and work with an amazing group of current and past fellow PhD students. I owe an enormous debt of gratitude to my "seniors", Giuseppe and Sam. Your presence, friendship and example made most of, if not all, my days. A similarly huge thank you goes to Ioannis, for being such a cheerful and good friend inside and outside the office, and to Mario, for his kindness, patience and for always providing ditto presentations at the DISCnet events. To all other friends I met, Fabio, MiniFab (aka Frodo), Nicola, Emma, Marco, Dani, Meirin, Ondra I simply say "thank you" from the bottom of my heart, thanking each of you would simply double the size of this thesis.

A special thanks goes to Fabrizio T- more family than friend to me - for the past 10+ years of friendship started on the first day of lab back in Catania. You saw me through my lowest and highest, and still you choose to be my neighbour. I cannot thank you enough. And also thank you to Leon, a special friend whom sharing time with is a pleasure.

My years at university in Catania were long, and so is the list of friends-for-life I met in those days. Michele, Miriam, Ruggero, Nicolò, Silvia, Stefano, Valeria, Jessica, Laura, Paola, Giulia, Giulia, Letizia, Nicola, Mimmo, Ferdinanda and many more. Thanks for the amazing memories we created around those BBQs, and most importantly thank you

for being such an incredible support and company right until these days, even if we are scattered across (at least) three continents! I am also grateful to all the friends back home in Siracusa, you guys are all in my heart. Too bad we can't meet as much as we used to.

Now down to my Family. Here is where the emotions really begin to intensify. I simply can't express how much I value the time spent with each and everyone of you, and the deep affection I feel for you. During the last months I learnt to value more and more each single message or video call. You have been a constant lifeline for my sanity. I am also very thankful to my in-laws (Nicola, Stella and Giovanni) for being such loving and caring people.

I was lucky enough to be able to express my feelings for my Mum in many occasions, but every time there is always so much more to add. You have always inspired me with your incredible strength, vitality and tenacity. Your presence during the darkest and brightest days is one of the things I cherish the most in my life, and I hope I managed to make you proud of your Son. About my Dad, this thesis is for Him. It says it all.

Lastly, but most importantly, I have to try and express in words the infinite love I feel for Lucia, my wife and more than that my everything. The day you jumped on that plane to Brighton I understood your strengths and hopes are unrivaled, as it is your amazing craziness and ability to lighten my every days. You really are the foundations of who I am, and I am most humbled by your love.

I would like to end these acknowledgements with a line from a song which kept me going over the last few months:

The last day for a dwarf is the first day of a story that is yet to come.
(Wintersaga).

Contents

Introduction

Galileo Galilei is considered one of the founders of modern science, which is based on the scientific method. This is the process of observing the Nature and trying to model it according to mathematical laws. From such laws theoretical predictions based on hypothesis are developed, and experiments can be designed to prove or disprove the hypothesis. A theoretical hypothesis becomes a *theory* if it is supported by experimental evidence. If a theory prediction is disproven by undisputable experimental evidence, the theory is discarded. Modern science is therefore based on the experimental measure of some predictions based on the mathematical description of physical phenomena. If the observations confirm the theoretical predictions, then the hypothesis is accepted; otherwise, a new theoretical hypothesis is formulated and the process starts again.

One of the most successful theories is the Standard Model of particle physics, a theoretical framework which describes the fundamental particles and their interactions and which is based on the mathematical language of quantum field theory. An important notion exploited by the Standard Model is that of *symmetry*. One of the first connections between symmetries and conservation laws of physics was demonstrated by Emmy Noether [4–6]. Symmetries have been thereafter used to describe and simplify the complex systems within particle physics.

The success of the Standard Model is based on decades of experimental discoveries and measurements, from the electroweak W and Z bosons to the quarks and gluons. The particles described by the Standard Model were originally massless, so the observation of massive electroweak bosons posed a central theoretical problem, as a mechanism to explain these masses was needed. The particles' mass problem was theoretically solved by Brout, Englert and Higgs, who introduced the *spontaneous symmetry breaking* mechanism. The mechanism, together with explaining the origin of the particles' masses, predicted the existence of a scalar boson. For decades scientists attempted to experimentally prove the existence of this boson, and with it the validity of the spontaneous symmetry breaking mechanism. This search ended with the discovery and measurement of a Standard Model Higgs boson by the ATLAS and CMS collaborations at LHC, CERN. This is the most recent success of the Standard Model.

Despite its numerous successes, the Standard Model is not the ultimate theory. There are theoretical shortcomings, such as the *hierarchy* problem to the Higgs boson mass: at energies much higher than the electroweak energy scale, the quantum corrections to the Higgs mass differ by ~ 30 order of magnitudes compared to the observed mass of ~ 125 GeV measured at the LHC. To remove this inconsistency, a large amount of fine tuning would be needed. This is considered *unnatural*, and theoretical physicists tried to achieve a more elegant and *natural* solution to this problem. Other Standard Model shortcomings arise from astrophysical observations. For example, the visible mass in the Universe, composed by the particles accounted for by the Standard Model, is not able to describe a wide range of observations such as the galaxies rotation velocity curve, or the observed anisotropy of the cosmic microwave background. The observed matter density in the Universe shows a large contribution due to an unknown type of matter. These observations are solved by assuming the existence of some sort of *Dark Matter*, which is not included in the Standard Model.

These are just some examples of the reasons to motivate the need for an extension of the Standard Model. An appealing possibility is the introduction of a new symmetry, namely a *supersymmetry*, between fermions and bosons. This postulates that to each Standard Model boson (fermion) corresponds a supersymmetric fermion (boson). If such additional symmetry was unbroken, supersymmetric particles with the same mass states as their Standard Model counterparts would exist, solving immediately the Higgs hierarchy problem. The supersymmetry would also provide an ideal candidate, the *lightest supersymmetric particle*, for Dark Matter, solving many, if not all, the Standard Model limitations. This extension to the Standard Model is also appealing as it provides clear signature observables, making it a testable hypothesis by the LHC experiments. The observation of no supersymmetric particles with the same mass of the Standard Model ones indicates that the supersymmetry, if exists, needs to be broken to some degree, leading to mass states of the supersymmetric particles larger than the Standard Model particles. The ability of supersymmetry to address the Standard Model shortcomings therefore depends on the scale of symmetry breaking one wants to allow. This for instance is a key element to consider when addressing the tuning of the Higgs boson mass.

If discovered, the lightest supersymmetric particle predicted by supersymmetry could provide a valid candidate for explaining Dark Matter. This implies that the relic density calculated for the lightest supersymmetric particle needs to be the same as the relic density observed by astrophysical experiments. It may happen that the calculated relic density differs from the observed one. To achieve this result the mechanism of *co-annihilation* is introduced. This assumes that the lightest supersymmetric particle is almost mass-degenerate with another supersymmetric particle, allowing the lightest supersymmetric particle relic density to match the observed relic density for the Dark Matter. A consequence of the co-annihilation is that the decay products of these supersymmetric particles would be characterized by low-momentum, or *compressed*, final states. These final states are not always easily investigated, and to reconstruct them dedicated tools are often required.

The work presented in this thesis is a search for third-generation supersymmetric particles pair produced and promptly decaying in final states with two b-jets and missing transverse momentum. The analysis is conducted on 139 fb^{-1} of proton-proton collision data at $\sqrt{s} =$ 13 TeV of centre-of-mass energy collected by the ATLAS detector. The analysis targets compressed final states, where b-hadrons with low transverse momentum are present. These are reconstructed by exploiting a dedicated, innovative tagging algorithm.

This thesis is structured as follows. Chapter 1 briefly presents the Standard Model of particle physics and its limitations. A supersymmetric extension of the Standard Model is discussed, and the phenomenology and state-of-the-art searches for supersymmetric particles by the ATLAS collaboration are presented. In Chapter 2 a description of the experimental apparatus, the Large Hadron Collider and the ATLAS experiment, is presented. Emphasis is given to each subdetector and to the hardware of the trigger system. Chapter 3 details the data acquisition procedure, the important step of Monte Carlo event simulation, and the physics object reconstruction of both recorded data and simulated events. Chapter 4 details the performance and impact on an analysis of a novel algorithm for the identification of low-momentum b-hadrons. In Chapter 5 the analysis strategy for the search of the decay products of pair-produced third-generation bottom squarks is presented. The strategy for the optimisation of signal regions and for the background estimation and validation, largely based on the new algorithm for the identification of low-momentum b-hadrons, is discussed. In Chapter 6 the statistical interpretation of the results from this search is discussed. The work done by the Author on the electron trigger calibration is presented in Appendix A.

In this thesis, natural units $\hbar = c = 1$ are used.

Theoretical Overview

1

This Chapter introduces the theoretical aspects explored by this thesis. A particular focus is given to the Standard Model of particle physics and its supersymmetric extension. Section 1.1 presents an overview of the Standard Model. Section 1.2 gives an overview of the current phenomenological limitations of the Standard Model. Finally Section 1.3 introduces a supersymmetric extension to the Standard Model as an appealing option to alleviate some of these shortcomings, and provides a motivation for exploring compressed supersymmetric scenarios.

1.1 The Standard Model of Particle Physics

All the interactions between particles in our Universe can be described by considering only four fundamental interactions: gravitational, electromagnetic, weak and strong interactions, plus a fifth Yukawa interaction. These forces behave in different ways, and occur at different distances and energy scales. Three of these interactions - electromagnetic, weak and strong interactions - can be expressed as quantum fields, and they are successfully described by the Standard Model (SM) of particle physics. The formalism of the SM is defined by a quantum field theory, which merges together the quantum and special relativity theories. Since its initial development in the 1970s, the SM has been confirmed by many experimental results and theoretical discoveries, last of which is the observation of the Higgs boson at the LHC [7,8].
Because of its weak magnitude, gravity does not play a significant role at the energies accessible to the current particle physics experiments. It also cannot be described in a quantum field theory because it can not yet be described in terms of quantized fields [5,6].

Quantum Field Theories

The quantum field theory (QFT) [5,6] is a theoretical framework used in the SM in which the particles and interactions are described by incorporating quantum mechanics and special relativity. In this framework the relativistic fields are quantized, while the particles are excitations of such fields.

QFT exploits a Lagrangian formalism: a system is described by a Lagrangian density, whose most general form is $\mathcal{L}(\phi, \partial\phi)$. This function depends on the relativistic field ϕ and its derivatives $\partial\phi$. The actual equations of motion are obtained by minimising the action $\mathcal{S}$, defined as the integral:

$$\mathcal{S} = \int d^4x \mathcal{L}. \tag{1.1}$$

When two (or more) fields scatter, the $\mathcal{S}$-matrix element is obtained by the interaction Lagrangian:

$$\mathcal{L} = \mathcal{L}_{\text{free}} + \mathcal{L}_{\text{int}}, \tag{1.2}$$

where $\mathcal{L}_{\text{free}}$ describes the kinematics of the free fields, while $\mathcal{L}_{\text{int}}$ represents the interaction between these fields.

Fundamental Interactions

In the introduction to this Section it was stated that only three fundamental forces can be described by the SM in terms of QFT theories: those are the electromagnetic (EM), weak and strong interactions. As discussed in Ref. [6], the interaction terms of the SM can be obtained by imposing an invariance under special local transformations of the fields, known as gauge transformations. Choosing a particular gauge symmetry fixes the structure of the couplings between the fermions, which compose the ordinary matter in the Universe, and spin-1 vector fields, commonly referred to as gauge fields, responsible for mediating the fundamental forces. Introducing these gauge fields maintains the invariance of the Lagrangian under the gauge transformation, hence there is a correlation between the imposed symmetry and the properties of the interaction.
The SM can be described by the following gauge symmetry group:

$$SU(3)_C \otimes SU(2)_L \otimes U(1)_Y, \tag{1.3}$$

where $SU(3)_C$ is the color symmetry group of the strong interaction, while $SU(2)_L \otimes U(1)_Y$ is the electroweak symmetry group.
In the following, the forces described by the SM are discussed.

Electroweak Force

According to the Glashow-Salam-Weinberg mechanism [9, 10] the EM and weak interactions are low-energy limits of a more general symmetry, the electroweak interaction (EW), which occurs at an energy scale of 246 GeV. The decoupling of the EW force into EM and weak is known as electroweak symmetry breaking, which is discussed further in the text.
The EW theory is described by the gauge group $SU(2)_L \otimes U(1)_Y$ which acts on fermionic spinor fields. These can be represented in terms of their left- or right-handed chiral projections:

$$\psi = \psi_L + \psi_R = \frac{1}{2}\left(1 - \gamma^5\right)\psi + \frac{1}{2}\left(1 + \gamma^5\right)\psi \tag{1.4}$$

where γ^5 is the fifth gamma matrix [11]. The left-handed fermions are grouped into doublets, while their right-handed counterparts are singlets under the $SU(2)_L$ symmetry group. Fermions with left (right) chirality carry a weak isospin charge $I = \frac{1}{2}$ (0), and only left-handed fermions, carrying a not-null weak isospin charge, couple via weak interaction. The Lagrangian describing the kinematic properties of massless fermions, described by Equation 1.4, can be written as:

$$\mathcal{L} = i\bar{\psi}\gamma^\mu \partial_\mu \psi, \tag{1.5}$$

where γ^μ represents the Dirac matrices [11]. To keep the Lagrangian invariant under the $SU(2)_L \otimes U(1)_Y$ local gauge group the covariant derivative is introduced:

$$\partial_\mu \rightarrow D_\mu = \partial_\mu + igW_\mu^a t^a + ig' B_\mu Y, \tag{1.6}$$

where a assumes values 1-3, g, g' are the coupling constants and Y is the hypercharge quantum number. In Equation 1.6, the mediator bosons W_μ and B_μ are introduced, and they represents the four gauge fields associated to $SU(2)_L$ and to $U(1)_Y$. The t^a matrices are defined as

$$t^a = \begin{cases} 0 & for \quad I = 0, \\ \sigma^a & for \quad I = \frac{1}{2} \end{cases} \tag{1.7}$$

where the I is the weak isospin for fermions with left or right chirality, σ^a are the Pauli matrices [11].

The mediator bosons from Equation 1.6 differ from the observed massive bosons associated to the charged and neutral currents. Such mass eigenstates are obtained by mixing the interaction eigenstates, postulated by the theory. In particular, the charged currents arise from the linear combination of $SU(2)_L$ eigenstates according to:

$$W_\mu^\pm = \frac{W_\mu^1 \mp iW_\mu^2}{\sqrt{2}}, \tag{1.8}$$

while the neutral currents are obtained from the mixing of $SU(2)_L$ and $U(1)_Y$:

$$\begin{pmatrix} Z_\mu \\ A_\mu \end{pmatrix} = \begin{pmatrix} \cos\theta_W & -\sin\theta_W \\ \sin\theta_W & \cos\theta_W \end{pmatrix} \begin{pmatrix} W_\mu^3 \\ B_\mu \end{pmatrix} \tag{1.9}$$

where θ_W is the Weinberg angle relating neutral and charged currents. The EM charge is related to the weak isospin and hypercharge by the Gell-Mann-Nishijima relation [12, 13]

$$Q = T_3 + \frac{Y}{2}, \tag{1.10}$$

where T_3 is the third component of the weak isospin with values $-\frac{1}{2}, \frac{1}{2}$.

As already mentioned, the SM fermions can be arranged into three generations of $SU(2)_L$ weak isospin doublets:

$$\begin{pmatrix} \nu_e \\ e \end{pmatrix}_L \begin{pmatrix} \nu_\mu \\ \mu \end{pmatrix}_L \begin{pmatrix} \nu_\tau \\ \tau \end{pmatrix}_L, \begin{pmatrix} u \\ d \end{pmatrix}_L \begin{pmatrix} c \\ s \end{pmatrix}_L \begin{pmatrix} t \\ b \end{pmatrix}_L \tag{1.11}$$

The EM charge difference between the *up* and *down* fermions is always of one unit. Each doublet corresponds to the familiar flavour pairs of leptons and quarks. Within the SM the neutrinos are massless, and since they only interact via weak force they have no right-hand counterparts. For any other left-handed fermion a right-handed singlet is introduced.

Strong force

Quarks and gluons also have a color charge, which makes them interact via the strong force described by quantum chromodynamics (QCD). Similarly to the EW interaction, QCD requires a gauge invariance under the $SU(3)_C$ symmetry group, where C stands for colour, the hidden quantum number introduced by this theory. By convention the three charges are labelled as red, green and blue. The quark spinors can hence be represented as an $SU(3)_C$ colour triplet

$$\begin{pmatrix} \psi_R \\ \psi_G \\ \psi_B \end{pmatrix}. \tag{1.12}$$

The gauge-invariant derivative under the $SU(3)_C$ group can be written as:

$$\partial^\mu \rightarrow D^\mu = \partial^\mu + ig_S G_a^\mu T^a, \tag{1.13}$$

where g_S is the coupling constant. T^a, with $a = 1, 2..., 8$ are the Gell-Mann matrices [11], which represent the basis of the $SU(3)_C$ group in the same way as the Pauli matrices are the basis of the $SU(2)_L$ group. The additional fields connected to the strong interaction are represented by the G_a^μ non-commutative matrices. The corresponding field strength tensor can be written as:

$$G_{\mu\nu}^a = \partial_\mu G_\nu^a - \partial_\nu G_\mu^a - g_S f_{bc}^a G_\mu^b G_\nu^c, \tag{1.14}$$

where f_{abc} are the structure constants associated with the gauge group. The term featuring such constants describes the gluons self-interaction. Because of the self-interaction, the coupling constant α_S depends strongly on the energy transfer of the interaction, Q^2 [11,14]. Considering $\alpha_S = \frac{g_S^2}{4\pi}$, at first order the dependency, or running, of this constant from Q^2 assumes the form:

$$\alpha_S(Q^2) = \frac{12\pi}{(33 - 2n_f)\log\left(\frac{Q^2}{\Lambda_{QCD}^2}\right)}, \tag{1.15}$$

where n_f is the number of quarks whose mass is below Q and $\Lambda_{QCD} \sim$ 200 MeV is the characteristic scale of the theory. Equation 1.15 points to important features of the QCD:

- the term $(33 - 2n_f)$ is positive within the SM, consequently the intensity of the interaction increases with the distance;
- when Q approaches Λ_{QCD} the interaction diverges, making the theory non-perturbative;
- when $Q >> \Lambda_{QCD}$ then $\alpha_S \rightarrow 0$.

From these feature, three essential characteristics of QCD emerge.

- *Asymptotic freedom*: as the energy increases the strength of interaction tends to zero and quarks can be treated as free particles.

– *Confinement*: at lower energies the coupling strength increases, leading to quarks and gluons being confined in bound states without any observable color charge.

– *Hadronisation*: when coloured object are separated, the potential energy between them increases until the extraction of new pair of quarks from the vacuum is energetically more convenient. This phenomenon is responsible for the production of hadronic jets at high-energy physics experiments [11, 14].

The Higgs Mechanism

The SM theory discussed so far describes massless fermions, as shown by Equation 1.5, in contrast with the observation of fermionic matter in the Universe. The same argument holds for the gauge bosons, which are as well described as massless particles, in contrast with e. g. the observations and measurement of the Z and W bosons masses at UA1 and UA2 [15]. This inconsistency is solved within the SM by introducing the Higgs mechanism [16–18].
This mechanism introduces a scalar potential assumed to be:

$$V(\phi) = \mu^2\phi^\dagger\phi + \lambda(\phi^\dagger\phi)^2, \tag{1.16}$$

where μ and λ are additional parameters of the theory, while ϕ stands for a $SU(2)_L$ complex scalar doublet which can be written as:

$$\phi = \begin{pmatrix}\phi^+\\ \phi^0\end{pmatrix} = \frac{1}{\sqrt{2}}\begin{pmatrix}\phi_1 + i\phi_2\\ \phi_3 + i\phi_4\end{pmatrix} \tag{1.17}$$

and which is identified as the Higgs field. Depending on the value of μ^2 the scalar potential can assume different shapes. The non-trivial case is obtained when $\mu^2 < 0$, in which case the potential assumes the *mexican hat* shape with a local maximum at $\phi = 0$ surrounded by a continuous minimum state defined by $|\phi| = \sqrt{\frac{-\mu^2}{\lambda}} \equiv v$. An illustration of such potential is shown in Figure 1.1. When the field assumes this vacuum expectation value (VEV) v, it spontaneously breaks the symmetry.
The Lagrangian associated to this scalar doublet can be written as:

$$\mathcal{L}_\phi = (D^\mu\phi)^\dagger\left(D_\mu\phi\right) - V(\phi), \tag{1.18}$$

where D^μ is the $SU(2)_L$ covariant derivative already introduced in Equation 1.6. The components of the scalar field spontaneously breaking the symmetry are arbitrary, and by convention it is convenient choosing

$$\phi = \frac{1}{\sqrt{2}}\begin{pmatrix}0\\ v + h\end{pmatrix}. \tag{1.19}$$

This particular state perturbs the vacuum v by a small quantity h. When expanding this perturbed vacuum state, mass terms related to h appear into the Lagrangian. Using this convention, the gauge bosons' masses can be written as

$$M_W^2 = \frac{1}{4}g^2v^2, \quad M_Z^2 = \frac{1}{4}(g^2 + g'^2), \quad M_A = 0, \tag{1.20}$$

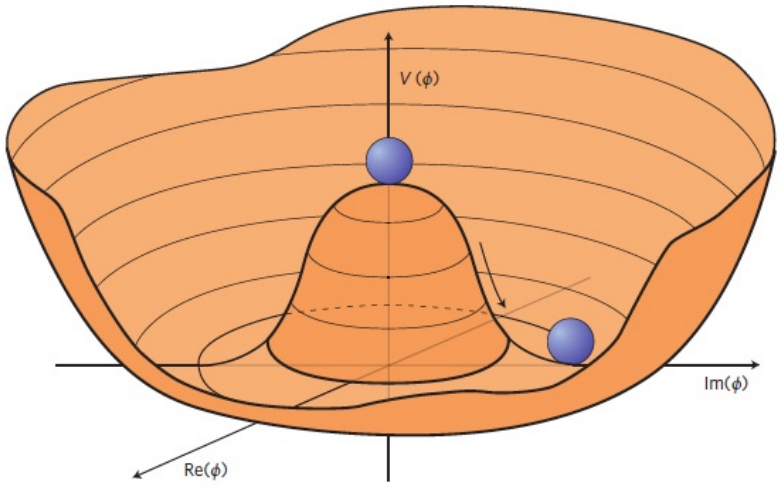

Figure 1.1: Illustration of the complex Higgs potential $V(\Phi)$ for the non-trivial case $\mu^2 < 0$. The vacuum is defined by the minima at $|\phi^2| = \frac{\mu^2}{\lambda}$. This potential is spontaneously broken when the field ϕ is forced on a vacuum state, while preserving the $SU(2)_L$ symmetry. Figure taken from Ref. [19].

where g, g' are the coupling constants of $SU(2)_L$ and $U(1)_Y$ respectively, which are related to the Weinberg angle [11] by

$$\sin\theta_W = \frac{g'}{\sqrt{g^2 + g'^2}}. \tag{1.21}$$

The process of spontaneous electroweak symmetry breaking (EWSB) induced by the Higgs mechanism is able to explain the origin of the masses of the weak gauge bosons. A similar approach can be exploited to confer mass to the fermion fields. One might want to express the Lagrangian term of a fermionic mass state as

$$\mathcal{L}_{mass} = -m\psi\bar{\psi} = -m\left(\bar{\psi}_L\psi_R + \bar{\psi}_R\psi_L\right), \tag{1.22}$$

but this violates the local gauge invariance because the left- and right-handed spinors transform differently under $SU(2)_L$. For this reason, the Yukawa coupling of the Higgs field to the fermions is considered. The Lagrangian term describing the fermion masses can be written as:

$$\mathcal{L}_f = -\lambda_d \bar{Q}_L \phi d_R + \text{higher order terms}, \tag{1.23}$$

where Q_L stands for the left-handed fermion doublet and ϕ is the same scalar field introduced in Equation 1.19. Under these assumptions, Equation 1.23 can be written as:

$$\mathcal{L}_f = -\lambda_d \frac{1}{\sqrt{2}}(\bar{u}_L, \bar{d}_L)\begin{pmatrix} 0 \\ v + h \end{pmatrix} d_R + \text{higher order terms}, \tag{1.24}$$

where $\lambda_d \frac{v}{\sqrt{2}}$ is the mass term of the down-type fermions. The up-type mass term can be similarly obtained by considering the charge-conjugate to the Higgs field $\phi^C = -i\sigma_2\phi^\star$ to transform the up-flavour component of the fermion doublet.
Finally, it is possible to identify a pure Higgs Lagrangian:

$$\mathcal{L}_h = \frac{1}{2}(\partial^\mu h)^2 - \frac{2\lambda v^2}{2}h^2 - \lambda v h^3 - \frac{\lambda}{4}h^4 + \frac{\lambda v^4}{4}, \tag{1.25}$$

where the expression for the VEV is exploited to substitute $\mu^2 = -v^2\lambda$. The above equation contains a kinetic term, cubic and quartic self-interactions and a mass term associated to the Higgs boson, whose bare mass is

$$M_h = 2\lambda v^2. \tag{1.26}$$

λ is a free parameter of the theory, which has to be determined experimentally.
In 2012 the ATLAS and CMS collaborations at the LHC announced the observation of a Higgs-like particle whose mas is 125 GeV [7, 8]. Since then, many decay channels of the Higgs boson have been studied, and the results so far do not yield any significant deviation from the SM.

Standard Model Recap

The SM describes the EW and strong interactions in a QFT framework, whose symmetry group is $SU(3)_C \otimes SU(2)_L \otimes U(1)_Y$. All the interactions of each elementary particle can be described by the QCD and EW sectors or the Higgs mechanism. Considering the lepton and quark fields, the SM provides with a complete theoretical framework for making phenomenological predictions that can be experimentally investigated.

The total number of SM free parameters, which are not set by the theory, is 19. This includes: 6 quark and 3 lepton masses, under the assumption that the neutrinos are mass-

Table 1.1: Summary of the particles described by the SM. Values taken from Ref. [20]

	Name	Mass	Charge (e)
Quarks spin $= \frac{1}{2}$	u	2.2 MeV	$+\frac{2}{3}$
	d	4.7 MeV	$-\frac{1}{3}$
	c	1.28 GeV	$+\frac{2}{3}$
	s	96 MeV	$-\frac{1}{3}$
	t	173.1 GeV	$+\frac{2}{3}$
	b	4.18 GeV	$-\frac{1}{3}$
Leptons spin $= \frac{1}{2}$	ν_e	< 2 eV	0
	e	0.511 MeV	-1
	ν_μ	< 0.19 MeV	0
	μ	106 MeV	-1
	ν_τ	< 18.2 MeV	0
	τ	1.78 GeV	-1
Gauge Bosons spin $= 1$	gluon, g	0	0
	photon, γ	0	0
	W bosons	80.385 GeV	± 1
	Z boson	91.1876 GeV	0
Scalar spin $= 0$	Higgs boson H	125.18 GeV	0

less; 3 coupling constants; 1 Higgs VEV and 1 Higgs mass; 3 angles and 1 phase from the Cabibbo-Kobayashi-Maskawa (CKM) mixing matrix and 1 strong Charge-Parity (CP) parameter. All these parameters have been experimentally determined, and are summarised in Ref. [20].
The number of free parameters in the SM might need to be extended to 26 in order to account for the evidence of neutrino oscillations [21]. The seven extra parameters would be the 3 neutrino masses and 4 mixing parameters, as it is described in Section 1.2.
The experimental properties of the SM are summarized in Table 1.1.

1.2 SM Limitations

The SM is a successful and self-consistent theory capable of correctly describing the EW and strong interactions. Many experimental results confirmed the SM predictions, and one of its recent successes is the discovery of the Higgs boson already mentioned.
Despite its success, there are reasons to believe the SM is not a complete theory, but it needs to be extended to address observations, mainly from neutrino, cosmological and astronomical experiments, and unanswered theoretical questions, such as the *naturalness* of the SM.
This section briefly comments on those shortcomings which are not addressed by the SM.

The Hierarchy Problem

In the SM, each fundamental interaction has its characteristic energy scale. This is $\mathcal{O}$ (200) MeV for the strong interaction, while for the EW interaction it is of the order of the Higgs field VEV, $v = 246$ GeV. Significant quantum gravity effects are supposed to play a major role at the Planck scale, $M_{\text{Planck}} = \mathcal{O}(10^{19})$ GeV [22]. The Higgs boson mass can be written in the form:

$$m_H^2 = m_{H_0}^2 + \delta m_H^2, \tag{1.27}$$

where $m_{H_0}^2$ is the bare mass of the Higgs boson, which is obtained from the Higgs Lagrangian, and δm_H^2 is its radiative correction. Because of the Yukawa coupling, the leading SM correction is described by the loop involving the top quark. For a generic fermion f, the radiative correction term would assume the form

$$\delta m_H^2 = -\frac{\lambda_f^2}{8\pi^2}\Lambda_{UV}^2, \tag{1.28}$$

where λ_f^2 is the coupling f to the Higgs boson and Λ_{UV}^2 is the highest mass scale in the theory. Above the EW scale, which occurs at the VEV, no interaction is assumed to exist up to gravity, occurring at the Planck scale. The radiative correction to the Higgs mass calculated at such a scale is $\sim$ 30 orders of magnitude larger than its bare mass. The observed Higgs mass can therefore be justified in two ways: by arbitrarily applying a fine-tune to each term of the radiative correction; or by hypothesizing the existence of new

particles or interactions at a lower scale than the Planck one, which would spontaneously cancel-out each divergent radiative term.
A fine-tune of 30 orders of magnitudes goes against the principle of naturalness [23], hence the preferred solution would be the hypothesis of new phenomena removing the need of fine tuning. These could provide additional particles to the SM, which would interact with the Higgs boson in other loops which would self-erase, leaving the bare mass at a value close to the observed one.

Dark Matter

There is plenty of astrophysical and cosmological evidence that points to the fact that the visible mass in the Universe is not enough to explain the observations.
An historical argument is the observation of the rotational speed of galaxies, which can not be explained by the observable mass of the galaxy [24]. An example of such rotation curve is presented in Figure 1.2. According to gravitational laws, if all the mass of the

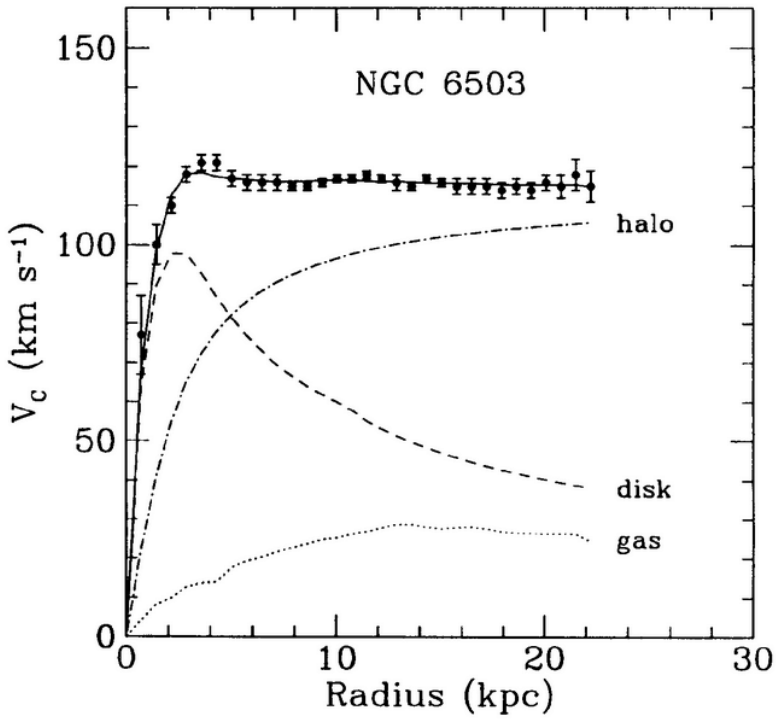

Figure 1.2: Rotation curve of the NGC 6503 galaxy [25]. The dotted line describes the contribution due to the gas, the dashed line is for the disk. These describe the total visible mass in the galaxy. An additional term is needed to describe the observed data. This is due to the invisible dark matter supposedly present in the galactic halo. This contribution is represented by a dash-dot line. Once this term is added, the experimental points, with their error, are in agreement with the solid line, which represent the three-parameter fit based on the three individual components.

galaxy corresponded to the observable matter, the rotation speed v_{tot} would decrease faster moving away from the galaxy centre. But observations show a nearly constant or slowly decreasing value of v_{tot}, which is assumed be due to unknown and invisible

matter (hence *dark* matter) in the galactic halo. The existence of dark matter (DM) is also supported by other observations, mainly the measurement of the cosmic microwave background (CMB) as measured by the WMAP [26] and Planck [27] collaborations. These experiments measured the the temperature power spectrum of the CMB. The height of the second and third peaks in the power spectrum is related to the relative abundance of DM in the Universe. By definition, dark matter needs to be quite massive, invisible, electrically and color neutral. As a consequence, good DM candidates would be weakly interacting massive particles (WIMPs) [28]. None of the SM particles would make for a good WIMP DM candidate, hence once again an extension to the SM is needed.

Other Issues

Together with the hierarchy problem and the presence of dark matter in the Universe, already discussed, there are other known phenomena which are not well addressed by the SM. These are briefly discussed in the following:

- *Matter-antimatter asymmetry.* In the Universe ordinary matter is more abundant than antimatter. This asymmetry arises from some CP violation according to the three Sakharov conditions [29]. Despite the presence of CP violation in the SM introduced by the CKM matrix [30], the amount of observed imbalance is too large to be described by the SM only. To explain this observation new CP-violating processes need to be included in new-physics scenarios.

- *Neutrino sector.* The SM accounts for three neutrino families, which are assumed to be massless. These particles can be converted into their electrically-charged counterparts by the EW interactions, which prevent violation of the lepton flavour numbers. The observation of neutrino oscillations violates the lepton flavour conservation and implies that at least two out of three neutrinos species need to be massive [31]. Similarly to the quark mixing CKM matrix, the mixing between neutrinos' mass and flavour eigenstates can be described in the SM by the Pontecorvo-Maki-Nakagawa-Sakata (PMNS) matrix [32], which is parametrised as a function of the angles between the three flavours, namely θ_{12}, θ_{13}, θ_{23} plus at least one extra phase.

- *Grand Unification.* The EW theory successfully unifies the EM and weak interactions as one process, at a given energy scale. Theorists have ever since been trying to develop a theoretical framework where all the known interactions are treated as low-energy limits of a single force, occurring at an energy scale μ_{GUT}. To do so, the evolution (running) of the coupling constant of each SM interaction is studied as a function of the energy scale [33]. In the SM, the evolution of such interaction couplings does not converge to a common value, in contrast with the idea of a Grand Unification energy scale. Introducing additional fermionic and bosonic degrees of freedom modifies the evolution of the couplings, possibly allowing unification.

– *Gravity.* It was already discussed that gravity is not included in the SM because of the small magnitude of its interaction at the current accelerators energy scales and because it is not possible to describe the theory in terms of quantised fields.

1.3 Extending the SM

As discussed in the previous Sections, the SM is a successful theory which nevertheless needs some extension to address all the physical phenomena observed in the Universe. A supersymmetric extension of the SM (SUSY) would introduce new particles by adding a fermion-boson symmetry. If discovered, this theory would have the potential to solve many of the SM limitations.

SUSY

The main reason for introducing a supersymmetric extention to the SM is that it would solve the naturalness problem of the Higgs mass [34]. This result is theoretically achieved by associating to each known SM fermion two complex scalar fields, which would naturally remove the divergences arising from the radiative corrections to the Higgs mass. The relation between the fermions and their supersymmetric scalar partners is expressed by a SUSY operator Q:

$$Q_\alpha \left|fermion\right\rangle^\alpha = \left|boson\right\rangle \;\; ; \;\; Q_\alpha \left|boson\right\rangle = \left|fermion\right\rangle_\alpha , \tag{1.29}$$

where α represents the spinor component of the fermion states. Between the initial and final state there is a spin-$\frac{1}{2}$ difference, hence the Q and its hermitian conjugate $Q^\dagger$ are fermionic operators, which anti-commute according to:

$$\left\{Q_\alpha, Q_\beta^\dagger\right\} = 2\gamma^\mu_{\alpha\beta} P_\mu, \tag{1.30}$$

$$\left[M^{\rho\sigma}, Q_\alpha\right] = -i\left(\sigma^{\rho\sigma}\right)^\beta_\alpha Q_\beta, \tag{1.31}$$

where P_μ is the generator of translations in a 4-dimension space and $M^{\rho\sigma}$ is the generator of the Lorentz transformations. Other important commutation and anti-commutation rules are:

$$\left\{Q_\alpha, Q_\beta\right\} = \left\{Q_\alpha^\dagger, Q_\beta^\dagger\right\} = 0, \tag{1.32}$$

$$\left[P^\mu, Q_\alpha\right] = \left[P^\mu, Q_\alpha^\dagger\right] = 0, \tag{1.33}$$

The particle described by the SM and their supersymmetric partners are arranged into supermultiplets, each of which contains two bosonic and two fermionic degrees of freedom. The fermions, described by Weyl spinors [35], are represented by two polarisations. A bosonic state is associated to each polarisation. The supermultiplets can be classified depending on the spin of their particles as:

– *Chiral supermultiplets.* These contain the spin-$\frac{1}{2}$ SM fermions with left- and right-handed chiral components together with their spin-0 scalar superpartners, usually referred to as sfermions or scalar fermions. The left- or right-handed fermions are conventionally labelled as f_L, f_R while their superpartners are labelled as $\tilde{f}_L$, $\tilde{f}_R$ where the tilde symbol identifies the SUSY partners of SM particles and L, R labels refer to their chirality.

– *Gauge supermupltiplets.* They contain the massless spin-1 SM gauge vector bosons fields, together with their two spin-$\frac{1}{2}$ Weyl superpartners labelled as gauginos.

– *Gravitational supermultiplets.* They contain the spin-2 graviton and its spin-$\frac{3}{2}$ supersymmetric partner, the gravitino.

Equation 1.33 implies that the operator Q also commutes with the mass operator, defined as $P^2 = m^2$. This would lead to the conclusion that the SUSY particles share the same mass values of their SM counterparts. If the condition on the masses was satisfied by the SUSY particles, these would have already been discovered, immediately solving the naturalness problem. The non-observation of any particle with the same mass of the SM ones but with different spin leads to the conclusion that SUSY has to be a broken symmetry. SUSY imposes a relation between the fermionic and bosonic interactions:

$$\lambda_S = |\lambda_F|^2 = \lambda. \tag{1.34}$$

Inserting both fermionic and the corresponding SUSY bosonic contributions in Equation 1.28, one obtains exact cancellation at tree level. However, the fact that SUSY is broken introduces radiative corrections to the Higgs boson mass that can be written as:

$$\delta m_H^2|_{S+F} = \frac{\lambda}{16\pi^2}\left[m_F^2 \log\left(\frac{\Lambda_{UV}}{m_F^2}\right) - m_S^2 \log\left(\frac{\Lambda_{UV}}{m_S^2}\right)\right]. \tag{1.35}$$

To minimise the amount of fine tuning, the mass difference between the SM and SUSY particles with large couplings λ to the Higgs boson needs to be not too large. The difference in mass between the SM particles and their superpartners implies that the SUSY Lagrangian has to contain two parts: a term respecting the gauge and Yukawa interactions, which preserves the SUSY invariance; and a soft term which breaks the SUSY invariance by only positive mass terms, which protects the quadratic cancellations of the Higgs boson mass. The Lagrangian can be then written as:

$$\mathcal{L} = \mathcal{L}_{\text{SUSY}} + \mathcal{L}_{\text{soft}}. \tag{1.36}$$

Minimal Supersymmetric Standard Model

The minimal supersymmetric standard model (MSSM) [36–38] is the supersymmetric extension of the SM which has a phenomenologically-consistent and low-energy SUSY theory by adding the fewest possible theoretical assumptions. The gauge group of the MSSM

is the same as the SM, $SU(3)_C \times SU(2)_L \times U(1)_Y$. The gauge and chiral superfields, summarised in Table 1.2, generate all the particle content of the MSSM, and to each SM doublet or singlet a corresponding spin-0 superpartner is included. This model does not include the right-hand neutrino singlets. In the MSSM, the SM Higgs sector is extended, as two doublets are introduced [20]. This is a two-Higgs-doublet model (2HDM) extension of the SM. In the 2HDM two Higgs doublets, ϕ_1 with hypercharge $Y = -1$ and ϕ_2 with hypercharge $Y = 1$, are required to generate mass for the down-type quarks and charged leptons, via the ϕ_1 doublet, and up-type quarks, via the ϕ_2 doublet [39]. The presence of two scalar doublets implies that there are eight degrees of freedom. After the EWSB [16–18] presented in Section 1.1, three parameters give mass to the vector bosons $Z, W^{\pm}$ and the remaining five are new scalar bosons, which are five physical Higgs particles in the MSSM spectrum: one charged Higgs pair, $H^{\pm}$; one CP-odd neutral scalar A; and two CP-even neutral states, H and h, where h is the lightest state identified with the Higgs boson discovered in 2012 [7,8]. At tree level, the Higgs sector is determined by only two free parameters: the ratio between the two Higgs doublets' vacuum expectation values, $\tan\beta = \frac{v_2}{v_1}$; and one Higgs boson mass, conventionally the mass of the CP-odd Higgs boson m_A. For $m_A \geqslant m_Z$ the observed Higgs boson's mass can be expressed as $m_h = M_Z \cos 2\beta$. The eight degrees of freedom SUSY partners correspond to the four spin-$\frac{1}{2}$ higgsinos.

Table 1.2: Summary of the Chiral and Gauge supermultiplets of the MSSM with their names and quantum numbers. The superpartners of SM particles are denoted with a tilde.

Name	spin $= 1$	spin $= \frac{1}{2}$	spin $= 0$	$(SU(3)_C, SU(2)_L, U(1)_Y)$
		Chiral Supermultiplets		
quarks, squarks	- - -	(u_L, d_L) u_R d_R	$(\tilde{u}_L, \tilde{d}_L)$ $(\tilde{u}_R)$ $(\tilde{d}_R)$	$(3,\ 2,\frac{1}{6})$ $(3,\ 1,-\frac{2}{3})$ $(3,\ 1,\frac{1}{3})$
leptons, sleptons	- -	(ν_L, ℓ_L) ℓ_R	$(\tilde{\nu}_L, \tilde{\ell}_L)$ $(\tilde{\ell}_R)$	$(1,\ 2,-\frac{1}{2})$ $(1,\ 1,\ 1)$
Higgs, higgsinos	- -	$(\tilde{h}_u^+, \tilde{h}_u^0)$ $(\tilde{h}_d^0, \tilde{h}_d^-)$	(h_u^+, h_u^0) (h_d^0, h_d^-)	$(1,\ 2,\frac{1}{2})$ $(1,\ 2,-\frac{1}{2})$
		Gauge Supermultiplets		
gluons, gluinos	g	$\tilde{g}$	-	(8,1,0)
W-bosons, winos	$W^{\pm}, W^0$	$\tilde{W}^{\pm}, \tilde{W}^0$	-	(1,3,0)
B-boson, binos	B	$\tilde{B}$	-	(1,1,0)

Lepton and baryon numbers are accidentally conserved in the SM, meaning that this conservation is not explicitly assumed. For this reason the SUSY models do not conserve lepton and baryon numbers either. The long mean life of the proton indicates that violations to the lepton and baryon numbers have to be very small in Nature, and this consideration

leads to the definition of a discrete R symmetry [40] in the MSSM, defined as:

$$R \equiv (-1)^{3(B-L)+2S} \tag{1.37}$$

where B, L are the baryon and lepton number respectively and S is the spin. With this definition, SM particles have R-parity equal to 1 while MSSM particles have R-parity equal to -1. When R-parity is conserved (RPC scenarios), the decay of SUSY particles into final states with only SM particles is prohibited. To conserve R-parity, stable SUSY particles, referred to as lightest supersymmetric particles (LSPs), are needed in the final states. If the LSP is also electrically neutral, then it would provide a good candidate for cold dark matter. This refers to non-relativistic DM, as opposite to the *hot* dark matter which refers to particles, such as neutrinos, in a relativistic regime.
A broken SUSY Lagrangian introduces 105 new parameters on top of the 19 from the SM. It is possible to reduce the complexity of the MSSM by assuming some phenomenological hypothesis:

- the CKM matrix is the only source of CP violation in the theory;
- no flavour changing neutral currents are introduced at tree level;
- sfermions from the first and second generation are assumed to be mass-degenerate.

As result of these assumptions, the MSSM introduces only 22 parameters, listed below:

- $\tan\beta$, the ratio of the VEVs of the Higgs doublets;
- μ, m_A, the masses for the Higgs fields;
- M_1, M_2, M_3, the three mass parameters for the gauginos;
- $m_{\tilde{q}}$, $m_{\tilde{u}_R}$, $m_{\tilde{d}_R}$, $m_{\tilde{\ell}}$, $m_{\tilde{e}_R}$, the mass parameters for the first and second generation squarks and sleptons;
- A_u, A_d, A_e, the trilinear couplings for the first and second generation;
- $m_{\tilde{Q}}$, $m_{\tilde{t}_R}$, $m_{\tilde{b}_R}$, $m_{\tilde{L}}$, $m_{\tilde{\tau}_R}$, the mass parameters for the third generation squark and stau;
- A_t, A_b, A_τ, the trilinear couplings for the third generation.

Under these assumption, the simplified version of the theory is known as phenomenological MSSM (pMSSM).

Mass States

Section 1.1 described how the mass eigenstates of SM particles fermions and vector bosons are obtained by the mixing of the interaction eigenstates. Similarly, in the MSSM, the mass eigenstates of the supersymmetric particles are obtained from the mixing of gauge eigenstates in the supersymmetric Lagrangian. A summary of such mass eigenstates, and the gauge eigenstates they originated from, is reported in Table 1.3. In the same table the R-parity and spin quantum numbers are also indicated.

Table 1.3: Summary of the interaction and mass eigenstates arising from MSSM.

Name	spin	R	Gauge Eigenstates	Mass Eigenstates
Higgs bosons	0	+1	$H_u^0\ H_d^0\ H_u^+\ H_d^-$	$h^0\ H^0\ A^0\ H^\pm$
squarks	0	-1	$\tilde{u}_L, \tilde{u}_R, \tilde{d}_L, \tilde{d}_R$ $\tilde{s}_L, \tilde{s}_R, \tilde{c}_L, \tilde{c}_R$ $\tilde{t}_L, \tilde{t}_R, \tilde{b}_L, \tilde{b}_R$	(∼same) (∼same) $\tilde{t}_1, \tilde{t}_2, \tilde{b}_1, \tilde{b}_2$
sleptons	0	-1	$\tilde{e}_L, \tilde{e}_R, \tilde{\nu}_e$ $\tilde{\mu}_L, \tilde{\mu}_R, \tilde{\nu}_\mu$ $\tilde{\tau}_L, \tilde{\tau}_R, \tilde{\nu}_\tau$	(same) (same) $\tilde{\tau}_1, \tilde{\tau}_2, \tilde{\nu}_\tau$
neutralinos	$\frac{1}{2}$	-1	$\tilde{B}^0, \tilde{W}^0, \tilde{H}_u^0, \tilde{H}_d^0$	$\tilde{\chi}_1^0, \tilde{\chi}_2^0, \tilde{\chi}_3^0, \tilde{\chi}_4^0$
charginos	$\frac{1}{2}$	-1	$\tilde{W}^\pm, \tilde{H}_u^+, \tilde{H}_d^-$	$\tilde{\chi}_1^\pm, \tilde{\chi}_2^\pm$
gluinos	$\frac{1}{2}$	-1	$\tilde{g}$	(same)

Sfermions (squarks, sleptons) mass eigenstates are obtained by mixing the left- and right-handed chiral fields via the mass matrix $\mathcal{M}_{\tilde{\mathrm{q}}}^2$ shown in Equation 1.38 [41]:

$$\mathcal{M}_{\tilde{\mathrm{q}}}^2 = \begin{pmatrix} m_{\tilde{\mathrm{q}}_L}^2 & a_{\mathrm{q}} m_{\mathrm{q}} \\ a_{\mathrm{q}} m_{\mathrm{q}} & m_{\tilde{\mathrm{q}}_R}^2 \end{pmatrix}. \tag{1.38}$$

The mixing, involving the off-diagonal elements, is relevant only for the third-generation quark/squark supermultiplet, due to the large mass of the top quark. Therefore, for third-generation squarks, the left- and right-handed masses in the diagonal can be expressed as:

$$m_{\tilde{\mathrm{q}}_L}^2 = M_{Q_3}^2 + m_Z^2 cos2\beta \left(I_3^{\mathrm{q}_L} - e_{\mathrm{q}} \mathrm{sin}^2\theta_W \right) + m_{\mathrm{q}}^2, \tag{1.39}$$

$$m_{\tilde{\mathrm{q}}_R}^2 = M_{\{U,D\}_3}^2 + m_Z^2 cos2\beta e_{\mathrm{q}} \mathrm{sin}^2\theta_W + m_{\mathrm{q}}^2, \tag{1.40}$$

while the off-diagonal term is:

$$a_{\mathrm{q}} m_{\mathrm{q}} = \begin{cases} (A_t - \mu \mathrm{cot}\beta) & (\tilde{\mathrm{q}} = \tilde{\mathrm{t}}) \\ (A_b - \mu \mathrm{tan}\beta) & (\tilde{\mathrm{q}} = \tilde{\mathrm{b}}). \end{cases} \tag{1.41}$$

In Equation 1.39, Equation 1.40 and Equation 1.41 $I_3^{\mathrm{q}_L}$ stands for the third component of the weak isospin, e_{q} is the fractional electric charge of the (s)quark q, m_Z is the mass of

the SM Z boson, μ stands for the Higgsino mass parameter in the MSSM while β is the ratio of the VEVs of H_u and H_d respectively. The remaining parameters are introduced by the broken SUSY Lagrangian $\mathcal{L}_{\text{soft}}$: M_{Q_3}, M_{U_3}, M_{D_3} are the third components of the mass matrices of the left- and right-handed third-generation squarks, while A_t, A_b are the coefficients of their trilinear coupling terms [42].

A similar mixing matrix to the one in Equation 1.38 can be defined to determine the mass eigenstates of the charginos and neutralinos, collectively known as electroweakinos. The MSSM theorises four charged, spin-$\frac{1}{2}$ mass eigenstates, the charginos $\tilde{\chi}^{\pm}_{1,2}$ whose mixing matrix is given by:

$$\begin{pmatrix} M_2 & \sqrt{2}m_W \sin\beta \\ \sqrt{2}m_W \cos\beta & \mu \end{pmatrix}, \tag{1.42}$$

in the $\left(\tilde{W}^{\pm}, \tilde{H}^{\pm}\right)$ basis. In Equation 1.42 M_2 stands for the wino mass parameter, μ is the Higgs field mass parameter, β is the VEVs ratio for the charged Higgs fields and m_W is the W boson's mass.

A similar procedure can be exploited also for the neutral eigenstates. In this case, the mixing of the neutral gauginos $\tilde{B}$, $\tilde{W}^0$ with the neutral higgsinos $\tilde{H}^0_d$, $\tilde{H}^0_u$ determines four neutral, spin-$\frac{1}{2}$ mass eigenstates, collectively known as neutralinos. The neutralino mixing matrix in the $(\tilde{B}, \tilde{W}^0, \tilde{H}^0_d, \tilde{H}^0_u)$ basis assumes the form

$$\begin{pmatrix} M_1 & 0 & -m_Z \cos\beta \sin\theta_W & m_Z \sin\beta \sin\theta_W \\ 0 & M_2 & m_Z \cos\beta \cos\theta_W & m_Z \sin\beta \cos\theta_W \\ -m_Z \cos\beta \sin\theta_W & m_Z \cos\beta \cos\theta_W & 0 & \mu \\ m_Z \sin\beta \sin\theta_W & -m_Z \sin\beta \cos\theta_W & -\mu & 0 \end{pmatrix}, \tag{1.43}$$

where m_Z and θ_W are the Z boson's mass and the Weinberg angle; β is the ratio of the VEVs of the Higgs doublet; M_1, M_2 and μ are the bino, wino and higgsino masses respectively. In the MSSM, the lightest neutralino $\tilde{\chi}^0_1$ is the LSP.

Third Generation and Compressed SUSY Motivations

As it is already discussed, the introduction of an unbroken SUSY would naturally solve the Higgs hierarchy mass problem [43]. This result would be achieved by introducing new scalar particles, doubling the particle content of the SM, whose additional loops [23] would cancel out with the SM fermion ones provided that the relation between the couplings of a SM fermion and its scalar superpartner obeys $\lambda_S = |\lambda_F|^2$. This requirement naturally removes the quadratic divergences occurring at the new-physics energy scale Λ_{NP}, at each perturbation order of the Higgs boson's mass. As discussed, the new symmetry is broken, leading to the conclusion that the SUSY masses differ from the SM ones. In the SM the most important contribution to the Higgs boson's mass is given by the top quark because of its large coupling to the Higgs boson. SUSY models impose that the couplings of the SUSY particles are the same as the SM ones. This implies that the third-generation

squarks, particularly the scalar tops, have the largest coupling to the Higgs boson. Naturalness arguments, introduced to control the quadratic divergencies to the Higgs boson's mass, would keep the mass of third-generation squarks lower than any other squark. This requirement leads to a natural MSSM mass spectrum [44], in which higgsinos, $\begin{pmatrix}\tilde{t}_L\\ \tilde{b}_L\end{pmatrix}$, $\tilde{t}_R$ and gluinos gain relatively low masses, while all the other SUSY particles may be decoupled, and may have higher masses. This scenario with natural and decoupled SUSY mass spectra is shown in Figure 1.3.

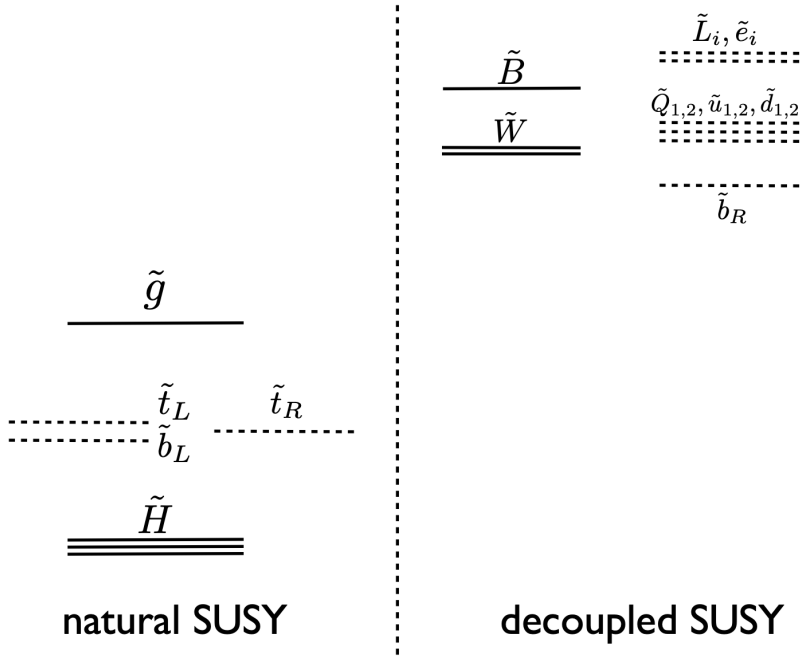

Figure 1.3: Natural MSSM mass spectrum from Ref. [44]. The particles on the left are constrained by naturalness arguments, and are supposed to be lighter than the remaining ones, which are decoupled.

Another argument in favor of a SUSY extention to the SM comes from the observation of dark matter in the Universe [24]. This might be made of massive particle which are not in a relativistic regime and which interact only weakly; for this reason they are collectively referred to as WIMPs. When considering SUSY scenarios where the decaying sparticle conserves the R-parity, it is implied that the LSP is stable. If the LSP is the lightest neutralino, it would satisfy all the requirements for the cold DM: a massive particle not in a relativistic regime; electrically and colour neutral; weakly interacting. Until now the only constraints to the nature of the neutralino arise from particle physics. One cosmological condition neutralinos need to meet is the ability to reproduce the relic cold dark matter density in the Universe, whose value measured by the Planck collaboration [27] is:

$$\Omega_c h^2 = 0.1200 \pm 0.0012 \tag{1.44}$$

where Ω_c is the cold dark matter density and h the Hubble constant. This value is theoretically well motivated by the WIMP miracle [20]. The relic dark matter density obtained from generic SUSY models does not agree with the measured value in Equation 1.44, but

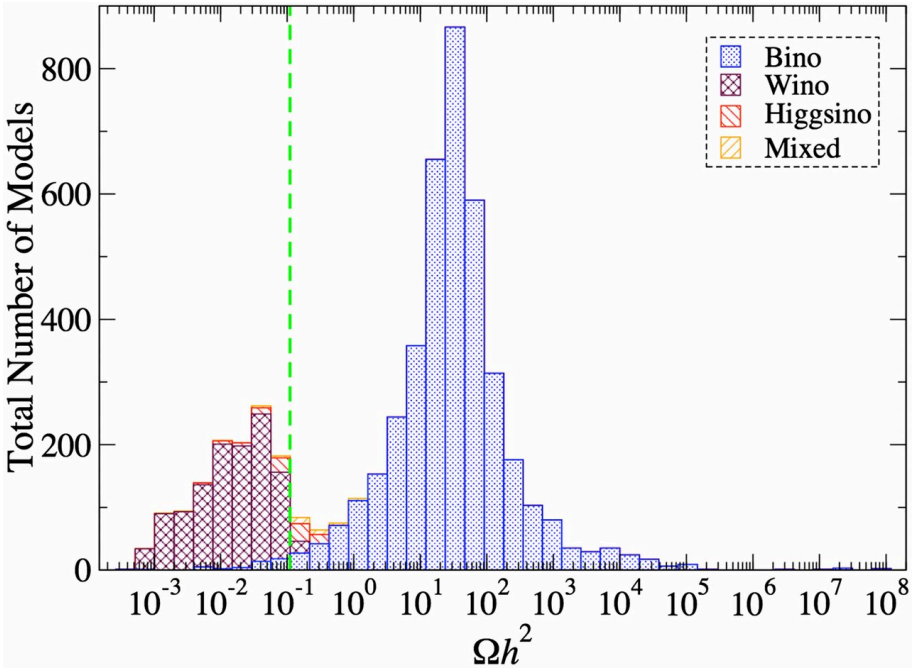

Figure 1.4: Prediction of the dark matter relic density depending on the SUSY model explored [45]. The green dashed line is the observed dark matter relic density observed in the Universe, while the bins refer to different SUSY hypothesis on the neutralino composition.

it can be larger or smaller as it is shown in Figure 1.4. In scenarios where the neutralino is mainly a bino (blue histograms) a mechanism able to reduce the relic dark matter density is needed. This is due to the neutralino-neutralino annihilation cross-section after the freeze-out being smaller than the one required. As a result, a higher relic density than the measured one is obtained. One possible process to fix this behaviour is the so called co-annihilation [46]. In co-annihilation models, the bino self-interaction cross-section is enhanced, leading to smaller values of the relic density. An important condition for co-annihilation to happen is the presence of a second, almost mass-degenerate, particle specie. This arises from the fact that the freeze-out temperature is $m_{\text{freeze}} \sim \frac{m}{20}$ [46], hence any particle whose mass is within m_{freeze} from the LSP and carries the same conserved quantum numbers can contribute to the annihilation of this quantum number [46]. In our case, the quantum number being annihilated is the R-parity. In sbottom-neutralino co-annihilation the mass difference is $\delta m_{\tilde{b}\tilde{\chi}_1^0} = \frac{\left(m_{\tilde{b}} - m_{\tilde{\chi}_1^0}\right)}{m_{\tilde{\chi}_1^0}} \sim 10\%$ or less, which allows one to obtain the correct relic density.

These *compressed* phase spaces produce final states characterised by low-momentum particles, which are challenging to detect at the current collider experiments. A new technique to explore such challenging phase spaces is described in Chapter 4.

Simplified Models

The theoretical framework described by the MSSM is quite complex, and it provides many model-dependent experimental signatures to explore. It is difficult to design an exper-

imental approach which is generic enough. To overcome this problem experimentalists often use simplified models [47–49] which present final state topologies which are phenomenologically simpler. These models allow one to broadly exclude some classes of SUSY models, and can be considered approximations to more realistic SUSY models with more complex spectra. If the LSP is assumed to be a bino and not to mix with other gauginos or higgsinos, then all the electroweakinos except the LSP are heavy. In a natural spectrum, squarks accessible to the LHC could be third generation squarks.
The simplified model assumed for this analysis is shown in Figure 1.5. The underlying

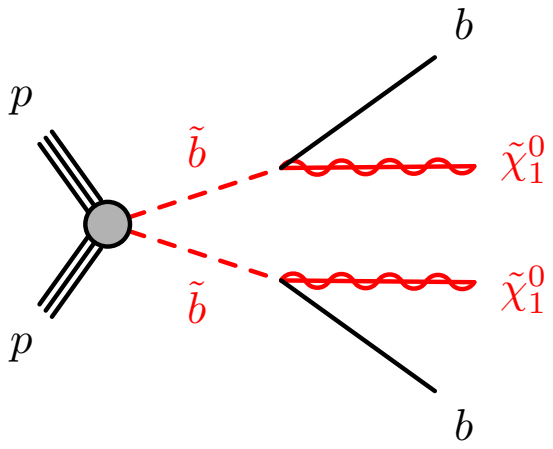

Figure 1.5: Simplified model for the production of scalar bottom quarks pairs decaying into a bottom quark and lightest neutralino.

assumptions behind this specific model are that the scalar bottoms are pair-produced, no other SUSY particles play a role either in the production nor the decay, and the scalar bottom decays into a bottom quark and a neutralino, assumed to be a bino, with a branching ratio (BR) of 100%. The simplified model considered in this analysis is consistent with the hypothesis of co-annihilation occurring between the bino and the scalar bottom quark.
The exclusion limits obtained by using any simplified model can be extended to any SUSY model sharing the same final state.

Other BSM Searches

The analysis presented in this work is based on the simplified model reported in Figure 1.5, and it is part of a rich physics programme for beyond the Standard Model (BSM) searches within the ATLAS collaboration. The production cross sections as function of the sparticle masses for different processes are shown in Figure 1.6. A brief summary of the searches of SUSY particles within the ATLAS collaboration is outlined below.

Strong production. As it can be seen in Figure 1.6, the direct production of gluinos ($\tilde{g}$) and squarks ($\tilde{q}$) benefits from a relatively large cross section, due to the colour charge they carry. In scenarios where the R-parity is conserved, these sparticles are pair-produced

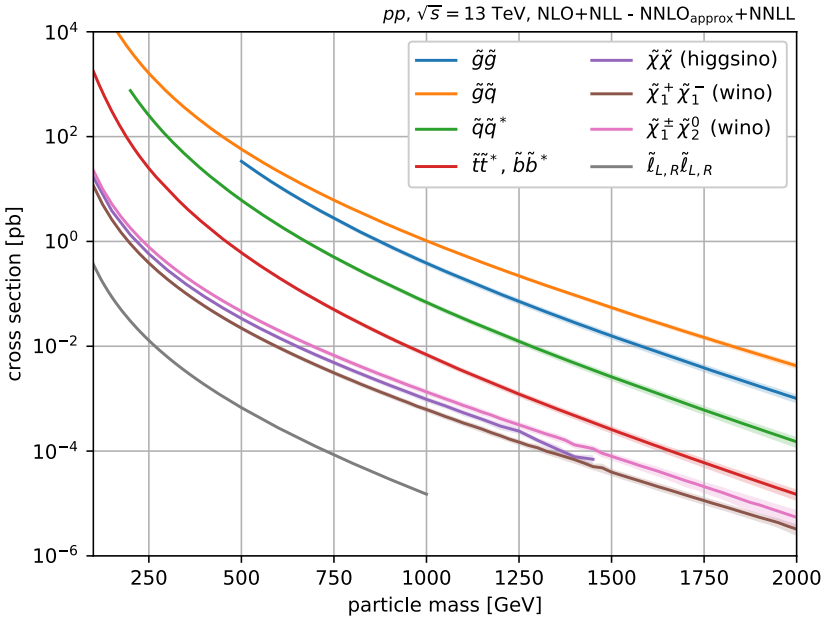

Figure 1.6: Typical cross sections for the production of SUSY particles at the LHC as function of their masses at a centre-of-mass energy of $\sqrt{s} = 13$ TeV.

and their decays always involve the presence in the final state of the LSP. Searches target either simple decays, e. g. a gluino decaying into two quarks and the LSP or a squark decaying into a quark and LSP; or more complex ones, where intermediate particle states are present, causing the presence in the final states of W (1-step) or W and Z (2-step). Due to the decay modes, the final states often present a large number of hadronic jets and large missing transverse momentum, and if the decay involves the presence of vector bosons additional jets or leptons can be required in the final state. Figure 1.7 summarizes the latest observed limit for the strong production for different signal models. 95% CL limits on gluino masses above 2 TeV and on squark masses above 1.8 TeV are set, depending on the model.

Third-generation squark production. The analysis presented in this thesis falls into this category. The motivations for third-generation searches were previously discussed in this Section. The decay of top/bottom squarks implies that common final states for these searches involve the presence of b-hadrons and missing transverse momentum, due to the LSP. The kinematic properties of the final states depend on the mass difference between the third generation squarks and the LSP, and different techniques are exploited to target these different kinematic regions. Chapter 4 presents one such method used to target b-hadrons with low transverse momentum, while other methods not exploited by this analysis but commonly used in third-generation searches involve the top-quark tagging and identification of hadronic jets originated by Initial State Radiation (ISR). Figure 1.8 shows the current 95% CL exclusion limits for third-generation squarks set by the ATLAS collaboration. Top squark masses up to 1.2 TeV are excluded for LSP masses up to 400

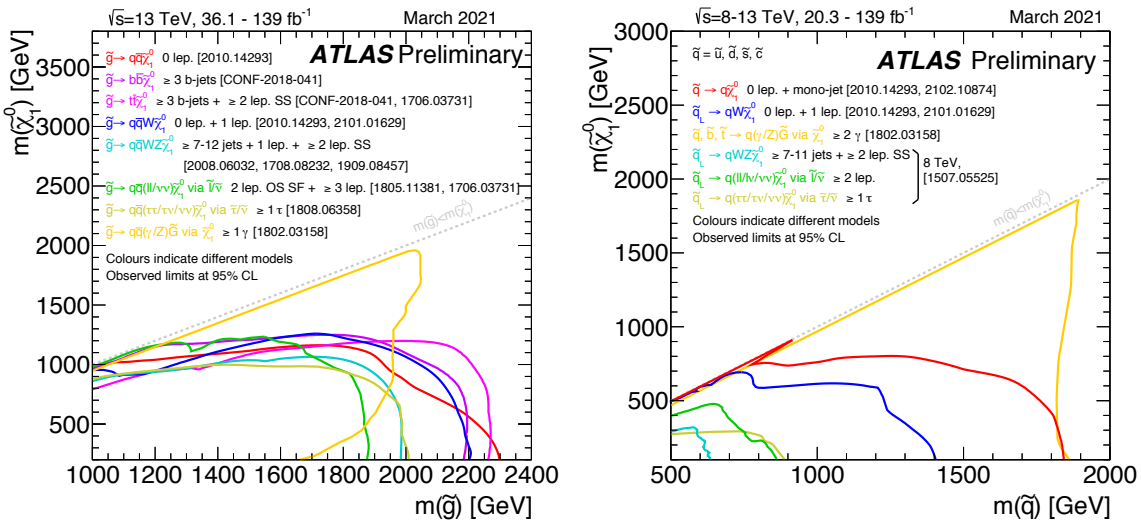

(a) (b)

Figure 1.7: Exclusion limits at 95% confidence limit based on $\sqrt{s} = 13$ TeV data for (a) gluino vs LSP and (b) squark vs LSP mass plane. Each limit refers to a different simplified model where the gluino or the squark decay to the LSP either directly or through an intermediate SUSY particle state. For each line, the decay mode is reported in the legend and it assumes a 100% branching ratio. Some limits depend on additional assumptions on the mass of the intermediate states, as it is reported in the references provided in the plots. Images taken from Ref. [50].

GeV, while the use of dedicated low-p_T b-tagging techniques described in Chapter 4 allows excluding top squark masses up to $\sim$ 600 GeV for LSP masses $\sim$ 600 GeV. Similar results are obtained when excluding models where bottom squark pairs are produced. The limits in Figure 1.8(b) include the analysis presented in this thesis, and which is discussed in Chapter 5 and Chapter 6.

Electroweak production. The direct production of neutralinos, charginos and sleptons, which are regulated by the electroweak interaction, have a smaller cross-section compared to other SUSY production processes mediated by the strong force, as it can be seen in Figure 1.6. These models might be dominant at the LHC if the masses of colour-charged sparticles are not accessible at the current collider energies. Final states originated by the decay of neutralinos and charginos are targeted by looking for missing transverse momentum and the presence of multiple leptons. These can be originated by the presence of intermediate slepton states, or by the production of the second-lightest neutralino together with the lightest chargino, which decay into the Z boson or Higgs boson and a LSP and W boson and a LSP, respectively. The presence of the Higgs boson allows for different final states topologies, e. g. the presence of b-hadrons. Figure 1.9 presents the current 95% CL exclusion limits for the production of charginos and neutralinos, either direct or mediated by the presence of a slepton. Masses of the lightest chargino or second-lightest neutralino up more than 1 TeV are excluded for different LSP masses, depending on the models.

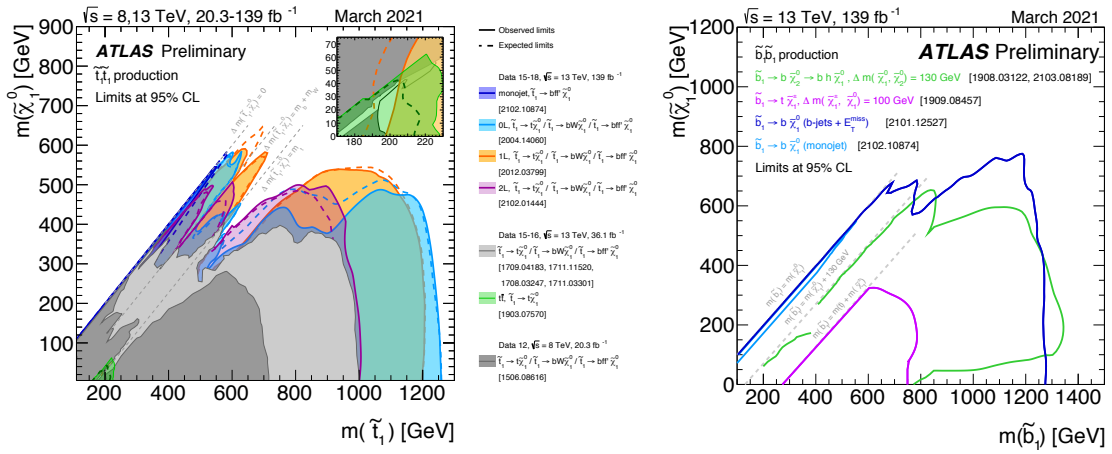

(a) (b)

Figure 1.8: Exclusion limits at 95% CL based on $\sqrt{s} = 13$ TeV data for (a) top squark and (b) bottom squark pair production. The limits are shown in the (a) $(\widetilde{t}_1, \widetilde{\chi}_1^0)$ or (b) $(\widetilde{b}_1, \widetilde{\chi}_1^0)$ mass plane. The solid lines refer to the observed limits while the dashed lines in Figure 1.8(a) refer to the expected limits. For each line, the decay mode is reported in the legend and it assumes a 100% brancing ratio. The green contour discontinuity observed in Figure 1.8(b) is due to the range of $m(\widetilde{b}_1)$ used in the interpretation of the results. Images taken from Ref. [50].

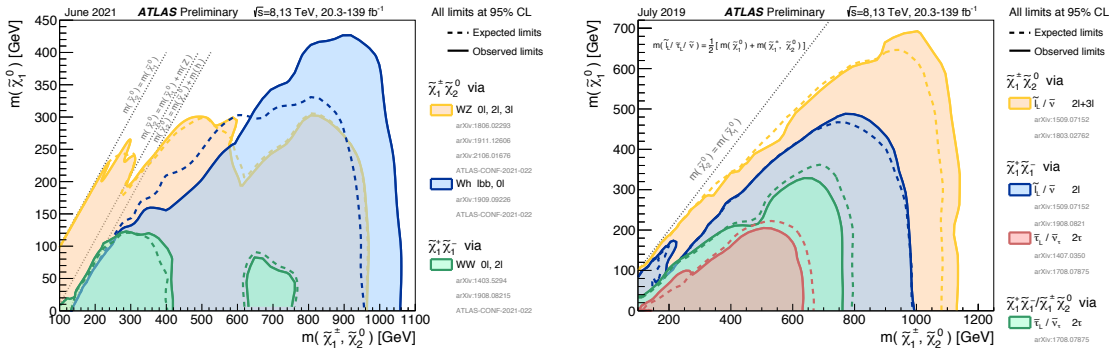

(a) (b)

Figure 1.9: Exclusion limits at 95% CL based on $\sqrt{s} = 13$ TeV data for (a) $\tilde{\chi}_1^+\tilde{\chi}_1^-$ and $\tilde{\chi}_1^\pm\tilde{\chi}_2^0$ production and (b) $\tilde{\chi}_1^+\tilde{\chi}_1^-$ and $\tilde{\chi}_1^\pm\tilde{\chi}_2^0$ production with an intermediate slepton as function as function of the $\tilde{\chi}_1^\pm, \tilde{\chi}_2^0, \tilde{\chi}_1^0$ masses. The solid lines refer to the observed limits while the dashed lines refer to the expected limits. Each individual exclusion contour represent a union of the excluded regions of one or more analyses. Images taken from Ref. [50].

Long-lived particle production. Long-lived particles appear in supersymmetric extensions of the SM, such as the split SUSY [51, 52], where the SUSY breaking occurs at energies $\gg 1000$ TeV, and the scalar bosons acquire mass at this high energy scale while the fermions are protected by the chiral symmetry. These scenarios imply that gluinos would decay via scalar quarks which are highly virtual. This results in a long lifetime which produces bound states known as R-hadrons. The final states of such models imply the presence of displaced vertices in the detector, which are due to the long lifetime of the

R-hadrons.

In SUSY models such as the anomaly-mediated SUSY breaking (AMSB) [53,54], the lightest chargino and neutralino are almost pure wino or higgsino, and they are almost mass-degenerate. This leads to a chargino long-lived particle which decays into a pion and a LSP. The disappearing track due to the pion provides an experimental signature that can be exploited by an analysis. Figure 1.10 presents the most recent limits obtained by the

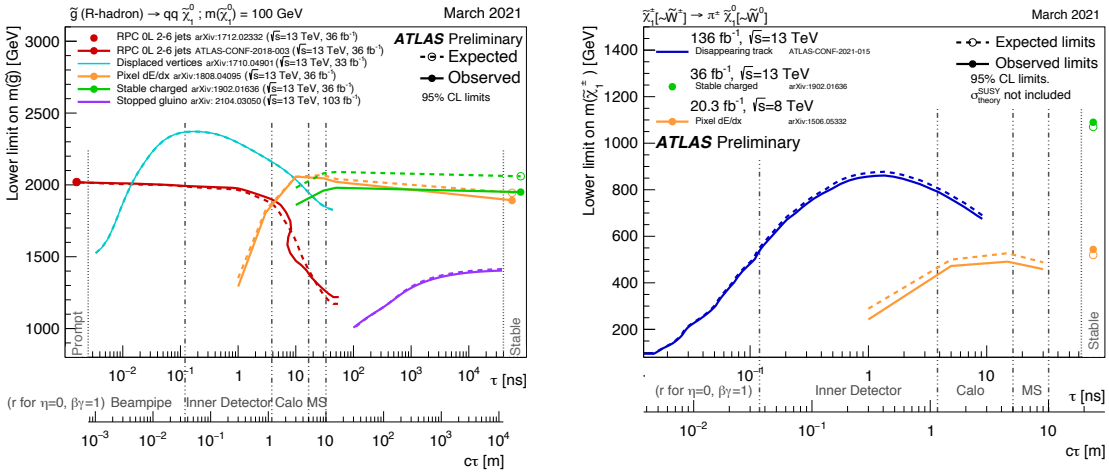

(a) (b)

Figure 1.10: Constraints based on $\sqrt{s} = 13$ TeV data on the (a) gluino and (b) chargino mass-vs-lifetime plane. (a) Split-SUSY model with the gluino *R*-hadron decaying into a gluon or light quarks and a neutralino with mass of 100 GeV. (b) AMSB model with $\tan(b) = 5$ and $\mu > 0$. The wino-like chargino is pair-produced and decays to the wino-like neutralino and a very soft charged pion. The solid lines indicate the observed limits, while the dashed lines indicate the expected limits. The area below the curves is excluded. In this context, stable means escaping the detector. Images taken from Ref. [50].

ATLAS collaboration for thee gluino and chargino masses as function of the long-lived particle lifetime. The sensitivity is scanned over various values of the gluino and chargino lifetimes, and stringent limits are set for a range of values.

***R*-parity violating processes.** So far only processes assuming *R*-parity conservation were discussed. If this conservation is not assumed a much larger parameter space can be studied. The SUSY Lagrangian for *R*-parity violating (RPV) processes has Yukawa and bilinear couplings which violates the lepton and baryon numbers:

$$\mathcal{L}_{\text{RPV}} = \frac{\lambda_{ijk}}{2} L_i L_j \bar{E}_k + \lambda'_{ijk} L_i Q_j \bar{D}_k + \frac{\lambda''_{ijk}}{2} \bar{U}_i \bar{D}_j \bar{D}_k + \kappa_i L_i H_u, \tag{1.45}$$

where: i, j, k are the quark and lepton generational indices; L_i and Q_i are the lepton and quark $SU(2)_L$ doublet superfields; H_u is the Higgs superfield coupling to the up-type quarks; $\bar{E}_i$, $\bar{D}_i$ and $\bar{U}_i$ are the lepton, down-type quark and up-type quark $SU(2)_L$ singlet superfields; κ is a dimensional mass parameter; λ, λ' and λ'' are the couplings which quantify the violation of the lepton and baryon numbers violation.

The final-state topology in a RPV model depends on the λ parameters in Equation 1.45. A key difference with the R-parity conserving models is that in RPV models the LSP decays into SM particles. Some examples of RPV models are presented below.

– *Gqq model*: it assumes that the only non-zero RPV coupling is the λ''_{112}. Scenarios where the gluiono is light and the lightest neutralino is the LSP, the gluino can decay via the usual $\tilde{g} \to qq\tilde{\chi}_0^1$ with the subsequent LSP decay as $\tilde{\chi}_0^1 \to qqq$.

– *Gtt model*: it assumes that the only non-zero RPV coupling is the λ''_{323}. This implies that the decay $\tilde{g} \to tt\tilde{\chi}_0^1$ is possible, and the LSP subsequently decays as $\tilde{\chi}_0^1 \to tbs$.

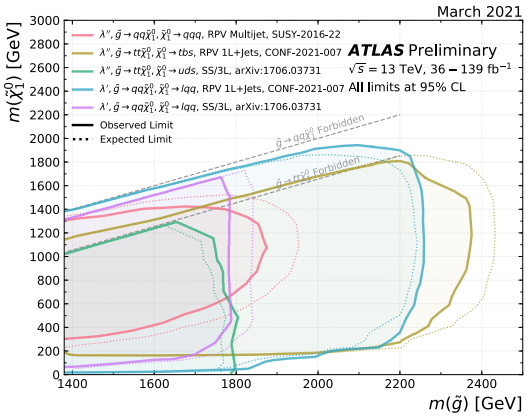

(a)

Figure 1.11: Exclusion limits at 95% CL based on $\sqrt{s} = 13$ TeV data in the $(\tilde{g}, \tilde{\chi}_1^0)$ mass plane for different simplified models. The gluino decay to the LSP, which in turn decays via R-parity violating couplings to SM particles. For each line, the gluino decay mode is reported in the legend and it assumes a 100% branching ratio. The solid lines refer to the observed limit, while the dashed lines refer to the expected limits. Some limits depend on additional assumptions, as described in the references provided in the plot. Image taken from Ref. [50].

Figure 1.11 shows the limits on the gluino mass as function of the LSP for different RPV scenarios.

So far the direct searches for SUSY were presented. It is possible to constrain SUSY indirectly, for example using data from flavour physics experiments. The rare $B_S \to \mu\mu$ decays are strongly suppressed and precisely determined in the SM. Many SUSY models predict deviations [55–59], which are investigated by the ATLAS and LHCb collaborations [60, 61]. So far no deviations are observed, placing indirect limits on SUSY models. Other constraints can be placed by looking for precision SM measurements in the Higgs sector [62, 63]. Astrophysical data, such as the determination of the dark matter relic densitiy, can place additional limits on many SUSY models [27].

1.4 Summary

The work of this thesis is based on the SM and SUSY theories introduced in this Chapter. The SM was described in Section 1.1. The spontaneous symmetry breaking mechanism leading to the Higgs interaction is described alongside the description of the electroweak and strong fundamental forces. Although the SM is a successful theory, it has some limitations such as the inability to explain the observation of dark matter in the Universe. These limitations were addressed in Section 1.2. Finally Section 1.3 presented the SUSY theory, which if discovered would provide with a powerful framework to address more of the open issues within the SM. Alongside the general definition and phenomenological consequences of the theory, some space was given to describe some of the compressed SUSY models which are investigated in this thesis.

LHC and the ATLAS Detector

2

The work of this thesis is based on data collected by the ATLAS detector at the Large Hadron Collider. This Chapter describes the experimental apparatus needed to perform this analysis.
Section 2.1 describes the Large Hadron Collider accelerator complex, while Section 2.2 presents the ATLAS detector.

2.1 The Large Hadron Collider Accelerator Complex

The Large Hadron Collider (LHC) [64] is the world's most powerful accelerator and particle collider. It is 26.7 km long and it is placed underground at a depth between 45 m and 170 m on the border between France and Switzerland. The LHC is a collider designed to accelerate and collide protons or heavy nuclei. Its design consists of two concentric superconducting rings where the particles run clockwise in one pipe and counterclockwise in the other. The superconducting magnets are kept at a temperature of approximately 2 K. The LHC hosts seven main experiments: the two *multi-purpose* experiments ATLAS [65] and CMS [66]; and five specialised experiments: ALICE [67], LHCb [68], LHCf [69], TOTEM [70] and MoEDAL [71].

The LHC accelerates protons from an initial energy of 450 GeV to 6.5 TeV providing proton-proton (pp) collisions at a centre-of-mass energy of $\sqrt{s} = 13$ TeV. The whole accelerator complex is diagrammatically presented in Figure 2.1. Protons are obtained by stripping off electrons from a hydrogen gas. The first step in the pre-acceleration chain is provided by the Linac2, a linear accelerator, which accelerates the protons up to an energy of 50 MeV. The protons are then accelerated by the Proton Synchrotron Booster (PSB) up to an energy of 1.4 GeV and by the Proton Synchrotron (PS) up to 25 GeV. The final pre-acceleration step is achieved in the Super Proton Synchrotron (SPS) where the protons are accelerated up to 450 GeV.

Another important characteristic of a particle accelerator is its nominal instantaneous luminosity, which is 10^{34} cm^{-2}s^{-1} for the LHC . This value is determined by several

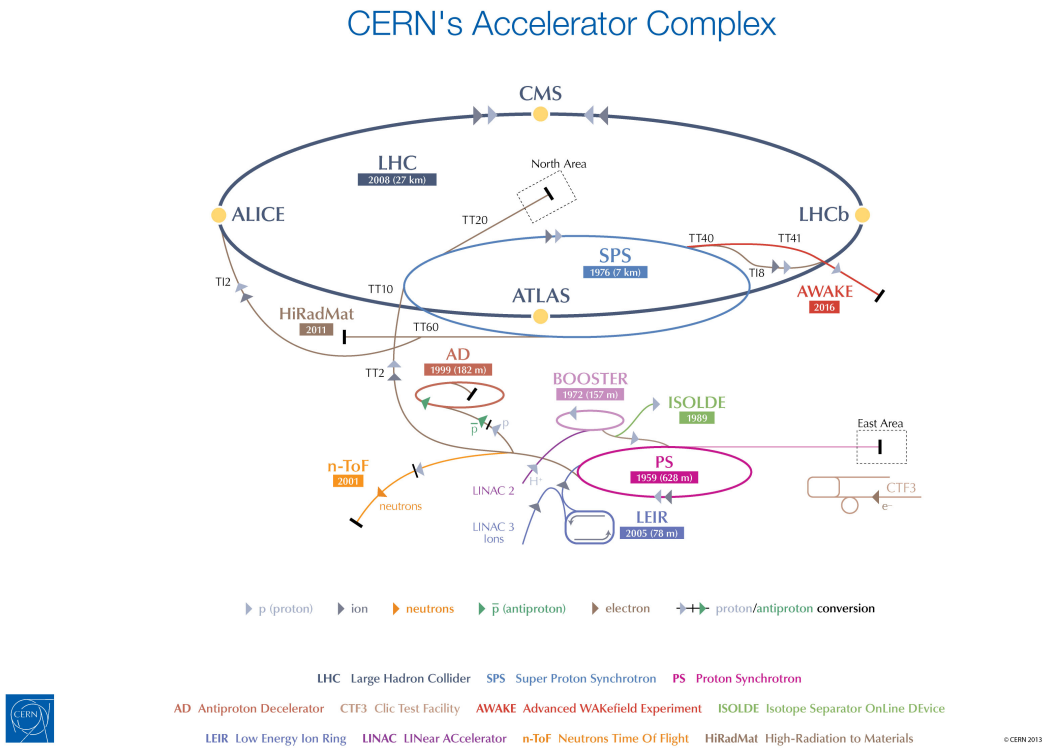

Figure 2.1: The CERN accelerator complex. Image taken from Ref. [72].

design parameters according to Equation 2.1:

$$\mathcal{L} = \frac{N_b^2 n_b f_{\text{rev}} \gamma}{4\pi \varepsilon_n \beta^*} F, \tag{2.1}$$

where:

- N_b is the number of protons in each bunch, nominally 1.15×10^{11} during Run 2;
- n_b is the number of bunches per beam, 2808;
- f_{rev} is the revolution frequency, 11245 kHz
- γ is the relativistic gamma factor;
- ε_n is the normalised transverse beam emittance, 3.75 μm . It is a measure of the spread of the beam particles in position and momentum phase-space. ε_n remains constant as the beam changes energy;
- β^* is the beta function at the collision point, 180 m. It is defined as the distance between the interaction point (IP) and the point where the beam width has double the width at this point. The β^* gives an idea of how squeezed the beam is;
- F is a reduction factor in the luminosity due to the beam crossing at an angle at the interaction point.

The total amount of data delivered by the LHC is given by the integrated luminosity:

$$\mathcal{L}_{\text{int}} = \int \mathcal{L} dt. \tag{2.2}$$

The total number of events for a given physical process with cross-section σ_{event} is therefore:

$$N_{\text{event}} = \mathcal{L}_{\text{int}} \sigma_{\text{event}}. \tag{2.3}$$

It is possible to express the instantaneous luminosity as function of the number of interactions per bunch crossing μ. The bunch luminosity is defined as:

$$\mathcal{L}_{\text{b}} = \frac{\mu f_{\text{rev}}}{\sigma_{\text{inel}}}, \tag{2.4}$$

where σ_{inel} is the pp inelastic cross-section. It is possible to recast Equation 2.1 using the average number of pp collisions per bunch-crossing $\langle\mu\rangle$ as:

$$\mathcal{L} = \sum_{b=1}^{n_b} \mathcal{L}_b = n_b \langle \mathcal{L}_b \rangle = \frac{\langle\mu\rangle n_b f_{\text{rev}}}{\sigma_{\text{inel}}}. \tag{2.5}$$

The mean number of interactions per bunch crossing during Run 2 is reported in Figure 2.2. The total integrated luminosity delivered by LHC during Run 2 is shown in

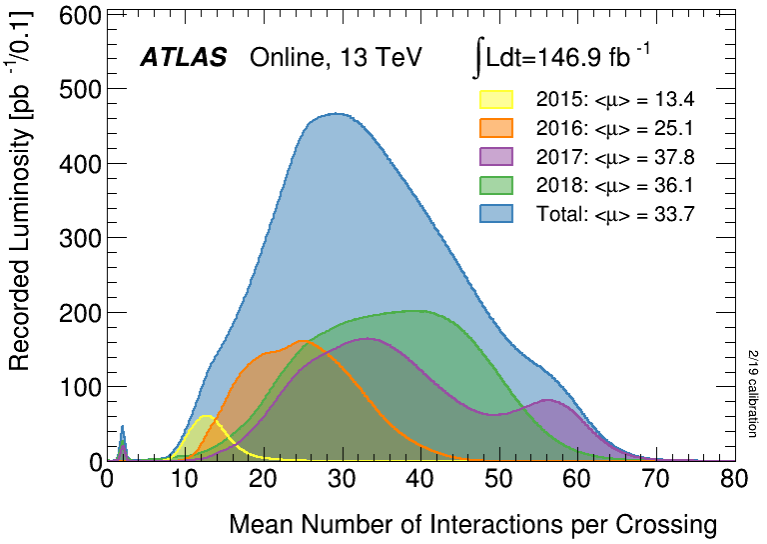

Figure 2.2: Distribution of the mean number of interactions per bunch crossing during Run 2. The distribution refers to pp collision data at $\sqrt{s} = 13$ TeV centre-of-mass energy. Data recorded during stable beams is shown. The total and year-by-year distributions of $\langle\mu\rangle$ are shown, together with the total recorded integrated luminosity. Imagine taken from Ref. [73].

Figure 2.3, together with the total luminosity recorded by the ATLAS experiment. This can be expressed as:

$$\mathcal{L}_b^{\text{recorded}} = \frac{\mu_{\text{vis}} f_{\text{rev}}}{\sigma_{\text{vis}}}, \tag{2.6}$$

where $\mu_{\text{vis}} = \epsilon\mu$ is the number of interactions per bunch crossing μ multiplied by the detector efficiency, and $\sigma_{\text{vis}} = \epsilon\sigma_{\text{inel}}$ is the pp inelastic cross section multiplied by the detector efficiency.

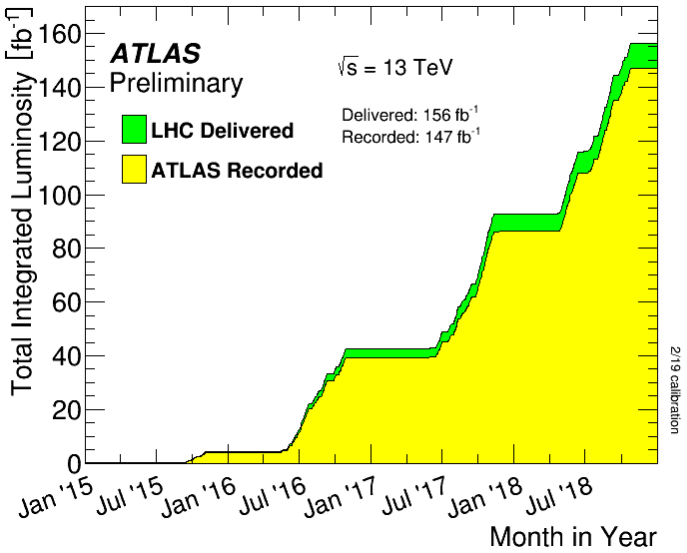

Figure 2.3: Integrated luminosity provided by the LHC (in green) and recorded by the ATLAS detector (in yellow) during Run 2. Image taken from Ref. [73].

2.2 The ATLAS Detector

The unprecedented luminosity provided by the LHC allows the exploration of a vast range of physical processes, ranging from precise SM measurements, to the search for the Higgs boson and the study of its properties and the search for new BSM phenomena, as introduced in Chapter 1. Pursuing such a vast physics program is possible by using so-called multi-purpose detectors. Two such detectors are located on the LHC ring: The ATLAS detector [65]; and the CMS detector [66].
The geometry of the ATLAS detector is presented in Figure 2.4.

Following the multi-purpose design, several sub-detectors are installed in a concentric, cylindrical geometry. Starting from the centre of the detector outwards, the sub-detectors are:

- the *Inner Detector (ID)*, whose goal is measuring charged particles' transverse momenta by tracking them in a solenoidal magnetic field. This sub-detector consists of pixel and micro-strip semiconductor detectors and a transition-radiation tracker;

- the *Calorimeter System*, whose goal is measuring the energy deposit originating from electromagnetically- and strongly-interacting particles. This sub-detector consists of liquid argon (LAr) electromagnetic (EM) calorimeter, LAr end-cap and forward hadronic calorimeters, and tile calorimeters;

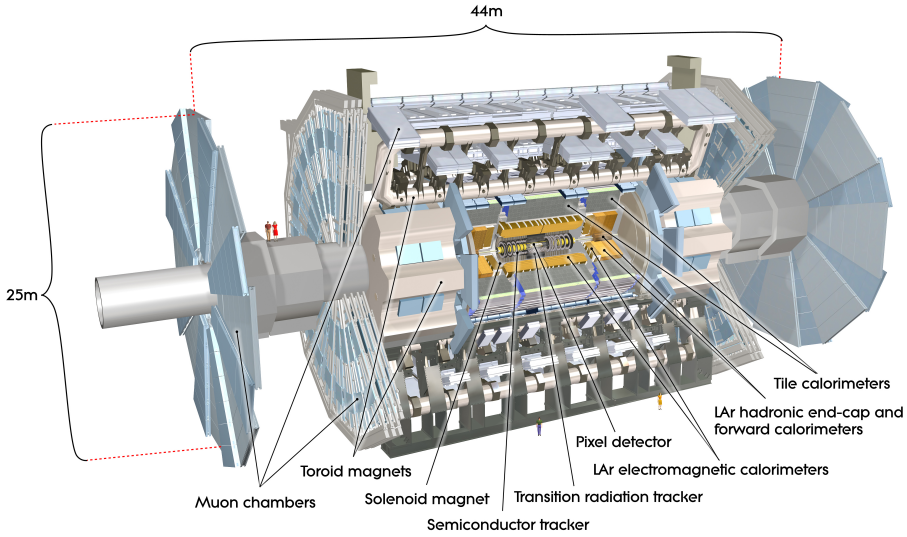

Figure 2.4: Schematic view of the ATLAS detector, with cartoon humans to give a sense of the scale. The detector measures 25 m in height and 44 m in length, with an overall weight of approximately 7000 tonnes. Image taken from Ref. [65].

– the *Muon Spectrometer*, which measures the muons' momenta by tracking them in a toroidal magnetic field. This sub-detector consists of monitor drift tubes, cathode strip chambers, resistive plate chambers and thin gap chambers.

The ATLAS detector is designed to achieve the resolution goals for of each sub-detector reported in Table 2.1.

To measure the momentum of charged particle in the ID and muon spectrometer a

Table 2.1: Designed resolution of each ATLAS detector component from Ref. [65]. Units for E and p_T are GeV.

Detector component	**Required resolution**	η **coverage**
Tracking	$\sigma_{p_T}/p_T = 0.05\% p_T \oplus 1\%$	± 2.5
EM calorimetry	$\sigma_E/E = 10\%/\sqrt{E} \oplus 0.7\%$	3.2
Hadronic calorimetry		
barel and end-cap	$\sigma_E/E = 50\%/\sqrt{E} \oplus 3\%$	3.2
forward	$\sigma_E/E = 100\%/\sqrt{E} \oplus 10\%$	$3.1 < \lvert\eta\rvert < 4.9$
Muon Spectrometer	$\sigma_{p_T}/p_T = 10\%$ at $p_T = 1$ TeV	± 2.7

magnetic field is needed. The ATLAS magnet system consists of two separate magnetic fields, generated by three sub-modules:

– a *solenoidal* magnetic field, which is generated by a thin solenoidal magnet surrounding the ID cavity. The solenoidal field is used to bend charged particles in the ID;

– a *toroidal* magnetic field, which is generated by a barrel and two end-cap toroidal magnets providing a magnetic field to the cylinder body surrounding the calorimeters

and the end-cap toroids. The toroidal field is used to bend the muons.

In the following the component of the ATLAS detector are presented in more detail.

Coordinate System

The ATLAS coordinate system has its origin at the nominal IP. Starting from that origin, the x-axis is the direction joining the interaction point and the LHC centre; the y-axis points upwards from the interaction point; the z-axis is defined by the beam direction. The three axes form a right-handed Cartesian reference frame. Because of the cylindrical geometry, it is convenient to use a spherical frame of reference. This is defined by the azimuthal angle ϕ on the $x-y$ transverse plane; and the polar angle θ, which is defined with respect to the z-axis. For LHC physics, when the mass of the particles cannot be neglected the θ angle can be replaced with the rapidity y, a quantity which is additive under Lorentz boosts in the z direction, defined as:

$$y = \frac{1}{2}\ln\left(\frac{E+p_z}{E-p_z}\right), \tag{2.7}$$

where p_z is the projection of the the particle momentum p on the z-axis. If the particle can be assumed massless, i. e. $m << |\mathbf{p}|$, then the pseudo-rapidity η can be defined as:

$$\eta = -\ln\left[\tan\left(\frac{\theta}{2}\right)\right]. \tag{2.8}$$

The angular difference ΔR in the azimuthal-pseudorapidity space is defined as

$$\Delta R = \sqrt{\Delta\eta^2 + \Delta\phi^2}, \tag{2.9}$$

which is Lorentz-invariant if the mass of the particle is negligible. If this condition is not met, the Lorentz invariance is kept by using the rapidity y in place of η.

Magnets

The ATLAS magnet system [74] features a unique hybrid layout, which is shown in Figure 2.5. It provides the magnetic field needed to bend the charged particle in both the ID and muon system. The magnet system measures 22 m in diameter and 26 m in length, and it consists of one solenoid and three toroid systems, and it is described below.

- The *solenoid* surrounds the ID and provides a magnetic field of 2 T obtained at a nominal operational current of 7.740 kA. The magnet, which is only ~ 0.66 radiation lengths thick, is required to be as thin as possible to avoid generating an EM shower before the electromagnetic calorimeter.
- The *toroid* magnet system consist of three modules: the barrel toroid and two end-cap toroids. The *barrel* magnet system and each of the two *end-cap* toroids are

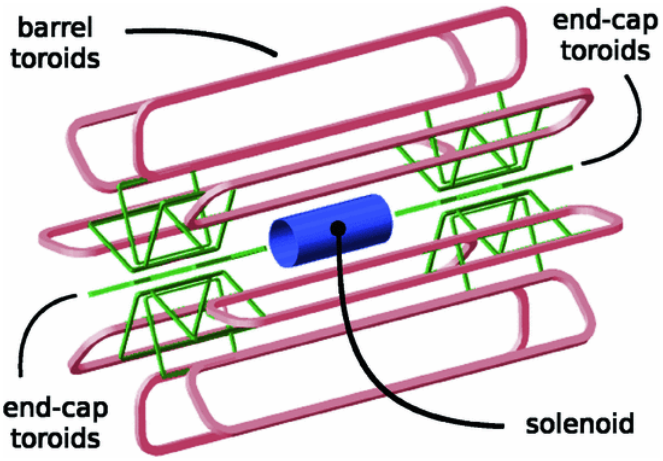

Figure 2.5: View of the ATLAS magnet system. Imagine taken from Ref. [74].

made up of eight coils, and they provides a peak magnetic field of 4 T at a nominal operational current of 20.5 kA used by the muon detectors in the central and end-cap regions.

Inner Detector

The ID is the first array of subdetectors surrounding the beam pipe, and it is designed to precisely measure the charged particles' tracks with high momentum resolution, and to perform vertex reconstruction. To do so, ID exploits the 2 T magnetic field provided by the barrel solenoid to bend the charged particles in the $x-y$ plane. The ID also provides an early identification of electrons in the transition radiation detector over $|\eta| < 2$ and in a p_T range of 0.5 GeV $< p_T <$ 150 GeV.
A charged particle entering a uniform magnetic field observes a helical trajectory, whose projection on the $x-y$ plane would be an arc of circumference. The radius of this circumference is related to the charged particle's momentum by:

$$p = eB \cdot R \tag{2.10}$$

where B is the magnetic field and e is the electric charge of the incoming particle.
The particle's momentum can be measured with a resolution expressed as:

$$\frac{\Delta p}{p} = \frac{\Delta R}{R} = \frac{L^2}{8Rs} \cdot \frac{\Delta s}{s}, \tag{2.11}$$

where s is the sagitta, Δs is the spatial resolution associated to the measure of the sagitta, and L is the thickness of the spectrometer. The sagitta s, the radius of the particle's trajectory R and the spectrometer thickness L are related by

$$s = \frac{L^2}{8R}. \tag{2.12}$$

By using this relation, it is possible to recast Equation 2.11 as

$$\frac{\Delta p}{p} = \frac{\Delta s}{L^2} \cdot 8R \sim p \cdot \frac{\Delta s}{eBL^2}, \tag{2.13}$$

which shows how the momentum resolution in a magnetic spectrometer decreases with the increasing particle momentum, and it depends on the spatial resolution Δs.
The ID, which is shown in Figure 2.6, extends radially from the beam pipe to a distance of 1150 mm and longitudinally to $|z| = 3512$ mm. This translates to an overall coverage of $|\eta| < 2.5$. At inner radii, given the larger particle density, a higher spatial resolution

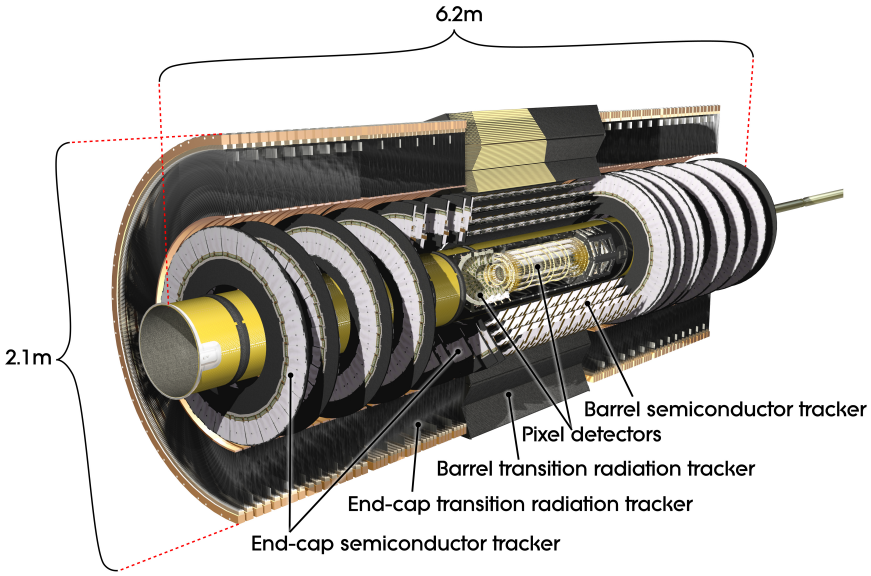

Figure 2.6: Cut view of the ATLAS inner tracker detector. The image, taken from Ref. [65], does not show the IBL.

is needed. This is achieved by using silicon pixel detectors which are surrounded by stereo pairs of silicon micro-strips. These sub-detectors are arranged on concentric cylinders around the beam axis in the barrel region, while in the end-cap regions they are arranged on disks perpendicular to the beam axis. Further from the beam pipe, and with lower particle density, the transtion radiation tracker (TRT) provides a complementary, continuous tracking to enhance pattern recognition and momentum resolution in the central region $|\eta| < 2.0$.
In the following, the sub-detectors constituting the ID are described in more detail.

Silicon Pixel Detector

The silicon pixel detector is the innermost module of the ID. According to the original design the barrel pixel detector is composed of three layers whose active surfaces range between 50.5 mm and 122.5 mm and cover the longitudinal length $|z| < 400.5$ mm in the barrel region. Each end-cap is instrumented with three disks placed at a radial distance ranging between 88.8 mm and 149.6 mm, and longitudinally between 495 mm $< |z| <$ 650 mm. The pixels are 250 μm thick, with a nominal size of 50 $\times$ 400 μm^2. This allows an intrinsic accuracy of 10 μm in the $(R - \phi)$ direction, and 115 μm along the z direction. Before the beginning of Run 2, an extra layer of pixel, the insertable B-layer (IBL) [75] has been placed closest to the beam pipe, at 33.25 mm. This module has been added to enhance

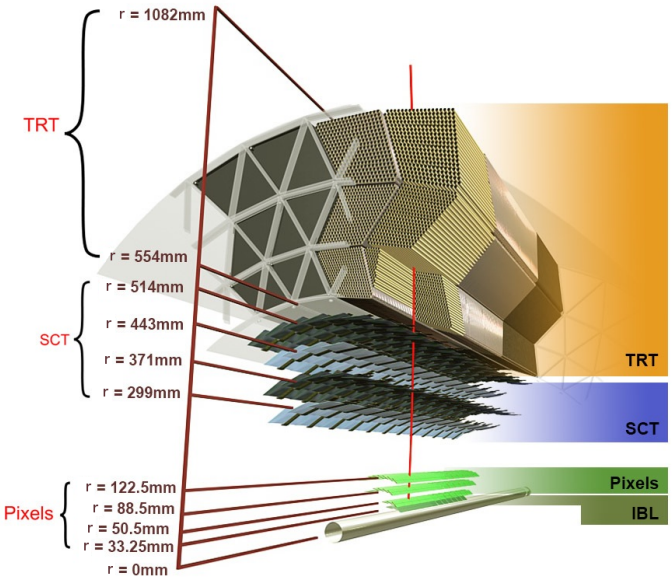

Figure 2.7: View of the ATLAS tracking system from Ref. [77]. The figure reports the distances of each layer from the pipeline. The IBL is included.

the tracking and the jet flavour and vertex identification by providing an extra measurement point, and to be more robust for the increased luminosity and pileup conditions. A radial view of the ID including the IBL is shown in Figure 2.7.
The pixel sensors are made by implanting high positive (p^+) and high negative (n^+) charges in a n-type bulk wafer [76]. The sensitive, depleted region is formed at the $p^+ - n$ junction, and it is extended by using a reverse-bias configuration. This extends the depleted region over the bulk volume, where is possible to collect and detect the charge generated in the sensitive volume by the ionising particles crossing the pixel.

Semi-Conductor Tracker

The semi-conductor tracker (SCT) is the intermediate module of the ID. By design it consists of four cylindrical layers in the barrel, it ranges between 299 mm and 514 mm in the radial direction, and it covers the longitudinal length $|z| < 749$ mm. Each end-cap region is instrumented with nine disks, ranging between 275 mm and 560 mm in the radial direction, and 839 mm $< |z| <$ 2735 mm in the beam pipe direction. Unlike the pixel detectors, the SCT strips offer a high spatial resolution in one direction only. For this reason the modules are two-sided, which means that two strips are glued together to provide a precise two-dimensional measurement. The strips are 285 ± 14 μm thick, 80 μm wide, 12 cm long and provide the SCT with an intrinsic accuracy of 17 μm in the $R - \phi$ direction and 580 μm in the z direction.

Transition Radiation Tracker

The TRT is the outermost module of the ID. In the barrel region, 73 straw tube planes are placed at a distance from the beam pipe ranging between 563 mm and 1066 mm, and it grants a longitudinal covering in the range $0 < |z| < 712$ mm. In the two end-cap regions 160 straw tubes are placed at a distance ranging between 644 mm and 1004 mm in the radial direction, and between 848 mm $< |z| <$ 2710 mm in the longitudinal direction. Each straw tube measures 4 mm in diameter, while their length varies from 37 cm for the end-cap to 144 cm for the barrel tubes. Their walls are made of polyimide and are 35 μm thick. Each tube is filled with a gas mixture of 70% Xe, 27% CO_2 and 3% O_2. The charges produced in the gas by ionising particles are collected in $\sim$ 50 ns with an operational drift-time accurance of $\sim$ 130 μm in the $R-\phi$ direction, while no information is provided along the z-direction. The TRT can discriminate between two signals, according to their amplitude: the lowest charge is due to the minimum-ionising particles (MIPs) crossing the gas, while the strongest signal is given by the transition-radiation photons absorbed in the gas. This last class of events is originated by the electrons, hence the TRT is able to contribute to electron identification on a straw-by-straw basis.

Calorimeter Systems

Calorimeters are designed to measure the total energy of a particle. To do so, the particle needs to release all its energy within the calorimeter, and this energy needs to be measured. Depending on how the particle interacts with the detector there are two different kind of calorimeters: electromagnetic and hadronic calorimeters.
The electromagnetic calorimeters measure the energy loss due to the ionisation. The particles whose energy can be entirely recorded by this calorimeter are photons and electrons, which interact with the calorimeter medium through electromagnetic processes such as bremsstrahlung and pair production. The characteristic parameters defining an electromagnetic calorimeter are the radiation length X_0, which is the length needed for an electron to reduce its energy to $1/e$ by radiative processes only, and the Moliere radius, which is the radius of the cone which contains the 90% of the particle's shower produced by the incoming particle. Both these parameters depend on the material. To fully contain a shower the electromagnetic calorimeters tend to be 15-30 X_0 deep.
The hadronic calorimeters are designed to measure the particle showers originated by nuclear interactions of hadrons with the detector. In this case the nature of the interaction is not continuous, but lumpy. The characteristic parameter is the interaction length λ_I, which depends on the material. To fully contain a shower the hadronic calorimeters tend to be 5-8 λ_I deep.
Calorimeters can be classified into two groups, depending on the building principle: the *continuous* calorimeter and the *sampling* calorimeter. The main difference between the two is in the material making up the calorimeter. In a continuous calorimeter the entire volume consists of active material, which means that the particle crossing the detector

continuously loses energy in the medium, and the deposited energy can be collected and measured across the entire volume. A sampling calorimeter is instead made of two different materials: there is an absorbing material, usually a metal, which is where the particle interacts; and an active material, a scintillator, which collects the deposited energy and creates the signal. As a consequence, only a fraction of the particle's shower energy is measured. This implies that sampling calorimeters typically have a worse energy resolution than the continuous calorimeters. The ATLAS calorimeters are sampling calorimeters.

Since calorimeters are devoted to fully reconstruct the particle energy, they need to fully contain the showers, and they are designed to cover as much of the solid angle as possible. The energy resolution of a calorimeter improves with the particle's energy, and it can be parametrised as:

$$\frac{\sigma_E}{E} = \frac{A}{\sqrt{E}} \oplus \frac{B}{E} \oplus C, \tag{2.14}$$

where:

- $\frac{A}{\sqrt{E}}$ is referred to as the *stochastic* term to the energy resolution. The interaction of the incoming particle with the detector and its energy loss are statistical processes, hence the energy resolution is related to the statistical fluctuation of factors like shower fluctuation, photoelectron statistics, dead material and sampling fluctuations for MIP. The statistical nature of this term is expressed by the energy dependence which reflects a Poissonian statistic. The value of A varies depending on the different kind of calorimeters, ranging from a few percent for the continuous calorimeters to several tens of percentage for the sampling calorimeters.

- $\frac{B}{E}$ is referred to as the *noise* term. It is due to electronic readout noise and it has a flat contribution to the energy resolution. Given the inverse proportionality to the energy, for high enough particle energies this term can be neglected.

- C is the *constant* term to the energy resolution. It has no energy dependence and it is due to detector non-uniformity and calibration uncertainties. High radiation environment due to high luminosity contributes as well. This term can be usually reduced down below one percent.

The ATLAS calorimeters are schematically reported in Figure 2.8. They cover almost the whole solid angle thanks to an azimuthal coverage down to $|\eta| < 4.9$ and full ϕ coverage due to the cylindrical geometry. The calorimeters are also thick enough allowing the full measurement of the particles' energy. This allows one to precisely measure the missing transverse momentum ($E_{\mathrm{T}}^{\mathrm{miss}}$) which is an essential requirement to perform SUSY searches. In the following the individual components of the ATLAS calorimeter system are presented.

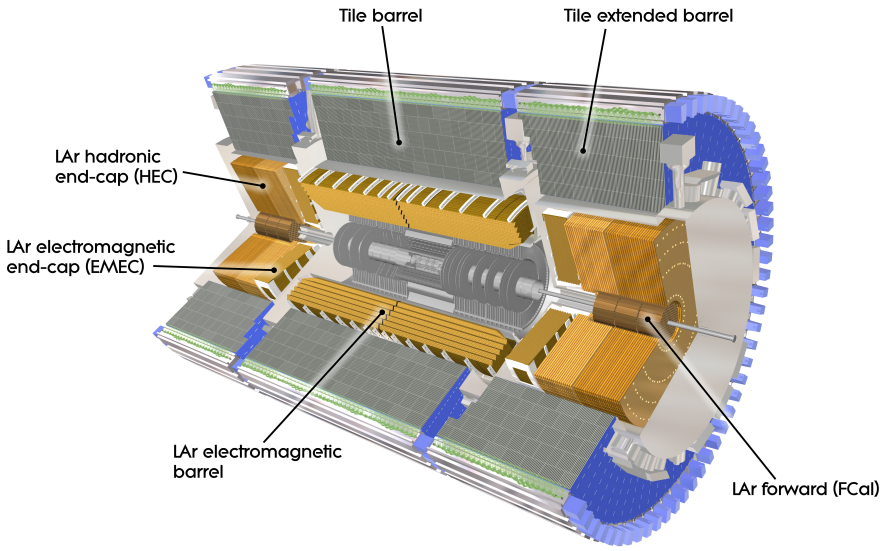

Figure 2.8: Cut view of the ATLAS calorimeter system. Image taken from Ref. [65].

Electromagnetic Calorimeter

The ATLAS electromagnetic calorimeter (ECAL) is made of three modules: the central barrel, with acceptance $|\eta| < 1.475$; and two end-caps covering $1.375 < |\eta| < 3.2$. ECAL is designed with an *accordion* geometry ensuring homogeneity of the detector in the azimuthal direction and reduced extraction time. The active material is LAr interleaved with copper and kapton electrodes, while the absorber material is lead. A LAr pre-sampler is placed in front of ECAL in the $|\eta| < 1.8$ region to correct for energy loss in the ID, solenoid and cryostat. The total thickness of ECAL is $> 22\ X_0$ in the barrel and $> 24\ X_0$ in the end-cap regions. The calorimeter designed energy resolution at $\eta = 0$ is of the order of

$$\frac{\sigma_E}{E} = \frac{10\%}{\sqrt{E}} \oplus 0.7\%. \tag{2.15}$$

Tile Calorimeter

The tile calorimeter is a hadronic calorimeter (HCAL) located in the barrel region. It entirely surrounds the ECAL. In this module plastic scintillator tiles are used as active material, which are interleaved with steel as absorbing material. Similarly to the ECAL, the tile calorimeter is divided into a central barrel module, covering $|\eta| < 1.0$, and two extended barrels either side covering $0.8 < |\eta| < 1.7$. It is segmented in depth into three layers, approximately 1.5, 4.1, 1.8 λ_I in the central barrel region, and 1.5, 2.6, 3.3 λ_I in the extended barrel regions. The total detector thickness at the outer instrumented region is 9.7 λ_I at $\eta = 0$. The scintillation light produced in the plastic scintillators is collected using wavelength-shifter optical fibres, and it is read by photomultiplier tubes.

Hadronic End-Cap

The hadronic end-cap (HEC) calorimeter is responsible for the measure of hadronic showers in the end-cap regions. It consists of two wheels per end-cap which are placed behind the ECAL end-caps. The active material is LAr with copper and kapton readout electrodes, while the absorbing material is copper. The HEC covers the pseudorapidity region $1.5 < |\eta| < 3.2$, hence overlapping with the tile and forward calorimeters. Both the tile calorimeter and HEC provide a designed energy resolution at $\eta = 0$ of the order of

$$\frac{\sigma_E}{E} = \frac{50\%}{\sqrt{E}} \oplus 3\%. \tag{2.16}$$

Forward Calorimeter

The forward calorimeters (FCALs) extend the ATLAS calorimeter system covering the region $3.1 < |\eta| < 4.9$. It is approximately 10 λ_I thick, and it uses LAr as active material. FCAL is divided into three modules per each end-cap: the first is optimised for measuring electromagnetic showers and its absorber material is copper; the other two modules are devoted to measure the showers originated by the hadronic processes and use tungsten as absorber material. The high thickness is needed to suppress the background radiation in the muon chambers. FCAL provides a design energy resolution at $\eta = 0$ of the order of

$$\frac{\sigma_E}{E} = \frac{100\%}{\sqrt{E}} \oplus 10\%. \tag{2.17}$$

Muon Spectrometer

Muons are the only charged particles which are not stopped by the calorimeters. They leave a track in the ID and subsequently in the muon chambers. The ATLAS muon system layout is shown in Figure 2.9. This system is devoted to the precise reconstruction of the muon's momentum. To do so it exploits the magnetic field provided by the toroidal magnet system, which creates a magnetic field mostly orthogonal to the muon momentum. The muon system is divided into four main sub-detectors which are placed around the barrel and in the end-caps. The sub-detectors in the barrel regions are arranged into three concentric layers in a cylindrical geometry, while in the end-cap regions there are always three layers placed orthogonally to the beam pipe. The standalone performance of the muon systems allows for a momentum resolution of 10% for 1 TeV muon tracks, corresponding to a sagitta along the z-axis of 500 μm measured with a resolution of 50 μm .

The four modules composing ATLAS muon system are described in the following.

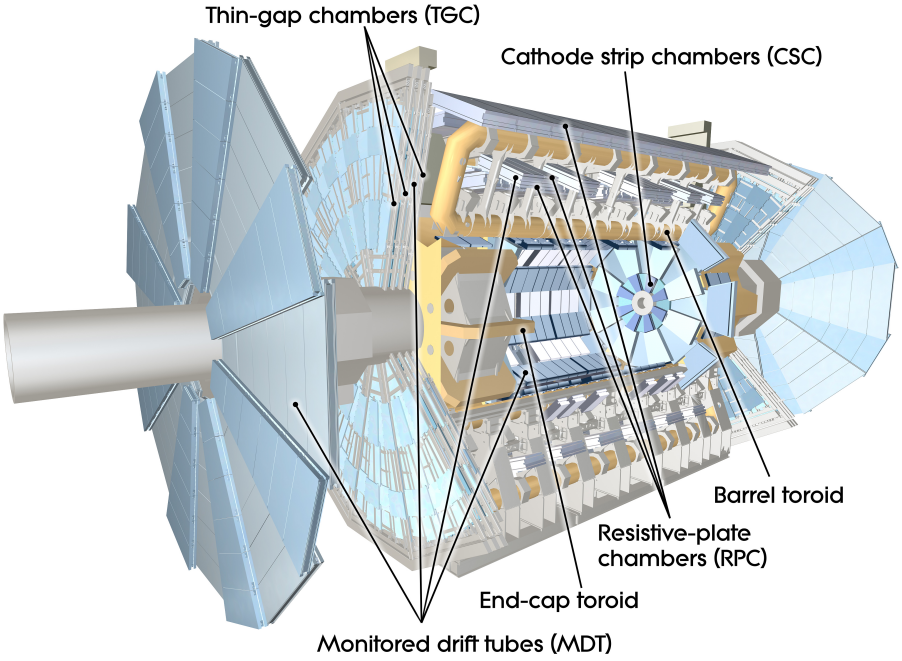

Figure 2.9: Schematic view of the ATLAS muon system. Image taken from Ref. [65].

Monitored Drift Tubes

The monitored drift tubes (MDTs) provide precision measurements of the track coordinates and muon's momentum in the central region of the detector, covering the pseudo-rapidity region $|\eta| < 2.7$. MDTs are pressurized tubes of diameter 29.970 mm and length 0.85-6.5 m filled with a gaseous mixture of Ar 97% and CO_2 3%. Each chamber consists of three to eight layers of drift tubes, which measure the ionisation effect originated by muons passing through the tube. The average resolution is approximately 80 μm for the single tube and approximately 35 μm for the chamber.

Cathode Strip Chambers

The cathode strip chambers (CSCs) allow precise measurements of the track coordinates and muon's momentum in the innermost region $2.0 < |\eta| < 2.7$ where a high neutron rate is expected. Background neutrons originate, for instance, from underlying events are abundant in the forward region of the detector. The CSCs have a low neutron sensitivity [65] are designed to operate in this high-radiation environment. A CSC consists of multi-wire proportional chambers oriented in the radial direction and whose cathodes are segmented into strips and oriented orthogonally in order to provide a two-coordinate position measurement. The chambers are filled with a gaseous mixture of Ar 80% and CO_2 20 %. The CSC spatial resolution is 40 μm in the bending plane and 5 mm in the orthogonal plane.

Resistive Plate Chambers

The resistive plate chambers (RPCs) are designed to provide a quick signal which can be used by the ATLAS trigger system. They cover the pseudorapidity region $|\eta| < 1.05$. To be used as a trigger, the RPCs are designed to have a much quicker response time compared with the CSCs. They also provide transverse momentum discrimination, bunch-crossing identification, and they quickly and coarsely measure a second tracking coordinate in the no-bending ϕ-projection to complement the MDT. RPCs are made of two parallel bakelite plates separated by 2 mm of insulating material which enclose a gaseous mixture of $C_2H_2F_4$ 94.7%, C_4H_{10} 5% and SF_6 0.3%. RPCs are chosen because of their good time and space resolution and rate capability. In particular, the ability to deliver a signal with a spread of 15-25 ns allows it to tag the beam-crossing.

Thin Gap Chambers

The thin gap chambers (TGCs) are designed to provide a triggering signal in the pseudorapidity region $1.05 < |\eta| < 2.4$. It also provides a second azimuthal coordinate, which complements the position measurements provided by the MDTs. The TGCs measure the muon's p_T in a similar way to the multi-wire proportional chambers. Here the gaps are 2.8 mm thick and are filled with a gas mixture of CO_2 55% and n-penthane 45%. Similarly to the RPC, the TGCs deliver a signal with a spread of 15-25 ns allowing it to tag the beam-crossing.

2.3 Trigger System

During Run 2 the LHC provided the ATLAS detector with a bunch crossing every 25 ns, or at a frequency of 40 MHz. It was not possible to store this large amount of data, most of which corresponds to well-known low-Q^2 hadron interactions. To select and store only the most interesting events, the ATLAS detector exploits a two-level trigger and data acquisition (TDAQ) system [65, 79], which is diagrammatically shown in Figure 2.10. TDAQ is designed to reduce the data rate from 40 MHz to $\sim$ 1 kHz.

The Level-1 (L1) trigger is the first TDAQ level, and it is hardware-based. It selects the interesting events by looking at reduced-granularity information from the calorimeter (L1Calo) and muon (L1Muon) detectors. L1Calo is based on inputs from the full electromagnetic and hadronic calorimeter systems. The analogue signals are digitised by the preprocessor and are fed in parallel to the cluster processor (CP) and to the Jet/Energy-sum processor (JEP). CP can identify photon, electron, τ-lepton candidates, while JEP can identify jet candidates and produces a global sum of the total missing transverse energy $E_{\mathrm{T}}^{\mathrm{miss}}$.

L1Muon takes inputs from the RPCs and TGCs. To reduce the high particle rate in the end-cap regions, which is due to particles not originating from the interaction point,

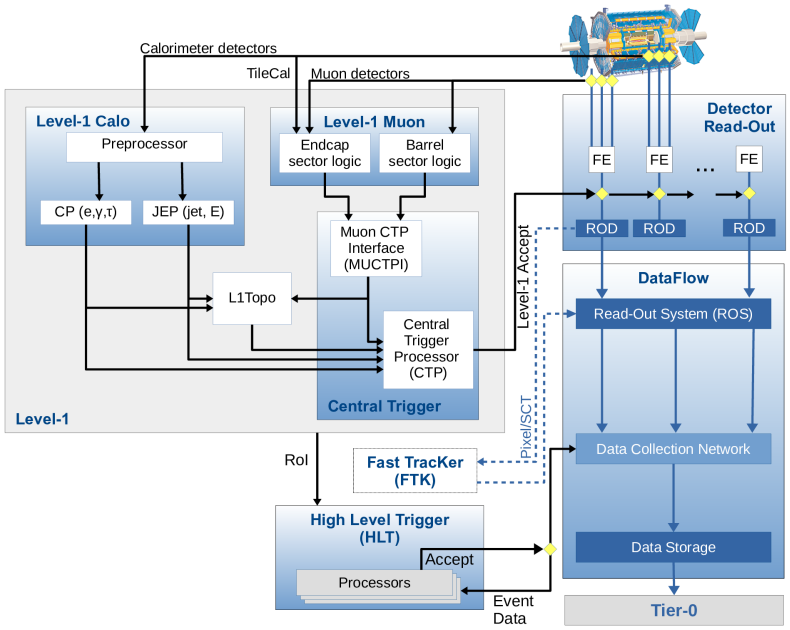

Figure 2.10: Diagrammatic representation of the Run 2 ATLAS TDAQ system. Image taken from Ref. [78]

L1Muon requires a coincidence criteria between the outer and inner TGC stations, and between TGC and the tile calorimeter.

Before the start of Run 2 a new electronic module was introduced in the data processing path. This is the level-1 topological processor (L1Topo) [80]. This module is introduced to cope with the higher luminosity provided by the LHC without increasing the energy thresholds in L1Calo and L1Muon. To achieve this goal, L1Topo analyses the angular and energy information of each trigger object such as requirement on the azimuthal angle ($\Delta\phi$), pseudorapidity ($\Delta\eta$) and radial separation (ΔR); and requirements on the invariant mass, transverse mass, effective mass and corrections to the $E_{\mathrm{T}}^{\mathrm{miss}}$.

L1 trigger decision is taken by the Central Trigger Processor (CTP). It is based on event-level quantities, object multiplicity above threshold inputs from L1Calo trigger and L1Muon Central Trigger Processor Interface (MUCTPI), or by considering topological requirements obtained from L1Topo. The L1 *accept* decision process takes 2.5 μs, and it reduces the event rate down to approximately 100 kHz.

For each L1-accepted event, the Front-End (FE) detector electronics readout the event from each sub-detector. These input are then sent to the ReadOut Drivers (RODs) which perform the initial processing and formatting. The RODs output is then sent to the ReadOut System (ROS) to buffer the data. The ROS feeds the information from each sub-detector to the second stage of the trigger, the High-Level Trigger (HLT). L1 provides the HLT with Regions of Interest (ROIs) defined in η and ϕ. The ROI definition differs between the L1Calo and L1Muon. The CP defines the ROIs as of 4×4 trigger towers, each with granularity 0.1×0.1 in η and ϕ. An E_T threshold, which can depend on η, is applied for object selection. The JEP ROIs are defined using 0.2×0.2 summations in η and ϕ. For

L1Muon, the ROIs are built from 0.1×0.1 regions in η and ϕ in one of the three layers composing the muon spectrometers. Then additional hits are searched within a window of addtitional ROI consistent with the trajectory of a muon with minumum p_T defined by a threshold.

High-Level Trigger (HLT) is the second trigger stage, which is software-based. Typically HLT makes use of dedicated fast trigger algorithms to early reject uninteresting sevents, followed by more precise and CPU-consuming algorithms. These algorithms are run on approximately 40000 Processing Units (PUs). PUs make the *accept* decision within few hundred milliseconds. The output event rate from HLT is on average 1.2 kHz.
The Fast TracKer (FTK) [81] is a hardware-based system designed to reconstruct ID tracks to be provided to HLT at the same rate as L1. It was commissioned during Run 2 but it was not used to take trigger decisions by HLT.

2.4 Summary

The work of this thesis is based entirely on the data collected by the ATLAS detector at CERN. In Section 2.1 CERN's accelerator chain and the performace of the LHC are described. Section 2.2 the ATLAS detector is presented, and its sub-modules are illustrated. The coordinate system is firstly introduced. Then, the magnetic fields exploited by the ATLAS magnet system are briefly described. The ATLAS detector exploits a solenoidal magnetic field in the ID region, and a toroidal one in the muon spectrometer. The performance and goals of the ID are presented, together with a brief discussion on the momentum measurement in a magnetic spectrometer and its uncertainty. The ID is composed of three sub-modules: a pixel and a micro-strip detector, both of which are silicon-based, are used to perform vertex and track reconstruction. The ID is completed by the TRT, which contributes to the track reconstruction. After discussing the general working principles of the calorimeters, the ATLAS calorimeter system is described in its elements: the ECAL devoted to the measure of electromagnetic showers; the tile and end-cap calorimeters which measure hadronic showers; and the forward calorimeter which extend the calorimetry in the highest η region. The ATLAS muon spectrometer is presented. This is made of four modules: the MDT and CSC devoted to the precise reconstruction of the muons' momenta; and the RPC and TGC which provide a trigger signal. Finally the ATLAS trigger system, which reduces the rate of acquired data from 40 MHz to $\sim$ 1 kHz is described. It exploits two-stages structure, with the L1 trigger system which is hardware-based; and the HLT which is software-based.

Events Simulation and Reconstruction

3

The work of this thesis is based on the data recorded by the ATLAS detector, described in the previous Chapter, and on data simulated exploiting Monte Carlo simulations. This Chapter describes the data quality procedures and presents the full dataset recorded by the ATLAS collaboration between 2015 and 2018 in Section 3.1. A discussion on how *pp* collisions are simulated is presented in Section 3.2. The reconstruction process of the physics object is performed in the same way for both simulated and recorded data. The reconstruction of online objects relevant for the trigger strategy defined for this analysis is reported in Section 3.3. Finally all the offline physics objects used in this work are defined in Section 3.4.

3.1 Data Quality and Dataset

This Section concludes the discussion on the ATLAS TDAQ system introduced in Section 2.3. Data Quality (DQ) is needed to ensure that only reliable events are used for physics analyses. The total dataset available for physics searches is described.

Data Quality

The data recorded by the ATLAS detector is required to satisfy standard quality criteria [82] in order to be used for offline analyses. The ATLAS data are recorded in luminosity blocks to monitor the performance of the detector during the data taking. The luminosity blocks are short periods of time, of approximately one minute, during which the configuration of each sub-detector is kept constant. Each sub-detector can be monitored during the operations by looking at a set of quality parameters. A record of the detector performance is kept in order to to compile a Good Run List (GRL) for each period of data taking. The GRL contains the list of luminosity blocks in each run where the detector has performed in line with the quality requirements.

Run 2 Dataset

The data analysed in this work were collected by the ATLAS collaboration between 2015 and 2018, referred to as Run 2, at a centre-of-mass energy of $\sqrt{s} = 13$ TeV with a 25 ns proton bunch crossing interval. The average number of pp interactions per bunch crossing, referred to as pileup, changed over the Run 2 data taking and it is shown in Figure 2.3. After applying beam, detector and data-quality criteria [82] a total integrated luminosity of 139 fb^{-1} of data is available for physics analyses.

3.2 Monte Carlo Simulation

The extraction of information from the pp collisions always goes through a process of comparison of a prediction with the data. A key tool in this sense is provided by Monte Carlo (MC) simulations, mimicking real data after the simulation of detector effects. The simulation process plays a crucial role as it provides the kinematic properties of the final state signatures of any physics process examined. Such a process involves many different ingredients, from the modelling of the physical aspects of the pp collisions to the interaction of the final-state particles with the detector. This Section focuses on the description of each stage of the MC simulation process within the ATLAS collaboration.

Events Generation

Any pp collision involves the interactions of the constituent partons, which are governed by perturbative and non-perturbative QCD processes at different energy scales. Asymptotic freedom [83] establishes that at low energy scales, QCD is not perturbative. The momentum distribution of the partons within the protons, determined by low-energy parton interactions within the proton, can not be determined by perturbative QCD, and it is therefore parametrised in terms of parton density functions (PDFs) determined empirically [84, 85]. As a consequence, the pp interaction cross section cannot be obtained using perturbative calculations; the *factorisation theorem* [86] is therefore exploited to compute the cross section through a product of probability functions [87]:

$$\sigma_{pp\to X} = \sum_{i,j} \int dx_i dx_j f_i(x_i, \mu_F^2) f_j(x_j, \mu_F^2) \hat{\sigma}_{ij\to X}(x_i, x_j, \mu_F^2, \mu_R^2), \tag{3.1}$$

where:

- $\sigma_{pp\to X}$ is the cross section for the pp interaction to produce a generic final state X;
- $f_i(x_i, \mu_F^2)$ is the PDF, that is the probability of finding the parton i with a fraction of the proton momentum x_i;
- μ_F^2 and μ_R^2 are the factorisation and renormalisation scales, respectively. The factorisation scale represents the energy scale which separates the high- and low-energy

processes, and it is somewhat arbitrary; the renormalisation scale is the regulator of the ultraviolet divergences of the theory. The dependence of the cross section from this scale imposes to vary μ_F^2 and μ_R^2 to determine the associated systematic uncertainty.

– $\hat{\sigma}_{ij\to X}$ is the partonic cross section generating the final state X.

The sum runs over all the possible combinations of partons that can originate the process. Therefore, the factorisation theorem allows to divide the pp interaction into distinct steps, as it is diagrammatically shown in Figure 3.1. For each step the modelling of the partons

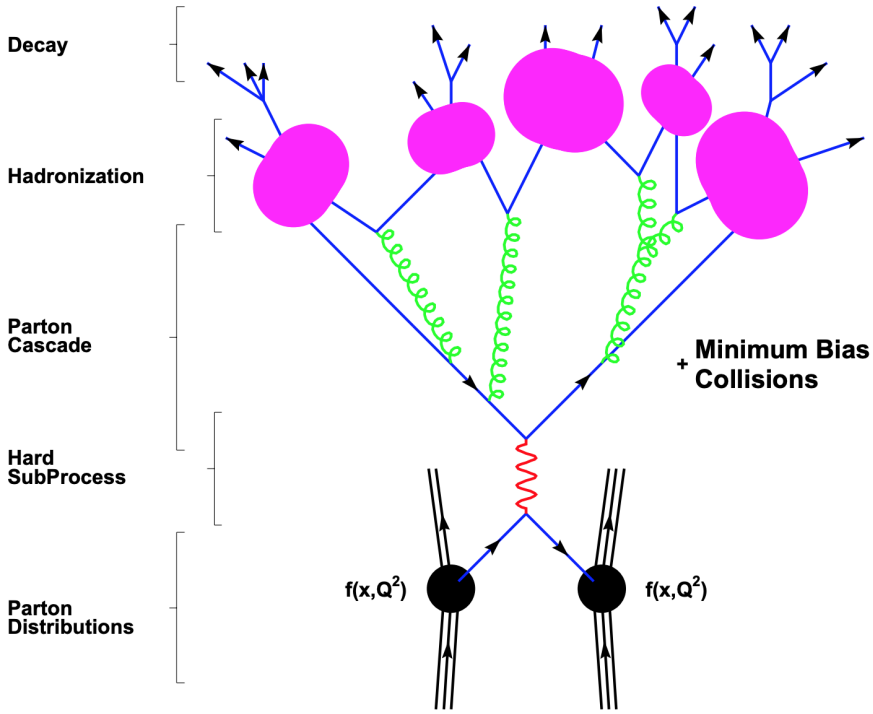

Figure 3.1: Representation of a physics process at the LHC. Each stage in this scketch corresponds to a different simulation step. Image taken from Ref. [88]

within the proton is factorised out. Each step of the simulation process is discussed in the following.

Parton Distributions. The PDFs are determined by experimental measurements at fixed energy scales measured indirectly by H1 [89], Zeus [90], D0 [91] and CDF [92] and other experiments through measurements of the deep inelastic scattering processes at $e^{\pm}$ [84] or $p\bar{p}$ [93, 94]colliders, and since they are independent of the specific process they are applied to, they can be used universally. The PDFs evolution at the LHC energy scales is obtained by applying the Dokshitzer-Gribov-Lipatov-Altarelli-Parisi (DGLAP) equations [95–97]. The PDFs used for this work are discussed in Ref. [98].

Hard Subprocess (Matrix Element). This step calculates the hard-scattering cross section $\hat{\sigma}_{ij\to X}$ between the i, j partons in the colliding protons that generates the process X. This is equivalent to calculating the Matrix Element (ME) of the process, which is the scattering matrix that relates the initial and final states. The hard subprocess occurs at high energies, so it is possible to use the perturbative calculations to determine the cross section. From Equation 3.1, it is possible to express the interaction cross section between the two partons initiating the process X as [87]:

$$\hat{\sigma}_{ij\to X} = \int d\Phi_n \frac{1}{2\hat{s}} \left|\mathcal{M}_{ij\to X}\left(\Phi_n; \mu_R, \mu_F\right)\right|^2 . \tag{3.2}$$

The partonic cross section depends on:

- the final state phase space Φ_n and the corresponding ME squared, which is averaged over the initial spin-states and colour degrees of freedom, $\mathcal{M}_{ij\to X}$;
- the parton flux $\frac{1}{2\hat{s}}$, where $\hat{s} = x_i x_j$ is the centre-of-mass energy squared.

The ME can be expressed as the sum over all the possible Feynman diagrams, $\mathcal{F}_{ij\to X}$, for the process:

$$\mathcal{M}_{ij\to X} = \sum_k \mathcal{F}^k_{ij\to X}. \tag{3.3}$$

The use of a perturbation theory implies that there might be as many perturbative orders as one may want. The ME calculation is therefore truncated to a fixed order, which includes effects from virtual corrections and real emissions. At that fixed order in the perturbation theory, the Kinoshita-Lee-Nauenberg theorem [99,100] states that the divergences are exactly cancelled, yielding a finite cross section. This implies that if the multiplicity of the real emissions is larger than the multiplicity of the virtual corrections the cancellation is spoiled and infrared divergences occur. This is handled by only including hard contributions that yield finite results in the ME calculation, while the soft contributions are calculated in the parton shower stage.

Parton Cascade or Shower. A parton *cascade*, or parton *shower* PS, originates because of the color charge carried by the partons participating to the hard collision. This is due to the potential energy between two partons increasing as they are separated, as it is described in Section 1.1. A shower might be radiated either by incoming partons of the hard subprocess (initial state) or outgoing products of the hard interaction (final states). Each of these processes may radiate further partons. This cascade process is ruled by soft QCD emissions which can not be described using a perturbative theory. For this reason an approximation scheme is used to simulate the parton cascade. The differential cross section describing a parton cascade can be written as [87]:

$$d\sigma \approx \sigma_0 \sum_i \frac{\alpha_s}{2\pi} \frac{d\theta^2}{\theta^2} dz d\phi P_{ij}(z, \phi), \tag{3.4}$$

where:

- σ_0 is the cross section of the parton of type i produced by the hard interaction;
- θ and ϕ are the angles of splitting;
- z is the momentum fraction carried by the parton j which arises from the fragmentation of the parton of type i;
- P_{ij} is the *splitting function*, or the probability distribution of the splitting process $i \to ij$.

Generic processes generating a parton cascade are $q \to qg$, $g \to gg$ and $g \to qq$. The PS generator exploits Sudakov form factors [101], which are derived from Equation 3.4. The Sudakov form factors describe the probability for a virtual gluon at an energy scale Q_a to evolve to a scale Q_b without radiating. The PS generator evolves the parton cascade until all partons fall below a threshold $Q_0 \approx 1$ GeV. The simulation procedure here described applies to cascades initiated by a Final State Radiation (FSR). For cascades started by an initial ISR, which are those parton showers initiated from incoming partons, the Sudakov form factors have to also include the partons' PDFs. In this case a *backward evolution* is exploited. The momentum fraction of each incoming parton is chosen, within kinematic constraints. These partons are then propagated in reversed time order, gaining energy at each stage until an energy threshold sufficient to initiate a cascade is reached.

Parton Shower to Matrix Element Matching. The ME and PS simulations are calculated independently, because of the factorisation theorem. To generate the event these results need to be combined avoiding double counting of the physics objects that might arise from overlapping phase space. The ME-PS matching is performed within the ATLAS collaboration by exploiting two matching schemes developed by Catani-Krauss-Kuhn-Webber (CKKW) [102] and by Michelangelo L. Magnano *et al.* (MLM) [103]. These two schemes rely on a common strategy [104]. First a jet measure is defined. The relevant cross sections for that process are calculated, considering all the possible jet multiplicities arising from the generic $pp \to X + n$ jets. The hard parton samples are then produced with a probability proportional to the respective total cross section. A kinematic configuration following the matrix element is considered. Each individual configuration is rejected or accepted depending on a probability that includes both the running coupling constants and Sudakov effects. If an event is rejected, a new one is generated. Finally the parton shower is invoked for each leg in the Feynman diagram. The parton shower is constrained not to produce additional jets, which means that configurations implying ME with a higher jet multiplicity are vetoed by the PS step. The differences between the matching schemes arise from different jet definitions used for the ME, the acceptance of parton samples, the initiation of the PS and the method used to separate the ME and PS phase spaces.
The CKKW matching defines a *shower history* by clustering the partons according to the k_t algorithm [105–107]. The clusters are tree-like structures of vertices connected by branches. Each branch is assigned a weight according to α_s and the Sudakov factor connecting the

vertices. This implies that each ME is re-weighted according to the shower history. Any parton shower emission is vetoed if it is harder than some threshold, and the initialisation of the shower is chosen in a way that it gives a smooth transition between the ME and the PS.
The MLM matching defines parton clusters based on a cone algorithm defined by a radius R_{min}. In this way a smaller tree-like structure is defined, and each branch is re-weighted. If each parton is contained within a jet, then the event is considered matched. An unmatched event occurs when for example two partons are too close to produce two independent jets, or if the parton has a too low momentum to generate its own jet. These unmatched events are rejected, preventing double counting between the ME and PS.

Hadronisation and Decay. The partons produced during the showering process reduce the energy scale of the strong interaction. When this energy falls below ~ 1 GeV the hadronisation process becomes dominant; as a consequence, the parton cascade stops evolving and colourless states are generated. The hadronisation is a non-perturbative process, so phenomenological models are used at this stage of the simulation. Two models are commonly used: the Lund string model [108, 109] and the cluster model [110, 111].
The Lund string model's physics grounds lay on the fact that the colour potential energy between partons is expected to grow linearly with the parton separation. This potential energy is represented by a gluonic string, and when the potential energy - which in this model is associated to the string - reaches the order of hadronic masses it breaks the parton system creating a new $q\bar{q}$ pair from the vacuum. A new string is therefore created between the new parton pairs and the process repeats until only colour singlet states remain.
The cluster model exploits the *preconfinement* property of QCD [112]. Such property implies that partons in showers developing at scales lower than that of the hard interaction cluster into colour singlet combinations with an invariant mass distribution which depends on the parton shower scale but not on the properties of the hard interaction. These colour singlets correspond to the stable final state hadrons.

Underlying Event. Together with the hard-interaction process, the additional hadronic activity in the final state also needs to be simulated. The underlying event mainly comes from the *spectator* partons within colliding hadrons that do not participate to the hard scattering. Since these processes happen at a non-perturbative energy scale, phenomenological models are used. These models are based on measurements of the underlying event as input. It is possible to measure the underlying event in data by exploiting minimum-bias triggers [113] which is composed of events with no identifiable hard collision. The underlying events can be generated by colour connection [114] between high-momentum partons and beam remnants, which is simulated using phenomenological models [115, 116].

Pileup. The final states present extra hadronic activity due to pileup collisions, that is low-momentum interaction between protons in the same and nearby bunch crossing as the

hard interaction. Pileup can be *in-time* (collisions in the same bunch crossing), which is simulated using minimum-bias data in a similar way to the underlying event; and *out-of-time* (collisions in nearby bunch crossings), which is simulated by considering previous bunch crossing and detector time response. Pileup collisions are simulated and overlaid on the MC event generated by the previous steps.

Monte Carlo Generators

The simulation steps described above are implemented in several MC generator tools. The generators exploited in this thesis are briefly introduced in the following.

- `Sherpa` [117]: it is a general-purpose generator used to perform leading-order (LO) and next-to-leading-order (NLO) calculations for $2 \to n$ processes. It uses the CKKW matching scheme and a phenomenological cluster-hadronisation model for parton fragmentation.
- `Pythia` [118]: it is a standard generator used to perform LO calculation for $2 \to 2$ or $2 \to 3$ processes. The initial- and final-state parton shower algorithms are based on p_T ordered evolution [119] and the hadronisation is based on the string model. The modelling of the PS and underlying event in `Pythia` presents several free parameters which need to be optimised to reproduce the measured observables in a reasonable way. This optimisation process is known as *tuning* [120]. The set of tuning used by the ATLAS collaboration is referred to as *A14*. This tuning leads to better description of the underlying events in data than the previous tunes.
- `Herwig` [121]: it is a general purpose generator used to perform LO simulations for $2 \to 2$ processes. This generator performs a parton shower by ordering by opening angle and the cluster model is used for hadronisation and the underlying event.
- `MadGraph` [122]: it is a generator used to perform LO and NLO calculations for $2 \to n$ processes, but it does not perform any parton shower. This work uses MadGraph5_aMC@NLO for ME calculation, interfaced with `Pythia` for parton showering, hadronsiation and simulation of the underlying events.
- `Powheg` [123]: it is a tool used to calculate the ME at NLO. In this work it is interfaced to `Pythia` for showering, hadronisation and to simulate the underlying events.

Detector Simulation

The output of the MC generators is a list of four-vectors of particles and particle decay vertices in the final state, which is recorded in the `HepMC` format [88]. Such a list can be used to study the kinematic properties of the physics processes. To compare the recorded data and the MC simulations, the interactions of the MC particles with the ATLAS detector need

to be simulated. The ATLAS simulation infrastructure [124] interfaced with the `Athena` software framework [125] is used to simulate the interactions with the detector and the resulting signals from the sub-systems. The detector simulation is implemented using the `Geant4` package [126], which simulates the passage of particles through the matter. The full reconstruction chain occurs in two steps: the interactions of the particles with the detector are firstly simulated; then the digitisation occurs, which converts the energy deposits into voltages and electric currents in the sub-detectors. As a result of this procedure the outputs of simulated and recorded events are the same, which allows one to process both outputs by the same reconstruction software. The simulation chain described so far occurs on a time scale of the order of minutes per event, depending on the event complextity. Most of this time is used to fully simulate the calorimeter system. To reduce the CPU processing time, the ATLAS collaboration makes use of faster simulation such as `ATLASFAST-II` [127] where a parametrised description of the detector response is implemented.

3.3 Trigger Objects Reconstruction

The ATLAS TDAQ system described in Section 2.3 selects events deemed interesting for physics analysis based on the definition of *trigger chains*. These are sequences of algorithms, from L1 to HLT, developed to identify specific physics signatures [79]. The complete list of active triggers during a given data taking period is called the trigger *menu*, whose evolution during Run 2 is documented in Ref. [128–131]. The ATLAS trigger menu includes many triggers dedicated to identify a variety of processes for different physics analyses. Each trigger obeys to the same naming convention:

$$\text{[LEVEL][TYPE][THRESHOLD][IDENTIFICATION][ISOLATION][SEED]}, \tag{3.5}$$

where the trigger level (HLT or L1) is indicated; the object type (electron, jets, etc.), multiplicity and its energy threshold are defined; identification and isolation criteria and L1 seed item (if present) are listed. Unless otherwise stated, the trigger chains discussed in this analysis refer to the HLT level. HLT items requiring looser criteria are used by ATLAS for several purposes, for example as part of a multi-object trigger chain. Loose triggers with high rates can be prescaled, meaning that only a fraction $1/P$ ($P > 1$) of events is recorded to control the trigger rate. The reconstruction of trigger objects exploits a two-step approach: the first step rejects events early by using a fast algorithm, while the second step performs the identification by applying precision algorithms. This two-step approach allows one to run the precise, time-consuming algorithms on a reduced number of events.

The triggers relevant to this analysis are presented in the following, and they are all unprescaled triggers, i. e. triggers where $P = 1$, resulting in no event loss.

Electron and Photon Triggers

To define the online[1] e/γ trigger objects at HLT, the full detector granularity is used in the ROIs. As discussed in Section 2.2, ROIs are broad regions of the detector identified by the L1 trigger according to energy deposit in the calorimeters or tracks in the muon chambers. ROIs are fed as input to the HLT to seed the trigger reconstruction algorithms. The HLT trigger sequence for reconstructing electrons and photons is illustrated in Figure 3.2. First the fast calorimeter preselection builds energy clusters from the calorimeter

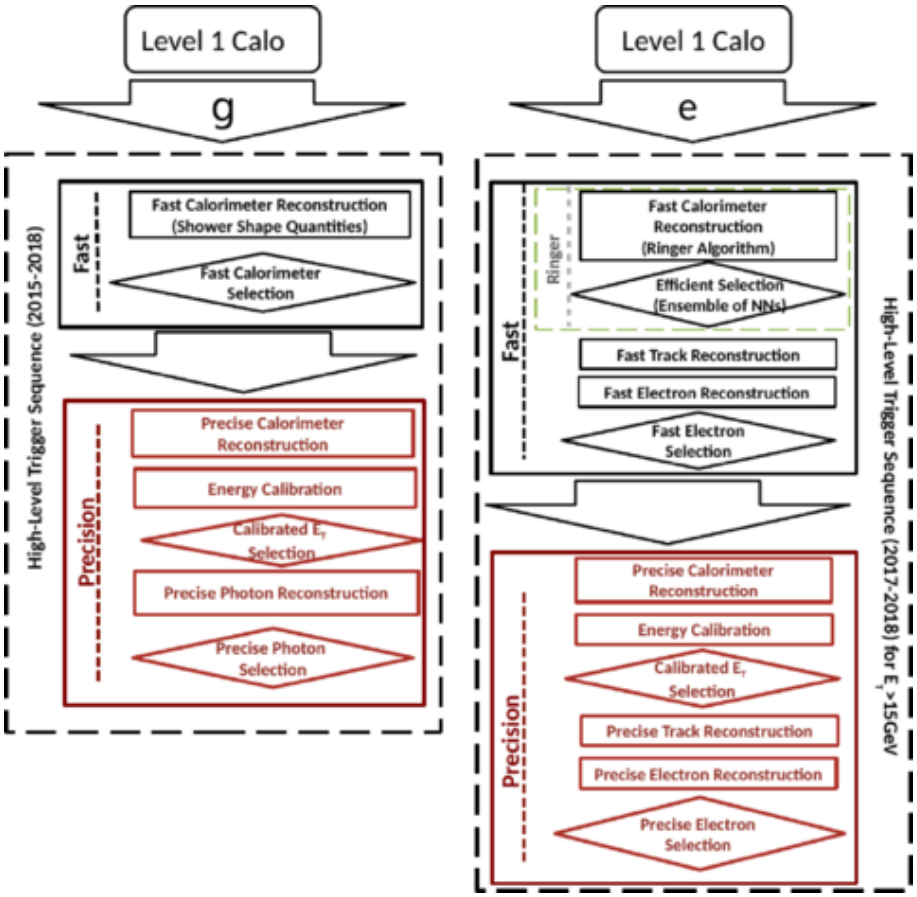

(a)

Figure 3.2: Simplified outline of individual steps for non-isolated photon (left) and electron (right) trigger sequences for *pp* data-taking. Image taken from Ref. [1].

cells, whose size in η and ϕ is 0.025×0.025 within the ROIs. The second ECAL layer, where most of the electrons and photons energy is released, is used to find the cell with the largest E_T in the ROI. The energy cluster size is chosen depending on the region of the detector: in the barrel the size is 3×7 cells, while in the end-caps it is 5×5 cells. The identification of photons and electrons depends on the total E_T and some variables describing the electromagnetic shower produced in the calorimeter. These variables are defined in terms of energy ratios and widths of grouped calorimeter cells within the cluster. The fast

[1] Conventionally, *online* objects refer to trigger objects, in contrast to the *offline* objects which are used by the analyses.

calorimeter selection is followed by the fast track reconstruction, which is based on hits in the silicon detectors. Tracks with $p_T > 1$ GeV are matched to a calorimeter cluster if they satisfy angular separation requirements. If tracks match the calorimeter cluster then the candidate is identified as an electron, otherwise if no matching tracks are found, the candidate is identified as photon.

The precision reconstruction is run on the candidates selected by the fast HLT sequence. The photon identification is performed exploiting cut-based selections on shower-shape variables [132], while the electron identification relies on a likelihood (LH) based discriminant. The LH method is based on the *projective likelihood estimator approach* [133], whose likelihood discriminant is defined as:

$$d_{\mathcal{L}} = \frac{\mathcal{L}_S}{\mathcal{L}_S + \mathcal{L}_B}, \tag{3.6}$$

from geometric sums $\mathcal{L}_{S(B)}$ of probability density functions $P_{S(B)}$ defined as:

$$\mathcal{L}_{S(B)} = \prod_{i=1}^{n} P_{S(B),i}(x_i), \tag{3.7}$$

where S (B) stands for signal (background)[2] and $\vec{x}$ is a vector of 22 electron track- and shower-based variables. The signal and background distributions of the $d_{\mathcal{L}}$ discriminant are well separated, with the background peaking at zero and the signal at one; this sharp distribution is not optimal for defining operating points (OPs) as an extremely fine binning would be required. To solve this problem the sharp distribution is smoothed by using an inverse sigmoid function:

$$d'_{\mathcal{L}} = -\tau^{-1} \ln\left(d_{\mathcal{L}}^{-1} - 1\right), \tag{3.8}$$

where the parameter τ is fixed to 15. Four OPs are defined, namely *lhvloose*, *lhloose*, *lhmedium*, *lhtight* where *lh* denotes the LH-based selection, and *vloose* stands for *very* loose. Each OP is defined on increasingly higher values of $d'_{\mathcal{L}}$, so that events selected by the *lhtight* OP are a subset of those selected by loose OPs.

Isolation requirements can be applied to the HLT selection to improve discrimination against hadronic activity. Track-based isolation criteria are used for electrons. The isolation is defined as the ratio of the p_T sum of non-electron-associated tracks in a given ΔR cone to the p_T of the electron candidate. Track isolation criteria were introduced in 2016, and the cone radius ranges between $\Delta R = 0.2$ and $\Delta R = 10$ GeV$/\ p_T$, where the transverse momentum of the electron is considered, describing a cone that narrows with the increasing electron p_T. This increasingly tight isolation requirements for high-p_T electrons is based on the expectation that those electrons are more isolated from hadronic activity.

One of the electron triggers exploited by this analysis is the `HLT_e26_lhtight_nod0_ivarloose`, whose efficiency is shown in Figure 3.3. Here `e26` denotes that this is a single electron trigger with and E_T threshold of 26 GeV; `lhtight`

[2] Here *signal* refers to prompt electrons, while *background* refers to the combination of jets that mimic the signature of prompt electrons, electrons from photon conversion and non-prompt electrons from the decay of hadrons conaining heavy flavours [134]

is the LH-based OP; `nod0` denotes that no transverse impact parameter requirements are applied (in contrast with the offline electron identification) and `ivarloose` indicates that track-based isolation requirements are applied. For physics analysis the trigger is used as part of a logical OR with higher E_T-threshold triggers applying looser identification criteria. Appendix A presents a more complete discussion of the methodology and results of this work.

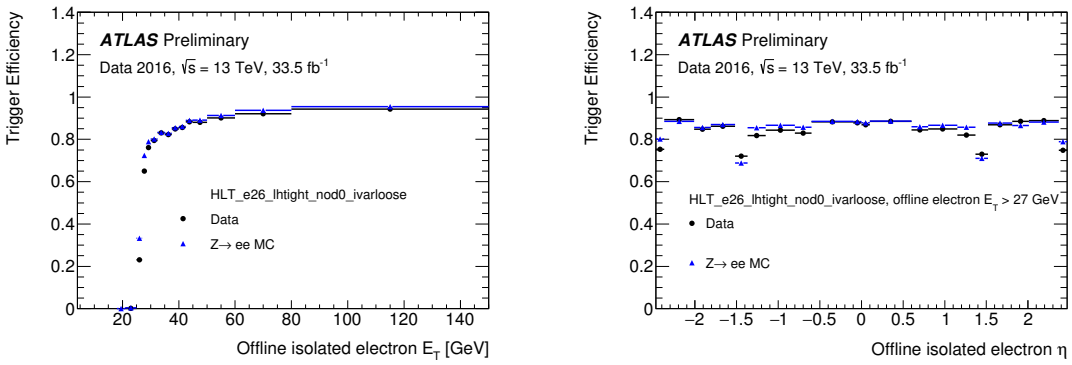

(a) (b)

Figure 3.3: Efficiency of `HLT_e26_lhtight_nod0_ivarloose` trigger as function of (a) the offline electron candidate's transverse energy E_T and (b) pseudorapidity η for the 2016 data taking. A total integrated luminosity of 33.5 fb^{-1} is considered. The blue traingles refer to the MC simulated $Z \to ee$ events, while the black dots are the recorded data. All efficiencies are measured with respect to offline isolated electrons using the Tag-and-Probe method, detailed in Appendix A. The error bars show binomial uncertainties. Images taken from Ref. [135]

Muon Triggers

The HLT muon trigger sequence [136] too follows the two-step approach. In the first, fast step muon tracks are reconstructed in the muon spectrometer only. The muon candidate is obtained by fitting the track hit positions and the drift times from the MDTs. The muon candidate p_T is assigned using a look-up table. The muon candidate identified in the muon spectrometer is then updated by looking at tracks in both the muon spectrometer and ID, and a combined fit is performed.

The second, precision step reconstructs the muon candidate in the ROI using information from the whole muon spectrometer. The combined muon candidate is obtained by extrapolating the muon spectrometer track to the ID by exploiting a precision reconstruction. If the fit over the combined muon fails, which might happen if the muon has low transverse momentum, another fit extrapolating the track from the ID to the muon spectrometer is performed. Muon candidates are required to satisfy some identification criteria based on the track fit quality, the p_T difference between the ID and the muon spectrometer and the charge and momentum significances, which are defined as the ratio between the measured value and their measured uncertainty. Isolation requirements are finally applied to improve

the hadronic activity rejection.
An example of muon trigger exploited by this analysis is the `HLT_mu26_ivarmedium`, whose efficiency performance are reported in Figure 3.4. The `HLT` refers to the trigger level, `mu26` denotes that this is a single muon trigger with E_T threshold of 26 GeV and `ivarmedium` indicates that a medium track-based isolation is required. The differences in efficiency between the barrel and the end-caps, more evidently shown in Figure 3.4(e), are due to the L1 muon trigger differences in the geometric acceptance and local detector inefficiencies.

$\mathbf{E}_{\mathrm{T}}^{\mathrm{miss}}$ Triggers

The $E_{\mathrm{T}}^{\mathrm{miss}}$ triggers [138] target events with a large energy imbalance, which originates from energetic invisible particles. The general definition of the $E_{\mathrm{T}}^{\mathrm{miss}}$ is:

$$E_{\mathrm{T}}^{\mathrm{miss}} = |\mathbf{p}_{\mathrm{T}}{}^{\mathrm{miss}}| = \left| -\sum_{i} \mathbf{p}_{\mathrm{T}}(i) \right|, \tag{3.9}$$

where i runs over all the reconstructed physics objects in the event. Assuming the massless approximation $E \approx |\vec{p}|$, the $\mathbf{p}_{\mathrm{T}}(i)$ of the i-th object can be expressed as function of the polar angle θ_i and the azimuthal angle ϕ_i according to:

$$p_{x,i} = E_i \sin\theta_i \cos\phi_i, \quad p_{y,i} = E_i \sin\theta_i \sin\phi_i. \tag{3.10}$$

The missing momentum is conserved in the transverse plane, so a large value of $E_{\mathrm{T}}^{\mathrm{miss}}$ in the event indicates the presence of an invisible object which is not reconstructed by the ATLAS detector. High $E_{\mathrm{T}}^{\mathrm{miss}}$ can also originate from detector effects, such as mis-measurement of jets, which are abundantly produced in high-cross section processes, like multijet production. This impacts the trigger rates, which can not be kept under control by the trigger threshold, without affecting the efficiency for $E_{\mathrm{T}}^{\mathrm{miss}}$-based analyses. To control the trigger rate, a variety of $E_{\mathrm{T}}^{\mathrm{miss}}$ algorithms for online data collection are defined [138]. The $E_{\mathrm{T}}^{\mathrm{miss}}$ trigger algorithms exploited by this work are introduced below:

- `cell` *algorithm.* This algorithm is very basic, and determines the missing transverse momentum by summing all the calorimeter cells without adjusting for the different calibration in the hadronic and electromagnetic calorimeters, nor does it consider pileup corrections. To reduce the effects of electronic noise or pileup, only cells satisfying

  $$|E_i| > 2\sigma_i, \quad E_i > -5\sigma_i, \tag{3.11}$$

  are included in the sum. In Equation 3.11 σ_i is the expected energy-equivalent noise in the cell i.

- *Jet-based algorithm* `mht`. In this algorithm the $E_{\mathrm{T}}^{\mathrm{miss}}$ trigger is based on the jets only, hence the $E_{\mathrm{T}}^{\mathrm{miss}}$ is calculated as the negative sum of the jets p_T in the event. This approach is motivated by the fact that in many events of interest jets dominate the

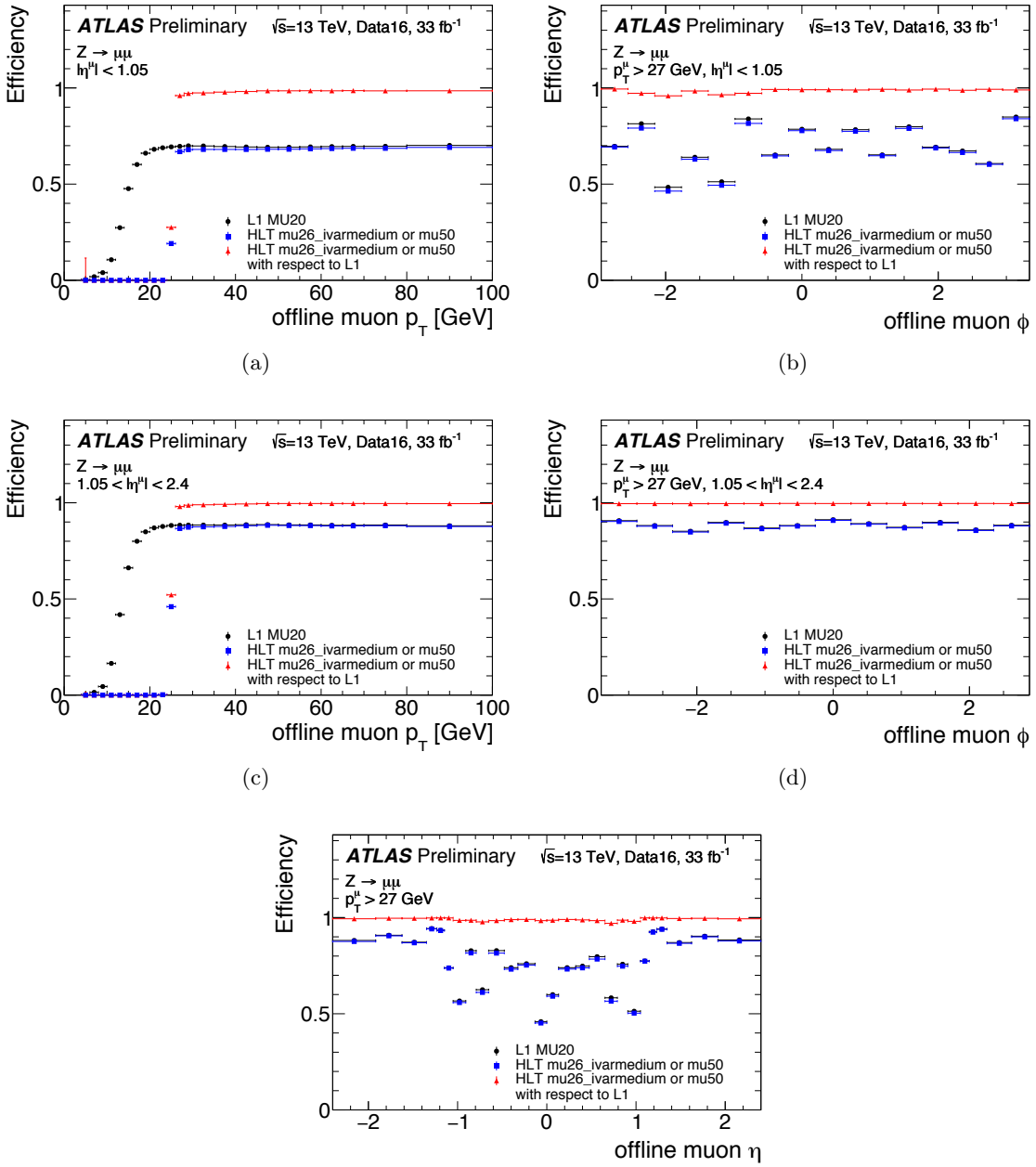

Figure 3.4: Muon trigger efficiency performance for the `L1_MU20` (black), `HLT_mu26_ivarmedium` (blue) chains in 2016 using 33 fb^{-1} of collected data. The efficiencies are shown in the barrel as function of (a) p_T and (b) ϕ, in the end-caps as function of (c) p_T and (d) ϕ and (e) as function of η. The $Z \to \mu\mu$ events are selected using a Tag-and-Probe method with respect to offline isolated muons satisfying medium identification criteria. Only statistical uncertainties are shown. Images taken from Ref. [137]

visible momentum. In addition to that, jets can be calibrated accurately and are corrected for pileup effects.

– *Pileup fit algorithm* `pufit`. This algorithm builds the transverse missing momentum from topological clusters (discussed in Section 3.4). The `pufit` algorithm calculates

the p_T and E_T in 112 towers of size approximately 0.71×0.79 in η and ϕ, corresponding to the size of a jet with $R = 0.4$. Towers with E_T less than 45 GeV are assumed to result from pileup. The average pileup energy density is calculated as the sum of all the towers below the threshold scaled by the total area of those towers in η and ϕ. The pileup contribution in each tower is estimated by performing a fit which uses the average pileup density and constrains the total $E_{\mathrm{T}}^{\mathrm{miss}}$ from pileup to be zero within the energy resolution. The obtained pileup contribution is subtracted from each cell, and the $E_{\mathrm{T}}^{\mathrm{miss}}$ is recalculated.

This analysis exploits the `mht` algorithm for the data collected until 2016, while from 2017 the `pufit`-based triggers combined with the `cell` algorithm are used to mitigate the effect of pileup. An example of a trigger chain from 2018 used in the analysis is the `HLT_xe110_pufit_xe70_L1XE50`. Here `xe110` is a $E_{\mathrm{T}}^{\mathrm{miss}}$ trigger with energy threshold of 110 GeV exploiting the `pufit` algorithm, which is combined with a lower-threshold trigger, `xe70`, which uses the `cell` algorithm; `L1XE50` refers to the L1 item used, with an energy threshold of 50 GeV. Figure 3.5 shows the efficiency performance of the `HLT_xe110_pufit_L1XE50` trigger, and the evolution of the lowest unprescaled $E_{\mathrm{T}}^{\mathrm{miss}}$ triggers during Run 2. Events are taken from data with a $Z \to \mu\mu$ selection as the muons are not used in the definition of the online $E_{\mathrm{T}}^{\mathrm{miss}}$, acting *de facto* as invisible objects.

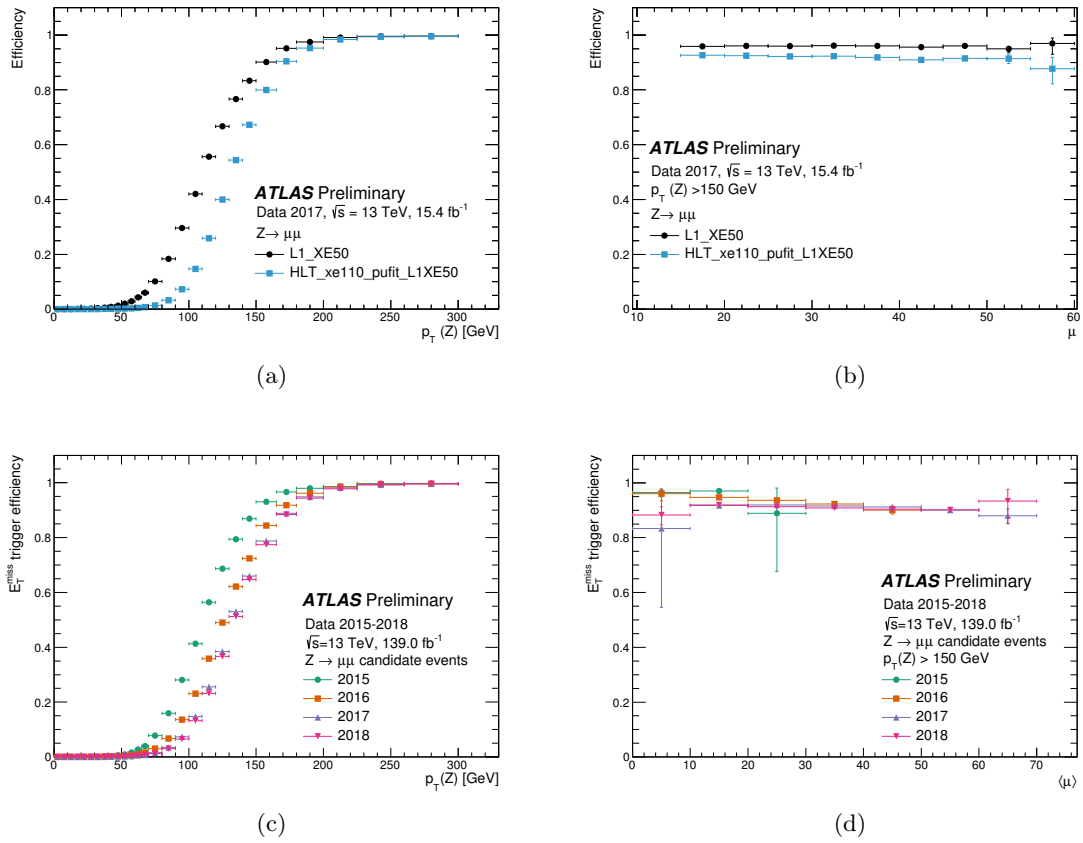

Figure 3.5: Performance of the missing energy triggers `HLT_xe110_pufit_L1XE50` and `L1_XE50` in 2017 as function of (a) Z-boson transverse mass and (b) mean number of pp interactions and combined L1 and HLT efficiency of the lowest unprescaled missing transverse energy triggers during Run 2 as function of (c) the Z-boson transverse momentum and (d) of the mean number of simultaneous pp interactions. The events are selected using a $Z \rightarrow \mu\mu$ selection and the Z-boson p_T in the event is used as a proxy for the missing transverse momentum in the event. Images taken from Ref. [139].

3.4 Offline Objects Reconstruction

The reconstruction of offline physics objects in the event is an essential step of the analysis of ATLAS data. The objects are reconstructed following the same procedure for both recorded data and simulated MC samples, with the only difference that for the latter the additional *truth* information is recorded. The definition of offline objects is kept as close as possible to the trigger objects discussed in the previous Section 3.3. This Section describes in detail the reconstruction of physics objects relevant for this work.

Tracks and Vertices

Tracks and vertices are the most basic reconstructed objects used by any ATLAS analysis. Primary vertices are crucial for identifying the hard-scattering interaction, while tracks are used in the reconstruction of any physics object related to a charged particle. Tracks

and vertices play a particularly important role for this thesis, as it is discussed more in Chapter 4.

Tracks

Tracks are reconstructed within the ATLAS detector by applying the ID new tracking reconstructor (NEWT) algorithm [140]. The algorithm is based on two sequences: the main *inside-out* track reconstruction and the subsequent *outside-in* tracking.

Inside-out sequence. This technique reconstructs tracks starting from the innermost module of the ID, to the SCT, and then it extends the track segments to the TRT. The input for reconstructing the tracks are the raw hits in the ID, which are grouped into three-dimensional space-points. A track seed is built from these objects, and it is passed to a Kalman filter [141], which either rejects the hits or adds them to the track candidate depending on how consistent they are with the seed track. The collection of track candidates obtained usually contains fake tracks or overlapping track segments. A cleaning module [142] is employed to solve the ambiguities by scoring the tracks in a reward/penalty schema. Fully reconstructed track candidates are favoured over track segments, and similarly more precisely measured hits, e. g. from the pixel detector, are preferred over measurements coming from less precise modules such as the TRT. The segments of track candidates identified in the silicon detector and surviving the cleaning process are then extended to the outer TRT by applying two consecutive modules: an extension algorithm that searches for seed candidates in the TRT; and an algorithm that processes and evaluates these extended input tracks. These algorithms do not modify the tracks reconstructed in the silicon detectors, but only extend them into the TRT. A line fit is performed to determine the compatibility of the TRT hits with the input track.

Outside-in sequence. This technique reconstructs tracks starting from the outer TRT towards the innermost modules. This second technique is needed because there might be seed tracks e. g. originating from secondary decays or photon conversions that may not satisfy the cleaning requirements in the silicon detector. Hits already associated to tracks reconstructed by the inside-out technique are not considered.

Charged particles interacting with the ID volume are subjected to ATLAS solenoidal magnetic field directed along the beam axis. As a consequence, the charged particles describe a helix, sketched in Figure 3.6. Track parameters are defined at the track *perigee*, the point of closest approach to the beam axis, and similarly to a helix it can be defined by five parameters:

- $\frac{q}{p}$, the charge versus momentum ratio;
- d_0, the transverse impact parameter. Its sign, which is negative for a positive angular momentum, indicates the direction of the angular momentum;

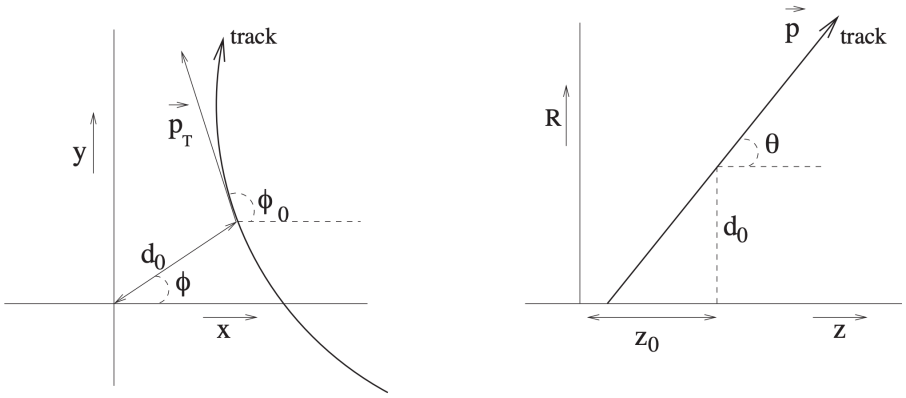

Figure 3.6: Illustration of the perigee track parametrisation in (left) the transverse plane and (right) the $R-z$ plane. Images taken from Ref. [143].

- z_0, the longitudinal impact parameter;
- ϕ_0, the angle with the x-axis on the transverse plane at perigee;
- θ, the angle with the z-axis on the $R-z$ plane.

Other important track variables that are commonly used are the track transverse momentum p_T^{trk} and the significance of the transverse and longitudinal impact parameters, defined as $\frac{d_0}{\sigma(d_0)}$ and $\frac{z_0}{\sigma(z_0)}$ respectively, where $\sigma(d_0)$ and $\sigma(z_0)$ are the uncertainties on d_0 and z_0.

Primary Vertexing Algorithm

Primary vertices (PVs) are reconstructed by extrapolating tracks to a single point in space. The beam spot is used as reference for the tracks during the PV reconstruction [144]. The beam spot is defined as the region where collisions take place within the ATLAS detector, and it is determined by the operating parameters of the beams and magnets of the LHC. Before the PV is defined, the transverse and longitudinal impact parameters, d_0 and z_0, refer to the beam spot. Tracks need to satisfy a number of quality criteria based on the transverse impact parameter, reconstructed p_T and overlapping space-points [144]. The vertex reconstruction is an iterative process based on the tracks surviving the quality requirements. The reconstruction is performed according to a four-step approach, as it is described in more detail in Ref. [144].

- A vertex seed position is defined with respect to the beam spot in the transverse plane, with the $x-$ and $y-$ coordinates taken from the centre of the beam spot. The z seed coordinate is the mode of the longitudinal impact parameter of the tracks calculated with respect to the centre of the beam spot.
- An iterative primary vertex finding procedure is applied. The starting points are the vertex seed position and the parameters of the tracks. The reconstructing algorithm

performs a fit by iteratively minimising the χ^2. A weight is assigned to each input track which determines how compatible the track is with the reconstructed vertex. The vertex position is calculated iteratively using the weighted tracks. The weights are then recalculated with respect to the new vertex position. The weight of each track is calculated according to

$$\omega(\chi^2) = \frac{1}{1 + exp\left(\frac{\hat{\chi}^2 - \chi^2_{\text{cutoff}}}{2T}\right)}, \tag{3.12}$$

where $\hat{\chi}^2$ is the χ^2 comparing the closest approach of the track and the vertex position in three dimensions. The constants χ^2_{cutoff} and T define the threshold where the weight of a track is 0.5 and the smoothness of the weighting procedure. Tracks with a low weight are not removed, but have a smaller impact on the calculated vertex position.

– The final weight of each track used to reconstruct the vertex is evaluated. The tracks with a $\hat{\chi}^2$ greater than seven standard deviations are found incompatible with the vertex and are removed from the vertex candidate.

– After a vertex candidate is created, the tracks rejected at the previous step are used as input for a new vertex finding iteration.

The four steps described are repeated until all the tracks are associated to a vertex or no additional vertices can be reconstructed from the remaining set of tracks. The PV corresponding to the hard-scattering pp interaction is the one with the largest $\sum p^2_{T,\text{track}}$, and it is labelled as PV_0. Any other reconstructed vertex is referred to as a pileup vertex. The tracks can be grouped in three categories:

– matched to the hard-scatter vertex;

– matched to a pileup vertex;

– unmatched, which arise primarily from combinatoric fakes.

These categories are useful for reconstructing higher-level physics objects which exploit track selections.

Secondary Vertexing Algorithm

The ability to identify secondary vertices (SVs) is an important feature for the particle physics community, because a SV can originate from the decay of long-lived hadrons. For the work presented in this thesis vertices coming from the fragmentation of b-hadrons are particularly important. The performance of the ATLAS detector to reconstruct such events, discussed in the following, is based on the identification of SV by the secondary vertex finder (SVF) algorithm [145]. In general, SVF consists of two main steps: first a

collection of two-track vertices is created; then those vertices satisfying dedicated selection criteria discussed in the following are merged together to reconstruct a multi-track secondary vertex. Such an algorithm only considers tracks matched to a jet. The matching is performed by looking at the angular distance ΔR between the jet axis and the track, defined as

$$\Delta R = \sqrt{(\eta_{\text{jet}} - \eta_{\text{trk}})^2 + (\phi_{\text{jet}} - \phi_{\text{trk}})^2}, \tag{3.13}$$

where η is the pseudorapidity and ϕ is the azimuthal angle of the jet and tracks considered. The maximum jet cone considered depends on the jet p_T, and ranges between $R = 0.45$ for a jet p_T of 20 GeV to $R = 0.24$ for a jet $p_T \geq 2$ TeV. The SVF algorithm takes as input the position of the PV_0, the jet axis and the list of tracks falling within the cone R.
The SVF algorithm is employed as a single secondary vertex finder (SSVF) algorithm, which means that only one secondary vertex can be associated to the jet. In principle, multiple vertices could be found within a jet if for instance the vertex associated to the decay of a c-hadron is reconstructed. These tertiary vertices are not always reconstructed because of the finite resolution of the ATLAS detector, hence only a single secondary vertex is reconstructed. If multiple SVs are identified within a jet, either they are merged together or the vertex with the highest track multiplicity is kept. Reconstructing two-tracks vertices has the effect of selecting a large number of fake ones. A vertex is regarded as *fake* if it is not associated to the decay of b- or c-hadron, and it can originate from different sources: tracks being randomly close to each other which are reconstructed as a vertex; decay of long-lived hadrons such as K^0 or Λ; hadrons interacting with the detector. Some cleaning criteria are applied to the two-tracks vertices to reduce as much as possible the fake contribution.

- A reconstructed two-tracks vertex is rejected if any track associated to it has hits at radius smaller then the radius of the vertex. This criteria reduces significantly the combinatoric fakes.

- The invariant mass of a two-tracks vertex is reconstructed. A vertex is rejected if its invariant mass is consistent with the invariant mass of a neutral hadron decaying into two particles, such as $K^0 \to \pi^+\pi^-$ or $\Lambda^0 \to p\pi^-$.

- A two-tracks vertex is rejected if its radius is consistent with the radii of cylindrical material layers. This criteria reduces the fake contribution generated by the interaction of the hadrons with the detector layers.

After this cleaning procedure, all the tracks associated to the surviving two-tracks vertices are combined into a list, which is supplied to the vertexing algorithm. This runs iteratively on all the tracks in the list, while it attempts to reconstruct a secondary vertex. At each iteration the track with the largest χ^2 is removed. The iterative process continues until the vertex invariant mass is < 6 GeV. If the reconstructed SV contains only two tracks, the vertex cleaning is reapplied. This procedure further reduces the fake vertices contribution.

Secondary vertices reconstructed by the SSVF algorithm are used to identify b-jets, as it discussed further in this work. A modified version of the SSVF algorithm, developed to apply the SSVF to tracks not matched to any calorimetric jet, is described in Chapter 4.

Electrons

The reconstruction of offline electrons in ATLAS [146] is kept as similar as possible to the online reconstruction described in Section 3.3. The key differences between online and offline reconstructions are:

- An upper threshold is applied on the d_0 and $|\frac{d_0}{\sigma(d_0)}|$ of tracks associated to the electron candidate in the offline reconstruction. $\sigma(d_0)$ is the uncertainty on the transverse impact parameter. These variables are not considered during the online reconstruction due to time constraints and to their poorer resolution.
- An optimised Gaussian Sum Filter (GSF) [147] is used during the offline reconstruction. The GSF is a generalisation of the Kalman filter which splits the noise into Gaussian components, to each of which a Kalman filter is applied. The GSF recovers radiative energy losses and improves the track variables by refitting the tracks associated to the electron candidate. The GSF cannot be applied online because it is time consuming. The variable $\frac{\Delta p}{p}$, which is the momentum lost by the track between the perigee and the last measurement point, relies on the GSF and it is only used offline.
- To improve signal/background separation the ratio of the cluster energy to the track momentum is used offline at high E_{T}.
- The offline pileup correction is performed by considering the number of reconstructed vertices, while online the $\langle\mu\rangle$ value is used.

The total electron identification efficiency can be expressed as the product of each individual selection efficiency for reconstruction, identification, isolation and trigger:

$$\epsilon_{\mathrm{total}} = \epsilon_{\mathrm{reconstruction}} \times \epsilon_{\mathrm{identification}} \times \epsilon_{\mathrm{isolation}} \times \epsilon_{\mathrm{trigger}}. \tag{3.14}$$

To correct any disagreement between data and MC scale factors (SFs) are applied to each component of the total efficiency. Figure 3.7 shows some examples of offline identification and isolation efficiencies.

Muons

Offline muons are reconstructed in a similar way to the online ones. The reconstruction is performed by combining separate measurements from the MS and the ID [148]. The ID tracks are required to satisfy the quality criteria already discussed, while the MS tracks

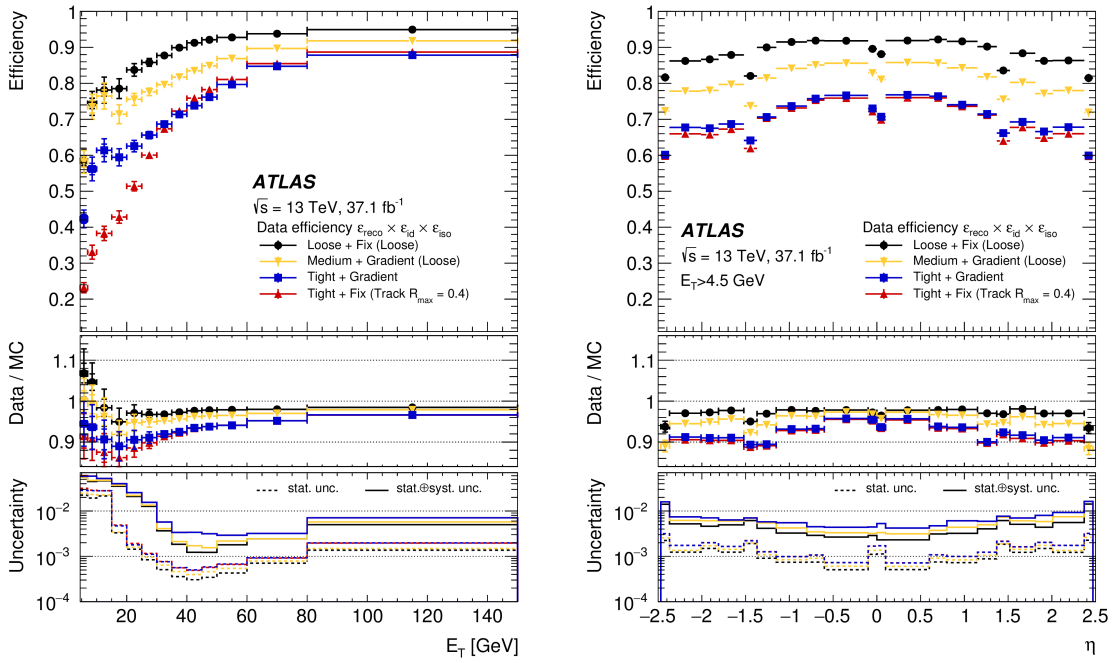

(a) (b)

Figure 3.7: Product of reconstruction, identification and isolation efficiencies $\epsilon_{\text{reconstruction}} \times \epsilon_{\text{identification}} \times \epsilon_{\text{isolation}}$ in a $Z \to ee$ sample using 37.1 fb^{-1} of data as function of (a) E_{T} and (b) η for $E_{\text{T}} > 4.5$ GeV for different operating points. The top panel of each image displays data only. The middle inset plot of each figure shows the data over MC simulations ratio. Statistical uncertainty only are considered. The lower inset plot of each image displays the relative statistical and total uncertainties (defined as the sum in quadrature of statistical and systematic uncertainties). Images taken from Ref. [146].

are reconstructed in a similar way to the online ones. The offline reconstruction proceeds by applying a set of algorithms based on the ID, MS and calorimeter information. Muons are classified into four groups.

– *Combined Muons.* This category includes muons reconstructed from independent ID and MS tracks, which are matched by a global fit.

– *Segment-Tagged Muons.* In this category the muons are reconstructed from an ID track with at least one associated track segment in the MDT or CSC chambers. This category is useful to recover reconstruction efficiency for muons with low p_T or muons interacting in regions of the MS with reduced acceptance. In these cases the muons might cross only one layer of the MS.

– *Calorimeter-Tagged Muons.* This category is used to recover reconstruction efficiency in the $|\eta| < 0.1$ region, where the MS is deficient due to the presence of material servicing upstream subdetectors. Calorimeter-tagged muons are reconstructed from ID tracks matched to a $\mathcal{O}(1$ GeV) calorimetric deposit consistent with a MIP.

– *Extrapolated Muons.* Muons in this category are reconstructed from tracks in the MS

with no matching ID track that are compatible with the interaction point. Extrapolated muons are used to recover efficiency in the $2.5 < |\eta| < 2.7$ region not covered by the ID.

The muons reconstructed in each of the above categories are grouped together. To avoid reconstructing the same muon with different algorithms an overlap removal procedure is applied. The resulting reconstructed muon sample is required to fulfil a set of identification criteria to select muons originated by the primary interaction, and to reject non-prompt muons, which are mainly originated by the decay of light hadrons. The selection criteria for the combined muons are based on:

- *q/p significance.* This is the charge to momentum ratio, normalised to their combined uncertainty.
- ρ'. This is the ratio of the absolute difference between the momenta of the tracks in the MS and the ID to the combined p_T.
- χ^2. This is the normalised χ^2 of the combined track fit.

Depending on the thresholds set for each variable, three muon identification OPs are defined. These are labelled as `Loose`, `Medium` and `Tight`. A fourth OP, labelled as `High-`p_T, is defined to achieve maximum resolution for tracks with $p_T > 100$ GeV. Isolation requirements on the muon candidates, which are defined in the same way as for the electron candidates, are exploited to obtain additional background rejection. Figure 3.8 shows some examples of offline reconstruction and isolation efficiencies. Figure 3.8(a) shows the reconstruction efficiency as function of the p_T for muons originated from the decay of the J/Ψ and Z boson. The efficiency is consistently above 98% for both data and MC simulation, and the data/MC ratio is close to one [148].

Jets

Offline jets are reconstructed by using the anti-k_t [149] algorithm to combine objects into jets. Two distance measures between the ith and jth objects and between the ith object and the beam are defined:

$$d_{ij} = \min(k_{ti}^{-2}, k_{tj}^{-2}) \frac{\Delta R_{ij}^2}{R^2}, \tag{3.15}$$

$$d_{iB} = k_{ti}^{-2}, \tag{3.16}$$

where $k_{ti(j)}$ is the transverse momentum of the ith (jth) object, ΔR_{ij} is the distance between the ith and jth object in the $\eta - \phi$ space and R is a parameter which defines the radius of the jet cone in the same $\eta - \phi$ space. If the minimum distance is d_{iB} the object is defined as a jet; otherwise if the minimum is one of the d_{ij}, the objects i and j are merged. The procedure is then iterated, and it continues until no object can be used

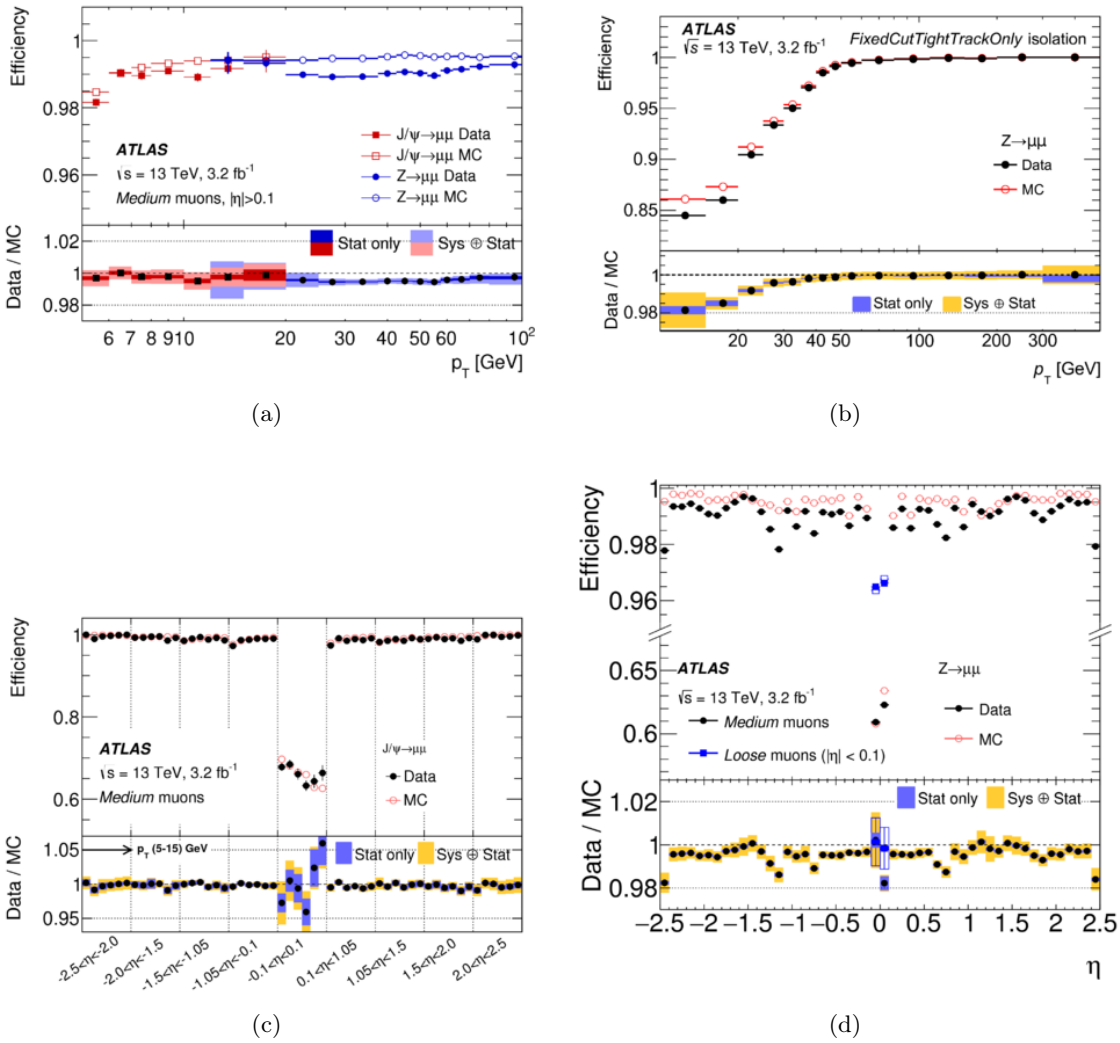

Figure 3.8: Reconstruction efficiency for the `Medium` muon selection as function of (a) the muon p_T $Z \to \mu\mu$ (blue) and $J/\Psi \to \mu\mu$ (red) events. The efficiencies are consistently above 98% for data and MC simulation, and any differences are magnified by the y-axis being very zoomed. The error bars on the efficiencies are statistical uncertainties only. The inset plot shows the ratio between the observed and MC simulated efficiencies, and the error bars include statistics and systematic uncertainties. (b) Isolation efficiency for the `FixedCutTightTrackOnly` muon isolation working point. The efficiency is computed as function of the muon p_T and it is measured in $Z \to \mu\mu$ events. The full (empty) circles indicate the efficiency measured in data (MC) samples. The inset plot shows the ratio between efficiency measured in data and MC simulation. The efficiency uncertainties are statistical only, while the inset plot displays statistical and systematic combined uncertainties. Muon reconstruction efficiency (c) as function of different η regions measured in $J/\Psi- \to \mu\mu$ events for the `Medium` selection and (d) as function of η measured in $Z \to \mu\mu$ events for the `Medium` and `Loose` muon selections. The efficiency loss for $|\eta| < 0.1$ is due to the presence of material servicing upsream subdetectors. The error bars in the efficieny plots indicate the statistical uncertainty only. The inset plots show the ratio of the measured and predicted efficiency, with statistical and systematic uncertainties. Images taken from Ref. [148].

to seed the anti-k_t algorithm. Figure 3.9 shows the jet reconstruction performed by the anti-k_t algorithm.

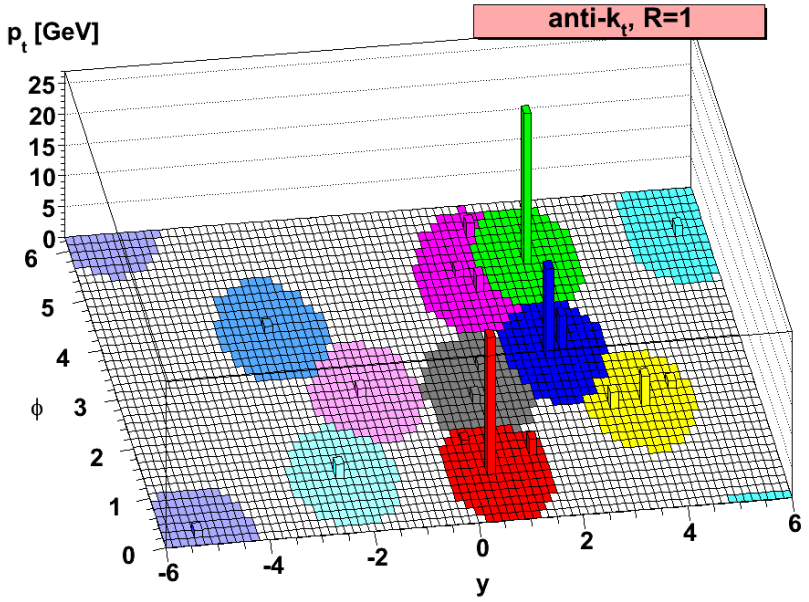

Figure 3.9: Pictorial representation of the behaviour of the anti-k_T algorithm with cone variable $R = 1$, showing the possible clustering configurations. Clusters with high p_T and conical reconstructed shape are represented as blue and red circles. An example of isolated low-p_T clusters are represented in light blue and pink. An example of a low-p_T cluster in proximity of an high-energy deposit in shown in magenta. Image taken from Ref. [149].

Objects with higher momenta are prioritised in the identification of the jets because of the inverse-momentum dependence in Equation 3.15. Reconstructed jets usually have a conical shape. Clusters with low momentum are reconstructed as conical-shape jets if they are isolated; otherwise possible overlaps between two clusters are assigned to the higher-momentum one, resulting in a non-conical shape for low momentum jets.
The anti-k_t algorithm can be applied to different input objects.

– *Topological cluster jets.* These jets are obtained by applying the anti-k_t algorithm to topological clusters [150] (topo-clusters). These are obtained by exploiting the lateral and longitudinal segmentation of the calorimeters to achieve a three-dimensional reconstruction of the particle showers. The topo-clusters are seeded by cells whose absolute energy measurement exceeds the expected noise, which includes both electronic noise and the average contribution from pileup, by four times its standard deviation. The topo-clusters are obtained by adding to the seed cell those cells whose energy deposit is at least two times higher than the standard deviation, and finally by adding all cells neighbouring the previous set. The topo-cluster algorithm is not designed to separate the energy deposits from different particles, but to separate continuous energy showers of different nature and to suppress noise.

– *Particle flow jets.* These jets are obtained by applying the anti-k_t algorithm to particle flow (PFlow) [151] objects. The PFlow algorithm performs a cell-based energy subtraction to remove overlaps between the momentum and the energy measurements made in the ID and calorimeters respectively. To achieve this, a list of tracks and a list of topo-cluster are used. The hadronic jets and soft activity, which is additional hadronic activity with energy deposit below the threshold for jet reconstruction, are reconstructed by combining tracking and calorimetric information.

The PFlow algorithm is briefly described in the following.

– Track selection. Stringent quality criteria are applied to the track selection. Each track is required to have at least nine hits in the silicon detectors and no missing hits in the pixel detector when such hits would be expected. Tracks are required to be within $|\eta| < 2.5$ and have $p_T > 0.5$ GeV. Tracks with $p_T > 40$ GeV are excluded from the algorithm, as such energetic particles are often not isolated from nearby activity, which would compromise the removal of the calorimeter energy associated with the track. Tracks matched to candidate electrons or muons with no isolation requirements and identified with medium quality criteria are rejected.

– Tracks to topo-clusters matching. This is obtained with a two-step approach. First the ratio between the energy of the topo-cluster, E^{clus}, and the track momentum, p^{track}, is required to satisfy $E^{\text{clus}}/p^{\text{track}} > 0.1$. Next, tracks are matched to one of the preselected topo-clusters using the distance $\Delta R'$, defined as:

$$\Delta R' = \sqrt{\left(\frac{\Delta\phi}{\sigma_\phi}\right)^2 + \left(\frac{\Delta\eta}{\sigma_\eta}\right)^2}, \tag{3.17}$$

with σ_η, σ_ϕ the angular topo-cluster widths. This criterion selects the correct topo-cluster with a high probability for all particles with $p_T > 5$ GeV. If no preselected topo-cluster is found in a cone of size $\Delta R' = 1.64$, then it is assumed that the particle associated with the track did not form a topo-cluster in the calorimeter, and no subtraction is performed.

– The expected energy deposited in the calorimeter by the same particle which originated the track, $\langle E_{\text{dep}} \rangle$, is computed according to:

$$\langle E_{\text{dep}} \rangle = p^{\text{trk}} \left\langle \frac{E^{\text{clus}}_{\text{ref}}}{p^{\text{track}}_{\text{ref}}} \right\rangle, \tag{3.18}$$

where the expectation value $\left\langle \frac{E^{\text{clus}}_{\text{ref}}}{p^{\text{track}}_{\text{ref}}} \right\rangle$ is obtained using single-particle samples without pileup by summing the energies of topo-clusters in a cone $\Delta R = 0.4$ around the track position, extrapolated to the second layer of the EM calorimeter [151].

– For each track/topo-cluster system, the algorithm evaluates the probability that the particle energy was deposited in more than one topo-cluster. If it is needed,

the algorithm adds more topo-clusters to the original track/topo-cluster system to recover the full shower energy.

– The expected energy deposited obtained in Equation 3.18 is then subtracted cell by cell from the set of matched topo-clusters.

– Finally if the remaining energy in the system is consistent with the expected shower fluctuations of a single-particle's signal, the topo-cluster remnants are removed; otherwise the remnant topo-cluster(s) are retained. This second case might be due to multiple particles depositing their energy in the vicinity.

After all these steps, the set of selected tracks and remaining topo-clusters in the calorimeter represents the reconstructed event with no double-counting of energy between the subdetectors. PFlow jets are reconstructed by using the anti-k_t algorithm with radius $R = 0.4$ [150]. The input objects for the jet reconstruction are a list of topo-clusters surviving the energy subtraction step and the list of selected tracks which are matched to the hard-scattering primary vertex, selected by requiring $|z_0 \sin\theta| < 2$ mm. PFlow jets are calibrated on the transverse momentum range 20 GeV $< p_T <$ 1500 GeV using the standard procedures described in Ref. [152]. A brief description of such calibration procedure is described in the following.

– *Vertex Correction*: the four-vectors of the jets reconstructed by the anti-k_t algorithm are adjusted to point to the PV_0 in the event.

– *Pileup correction*: the tracks associated to pileup vertices are omitted, together with a large fraction of the energy deposits from charged particles generated by the pileup interactions. The jet-area subtraction technique therefore mainly corrects for the pileup contributions due to neutral particles produced at the pileup vertices. The area of the jet is calculated using the *ghost association* [153, 154] method, in which particles with infinitesimal momenta are added to the event with uniform density in solid angle. After the jet reconstruction procedure is re-applied to the event, the jet area is defined proportional to the number of ghost particles associated to it. This area is used to define the momentum density from which the pileup corrections are derived.

– *Jet energy scale*: the absolute Jet Energy Scale (JES) [155] and η calibrations correct the jet four-momentum to the particle-level energy scale. This calibration corrects for detector effects, energy losses in dead material, out-of-cone effects and biases in the jet η reconstruction.

– *Global Sequential correction*: together with the energy and η dependency on the jet response already discussed, the jet four-momentum needs to be corrected for other factors such as the flavour of the originating parton and the composition of the hadrons created in jet fragmentation. Three variables are used to calculate

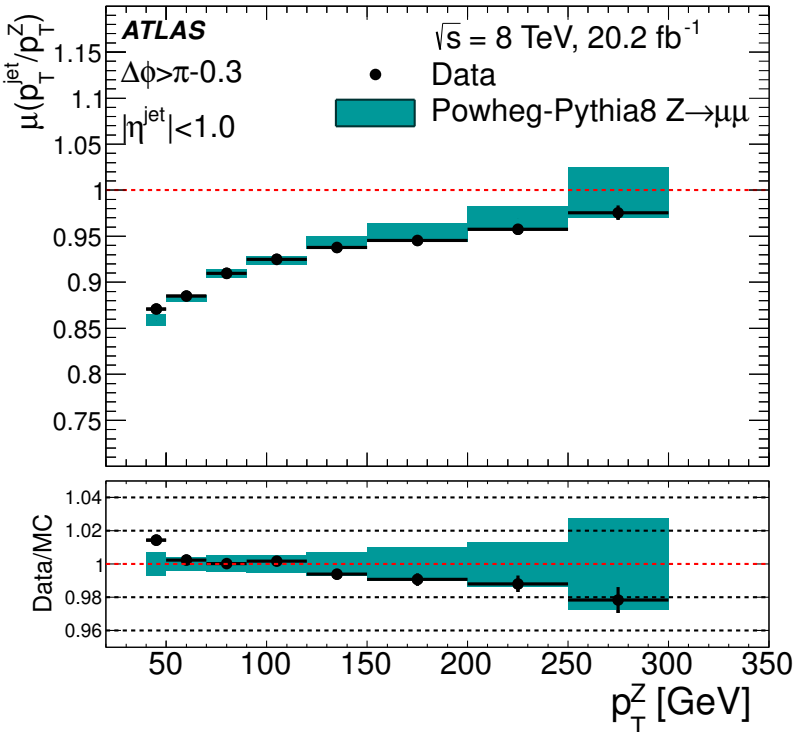

Figure 3.10: The mean value of the ratio of the p_T of a jet to that of a reconstructed Z-boson decaying into $\mu\mu$, used to validate the JES. The inset plot shows the ratio between the observed data (black circles) and the MC simulated samples (teal boxes). The uncertainties shown are statistical only. Image taken from Ref. [151].

the correction: the charge fraction, which is fraction of the jet energy measured from tracks associated to it; the fraction of jet energy measured in the third EM calorimeter layer; the fraction of jet energy measured in the first tile calorimeter layer. The corrections corresponding to each variable are applied consecutively.

– *JES validation*: no full *in situ* calibration of the uncertainties on the JES [156] is performed for PFlow jets [151]. To confirm that the ATLAS simulations describe the PFlow jet characteristics well, a validation of the jet calibration is performed. This is done by selecting a sample of $Z \to \mu\mu$ recoiling against a jet. Figure 3.10 shows the mean value of the ratio of the jet p_T against that of the Z boson for data and MC simulation for jets reconstructed within $|\eta| < 1$. The simulation reproduces the data within 2% and it is consistent with the data points within statistical uncertainties.

Only corrected jet candidates with $p_T > 20$ GeV and $|\eta| < 2.8$ are considered when selecting events in this analysis, while jet candidates with $|\eta| \leq 4.5$ are used to calculate the $E_{\mathrm{T}}^{\mathrm{miss}}$. Jet cleaning criteria [157] are required in order to identify and reject mis-reconstructed fake jets. These arise for example from detector noise, beam background and cosmic particles. Fake jets originated by detector noise in the HEC calorimeter are suppressed by vetoing jets for which the 90% or more of their energy is deposited in the HEC. Fake jets reconstructed because of unwanted cross-talk between neighbouring cells are suppressed by rejecting those jets which released 90% or more of their energy in five or less cells. Fake

jets reconstructed from coherent noise in the EM calorimeter are rejected by looking at the fraction of jet energy in the ECAL and the fraction of energy measured in bad-quality calorimeter cells. Out-of-time jets are rejected if they have an energy-weighted cell time greater than two bunch crossings.

A Jet Vertex Tagger (JVT) discriminant [158] is applied to further suppress jets arising from pileup vertices. The tagger is based on two variables: R_{p_T} and corrJVF. The first variable, R_{p_T}, is defined as:

$$R_{p_T} = \frac{\sum_k p_T^{\mathrm{trk}_k}(\mathrm{PV}_0)}{p_T^{\mathrm{jet}}}, \tag{3.19}$$

where the sum runs over all the tracks associated to the jet and the hard-scattering vertex PV_0; the jet transverse momenta are fully calibrated. The R_{p_T} distribution has a sharp peak at zero for pileup jets due to the fact that the tracks associated to a pileup jet are not matched to PV_0, while jets originating from the hard-scattering interaction display a more broad distribution. The second variable, corrJVF, is defined as:

$$\mathrm{corrJVF} = \frac{\sum_k p_T^{\mathrm{trk}_k}(\mathrm{PV}_0)}{\sum_k p_T^{\mathrm{trk}_k}(\mathrm{PV}_0) + \frac{p_T^{\mathrm{PU}}}{(k \cdot n_{\mathrm{trk}}^{\mathrm{PU}})}}, \tag{3.20}$$

where the scalar sum of the transverse momentum of each track associated to the hard-scattering vertex and the weighted scalar p_T sums of each pileup vertex contribute in the denominator of corrJVF. The weight $(k \cdot n^{\mathrm{PU}})$, with the parameter $k = 0.01$ and the multiplicity of tracks associated to the pileup vertices n^{PU} accounts for the linear dependence of the average p_T of pileup jets on the total pileup. The corrJVF variable is a measure of the fraction of tracks in the jet coming from the PV_0 compared to the total number of tracks matched to the PVs. The two variables R_{p_T} and corrJVF are combined [133] into the JVT score, which is used to reject pileup jets.

b-tagged jets

Hadronic jets can be initiated by a variety of different particles. Of particular interest for this work, and for many analyses within ATLAS, are jets initiated by b-quarks, commonly referred to as b-jets. In this work any jet which is not a b-jet is usually labelled as *light jet*. A representation of the differences between light- and b-jets is shown in Figure 3.11. b-hadrons can travel a sizeable distance in the detector before decaying because of their lifetime of $\mathcal{O}(10^{-12})$ s. Jets initiated by c quark display a similar behaviour, although with a smaller lifetime [159]. Jets initiated by these heavy quarks have a SV, which allows for a discrimination tool for jet flavour. b-jets are reconstructed using the same procedure for light-jets described before, with the addition of dedicated b-tagging algorithms [160], which are described in the following. The b-tagging algorithms are multivariate classifiers, which require a number of input variables which are provided by several low-level tagging algorithms. These are presented in the following.

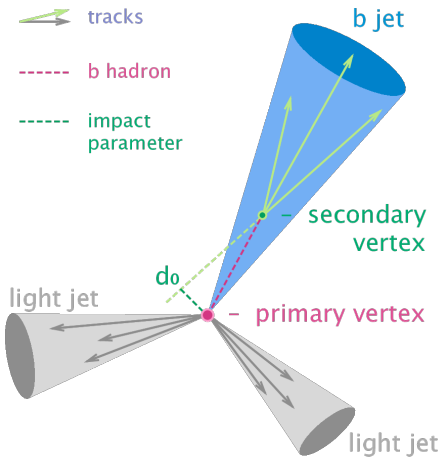

Figure 3.11: Illustration of the common principle of identification of jets initiated by b-quark decays. In this example the presence of a secondary vertex and the transverse impact parameter d_0 are highlighted. Image taken from Ref. [161].

- Impact-parameter based algorithms, IP2D and IP3D [162]. These algorithms exploit the b- and c-hadrons long lifetimes to identify tracks which are displayed from the hard-scattering PV_0. Both algorithms apply a common track selection based on p_T, d_0, $z_0 \sin\theta$ and pixel detector hits; the significance of the transverse impact parameter of the tracks, $\frac{d_0}{\sigma_{d_0}}$, is exploited by the two taggers, while IP3D also uses the longitudinal impact parameter $\frac{z_0 \sin\theta}{\sigma_{z_0 \sin\theta}}$. σ_{d_0} and $\sigma_{z_0 \sin\theta}$ are the uncertainties associated to d_0 and $z_0 \sin\theta$ respectively. These variables are used to build probability density functions, which are combined into a log-likelihood ratio based discriminant.

- Displaced-secondary-vertex based algorithm. It exploits the SVF [145] algorithm already described to reconstruct the decay vertex of a heavy-flavour hadron within a jet.

- Topological multi-vertex finding algorithm, JetFitter [163]. This algorithm exploits the topological structure of weak b- and c-hadron decays inside the jet to try to reconstruct the full b-hadron decay chain. The trajectory of the b-hadron and its decay products is reconstructed using a Kalman filter [141]. This approach can resolve b- and c-hadrons decay vertices even if a single track is attached to them. The output variables are parametrised for the three jet flavours, b-jets, c-jets and light jets.

The output variables obtained from the low-level algorithms are combined using multivariate classifiers. Two such classifiers [164] are defined. The first, MV2, is based on a boosted decision tree (BDT) discriminant; the second, DL1, is based a neural network (NN). A description of the two algorithms is reported in the following.

- MV2. This algorithm is based on a BDT combining the outputs of the low-level algorithms discussed above, together with the jet p_T and $|\eta|$. The BDT is trained

using the ROOT Toolkit for Multivariate Data Analysis (TMVA) [133] on the $t\bar{t} + Z'$ sample.

– DL1. This algorithm is based on a NN, whose multidimensional output corresponds to the probability for a jet to be a b-jet, a c-jet or a light-flavour jet. The same input variables as the MV2 algorithm are used, together with some extra variables from JetFitter related to the c-jets. The DL1 b-tagging algorithm is defined as:

$$D_{DL1} = \log\left(\frac{p_b}{f_c \cdot p_c + (1 - f_c) \cdot p_{\text{light}}}\right), \tag{3.21}$$

where p_b, p_c, p_{light}, and f_c are respectively the b-jet, c-jet and light flavour jet probabilities, and the effective c-jet fraction in the background training sample.

The output discriminant of the MV2 and DL1 b-tagging algorithm for b-jet, c-jet and light-flavour jets in the baseline $t\bar{t}$ simulated events are shown in Figure 3.12. Different

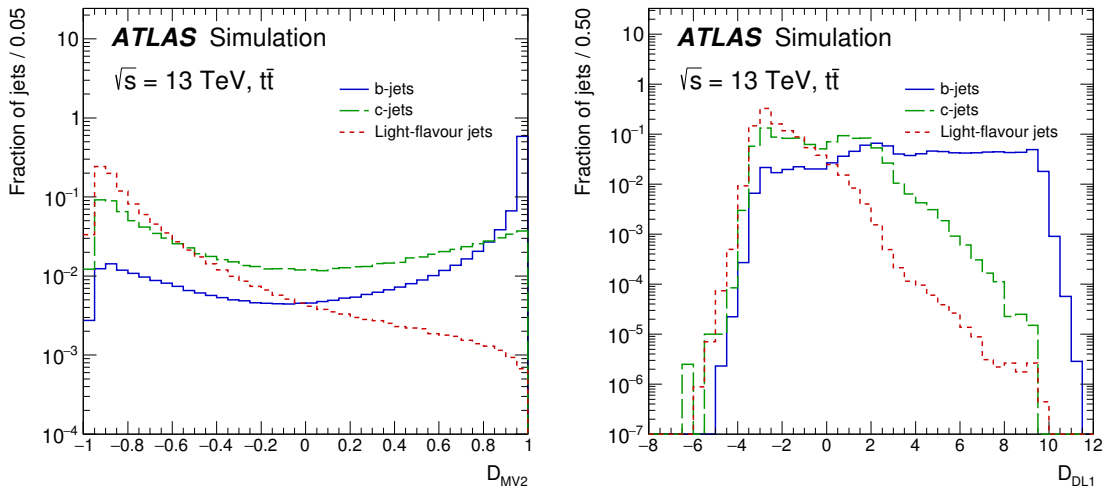

(a) (b)

Figure 3.12: Distribution of the output discriminant of (a) MV2 and (b) DL1 b-tagging algorithms for b-jets (blue), c-jets (green) and light-flavour jets (red) in $t\bar{t}$ simulated events. Images taken from Ref. [160].

OPs are defined by applying single-cut selections on the discriminant distributions. Each OP ensures a specific b-jet tagging efficiency, ϵ_b, for the b-jet present in the $t\bar{t}$ simulated sample. To each OP is associated also a c-jet and light-flavour jet rejection factor. The b-tagging efficiency and c- or light-flavour jet rejection factors are summarised in Table 3.1. This analysis exploits the DL1 tagging algorithm with OP selecting the 77% b-tagging efficiency. Figure 3.13 shows the b-tagging efficiency SF for the 77% DL1 OP used in this analysis. The results are consistent with the unity, and the total uncertainty is of the order of few percent, indicating that the MC simulations precisely model the observed data. The b-jet efficiency is calculated on $t\bar{t}$ events in di-leptonic final states. The mis-tagging c-jets efficiency is measured by selecting events with c-jets produced in association with a W

Table 3.1: Selection and c-jet, τ-jet and light-flavour rejections corresponding to the different b-tagging efficiency single-cut OP for the MV2 and DL1 algorithms. The rejection factors are evaluated on simulated $t\bar{t}$ events. Table taken from Ref. [160].

ϵ_b	MV2				DL1			
	Selection	Rejection			Selection	Rejection		
		c-jet	τ-jet	Light-flavour jet		c-jet	τ-jet	Light-flavour jet
60%	> 0.94	23	140	1200	> 2.74	27	220	1300
70%	> 0.83	8.9	36	300	> 2.02	9.4	43	390
77%	> 0.64	4.9	15	110	> 1.45	4.9	14	130
85%	> 0.11	2.7	6.1	25	> 0.46	2.6	3.9	29

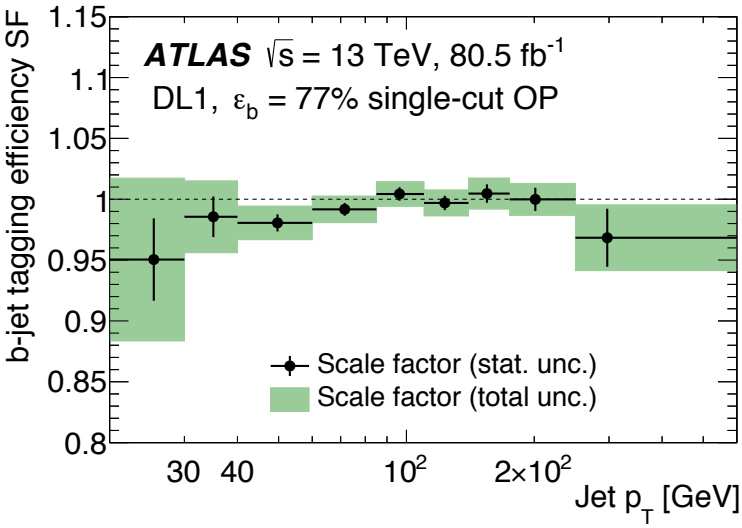

Figure 3.13: Distribution of the b-tagging efficiency simulation-to-data scale factor for the $\epsilon_b = 77\%$ single-cut OP of the DL1 tagger as function of the jet p_T. The vertical error bars include data statistical uncertainties only, while the green bands correspond to the sum in quadrature of statistical and systematic uncertainties. Image taken from Ref. [160].

boson decaying into a lepton and neutrino [165]. The c-jet is identified by reconstructing a soft muon from the semi-leptonic decay of the c-hadron. The mis-tag rate due to the light-flavour jets is computed by exploiting a negative-tag method [166].

Missing transverse momentum

The missing transverse energy $\mathbf{E}_{\mathrm{T}}^{\mathrm{miss}}$ is calculated as the negative vectorial sum of the transverse momenta of all the objects previously defined. Two main contributions can be considered: a *hard* contribution arising from the fully reconstructed and calibrated physics objects; and a *soft* contribution which originates from the reconstructed tracks in the ID which are matched to the PV_0, but not to any of the physics objects. The $\mathbf{E}_{\mathrm{T}}^{\mathrm{miss}}$ is obtained by considering the hard contribution arising from electrons, photons, jets and

muons together with the soft contribution, according to Equation 3.22:

$$E_{\mathrm{T}}^{\mathrm{miss}} = |\mathbf{p}_{\mathrm{T}}^{\mathrm{miss}}| = \left| - \sum_{\text{electrons}} \vec{p_T}^{e} - \sum_{\text{photons}} \vec{p_T}^{\gamma} - \sum_{\text{jets}} \vec{p_T}^{j} - \sum_{\text{muons}} \vec{p_T}^{\mu} - \sum_{\text{tracks}} \vec{p_T}^{\text{tracks}} \right|, \tag{3.22}$$

where $\sum_{\text{tracks}} \vec{p_T}^{\text{tracks}}$ is the vectorial sum of the unmatched tracks, which defines the soft contribution to the $E_{\mathrm{T}}^{\mathrm{miss}}$. From the x- and y-component of $E_{\mathrm{T}}^{\mathrm{miss}}$ an additional variable can be defined as

$$\phi^{miss} = \arctan\left(E_y^{miss}/E_x^{miss}\right). \tag{3.23}$$

An overlap removal (OR) procedure is applied to avoid the risk of double counting. Firstly the $\mathbf{p}_T$ associated to electrons is added, followed by photons and jets. Muons have little overlap with electrons, photons and jets and are not considered for overlap removal.
The $E_{\mathrm{T}}^{\mathrm{miss}}$ is therefore reconstructed from physics objects which have different p_T resolutions. Also, the set of objects used to determine $E_{\mathrm{T}}^{\mathrm{miss}}$ fluctuates significantly on an event-by-event basis. The fact the $E_{\mathrm{T}}^{\mathrm{miss}}$ strongly depends on the event composition results in a strong dependence on the event type and pileup activity. The reconstruction performance and its systematic uncertainty are assessed [167] using data vs MC comparisons of the $E_{\mathrm{T}}^{\mathrm{miss}}$ based quantities. The quality of the MC simulation is independently determined for individual type of physics objects, including the soft contribution, and then propagated to the final $E_{\mathrm{T}}^{\mathrm{miss}}$ calculation at event level.

Overlap Removal

This Section describes the OR procedure exploited in this thesis to avoid the reconstruction of the same particle as different objects in the detector. This procedure is applied event-by-event to all physics objects. The steps taken to perform the OR procedure are listed below.

- If a muon and an electron share an ID track and the muon is reconstructed as a calorimeter-tagged muon, the electron is kept and the muon is rejected.
- In a similar situation as above where the muon is not reconstructed as calorimeter-tagged muon, the muon is kept and the electron is rejected.
- If a jet and an electron are within a cone of radius $\Delta R < 0.2$ and the jet is not a b-jet, then the electron is kept and the jet is rejected. If the jet is a b-jet then the jet is kept and the electron is rejected.
- If a jet and an electron are within a cone of radius $\Delta R < 0.4$ then the jet is kept and the electron is rejected.
- If a jet and a muon are within a cone of radius $\Delta R < 0.2$ and the jet is not a b-jet and less than three tracks are matched to the jet, then the muon is kept and the jet is rejected. If the jet is a b-jet then the jet is kept and the muon is rejected.

– If jet and a muon are within a cone of radius $\Delta R < 0.4$, then the jet is kept and the muon is rejected.

3.5 Summary

The object simulation and reconstruction processes exploited by the ATLAS collaboration are described in this Chapter. Section 3.1 describes the standard data quality criteria used to select reliable data, and the full Run 2 dataset properties are discussed.
Section 3.2 presents the MC simulation process within ATLAS, which is based on the factorisation theorem. The MC generators used to implement the different stages of the event simulation are introduced. A brief description of the detector simulation is finally discussed.
In Section 3.3 a description of the reconstruction of the trigger objects exploited by this work is presented. These are the $E_{\mathrm{T}}^{\mathrm{miss}}$, electron and muon triggers. Finally Section 3.4 describes in detail the offline objects used in this work. Of particular importance for this work are the tracks and vertices, in particular the secondary vertices. The offline reconstruction of these objects is described in detail. Together with the offline counterpart of the trigger objects, the jet reconstruction process is described. This is performed using the PFlow reconstruction algorithm. Jets initiated by a b-quark are particularly useful for this analysis, so the reconstruction technique and performance of the b-tagging algorithm are discussed. The overlap removal procedure, useful to avoid multiple reconstructions of the same object, is finally described.

Studying Compressed SUSY Scenarios with low-p_T b-tagging

4

This Chapter describes a novel low-p_T b-tagging algorithm which extends the ATLAS detector ability to detect low-p_T b-hadrons. Section 4.1 introduces the motivations leading to the definition of a low-p_T b-tagging strategy in the context of third-generation SUSY searches at CERN. Section 4.2 summarises some preliminary studies performed by the Author on the impact of such an algorithm on a SUSY analysis. Section 4.3 introduces the tagging algorithm which is used throughout this work. Finally Section 4.4 describes the algorithm calibration efforts, mainly led by Dr. Vadim Kostyukhin from the University of Sheffield and Dr. Thomas Stevenson from the University of Sussex.

4.1 State of art of compressed third-generation SUSY searches

The importance of third-generation (3G) SUSY searches was already addressed in Chapter 1.3. One common feature of the decays of 3G scalar quarks (scalar top, $\tilde{t}$ or scalar bottom, $\tilde{b}$) is the presence of b-hadrons in the final state. The ability of the ATLAS detector to identify the decay of a b-hadron in an event is described in Section 3.4. The jet energy calibration intrinsically limits the b-tagging performance in events where the b-hadron has a low transverse momentum, as it can be seen in Figure 3.13 where b-jets with p_T lower than 20 GeV are not reconstructed. These scenarios are physically well motivated in Section 1.3. Early Run 2 results from ATLAS [168–171] and CMS [172, 173] show this clearly: the exclusion limits observed in the compressed scenarios are not as stringent as those where the mass difference between the pair-produced particle and the LSP is larger. The reason for this behaviour is that the standard b-tagging algorithms are not sensitive to the b-hadron p_T spectrum generated by the decay of compressed 3G scenarios. Figure 4.1 shows some common features of these final states. The simulated b-hadron p_T spectra coming from the $\tilde{t}_1 \to ff'b\tilde{\chi}_1^0$ and the $\tilde{b}_1 \to b\tilde{\chi}_1^0$ decays with $\Delta m(\widetilde{b}_1/\widetilde{t}_1, \widetilde{\chi}_1^0) = 20$ GeV are shown in Figure 4.1(a). In this scenario, the distribution of the p_T of the b-hadrons tends to peak towards low values, as it can be seen in Figure 4.1(a). The different spectra are due to the different final states arising from the decays of $\widetilde{t}_1$ (four-body decay) and $\widetilde{b}_1$ (two-body

decay). As it is already discussed, the standard b-tagging algorithms are less efficient in reconstructing low-p_T b-hadrons, such as the ones arising from the compress decay of 3G scalar quarks. As a consequence of the low-p_T b-hadrons distribution, the number of reconstructed b-jets with $p_T > 20$ GeV is often zero, as it can be seen in Figure 4.1(b). The $p_T > 20$ GeV threshold is imposed by the jet energy calibration.

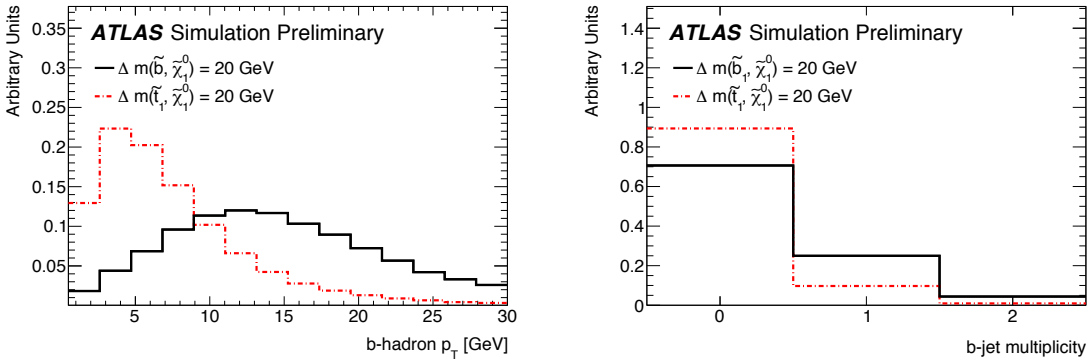

(a) (b)

Figure 4.1: (a) Truth b-hadron p_T distribution and (b) b-jet multiplicity distribution for a $\widetilde{b}_1$ (black curve) and $\widetilde{t}_1$ (dashed red curve) sample with $\Delta m(\widetilde{b}_1/\widetilde{t}_1, \widetilde{\chi}_1^0) = 20$ GeV.

A standard strategy to enhance the sensitivity of experiments to these compressed 3G scenarios is by requiring a mono-jet like topology. This is obtained by requiring the presence of a high-p_T leading jet, which is referred to as ISR, against which final state objects recoil. The effect of the ISR jet is to boosts the final-state objects. When considering a $\widetilde{b}_1$ decay, the final state particles are b-hadrons and neutralinos, as it is discussed in more detail in Chapter 5. The energy of the boost is split by the final-state objects roughly proportionally to their masses. For the signals examined by this analysis most of the boost is absorbed by the neutralino, which implies the b-jets remain characterised by a low-p_T.
Assuming that the sbottom and the neutralino are mass-degenerate, and the mass of the b-quark is negligible, in the sbottom rest frame (denoted by a *) one has:

$$\begin{cases} E^*_{\widetilde{\chi}_1^0} + E^*_b = m_{\widetilde{b}_1} \\ \overrightarrow{P}^*_{\widetilde{\chi}_1^0} = -\overrightarrow{P}^*_b. \end{cases}$$

From the assumption $m_{\widetilde{\chi}_1^0} \sim m_{\widetilde{b}_1}$, at order zero one has:

$$\begin{cases} E^*_{\widetilde{\chi}_1^0} = m_{\widetilde{\chi}_1^0} \\ E^*_b = \overrightarrow{P}^*_{\widetilde{\chi}_1^0} = \overrightarrow{P}^*_b = 0. \end{cases}$$

When a boost is applied one obtains:

$$\begin{cases} P_{\widetilde{\chi}_1^0} = \gamma(P^*_{\widetilde{\chi}_1^0} + \beta E^*_{\widetilde{\chi}_1^0}) \sim \beta\gamma m_{\widetilde{\chi}_1^0} \\ P_b = \gamma(P^*_b + \beta E^*_b) \sim 0, \end{cases}$$

which shows that b-hadron momenta are expected to be small even in presence of a significant boost.

A different approach to improve the sensitivity to compressed 3G scenarios relies on the definition of dedicated algorithms to reconstruct low-p_T b-hadrons. A public result from CMS, presented in Figure 4.2, shows the 95% CL exclusion limit for the production of top squarks when dedicated low-p_T b-tagging algorithms are exploited.

To increase the sensitivity to low-p_T b-hadron decays, the ATLAS collaboration de-

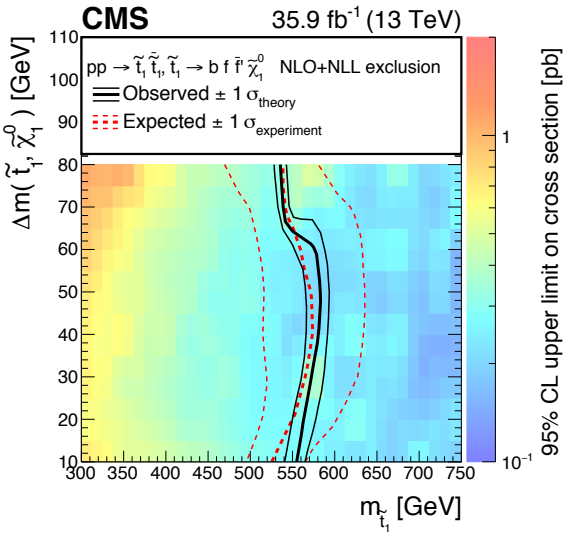

Figure 4.2: Exclusion limits at 95% CL for top squark pair production followed by the four-body decay $\tilde{t}_1 \to ff'b\tilde{\chi}_1^0$ in the $(m_{\tilde{t}_1}, \Delta m(\tilde{t}_1, \tilde{\chi}_1^0))$ plane measured by the CMS collaboration. The areas to the left and below the solid black curves represent the observed exclusion and the $\pm 1\ \sigma$ contours for the cross section calculations. The dashed red curves represent the corresponding expectation at 95% CL and $\pm 1\ \sigma$ deviation contours for the associated experimental uncertainties. The use of low-p_T b-tagging algorithm allows to improve sensitivity in the low $\Delta m(\tilde{t}_1, \tilde{\chi}_1^0)$ mass range. Image taken from Ref. [173].

veloped three soft-b-tagging algorithms, described in Ref. [2]. Two different approaches are pursued:

- *Track-jet-based b-tagging*: the aim is to extend the b-tagging sensitivity by applying the b-tagging techniques described in Section 3.4 to jets reconstructed from tracks [174]. The use of track-jets allows lowering the b-tagging p_T threshold, as it does not rely on the low-energy calorimeter deposit.

- *Vertex-based b-tagging*: the aim is to lower the b-tagging p_T threshold by abandoning the idea of a jet but focusing only on the presence of a secondary vertex arising from the decay of a b-hadron. In Ref. [2] two different implementations of this approach are described. The main difference between the two is the original vertexing algorithm being modified. The first implementation, referred to as the *Track-based Low-p_T Vertex Tagger* (T-LVT), relies on a vertexing algorithm developed for the detection of long-lived particles [175]. The second implementation, referred to as the *Track-*

Cluster-based Low-p_T Vertex Tagger (TC-LVT), relies on the vertexing algorithm commonly used to find secondary vertices within or in the vicinity of a jet [145].

This work is based on the TC-LVT algorithm, which is described in more detail in the following.

4.2 Low-$\mathbf{p}_T$ *b*-tagging impact on a SUSY analysis

This Section presents some preliminary feasibility studies of the potential impact a low-p_T b-tagging algorithm exploiting the presence of secondary vertices can have on a third-generation SUSY analysis. These studies are the Author's contributions. The impact of a low-p_T b-tagging algorithm is studied by emulating its efficiency and fake rate performance, as it is described in the following way:

- *Efficiency.* The tagging efficiency is emulated in signal and background MC events in which at least one truth b-hadron is found. If this condition is met, a random number is generated and if it is less than or equal to the efficiency, a secondary vertex is found if the true b-hadron p_T is in the range 5-30 GeV.
- *Fake rate.* The per-event fake rate is emulated in signal and background events without any requirements on the presence of a truth b-hadron. If the generated random number is below or equal to the fake rate, then a secondary vertex is found.

At the time of this study the algorithm was not fully developed, therefore a scan on the efficiency and fake rate was performed. Two samples are considered for this study: the signal sample is a bottom squark pair production where $\Delta m(\widetilde{b}_1, \widetilde{\chi}_1^0) = 20$ GeV, while the background sample is $Z \to \nu\bar{\nu}$. Two regions, respectively with no or one b-jet, are defined and the kinematic selections are reported in Table 4.1. The percentage of signal (background) events with at least one b-hadron, %S (%B) is reported, together with the signal/backround ratio (S/B) before requiring the presence of b-hadrons. The logic of this selection is to boost the bottom squark pair system to recoil against a high-p_T ISR jet, as it is discussed in Section 4.1. Please refer to Chapter 5 for more details. The truth b-hadron p_T distribution for signal and background are compared in shape, and they are shown in Figure 4.3. The measure used to study the impact of the algorithm is the S/B. As benchmark, S/B ratios obtained for the regions defined in Table 4.1 are considered. In this case, the S/B ratio is 1.2% for the 0 b-jet region and 6% for the 1 b-jet region before applying the vertexing emulation. As it can be seen in Table 4.2 requiring the presence of a low-p_T secondary vertex increases the S/B ratio up to a factor ~ 8. These results prove that the low-p_T b-tagging algorithm has the potential to improve the signal/background discrimination and extend an analysis's sensitivity towards lower b-hadron p_T values.
To further test its impact on a SUSY analysis a selection inspired by Ref. [176] is applied in order to quantify the change in sensitivity when secondary vertices associated to low-p_T

Table 4.1: Kinematic selection for the 0 b-jet and 1 b-jet regions. The percentage of signal (background) events %S (%B) containing a b-hadron and the S/B ratio are calculated before applying the $\Delta R(jet, b-\text{hadron})$ cut. For the 1 b-jet region, an overlap removal between the b-jet and the associated b-hadron is performed.

	0 b-jet	1 b-jet
$N_{b-\text{jets}}$	0	1
$\text{p}_\text{T}^{j_1}$ [GeV]	>250	>250
E_T^miss [GeV]	>250	>250
$\Delta R\,(\text{jet}, b-\text{hadron})$	>0.3	> 0.3
%S	18%	63%
%B	7%	22%
S/B	1.2%	6%

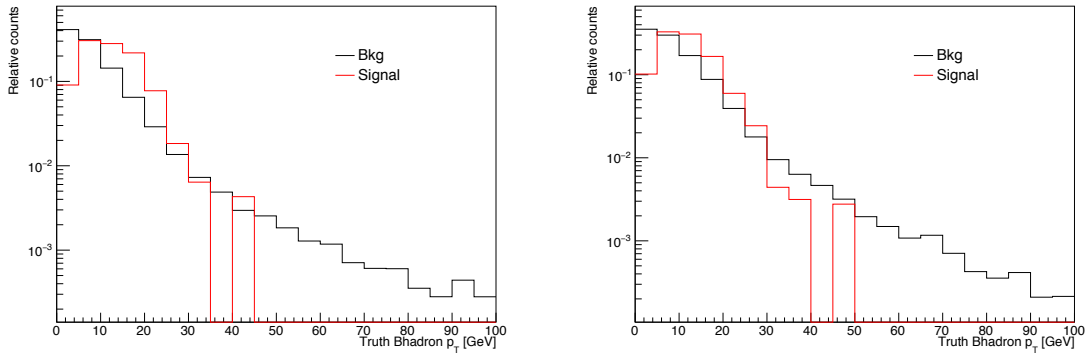

(a) (b)

Figure 4.3: Distribution of the truth b-hadron p_T distribution for $Z \to \nu\bar{\nu}$ (black curve) and $\widetilde{b}_1$ pair production (red curve) samples in a (a) 0 b-jet or (b) 1 b-jet region. Only events with a truth b-hadron are considered.

Table 4.2: S/B for the 0 b-jet and 1 b-jet regions for two (efficiency, fake rate) values.

(Efficiency, Fake) Rate (%)	S/B	
	0 b-jet	1 b-jet
(15, 2)	9.7%	15.1%
(15, 40)	4.3%	10.2%
(40, 2)	10.2%	16.1%
(40, 40)	5.4%	11.8%

b-hadrons are introduced. The kinematic selection exploited for this study is reported in Table 4.3.

Two b-jets and one b-jet regions are defined, as benchmark. The same background samples considered in Ref. [176] are used for this study, while three $\widetilde{b}_1$ pair production samples with $\Delta m(\widetilde{b}_1, \widetilde{\chi}_1^0) = 20$ GeV are studied. A total luminosity of 139 fb^{-1}, corresponding to the full Run 2 luminosity, is considered. Table 4.4 reports the background and signal yields, their ratio and the expected significance obtained by using the

Table 4.3: Kinematic selection defined to study the change in significance when introducing low-p_T b-tagging variables.

	2 b-jet	1 b-jet
j_1 b-tagged	0	0
N_{leptons}	0	0
$N_{b-\text{jets}}$	2	1
N_{vtx}	0	≥ 1
$\text{p}_{\text{T}}^{j_1}$ [GeV]	≥ 700	≥ 650
$E_{\text{T}}^{\text{miss}}$ [GeV]	≥ 650	≥ 500
$\text{H}_{\text{T;4}}$ [GeV]	≤ 80	≤ 80
A	≥ 0.86	≥ 0.86
m_{jj} [GeV]	≥ 350	-
m_{vtx} [GeV]	-	> 0.6
p_T^{vtx} [GeV]	-	> 3

Table 4.4: Signal and background yield, S/B and expected significance for the two b-jets and one b-jet regions for three $\widetilde{b}_1$ pair production samples.

Samaple [GeV]	Signal	Background	S/B	Significance
		2 b-jets		
$m\left(\tilde{b}_1, \tilde{\chi}_1^0\right) = 400{,}380$	35.61	3.03	11.75	8.32
$m\left(\tilde{b}_1, \tilde{\chi}_1^0\right) = 500{,}480$	10.08	3.03	3.33	3.14
$m\left(\tilde{b}_1, \tilde{\chi}_1^0\right) = 600{,}580$	5.09	3.03	1.67	1.85
		1 b-jet		
$m\left(\tilde{b}_1, \tilde{\chi}_1^0\right) = 400{,}380$	14.95	3.40	4.40	4.32
$m\left(\tilde{b}_1, \tilde{\chi}_1^0\right) = 500{,}480$	6.44	3.40	1.89	2.16
$m\left(\tilde{b}_1, \tilde{\chi}_1^0\right) = 600{,}580$	5.46	3.40	1.61	1.86

`RooStats::NumberCountingUtils::BinomialExpZ` [177] from the ROOT Framework [178] with an arbitrary 30% systematic uncertainty. The significance obtained for the 2 b-jets and 1 b-jet regions are combined by adding them in quadrature leads to the results shown in Table 4.5.

Table 4.5: Two b-jets, one b-jet and combined significances for the three $\widetilde{b}_1$ pair production samples.

Samaple [GeV]	Significance		
	2 b-jets	1 b-jet	Combined
$m\left(\tilde{b}_1, \tilde{\chi}_1^0\right) = 400{,}380$	8.32	4.32	9.37
$m\left(\tilde{b}_1, \tilde{\chi}_1^0\right) = 500{,}480$	3.14	2.16	3.81
$m\left(\tilde{b}_1, \tilde{\chi}_1^0\right) = 600{,}580$	1.85	1.86	2.65

The improved significance led to the decision to define an analysis strategy based on the presence of secondary vertices associated to low-p_T b-hadrons. In the following Section 4.3 the implementation of such low-p_T b-tagging algorithm is discussed.

4.3 Low p_T b-hadron identification with Track Clustering

The ATLAS detector performance for detecting and identifying b-hadrons is remarkable, as described in Section 3.4. A key element when reconstructing a b-jet is the ability to identify a secondary vertex, which originates from the decay of the b-hadron, in association with a calorimetric jet. Such secondary vertices are effectively reconstructed by the SSVF algorithm [145].
This Section describes the TC-LVT algorithm for detecting low-p_T b-hadrons in events with no or low calorimetric energy deposit. This algorithm exploits the well-established SSVF algorithm to reconstruct secondary vertices originating from the decay of low-p_T b-hadrons. The key difference with the standard b-tagging algorithm is that no calorimetric activity associated to the secondary vertex is required. As a consequence, the only objects available to detect the b-hadron are the tracks reconstructed in the ID. The tracks are required to be associated to the hard-scattering primary vertex PV_0, which is the PV whose scalar sum of all tracks p_T^2 is the highest. Tracks associated to pile-up vertices are then rejected. These tracks need to satisfy some preliminary quality criteria:

- at least seven hits in the silicon detectors;
- no more than one hit shared with other tracks in the silicon detectors;
- no more than one missing hit in the pixel detector;
- no more than two missing hits in the SCT detector;
- $|z_0 \sin\theta| < 3$ mm
- $|\eta_{\text{trk}}| < 2.5$ at perigee;
- $p_T^{\text{trk}} > 0.5$ GeV;

where $|z_0 \sin\theta|$ is the longitudinal impact parameter of the track with respect to the PV_0. The TC-LVT algorithm proceeds in a few steps to provide a collection of topologically close-by tracks (a *cluster* of tracks) as input to SSVF, to identify the presence of secondary vertices. The first step is the identification of a subset of *seed* tracks, characterised by relatively high-p_T and displacement. The second step is to identify tracks *close* to the seed (in terms of physical distance and momentum), to build a track cluster from the seed. Finally, the track cluster is passed to SSVF. The tracks used as seed and those used to expand the cluster need to satisfy dedicated selections, which have been optimised to yield a high efficiency to identify b-hadrons with p_T in the range $5 - 15$ GeV, while keeping the

Table 4.6: Summary of the TC-LVT working points defined according to the seed track and cluster selection criteria.

	Seed track		Cluster		
Working point	$\frac{d_0}{\sigma d_0}$	p_T [GeV]	$\frac{d_0}{\sigma d_0}$	$\Delta R^{\text{track}}_{\text{seed}}$	$r^{\text{track}}_{\text{seed}}$ [mm]
Loose	>1.25	> 1.5	> 1.25	< 0.75	< 0.2
Medium	>0.75	> 2	> 1.25	< 0.75	< 0.2
Tight	>0.9	> 2	> 0.9	< 0.7	< 0.6

fake rate under control. Only tracks that are not ghost associated [153, 154] to a jet are not considered by the TC-LVT algorithm. The selection criteria for the seed and cluster tracks are discussed in the following.

- *Seed tracks* are identified according to requirements on the impact parameter significance, $\frac{d_0}{\sigma(d_0)}$, and track p_T. The seed tracks are then ordered in decreasing p_T values.

- *Cluster tracks*: for each seed track, a cluster is created by adding tracks with high impact parameter significance, $\frac{d_0}{\sigma(d_0)}$. Other criteria the tracks have to satisfy are the seed-track angular distance, $\Delta R^{\text{track}}_{\text{seed}}$, and the seed-to-track distance at the closest approach, $r^{\text{track}}_{\text{seed}}$. The tracks are exclusively associated to one cluster only.

The SSVF algorithm then uses each cluster to reconstruct a secondary vertex, using the vectorial sum of momenta of the tracks in the cluster as seed direction. The properties of the reconstructed secondary vertices are saved in a dedicated container which provides all the kinematic variables which can be employed when defining an analysis.
Three working points are defined according to the requirements on the selections to identify the seed and cluster tracks, as it is reported Table 4.6 . The working point definitions differ compared to what is reported in Ref. [2], as the `Loose` working point is modified and a new `Medium` working point is introduced, while the `Tight` working point is unchanged. The performance of the TC-LVT algorithm is studied for the `Tight` working point by looking at the data/ MC modelling. To do so, a set of events dominated by $t\bar{t}$ production is defined [2] by requiring the presence of one electron and one muon with opposite sign, at least two calorimeter jets with $p_T > 30$ GeV, one of which is b-tagged by using the MV2 algorithm with the 77% efficiency OP [160]. Figure 4.4 compares the data to the MC prediction for vertex-related variables. Overall the agreement between the MC prediction and the observed data is satisfactory.
It is possible to match the TC-LVT vertices to generator-level particles using the truth-level information. The vertex angular direction is defined as the vector $\vec{r}_{\text{vtx}}$ pointing from the PV_0 to the TC-LVT vertex. If a b-hadron momentum vector is found within a cone of size $\Delta R < 0.3$ from the TC-LVT vertex angular direction, then the vertex is labelled as *matched to a b-hadron*. Otherwise, if no matching is found, the TC-LVT vertex is labelled as *unmatched*.

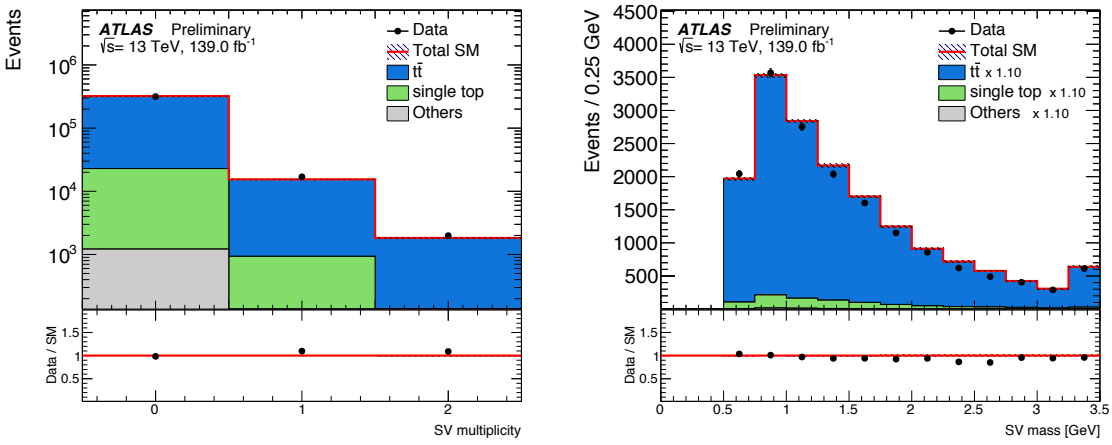

(a) (b)

Figure 4.4: Comparison between data and MC simulated events for (a) the number of TC-LVT vertices per event and (b) the reconstructed TC-LVT vertex mass in a $t\bar{t}$-dominated region. A scale factor of 1.1 is applied to the simulated events in (b) to allow for a shape comparison with the observed data. Overflow events are included in the last bin. The ratio between data and MC simulations is shown in the inset plot. Images taken from Ref. [2].

The three low-p_T b-tagging algorithms performance are compared in terms of efficiency per fake rate. These are defined as:

- *Efficiency.* This is the fraction of b-hadrons identified by a tagged object[1], and it is expressed as the product of the acceptance and tagging efficiency. The acceptance is the fraction of b-hadrons associated to the reconstructed objects, while the tagging efficiency is defined as the fraction of reconstructed objects matched to a b-hadron that satisfy the tagging conditions.
- *Fake rate.* It is expressed as the average number of unmatched tagged objects per event, evaluated on the $\tilde{t}_1 \to ff'b\tilde{\chi}_1^0$ events.

Figure 4.5 shows a comparison of the performance of the three low-p_T b-tagging algorithm as function of the efficiency and per-event fake vertices number in a $\widetilde{t}_1$ pair production sample. The TC-LVT performance differs from Ref. [2] because the newly defined working points performance are presented.

[1] In this context a *tagged object* is a track-based b-tagged jet, a T-LVT or TC-LVT vertex.

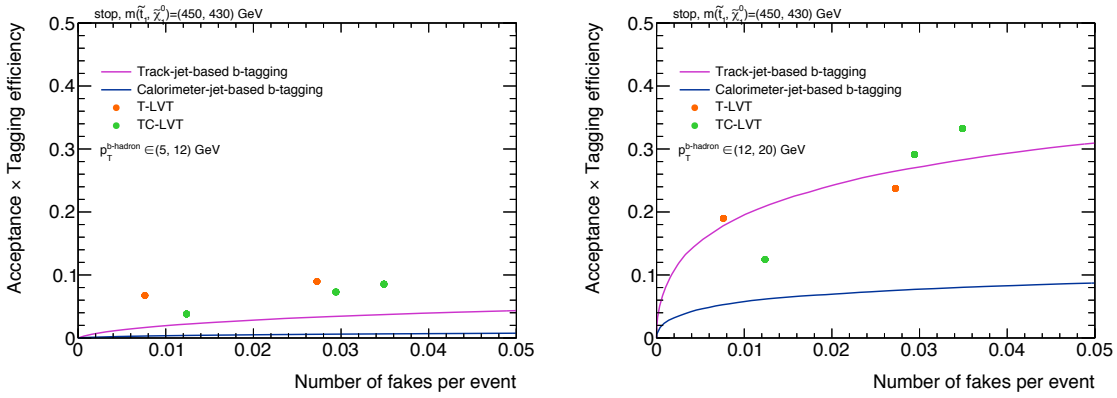

(a) (b)

Figure 4.5: Efficiency for tagging b-hadrons against the number of fake vertices expected in a $\widetilde{t}_1$ pair production sample in two b-hadron p_T ranges: (a) 5 GeV $< p_T <$ 12 GeV and (b) 12 GeV $< p_T <$ 20 GeV. The performance of T-LVT, track-jet and calorimeter-jet based b-tagging are taken from Ref. [2] while for the TC-LVT algorithm the new working points performance are shown.

4.4 TC-LVT Calibration

The TC-LVT algorithm implementation is described in Section 4.3, while its potential impact on a SUSY-like analysis is discussed in Section 4.2. This Section describes the TC-LVT calibration strategy for the `Loose` working point applied in this work. Two features are studied: the *efficiency* calibration, i. e. the procedure to calibrate the tagging efficiency of a vertex originated by the decay of a low-p_T b-hadron; and the *fake rate* calibration, which targets those events where there is no b-hadron in the event but a TC-LVT vertex is still reconstructed. The efficiency calibration is found to be mostly independent from the phase space investigated. The fake rate calibration on the contrary is more dependent on the specific final states targeted by the analysis. For this reason, the kinematic selections defined to study the fake rate calibration are inspired by the phase space definition presented in Chapter 5. This calibration work was largely developed by Dr. Vadim Kostyukhin from University of Sheffield and Dr. Thomas Stevenson from University of Sussex.

Efficiency Calibration

As anticipated in the introduction to this Section, the choice of the phase space does not affect the efficiency calibration measurement due to the presence of a b-hadron whose decay induces the presence of a secondary vertex in the event. This is demonstrated in the following, as the TC-LVT efficiency rate is calibrated using two different approaches: exploiting the events dominated by the $t\bar{t}$ decay; and studying events dominated by the decay of b-hadrons.

$t\bar{t}$ calibration

The decay of $t\bar{t}$ pairs typically results in events with two b-hadrons. A pure sample of $t\bar{t}$ events is selected by requiring the presence of exactly one b-tagged jet, one electron and one muon. This selection provides one with an unbiased dataset where the untagged b-hadron can be used to calibrate the TC-LVT efficiency. The kinematic selections applied for this analysis are:

- exactly one muon and one electron with opposite charge and transverse momentum $p_T^{\ell} > 20$ GeV;
- exactly one b-jet;
- number of jets $1 \leq N_{\text{jets}} \leq 3$;
- leading jet with transverse momentum $p_T^{j_1} > 150$ GeV;
- missing transverse energy $E_T^{\text{miss}} > 150$ GeV;
- jets with transverse momentum $p_T^{j_i} > 20$ GeV;
- no jet with $|\eta| > 2.5$ and $p_T^{j} > 25$ GeV.

Some data/MC distributions for this selection are reported in Figure 4.6. It is observed that the investigated region is highly pure in $t\bar{t}$ and single top processes, and that the MC simulations correctly model the observed data. The disagreement between data and MC simulated events observed in Figure 4.6(a) is well understood within the ATLAS collaboration, and it is due to missing high-order Feynman diagrams. Almost all the selected events feature the presence of two b-hadrons, as it is shown in Figure 4.6(c).
The transverse momentum spectrum of the b-hadron not angularly matched to the b-tagged jet starts from very low values, as it is demonstrated by Figure 4.7(a), hence it is likely that the TC-LVT algorithm is able to reconstruct its decay vertex. Requiring the presence of a TC-LVT vertex in the event modifies the b-hadron p_T spectrum as shown in Figure 4.7(b). This confirms that the selected dataset is suitable to perform the efficiency calibration of the TC-LVT algorithm. Having confirmed that there is an untagged sample of b-hadrons that can be used to calibrate the TC-LVT efficiency, it is possible to determine the tagging efficiency scale factor to rescale the MC yields. The scale factor is defined as:

$$S^{\text{eff}}_{\text{TC-LVT}} = \frac{N^{\text{data}}_{\text{N}_{\text{vtx}}>0}}{N^{\text{MC}}_{\text{N}_{\text{vtx}}>0}} \cdot \left(\frac{N^{\text{data}}_{\text{N}_{\text{vtx}}=0}}{N^{\text{MC}}_{\text{N}_{\text{vtx}}=0}} \right)^{-1} . \tag{4.1}$$

Equation 4.1 is a ratio of ratios, where $\frac{N^{\text{data}}_{\text{N}_{\text{vtx}}>0}}{N^{\text{MC}}_{\text{N}_{\text{vtx}}>0}}$ is the data/MC ratio of the number of events with at least one TC-LVT vertex and $\frac{N^{\text{data}}_{\text{N}_{\text{vtx}}=0}}{N^{\text{MC}}_{\text{N}_{\text{vtx}}=0}}$ is the data/MC ratio of the number of events with no TC-LVT vertices. No selection on the angular distance between the b-jet and the TC-LVT vertex is required. This implies that there might be events in which the

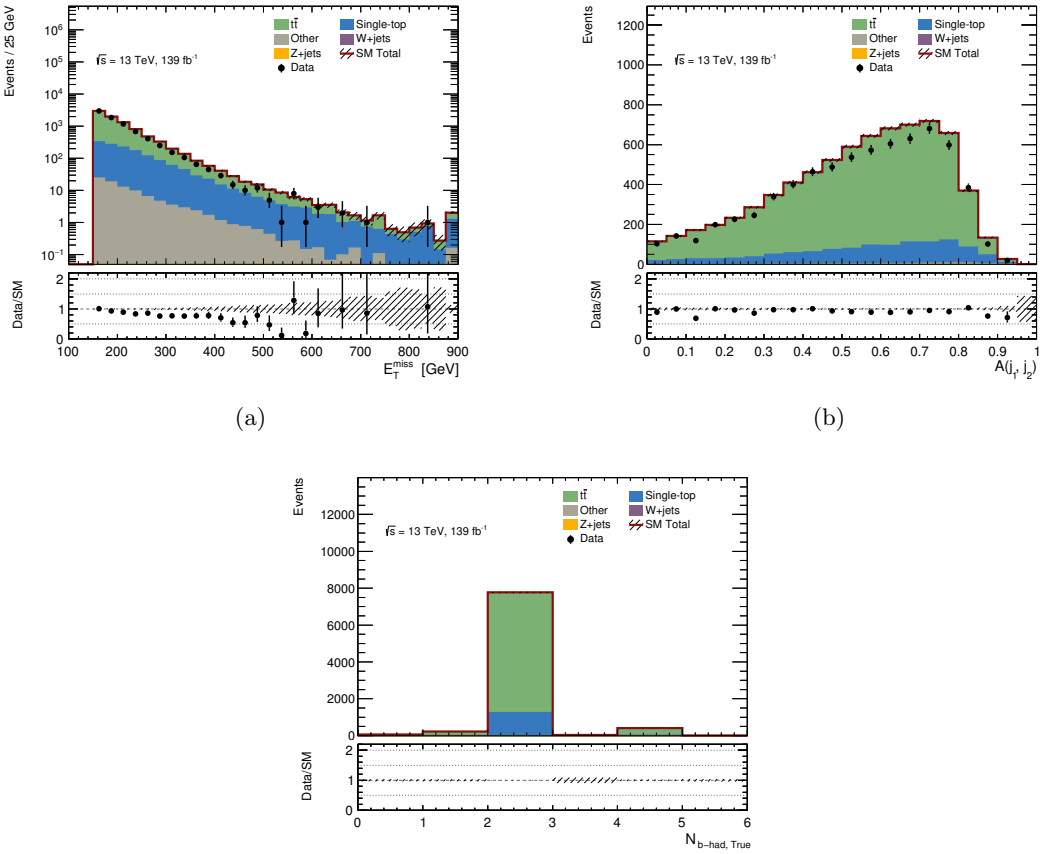

(a) (b)

(c)

Figure 4.6: Comparison between data and MC simulated events for (a) $E_{\mathrm{T}}^{\mathrm{miss}}$ and (b) A, the p_T asymmetry of the two leading jets, in a $t\bar{t}$-dominated region. The inset plot shows the ratio between the data and the simulated MC events. The uncertainties are statistical only. The overflow events are included in the last bin. (c) shows simulated only events displaying the truth b-hadrons multiplicity in the same region.

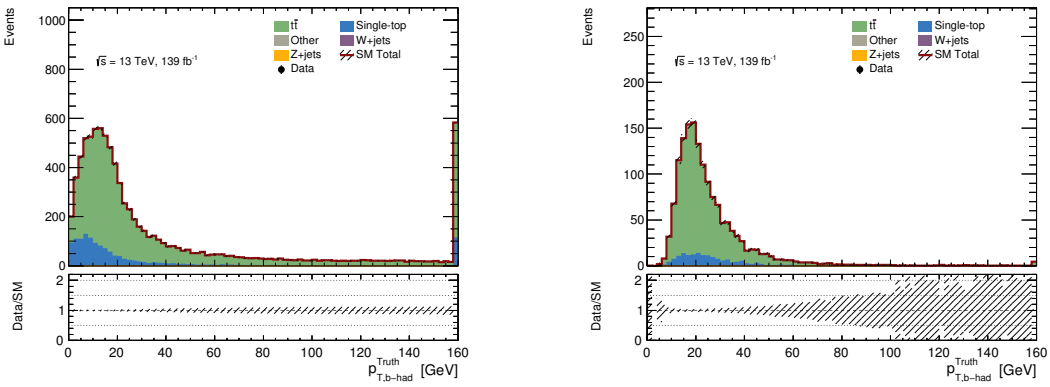

(a) (b)

Figure 4.7: Truth b-hadron p_T distribution for the b-hadron not associated to a b-tagged jet (a) before and (b) after requiring the presence of a TC-LVT vertex. The overflow events are included in the last bin.

b-hadron is tagged twice: by the standard b-tagging algorithm and by TC-LVT. This can be seen in Figure 4.8, where the events tagged twice are those where $\Delta\phi\,(b-\text{jet},\text{vtx}) \sim 0$ and $\Delta\eta\,(b-\text{jet},\text{vtx}) \sim 0$. This category of events is referred to as *overlap*, while the category of events where the TC-LVT vertices are isolated from the b-jet is referred to as *isolated*.

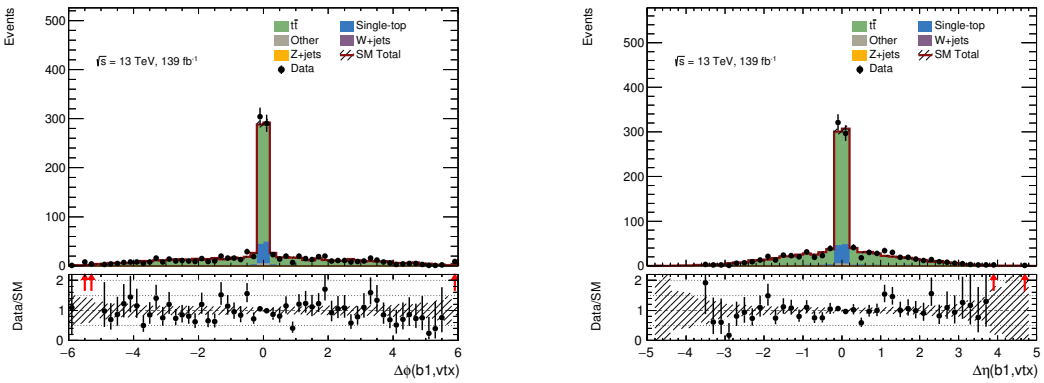

(a) (b)

Figure 4.8: Comparison between data and MC simulated events for (a) $\Delta\phi\,(b-jet,\text{vtx})$ and (b) $\Delta\eta\,(b-jet,\text{vtx})$. Events where the difference is ~ 0 feature a b-hadron tagged by both the TC-LVT and standard b-tagging algorithms. The inset plot shows the ratio between data and simulated MC events. The uncertainties are statistical only.

The presence of overlap and isolated events allows one to define three different categories:

- Events where the leading jet is b-tagged. In this case there is no overlap because the b-jet transverse momentum is outside the TC-LVT acceptance.
- Events where the sub-leading jet is b-tagged. In this case the TC-LVT is isolated if $\Delta R_{\text{b}-\text{jet},\text{vtx}} > 0.4$.
- Events where the sub-leading jet is b-tagged. In this case there is overlap if $\Delta R_{\text{b}-\text{jet},\text{vtx}} < 0.4$.

The first two categories, which are the isolated ones, are used to calibrate the efficiency rate, while the overlap category is exploited to estimate the systematic uncertainties on the SF. The efficiency SF for the `Loose` working point of the TC-LVT algorithm obtained by combining the two isolated sub-samples is:

$$S^{\text{eff}}_{\text{TC}-\text{LVT}} = 1.01 \pm 0.03, \tag{4.2}$$

where only the statistical uncertainty is taken into consideration. To evaluate the systematic uncertainty associated to the scale factor a few sources are considered, which are discussed in more detail in Section 6.1:

- Modelling of the $t\bar{t}$ decay systematics. This involves the variations on the production matrix element, hadronisation and initial state radiation effects.

– Reconstruction systematics. This contribution involves mainly the b-tagging SF.

On top of these sources of systematic uncertainty the overlap between the b-jet and the TC-LVT vertex is considered. This systematic contribution is obtained from the difference between the isolated and overlap scale factor. Having considered these sources of systematic uncertainty, the efficiency SF measured on di-lepton $t\bar{t}$ events is:

$$\begin{aligned} S^{\text{eff}}_{\text{TC-LVT}} &= 1.014 \pm 0.028(\text{stat}) \pm 0.057(\text{syst}) \\ &= 1.014 \pm 0.064(\text{tot}). \end{aligned} \tag{4.3}$$

b-physics calibration

A different approach to the TC-LVT efficiency calibration is studied by exploiting events containing b-hadrons coming from the process $pp \to b\bar{b} + X$, where X is any final state resulting from the pp collision. For this study the 36.1 fb^{-1} of data recorded until 2016 are used. A sample of b-hadrons is obtained by selecting $B^+ \to J/\Psi(\to \mu\mu)K^+$ events. The b-hadron is selected according to the following criteria [179]:

– First the $J/\Psi \to \mu\mu$ decay is reconstructed. The muons' transverse momentum is required to be $p_T^\mu > 6(4)$ GeV for the leading (sub-leading) μ, identified using the `Loose` OP. The muon pair invariant mass is required to satisfy 2.8 GeV $< m_{J/\Psi} <$ 3.4 GeV and the vertex fit is required to have a reduced χ^2 of $\chi^2/\text{ndf} < 10$.

– The K^+ is reconstructed selecting a track which is not associated to an electron or muon with $p_T^{\text{trk}} > 1$ GeV and $|\eta| < 2.5$.

– Finally the reconstructed B^+ is required to satisfy 4.7 GeV $< m_B <$ 6.0 GeV, $p_T^{B^+} > 8$ GeV, $|\eta| < 2.5$, and the vertex fit is required to have a reduced χ^2 of $\chi^2/\text{ndf} < 6$.

To obtain a pure sample the b-hadron is required to satisfy two more requirements:

– $c\tau_{\text{sig}} > 3 \cdot 10^{-4}$ m, where c is the speed of light and τ_{sig} is the b-hadron lifetime;

– a mass window of 5080 MeV $< m <$ 5480 MeV.

For calibrating the TC-LVT efficiency the fake rate is assumed to be negligible. In general, the tagging efficiency for both data and MC can be expressed as a differential function of the b-hadron and vertex p_T and η:

$$\epsilon^{\text{vtx}}_{\text{diff}}(p_T^B, \eta^B, p_T^{vtx}, \eta^{vtx}) = \frac{N_{\text{vtx}}(p_T^{vtx}, \eta^{vtx})}{N_B(p_T^B, \eta^B)} \tag{4.4}$$

where N_{vtx} is the number of secondary vertices reconstructed by the TC-LVT algorithm. To express the efficiency as a function of the vertex variables only it is possible to integrate Equation 4.4 over the b-hadron variables:

$$\epsilon^{\text{vtx}}(p_T^{vtx}, \eta^{vtx}) = \int dp_T^B \int d\eta^B \epsilon^{\text{vtx}}_{\text{diff}}(p_T^B, \eta^B, p_T^{vtx}, \eta^{vtx}). \tag{4.5}$$

The efficiency scale factor is then obtained by simply dividing the data and MC efficiencies:

$$SF(p_T^{vtx}, \eta^{vtx}) = \frac{\epsilon^{\text{vtx}}_{\text{data}}(p_T^{vtx}, \eta^{vtx})}{\epsilon^{\text{vtx}}_{\text{MC}}(p_T^{vtx}, \eta^{vtx})} \tag{4.6}$$

The two-bins SF map as function of the TC-LVT vertex p_T is shown in Figure 4.9. The chosen binning is reminiscent of preliminary studies on the overlapping of the three low-p_T b-tagging algorithms. The algorithms are not used in combination, but during the development stage there were discussion on how to combine them, and one solution could have been using different algorithms in different p_T ranges, with a threshold on the reconstructed b-hadron p_T of 15 GeV.

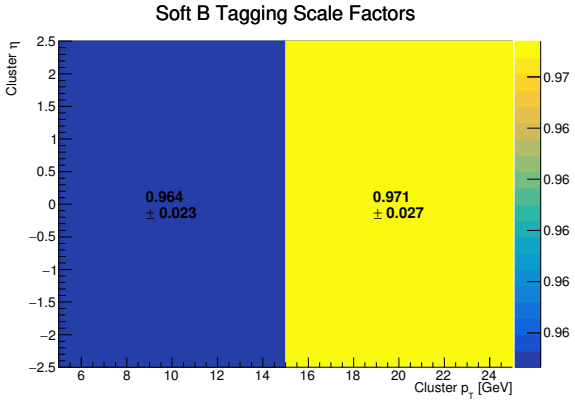

Figure 4.9: Differential calibration scale factor for the TC-LVT tagging efficiency as function of the cluster p_T. The values of the scale factors are compatible with 1 within the uncertainties. Only statistical uncertainties are considered.

The inclusive efficiencies in data and MC are respectively 0.354 ± 0.003 and 0.366 ± 0.006, where the uncertainties are statistical only. This leads to the inclusive efficiency scale factor of:

$$SF = 0.967 \pm 0.021 \tag{4.7}$$

where the uncertainty is only due to the statistics. The systematic uncertainty in this case is related to the track variables only, and it is found negligible for this study. The result presented in Equation 4.7 agrees within the uncertainties to the scale factor shown in Equation 4.3, which was obtained by using $t\bar{t}$ samples.

Fake Rate Calibration

A fake TC-LVT vertex is reconstructed when two or more tracks randomly cross and are reconstructed as a secondary vertex. The combinatorial nature of these crossings depends

on the number of tracks present in an event, and the fake rate calibration is dependent on the specific phase space targeted by the analysis. The fake rate calibration discussed in this Section is inspired by the kinematic selections discussed in Section 5.3. Also, because no b-hadrons are present in those events where a fake vertex is reconstructed, a different calibration technique compared to the efficiency rate calibration is needed. For this purpose Z/W+jets -dominated events are studied. The kinematic selection used to estimate the fake rate is reported below:

- no leptons with $p_T > 20$ GeV;
- number of jets $2 \leq N_{\text{jets}} \leq 5$;
- missing transverse momentum $E_T^{\text{miss}} > 250$ GeV;
- jet asymmetry $A > 0.4$;
- minimum angular distance between the $E_{\text{T}}^{\text{miss}}$ and any jet $\min[\Delta\phi(\text{jet}_{1-4}, E_{\text{T}}^{\text{miss}})] > 0.4$;
- $N_{\text{vtx}} > 0$ for events where $N_{b-\text{jets}} < 2$.

Figure 4.10 shows some properties of the region investigated. As required, this region is highly pure in the Z/W+jets production processes. In Figure 4.10(b), the bin at $N_{vtx} = 0$ is due to events featuring more than one b-tagged jet. Figure 4.10(c) shows that the selected region mainly features events with either two or no b-hadrons. The presence of events with two b-hadrons would in principle allow for calibrating the TC-LVT efficiency as well, but the procedures for calibrating the TC-LVT using $t\bar{t}$ events previously described allows to use the Z/W+jets region only to calibrate the fake rate efficiency.
To compute the fake rate scale factor the following system of equations is exploited:

$$\begin{cases} N_{\text{Reg}_0}^{\text{Data}} = S \cdot N_{\text{Reg}_0}^{\text{B}} + \lambda \cdot N_{\text{Reg}_0}^{\text{NoB}} \\ N_{\text{Reg}_1}^{\text{Data}} = S \cdot N_{\text{Reg}_1}^{\text{B}} + \lambda \cdot N_{\text{Reg}_1}^{\text{NoB}} \end{cases} , \tag{4.8}$$

where:

- Reg_0, Reg_1 are two subsets of the phase space under study with $N_{vtx} > 0$ and $N_{b-\text{jets}} = 0$ or $N_{b-\text{jets}} = 1$ respectively;
- N^{Data} is the number of observed data events in each region;
- N^{B} is the number of MC events featuring b-hadrons while N^{NoB} is the number of MC events with no b-hadrons;
- S is a common data/MC normalisation factor;
- λ is the TC-LVT fake rate scale factor.

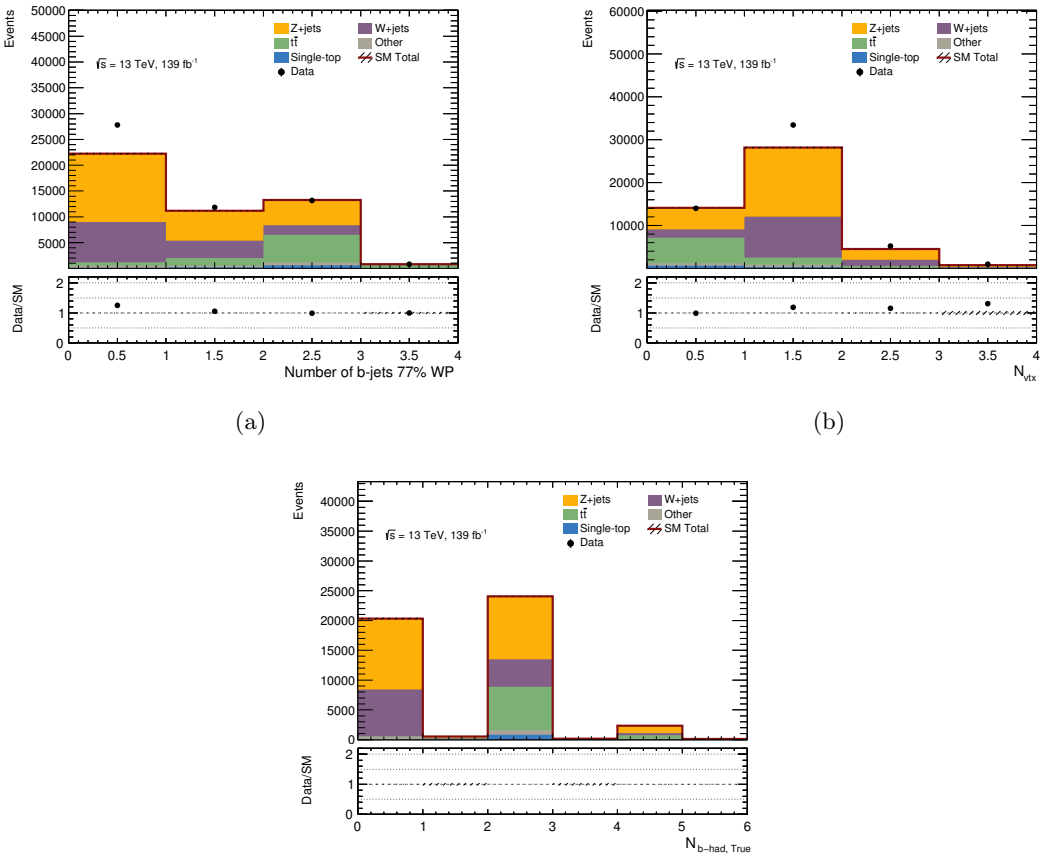

(a) (b)

(c)

Figure 4.10: Comparison between data and MC simulated events for (a) number of b-jets distribution and (b) number of TC-LVT vertices distribution in a Z/W+jets -dominated region. The inset plot shows the ratio between the data and the simulated MC events. The uncertainties are statistical only. (c) shows simulated only events displaying the truth b-hadrons multiplicity in the same region.

Solving the system of equations, the common data/MC normalisation factor is $S = 0.89 \pm 0.04$, while the fake rate scale factor is:

$$\lambda = 1.58 \pm 0.08 \tag{4.9}$$

where the uncertainty is only due to the statistical fluctuations. To estimate the systematic uncertainty, four categories of variations are considered:

- TC-LVT efficiency SF;
- b-tagging efficiency and fake rate SFs;
- Z/W+jets modelling;
- pileup.

A detailed description of how these systematic variations are measured is presented in Chapter 6.1. After considering these systematic variations, the TC-LVT fake rate SF for

the Loose working point on selected Z/W+jets events is

$$\begin{aligned}\lambda &= 1.58 \pm 0.08\ (\text{stat}) \pm 0.23\ (\text{syst}) \\ &= 1.58 \pm 0.25\ (\text{tot}).\end{aligned} \tag{4.10}$$

The results from the fake rate calibration SF shown in Equation 4.5 are in line with the measurement of the misidentification rate of light-flavour jets and c-jets discussed in Refs. [165, 180].

4.5 Summary

This Chapter describes the new TC-LVT algorithm developed by the ATLAS collaboration which extends the conventional b-tagging sensitivity to lower transverse momenta of the b-hadron. Section 4.1 describes the state of art of 3G SUSY searches within the ATLAS and CMS collaborations before the introduction of dedicated algorithms to detect low-p_T b-hadrons, and it briefly introduces the different approaches attempted within the ATLAS collaboration. Section 4.2 summarises the Author's work on the studies of the possible impact of a low-p_T b-tagging algorithm in a 3G SUSY-like analysis. Section 4.3 describes in more details the TC-LVT algorithm which is exploited by this analysis work. Finally Section 4.4 describes the TC-LVT calibration efforts, mainly led by Dr. Vadim Kostyukhin from University of Sheffield and Dr. Thomas Stevenson from University of Sussex. Two different approaches to calibrate the TC-LVT efficiency for the Loose working point are described, based on $t\bar{t}$ and b-physics samples. An efficiency SF of

$$\begin{aligned}S^{\text{eff}}_{\text{TC-LVT}} &= 1.014 \pm 0.028(\text{stat}) \pm 0.057(\text{syst}) \\ &= 1.014 \pm 0.064(\text{tot}),\end{aligned}$$

is applied, which is consistent with both calibration techniques within the uncertainties. The TC-LVT fake rate efficiency is calibrated using Z/W+jets samples, and the fake rate SF is found to be

$$\begin{aligned}\lambda &= 1.58 \pm 0.08\ (\text{stat}) \pm 0.23\ (\text{syst}) \\ &= 1.58 \pm 0.25\ (\text{tot}).\end{aligned}$$

Both the efficiency and fake rate SFs are consistent with the performance of the standard b-tagging algorithms from Refs. [160, 165, 180].

Searching SUSY in finals states with b-jets and $E_{\mathrm{T}}^{\mathrm{miss}}$

5

This Chapter presents the searches for direct pair production of bottom squarks in final states with large $E_{\mathrm{T}}^{\mathrm{miss}}$ and b-jets. The search exploits the 139 fb^{-1} of pp collision data recorded by the ATLAS detector at centre-of-mass energy of $\sqrt{s} = 13$ TeV.
Section 5.1 discusses the signal model analysed, together with the main SM production processes acting as background.
Section 5.2 focuses on the preliminary selections applied to the data-set, and on the modelling of some key kinematic variables used to define the analysis strategy.
Section 5.3 presents the full analysis strategy, by defining signal regions, control regions and validation regions.

5.1 Signal Model

The LHC produces a rich variety of final states. These originate from the decay of SM particles potentially together with those due to new-physics processes. Some of the possible new-physics final state topologies were discussed in Section 1.3. This Section describes the specific signal model investigated in this thesis, and the topology of its final states. The SM production processes which share the same topology constitute a background to the search, and they are therefore introduced.
The analysis relies on the MC simulation of both SM and signal processes, hence this Section briefly describes how the relevant MC datasets were produced.

Bottom Squarks

This work focuses on the direct pair production of bottom squarks, each of them decaying according to a RPC model to b-quarks and the lightest neutralino with a BR of 100%. The diagram associated to this simplified model is sketched in Figure 5.1. The signal samples are generated by MadGraph v5-2.6.2 [122] integrated with Pythia 8.230 [118] with the ATLAS 14 tune [120] for the modelling of the bottom squark decay, of the PS, hadronisation and underlying event. A tree-level calculation for the ME is performed, and the emisision of up to two additional partons is included. The PDF used for the generation

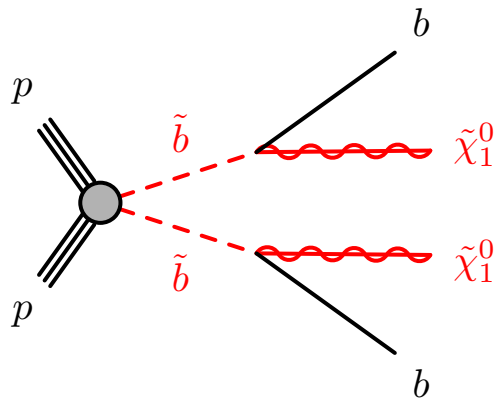

Figure 5.1: Diagram for the pair production of bottom squarks decaying into a bottom quark and lightest neutralino.

is NPDF23LO [181]. The ME-PS matching is done using the CKKW-L [182] prescription, and the matching scale is set to one quarter of the pair-produced superpartner mass. All the signal MC samples were generated using a 25 ns bunch spacing, to match the LHC bunch-crossing rate. The simulation of the interaction of the particles with the detector is performed by a fast simulation [127] which exploits a parametrisation of the calorimeter response and GEANT4 [126] for the other parts of the detector. The simulation process in ATLAS is more extensively discussed in Section 3.2.

The signal cross sections are calculated at next-to-next-to-leading-order (NNLO) accuracy in the strong coupling constant, adding the resummation of soft gluon emission at next-to-next-to-leading-logarithmic (NNLL) accuracy (NNLO+NNLL) [183–185]. The cross section calculation depends on the bottom squark mass according to Figure 5.2.

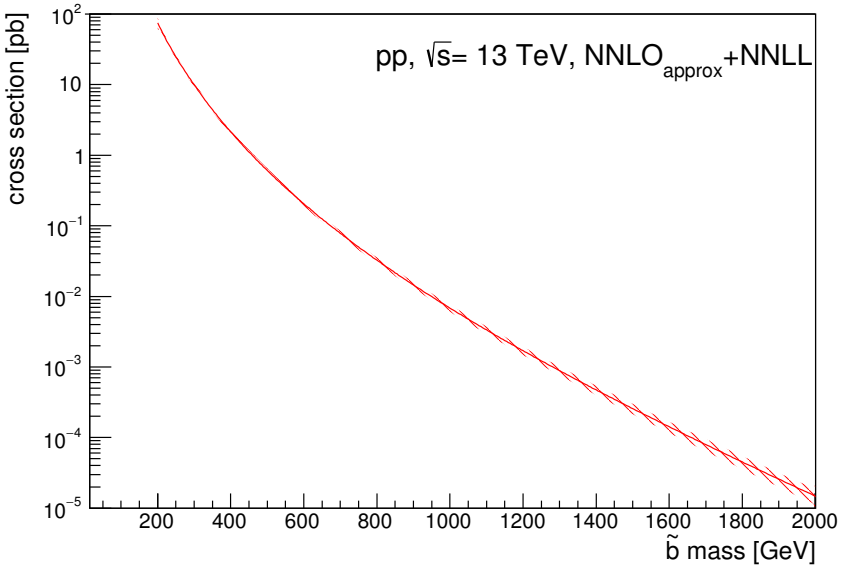

Figure 5.2: Cross section for the bottom squark pair production as function of the $\widetilde{b}_1$ mass.

Benchmark Points

This work is part of a larger analysis, as it is discussed in more detail in Chapter 6, and it focuses on signals with a mass splitting between the bottom squark and the lightest neutralino of $\Delta m(\widetilde{b}_1, \widetilde{\chi}_1^0) \leq 25$ GeV. These scenarios are referred to as *compressed*, due to the small mass splitting. Compressed final states often feature low-p_T b-hadrons, which are difficult to detect using the standard b-tagging algorithms. The analysis strategy for this work benefits of the novel low-p_T b-tagging algorithm described in Chapter 4. The compressed scenarios produce final states characterised by: the presence of $E_{\mathrm{T}}^{\mathrm{miss}}$ and the presence of low-p_T b-hadrons, which are not easily reconstructed as b-jets due to their low transverse momentum.
Physical models sharing this final state are discussed in Section 1.3, while the final-state objects are introduced in Section 3.4 and Chapter 4.
Final states with low-p_T b-hadrons and high $E_{\mathrm{T}}^{\mathrm{miss}}$ pose an interesting case of study for two reasons:

- *Physics motivations*: there are a number of models, including RPC SUSY, light Higgs boson searches and dark matter production which, depending on the model parameters, may generate low-p_T b-hadrons in the final state, as discussed in Section 1.3.

- *Experimental limitations*: the standard b-tagging techniques have a small probability to reconstruct the b-jets coming from the fragmentation of low-p_T b-hadrons. These final states pose an interesting experimental problem. Chapter 4 describes the TC-LVT algorithm dedicated to the reconstruction of such low-p_T b-hadrons.

Figure 5.3 displays the b-hadron p_T and the reconstructed b-jet multiplicity distributions for $\widetilde{b}_1$ mass points for four different mass splittings. The bulk of the momentum distribution in Figure 5.3(a) is below $p_T < 20$ GeV; the efficiency of the standard b-tagging approach is very small at such low momenta [186].

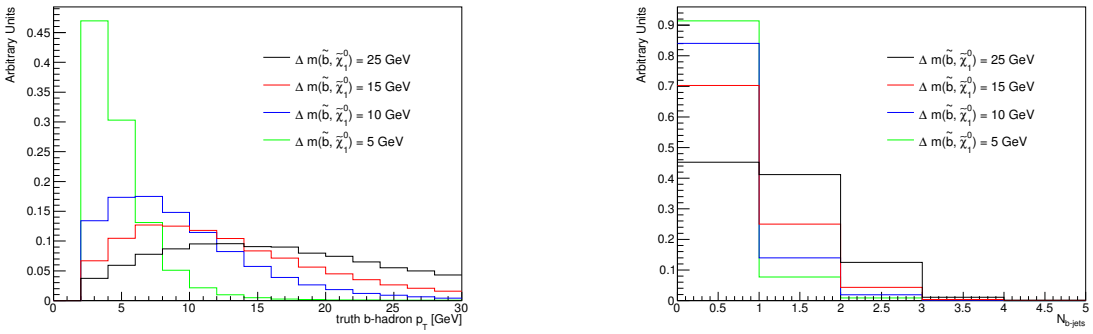

(a) (b)

Figure 5.3: (a) b-hadron p_T distribution and (b) b-jet multiplicity distribution for a $\widetilde{b}_1$ mass point with different $\Delta m(\widetilde{b}_1, \widetilde{\chi}_1^0)$.

Four benchmark mass points are used to define the analysis strategy: $m_{\widetilde{b}_1} = 500$, 600 GeV with $\Delta m(\widetilde{b}_1, \widetilde{\chi}_1^0) = 15$, 25 GeV. In Section 5.3 the benchmark mass points are used to determine the whole analysis strategy, which can be outlined in its key elements:

- fully-hadronic final states should be required in the event;
- large $E_{\mathrm{T}}^{\mathrm{miss}}$ is obtained by requiring an ISR jet with large transverse momentum recoiling against the bottom squarks pair system.

As introduced in Section 4.1, the ISR jet boosts the final-state objects (b-hadrons and neutralinos). Despite the boost, b-hadron momenta are expected to be small. The analysis strategy therefore relies on the TC-LVT algorithm described in Chapter 4 to identify those low-p_T b-jets.

Standard Model Processes

The SM background production processes that populate the search regions are discussed in this Section. It has been discussed how some important features which characterise the signal final state are high $E_{\mathrm{T}}^{\mathrm{miss}}$, no leptons and two b-jets. This final state is common to some SM production processes, which act as a background to the signal. The SM background production processes can be grouped into two classes: the *irreducible* backgrounds, which are those SM processes which have the same topology as the signal; and the *reducible* backgrounds, which are those with a different final-state topology, but that satisfy the event selection following misreconstruction or misidentification of some of the final state objects.
The main SM processes studied for this analysis are Z+jets , W+jets , $t\bar{t}$, single top, Diboson and ttV production. Figure 5.4 shows an example diagram for the production of each of the SM processes listed before at a pp collider.

Z+jets. This is the main SM background process for this analysis [176]. The decay of the Z boson into neutrinos $Z \to \nu\bar{\nu}$ provides real $E_{\mathrm{T}}^{\mathrm{miss}}$ in the final state, and additional radiation provides the b-hadrons. This process is an irreducible background. Events where the identified b-hadron are fake constitute in general a minor contribution to the background.
Z+jets events are simulated with Sherpa 2.2.1 [117]. The PDF used for the generation are NNPDF3.0NNLO, while the parton shower and hadronisation is performed using Sherpa with a default tune. The cross section is calculated at NNLO [187].

W+jets. This is a common SM background process, and it has a major role for this analysis as discussed in Section 5.3. It is a reducible background: even assuming that the W boson is produced in association with heavy flavour quarks, the high $E_{\mathrm{T}}^{\mathrm{miss}}$ from a neutrino is always associated to a lepton in the $W \to \ell\nu$ decay. Therefore, W+jets

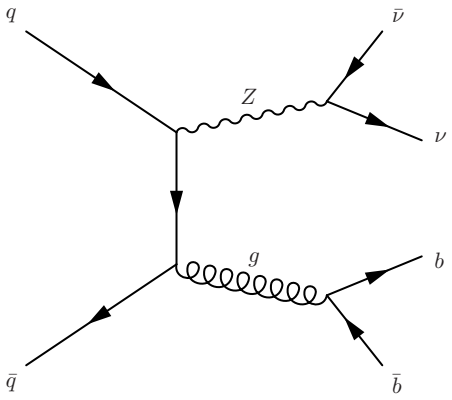

(a) Z+jets production

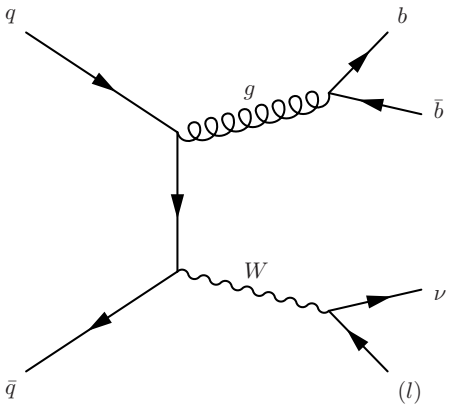

(b) W+jets production

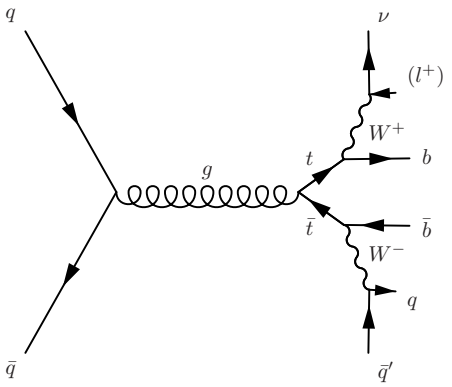

(c) $t\bar{t}$ production

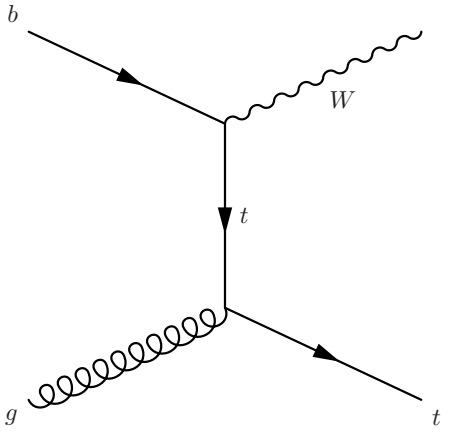

(d) single top production

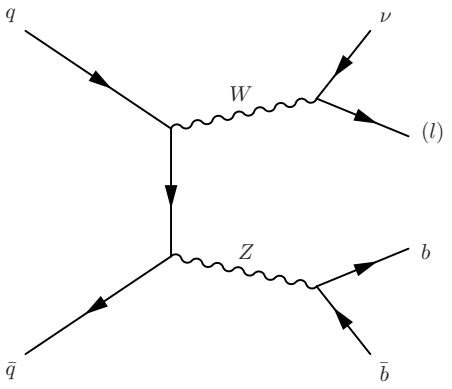

(e) Diboson production

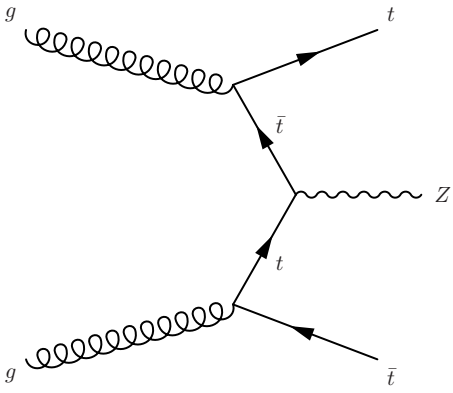

(f) ttV production

Figure 5.4: Examples of the main SM background processes production. The leptons in parentheses are misreconstructed for the event to pass a zero-lepton selection.

events satisfy the event selection only if the lepton fails to be reconstructed, or it is a hadronically-decaying tau.[1]
W+jets events are simulated with SHERPA 2.2.1 [117]. The PDF used for the generation are NNPDF3.0NNLO, while the parton shower and hadronisation is performed using SHERPA with a default tune. The cross section is calculated at NNLO [187].

$t\bar{t}$. It is another important SM background process. Again, this is a reducible background: despite the presence of two b-hadrons in the final state coming from the decay of the top quark, similarly to the W+jets case, high $E_{\mathrm{T}}^{\mathrm{miss}}$ must be associated with the production of a lepton.
$t\bar{t}$ events are simulated with POWHEG-BOX [123]. The PDF used for the generation are NNPDF2.3LO, and the parton shower and hadronisation is performed using PYTHIA 8 [118] with the $A14$ tune. The cross section is calculated at NNLO+NNLL [188–193].

Single Top. It is a fairly important process because of the presence of a b quark or a W boson in the final state. Similarly to the $t\bar{t}$ and W+jets productions, this process is a reducible background. As shown in Figure 5.4(d), the dominant Single Top production process is the Wt process.
Single top events are simulated with POWHEG-BOX [123]. The parton density functions used for the generation are NNPDF2.3LO, and the parton shower and hadronisation is performed using PYTHIA 8 with $A14$ tune. The cross section is calcuated at NNLO+NNLL [194–196].

$t\bar{t}$+V. $t\bar{t}$ pairs can be produed in association with γ, W and Z electroweak bosons, or in association with the Higgs boson. Despite the relatively small cross section compared to the other processes, this class of SM processes can be an irreducible background when the $Z \to \nu\bar{\nu}$ decay is considered because it produces high $E_{\mathrm{T}}^{\mathrm{miss}}$, while the b-hadrons are obtained from the top decay.
$t\bar{t}$ +V events are generated with MADGRAPH 5_ aMC@NLO 2.3.3 [122]. The parton density functions used for the generation are PYTHIA 8, and the parton shower and hadronisation is performed using PYTHIA 8 with $A14$ tune. The cross section is calculated at NLO [122].

Diboson it is a class of processes involving the production of two electroweak bosons like ZZ, WW or WZ. The ZZ process can provide an irreducible background when one Z boson decays into heavy flavour while the other into neutrinos. The WZ process can provide an irreducible background too when the W boson decays hadronically and the Z boson into neutrinos.
Diboson events are generated with SHERPA 2.2.1-2.2.2 [117]. The PDFs used for the

[1] No attempt to identify hadronically-decaying τ leptons is done in this analysis.

generation are NNPDF3.0NNLO, and the parton shower and hadronisation is performed using SHERPA with default tune. The cross section is calculated at NLO [123].

5.2 Event Selection and Modelling

The LHC provides the ATLAS detector with a large number of collisions per second, resulting in a large amount of recorded data. Section 2.3 described the data acquisition system by which the ATLAS detector is able to select a small fraction of interesting events originating from the collisions provided by LHC to be sent to permanent storage. This Section aims to describe the trigger strategy adopted for the online event selection, to introduce the key selection variables, and to determine the quality of the modelling of the SM production processes.

Trigger Strategy

Section 2.3 describes the ATLAS trigger and data aquisition system. Here the specific trigger menus exploited by the analysis are introduced. It has been discussed how the signal has a large missing transverse momentum. This feature suggests the use of HLT-$E_{\mathrm{T}}^{\mathrm{miss}}$ triggers (`HLT_xe`) [128–131]. Table 5.1 lists the HLT $E_{\mathrm{T}}^{\mathrm{miss}}$ thresholds required per each year.

Table 5.1: HLT $E_{\mathrm{T}}^{\mathrm{miss}}$ triggers thresholds per each year.

Data Period	`HLT_xe` Threshold
Data 2015	$>$ 70 GeV
Data 2016-18	$>$ 110 GeV

The offline selection is fully efficient for events with $E_{\mathrm{T}}^{\mathrm{miss}} > 250$ GeV, as it is shown in Figure 5.5. These plots are produced by considering events triggered by a single-muon trigger. Depending on its configuration, the HLT can reconstruct the $E_{\mathrm{T}}^{\mathrm{miss}}$ by ignoring muons, that is, by treating them as invisible. The efficiency of the $E_{\mathrm{T}}^{\mathrm{miss}}$ trigger can therefore be measured by counting the fraction of events with a given value of the (muon corrected) $E_{\mathrm{T}}^{\mathrm{miss}}$ for which the $E_{\mathrm{T}}^{\mathrm{miss}}$ trigger has fired.

Despite the fact that the signal topology requires a 0-lepton selection, there is the need to define 1-lepton and 2-leptons regions to estimate the background contribution, as it is detailed in Section 5.3. These two classes of events might have a smaller $E_{\mathrm{T}}^{\mathrm{miss}}$, which might cause the HLT-$E_{\mathrm{T}}^{\mathrm{miss}}$ triggers to be not optimal. For this reason, single-lepton triggers are used. These rely on the presence of either an electron or a muon. The HLT thresholds for these triggers are listed in Table 5.2. The increased HLT threshold required in years 2016 to 2018 for both $E_{\mathrm{T}}^{\mathrm{miss}}$ and single-lepton triggers was introduced to deal with the increased pileup generated by the higher luminosity provided by the LHC.

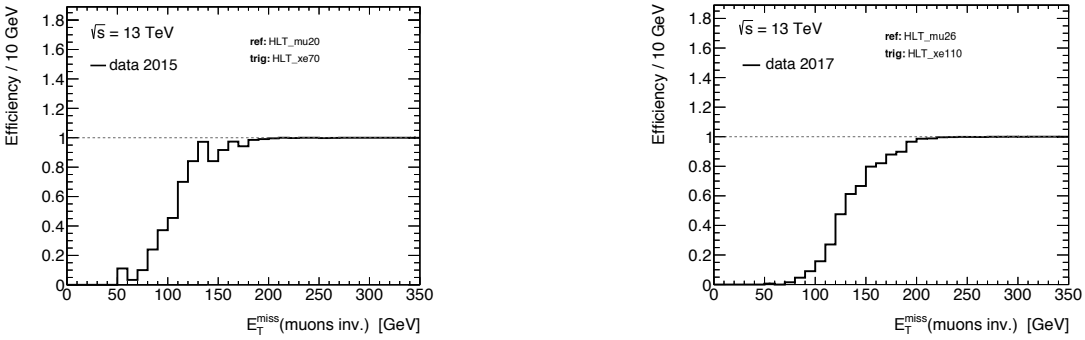

(a) (b)

Figure 5.5: HLT $E_{\mathrm{T}}^{\mathrm{miss}}$ efficiency for (a) 2015 and (b) 2017. The $E_{\mathrm{T}}^{\mathrm{miss}}$ trigger efficiency is computed against a single muon trigger, as reported in the legend.

Table 5.2: HLT single-lepton triggers thresholds per each year.

Data Period	`HLT_e` Threshold	`HLT_mu` Threshold
Data 2015	$>$ 24 GeV	$>$ 20 GeV
Data 2016-18	$>$ 26 GeV	$>$ 26 GeV

Signal Objects

Based on the definitions of the physics objects described in Section 3.4 and the relative OR procedure, the signal objects exploited in this analysis have to satisfy the following requirements.

– *Jets.* Baseline jets which are likely to originate from pileup interaction vertices are rejected by requiring the JVT [197] to be $w_{\mathrm{jvt}} > 0.5$ for jets with $p_T \in [20, 60]$ GeV and $|\eta| < 2.4$. These requirements correspond to the `Tight` JVT working point for PFlow jets.

– *Electrons.* Reconstructed electrons are required to be identified with the `TightLLH` identification OP. Additionally, the impact parameter significance is required to satisfy $\left|\frac{d_0}{\sigma(d_0)}\right| < 5$. Signal electrons are required to have a $p_T > 20$ GeV in order to select only those electrons produced during the hard-scattering interaction. Events with two electrons are collected by single-electron triggers, and the leading electron is required to have $p_T > 27$ GeV.

– *Muons.* Reconstructed muons are required to be identified with the `Medium` identification OP and isolated according to the `FCTightTrackOnly` OP. Additionally, the impact parameter significance is required to satisfy $\left|\frac{d_0}{\sigma(d_0)}\right| < 3$. Signal muons are required to have a $p_T > 20$ GeV in order to select only those muons produced during the hard-scattering interaction. Events with two muons are collected by single-muon triggers, and the leading muon is required to have $p_T > 27$ GeV.

Kinematic Variables

Some of the kinematic and topological properties of the signal can be effectively exploited to design selections characterised by favourable signal-to-background yield ratios. The variables listed below are useful in this sense. In the following a list of variables used to define the various regions of the analysis is reported. Where sensible the objects are p_T-ordered.

- $E_{\mathrm{T}}^{\mathrm{miss}}$: the real missing energy in the event, it is the magnitude of $\mathbf{E}_{\mathrm{T}}^{\mathrm{miss}}$.
- $E_{\mathrm{T},\ell\ell}^{\mathrm{miss}}$: the 'corrected' $E_{\mathrm{T}}^{\mathrm{miss}}$. It is used in the 2-leptons selections to mimic the $Z \to \nu\nu$ contribution. In this case, the transverse momentum of the lepton pair is subtracted from the real missing energy. Therefore $\mathbf{E}_{\mathrm{T},\ell\ell}^{\mathrm{miss}} = \mathbf{E}_{\mathrm{T}}^{\mathrm{miss}}$- $\mathbf{p_T}^{\ell\ell}$, where $\ell = \mathrm{e}, \mu$.
- $\min[\Delta\phi(\mathrm{jet}_{1-\mathrm{N}}, \mathbf{E}_{\mathrm{T}}^{\mathrm{miss}})]$: the minimum azimuthal distance between the first N, p_T-ordered jets and the $\mathbf{E}_{\mathrm{T}}^{\mathrm{miss}}$. It is used to reduce multi-jet background, where the $\mathbf{E}_{\mathrm{T}}^{\mathrm{miss}}$ direction tends to be angularly close to one of the jet transverse momenta. This is because the $\mathbf{E}_{\mathrm{T}}^{\mathrm{miss}}$ in multijet events arises either from a mis-measured jet or because of a hadron weak decay producing neutrinos. In both cases, $\mathbf{E}_{\mathrm{T}}^{\mathrm{miss}}$ tends to be aligned with one of the jets. This implies that requiring a minimum value on the $\min[\Delta\phi(\mathrm{jet}_{1-\mathrm{N}}, \mathbf{E}_{\mathrm{T}}^{\mathrm{miss}})]$ variables suppresses the multi-jet background.
- $\Delta\phi(j_1, E_{\mathrm{T}}^{\mathrm{miss}})$: the azimuthal distance between the leading jet and $E_{\mathrm{T}}^{\mathrm{miss}}$. It is used to select events where the sbottom pair system is recoiling against a ISR jet.
- $\mathrm{H}_{\mathrm{T};3}$: the scalar sum of jet p_T in the event, starting from the third jet. It is defined as:

$$H_{T;3} = \sum_{i=3}^{N-\mathrm{jets}} p_T^{\mathrm{j_i}}. \tag{5.1}$$

  It provides extra rejection of $t\bar{t}$ which usually displays larger hadronic activity than the signal.
- A: the p_T asymmetry of the leading two jets, defined as:

$$A = \frac{p_T(\mathrm{j}_1) - p_T(\mathrm{j}_2)}{p_T(\mathrm{j}_1) + p_T(\mathrm{j}_2)}. \tag{5.2}$$

  This variable tends to take values close to one for signal events where a high-p_T leading jet is accompanied by soft activity, while it is more balanced for SM processes characterised by the presence of higher p_T jets.
- $m_{\ell\ell}$: the invariant mass of the two leading leptons, where $\ell = \mathrm{e}, \mu$. It is used for the background estimation to select events where $m_{\ell\ell} \sim m_Z$.
- m_{jj}: the invariant mass of the two leading jets in the event.

– N_{jets}: the number of jets in the event.

– $N_{b-\text{jets}}$: the number of b-tagged jets in the event.

– N_{leptons}: the number of signal leptons in the event, where $\ell = \text{e}, \mu$.

– m_T: the transverse mass between the leading lepton and the $E_{\text{T}}^{\text{miss}}$, defined as:

$$m_T = \sqrt{2\text{p}_{\text{T}}^{\ell} E_{\text{T}}^{\text{miss}} - 2\text{p}_{\text{T}}^{\ell} \cdot \mathbf{E}_{\text{T}}^{\text{miss}}}. \tag{5.3}$$

It is used to reject events with fake leptons in the 1ℓ regions.

– N_{vtx}: the number of secondary vertices reconstructed by TC-LVT.

– p_T^{vtx}: the total transverse momentum of the tracks associated to a secondary vertex reconstructed by TC-LVT.

– m_{vtx}: the invariant mass computed from the tracks associated to a secondary vertex reconstructed by TC-LVT.

– η_{vtx}: the pseudorapidity associated to the TC-LVT vertex with largest momentum in the event.

Preliminary Selections

A dataset populated by many events can be used to inspect the modelling of kinematic variables with small statistical uncertainties. This study gives the opportunity to identify mismodelling of the data, such as a misprediction of the kinematic properties of a SM process. Preliminary sets of selections, or *pre-selections*, are applied to some of the variables. They are defined by the lepton multiplicity: 0-lepton, 1-lepton and 2-leptons in Table 5.3.

Table 5.3: Definition of the initial pre-selections according to the lepton multiplicity. `HLT_xe`, `HLT_mu` and `HLT_e` refer to the HLT $E_{\text{T}}^{\text{miss}}$ trigger and single-muon or single-electron triggers described in Section 3.3.

Criterion	0-Lepton	1-Lepton	2-Lepton
Lowest unprescaled trigger	`HLT_xe`	`HLT_xe`	`HLT_mu` || `HLT_el`
Event Cleaning	✓	✓	✓
N_{leptons}	0	1	2 (SF, OS)
$E_{\text{T}}^{\text{miss}}$	-	-	< 100 GeV
$\text{p}_{\text{T}}^{l_1}$	-	> 20 GeV	> 27 GeV
$\text{p}_{\text{T}}^{l_2}$	-	-	> 20 GeV
m_T	-	> 20 GeV	> 20 GeV
$m_{\ell\ell}$	-	-	76 GeV $< m_{\ell\ell} <$ 106 GeV

For each lepton multiplicity (0, 1, 2 leptons), two additional sets of pre-selections are needed to select events based on the presence of TC-LVT vertices, and they are defined

in Table 5.4. That makes a total of six preliminary selections defined according to the leptons, b-tagged jets and TC-LVT multiplicities. They are listed in Table 5.5.

Table 5.4: Selections defined according to the number of b-jets and TC-LVT vertices.

Criterion	pre-2b-2j	pre-1sb-2j
N_{jets}	2-5	2-5
$N_{b-\text{jets}}$	≥ 2	-
N_{vtx}	-	≥ 1
$\mathrm{p_T^{j_1}}$	> 100	> 400
$\mathrm{p_T^{j_2}}$	> 50	-
$\min[\Delta\phi(\text{jet}_{1-2}, \mathbf{E}_{\mathrm{T}}^{\text{miss}})]$	-	> 0.2
$\min[\Delta\phi(\text{jet}_{1-4}, \mathbf{E}_{\mathrm{T}}^{\text{miss}})]$	> 0.4	-
$E_{\mathrm{T},\ell\ell}^{\text{miss}}$	> 250	> 400

Table 5.5: Selections defined according to the number of leptons, b-jets and TC-LVT vertices.

	$N_{b-\text{jets}} \geq 2$	$N_{vtx} \geq 1$
0L	pre-2b-2j-0l	pre-1sb-2j-0l
1L	pre-2b-2j-1l	pre-1sb-2j-1l
2L	pre-2b-2j-2l	pre-1sb-2j-2l

These preliminary selections allow to assess the modelling of some key kinematic variables, as shown in Figure 5.6. More preliminary plots are available in Appendix B. Figure 5.6 shows a good agreement between the observed data and the MC simulations. With a closer inspection, one might wonder about the mismodelling present in the region at low-p_T shown in Figure 5.6(b), Figure 5.6(d) and Figure 5.6(f). This behaviour is in line with the TC-LVT algorithm performances discussed in Chapter 4, and it is due to the reconstruction of vertices not associated to a low-p_T b-hadron. Such vertices are originated from the random crossing of tracks clustered into a fake vertex by TC-LVT. The trend shown is corrected by the TC-LVT SFs described in Section 4.4. Moreover, a tighter selection is applied for all regions in the analysis, as documented in Section 5.3.
Figure 5.7 shows the $E_{\mathrm{T}}^{\text{miss}}$ distribution in data and MC for all the pre-selections presented. The disagreement observed in Figure 5.7(c) is due to a known mismodelling of the top momentum by the MC generator used for $t\bar{t}$ and single top [188–192]. It is corrected by the use of a dedicated control region, as described in Section 5.3.

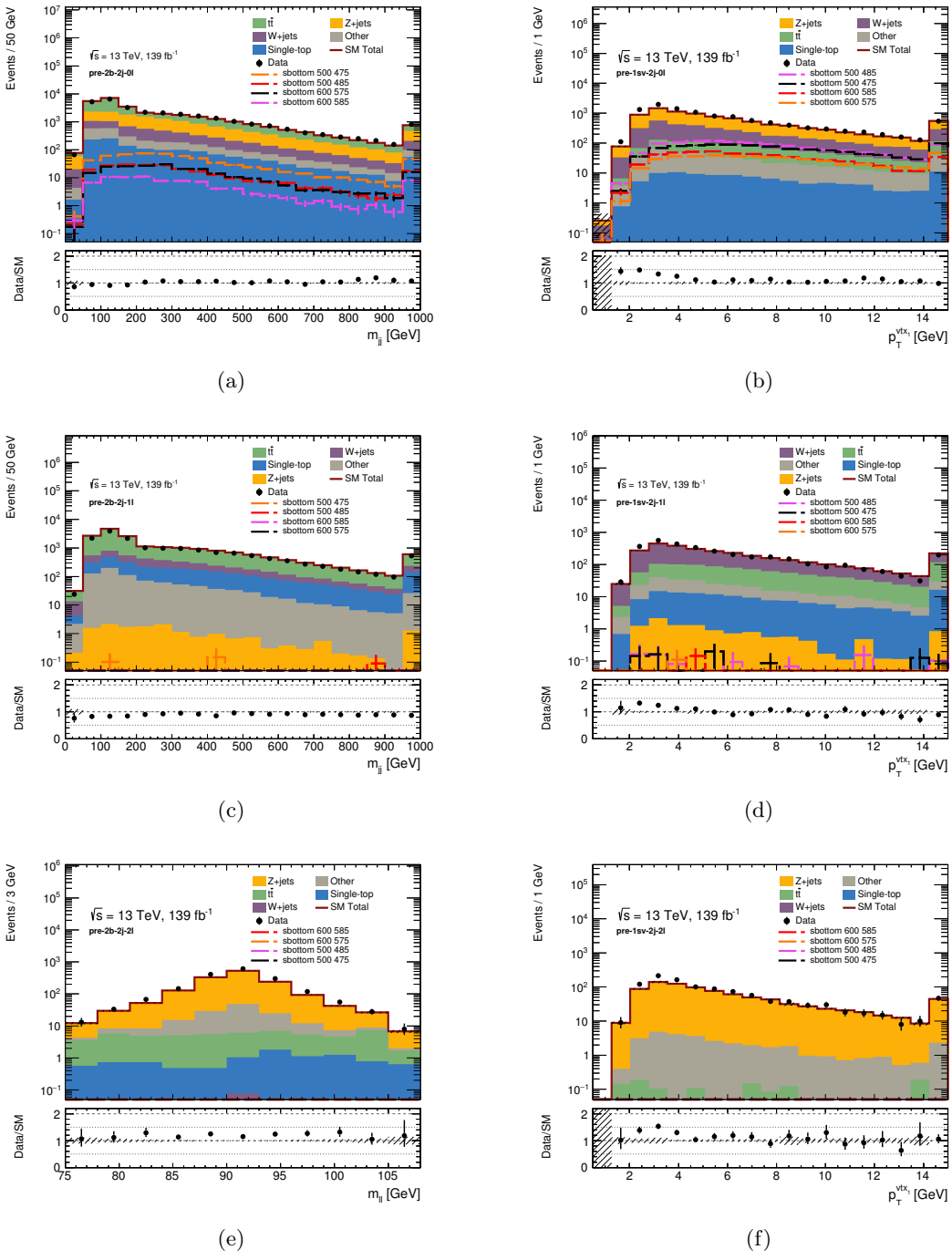

Figure 5.6: Distribution of (a) m_{jj} for pre-2b-2j-0l, (b) p_T^{vtx} for pre-1sb-2j-0l, (c) m_{jj} for pre-2b-2j-1l, (d) p_T^{vtx} for pre-1sb-2j-1 l, (e) $m_{\ell\ell}$ for pre-2b-2j-2l, (f) p_T^{vtx} for pre-1sb-2j-2l. The four signal benchmark points are shown, and their yield in 1L and 2L regions is negligible as expected. The plots do not include the background normalisation factors derived as part of the fit procedure described in Section 5.3, and only the statistical uncertainties are considered. The plots for selections where at least one TC-LVT vertex is required do not include the TC-LVT SF. The inset plot shows the ratio between the data and the MC prediction.

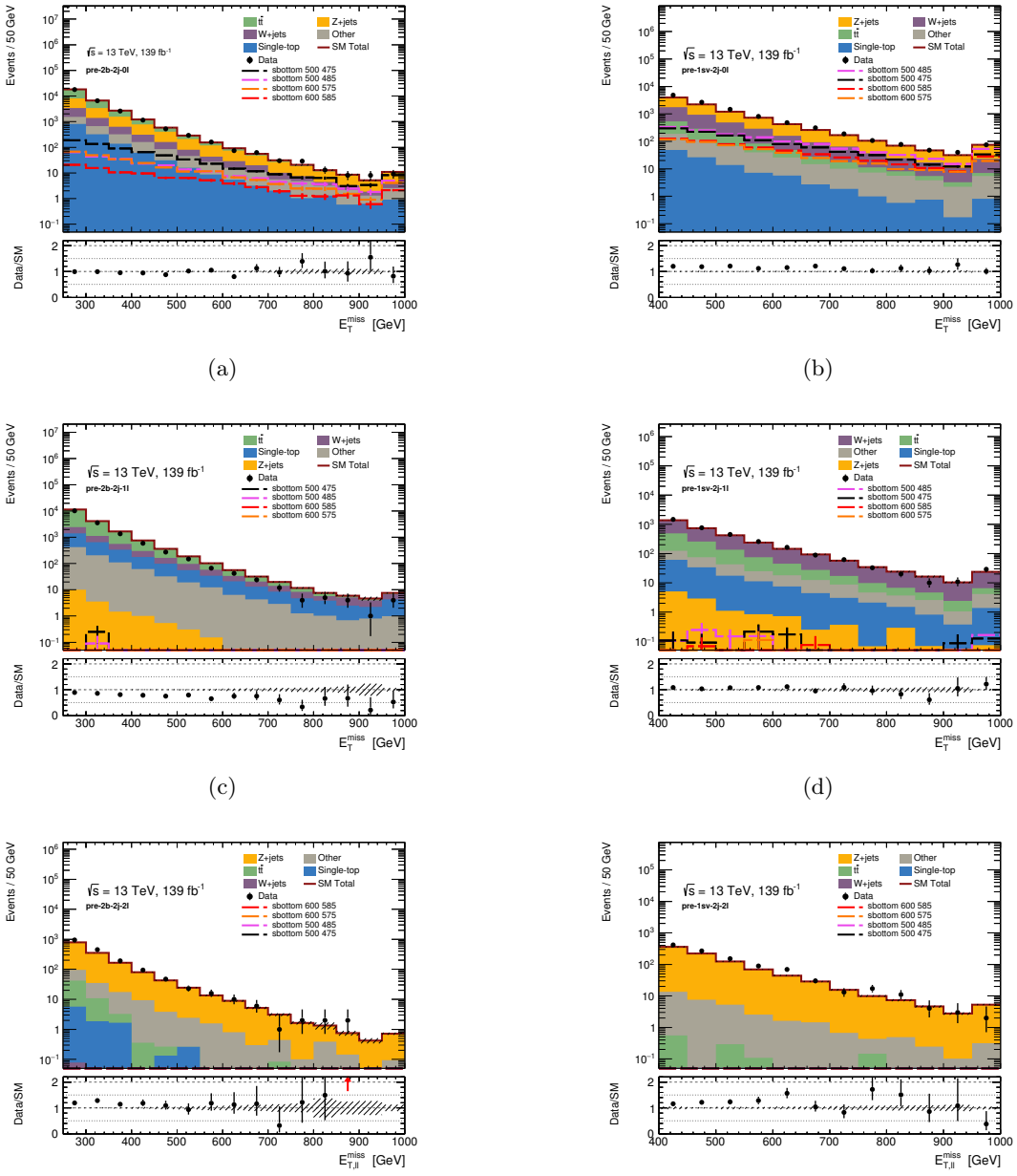

Figure 5.7: $E_{\mathrm{T}}^{\mathrm{miss}}$ distribution in (a) pre-2b-2j-0l, (b) pre-1sb-2j-0l, (c) pre-2b-2j-1l, (d) pre-1sb-2j-1l, and $E_{\mathrm{T},\ell\ell}^{\mathrm{miss}}$ distribution in (e) pre-2b-2j-2l, (f) pre-1sb-2j-2l. The four signal benchmark points are shown, and their yield in 1L and 2L regions is negligible as expected. The plots do not include the background normalisation factors derived as part of the fit procedure described in Section 5.3, and only the statistical uncertainties are considered. The plots for channels where at least one TC-LVT vertex is required do not include the TC-LVT SF. The inset plot shows the ratio between the data and the MC prediction.

5.3 Analysis Strategy

This Section defines the analysis strategy for this work, whose main observable is the $E_{\mathrm{T}}^{\mathrm{miss}}$ distribution. The strategy exploits the new TC-LVT algorithm described in Chapter 4, which allows one to reconstruct secondary vertices associated to low-p_T b-hadrons. The analysis strategy is based on three types of regions, which are:

- *Signal Region (SR)*: it is a signal-enriched region. The goal is to apply a set of selections able to suppress the SM background processes while having a high efficiency on signal. If a significant excess is observed, a discovery can be claimed. Otherwise exclusion limits can be set.
- *Control Region (CR)*: it is a region enriched with a specific SM background process that is expected to have a large contribution to the SR. Control regions play a crucial role in the determination of specific background process normalisations.
- *Validation Region (VR)*: it is a signal-depleted region but with background composition similar to the SR. This region is used to assess the validity of the background normalisation extrapolation from the CR to the SR.

These three sets of regions are used to define the statistical procedure for this work, described below. Next, the SRs, CRs and VRs are presented. The last part of this Section presents the study of the background composition of the CRs, VRs and SRs, with focus on the so-called *heavy flavour content*, that is, the average fraction of jets and vertices associated with b and c quarks.

Statistical Analysis

In the following the statistical procedure used in the analysis is described. The procedure allows to assess whether there is an excess of events on top of the SM predictions. If no excess is observed limits can be set on the cross section of BSM processes. For the case of sbottom pair production, such limits can be converted to limits on sbottom masses.

Likelihood

The expected number of events populating each of the regions previously described can be modelled [198] as:

$$N = \mu_s n_s (1 + \sum_j \theta_s^j \sigma_s^j) + \mu_b^i n_b^i (1 + \sum_j \theta_b^j \sigma_b^{ij}), \tag{5.4}$$

where:

- μ_s is the signal strength. It is zero for the background-only hypothesis.

- $n_s(1+\sum_j \theta_s^j \sigma_s^j)$ is the signal yield, depending on $(1+\sum_j \theta_s^j \sigma_s^j)$, predicted by the model under study.
- μ_b^i is the normalisation factor for the background process i. It is estimated from the fit procedure. $\mu_b^i = 1$ for processes estimated by MC only.
- $n_b^i(1+\sum_j \theta_b^j \sigma_b^{ij})$ is the predicted yield, depending on $(1+\sum_j \theta_b^j \sigma_b^{ij})$, for the background process i.
- θ^j refers to the nuisance parameters (NPs) associated with each systematic uncertainty. The value of these parameters are determined as part of the fit.
- σ_b^{ij} is the standard deviation of the j-th systematic uncertainty calculated for the background production process i.
- σ_s^j is the standard deviation of the j-th systematic uncertainty calculated for the signal production process.

The number of MC predicted and observed event in each region can be described using the Poisson statistic with mean N as defined in Equation 5.4. The likelihood function L is defined as the product of Poisson probabilities P in each SR (P_{SR}) and CR (P_{CR}). The full likelihood L is defined in Equation 5.5:

$$\begin{aligned} L(\mathbf{n}^{obs}, \boldsymbol{\theta}^0 | \mu_s, \boldsymbol{\mu}_b, \boldsymbol{\theta}) &= P_{SR} \times P_{CR} \times C_{syst} \\ &= P(n_{SR}^{obs} | N_{SR}(\mu_s, \boldsymbol{\mu}_b, \boldsymbol{\theta})) \times \prod_{i \in CR} P(n_i^{obs}, N_i(\mu_s, \boldsymbol{\mu}_b, \boldsymbol{\theta})) \times C_{syst}(\boldsymbol{\theta}^0, \boldsymbol{\theta}), \end{aligned} \quad (5.5)$$

where μ_s, $\boldsymbol{\mu_b}$ and $\boldsymbol{\theta}$ are the same parameters defined in Equation 5.4. These parameters are estimated by maximising the likelihood L through a numerical procedure. $C_{syst}(\boldsymbol{\theta}^0, \boldsymbol{\theta})$ takes into consideration the deviations of the j-th systematic uncertainty by an amount θ^j. It is defined as:

$$C_{syst}(\boldsymbol{\theta}^0, \boldsymbol{\theta}) = \prod_{j \in S} G(\theta_j^0 - \theta_j), \quad (5.6)$$

where G is a normal distribution and S represents the full set of systematics. C_{syst} is effectively a constraint on the values of the nuisance parameters: values of $\boldsymbol{\theta}_j$ significantly different from $\boldsymbol{\theta}_j^0$ lead to a suppression in the value of the likelihood.
The specific configurations of different fit procedures adopted by this analysis are presented in Section 6.2.

Hypothesis Test

The outcome of an experiment can be estimated by the agreement of the observed data with a given hypothesis H [199]. Such agreement can be estimated by looking at the probability, or p-value, of the observed data to be equally or less compatible with the

predicted hypothesis H. The p-value is commonly converted into the equivalent significance Z according to:

$$Z = \Phi^{-1}(1-p), \tag{5.7}$$

where Φ^{-1} is the inverse of the cumulative distribution of the standard Gaussian.
Within the particle physics community, it is customary to claim the rejection of the background-only hypothesis, and therefore the discovery of the researched physical process, when the significance is at least $Z = 5$, which corresponds to a p-value of $p = 2.87 \times 10^{-7}$ [199]. In this case, the null hypothesis H_0 refers to the known SM processes acting as a background, and it is tested against the H_1 hypothesis which refers to the presence of both signal and background processes.
The exclusion of a signal hypothesis requires instead a significance $Z = 1.67$ corresponding to a p-value of $p = 0.05$; this is also referred to as a 95% CL. In this case, the null hypothesis H_0 refers to the existence of a signal process, which is tested against the H_1 hypothesis which assumes the existence of SM only processes.
The test of the hypothesis of the existence of a signal process with strength μ_s is performed by using a profile likelihood ratio $\lambda(\mu_s)$, defined as:

$$\lambda(\mu_s) = \frac{L(\mu_s, \hat{\hat{\boldsymbol{\mu}}}_{\boldsymbol{b}}, \hat{\hat{\boldsymbol{\theta}}})}{L(\hat{\mu}_s, \hat{\boldsymbol{\mu}}_{\boldsymbol{b}}, \hat{\boldsymbol{\theta}})}, \tag{5.8}$$

where the likelihood L is the one defined in Equation 5.5. In Equation 5.8 the numerator maximises the likelihood by using the parameters $\hat{\hat{\boldsymbol{\mu}}}_{\boldsymbol{b}}$, $\hat{\hat{\boldsymbol{\theta}}}$ obtained when fixing a specific μ_s. The denominator instead features those parameters $\hat{\boldsymbol{\mu}}_{\boldsymbol{b}}$, $\hat{\boldsymbol{\theta}}$ which maximise the likelihood for a value of the signal strength $\hat{\mu}_s$ which is allowed to vary in the fit. Under these assumptions, the statistic $\lambda(\mu_s)$ is a unique function of the signal strength, and it satisfies $0 \leq \lambda(\mu_s) \leq 1$.
The test statistic t_{μ_s} can be defined as:

$$t_{\mu_s} = -2\ln\lambda(\mu_s). \tag{5.9}$$

High values of that statistic indicates greater incompatibility between the observed value and the tested hypothesis μ_s. Figure 5.8 graphically shows the relation between a generic test statistic t, the p-value and the significance Z.

The p-value, which is the measure used to assess that incompatibility, is defined as:

$$p_{\mu_s} = \int_{t_{\mu_s,\text{obs}}}^{\infty} f(t_{\mu_s}) dt_{\mu_s}, \tag{5.10}$$

where $t_{\mu_s,\text{obs}}$ refers to the observed value of the statistic t_{μ_s}, and $f(t_{\mu_s})$ represents the probability density function of t_{μ_s} under the assumption of a signal model with strength μ_s.

The signal models considered in this work are supposed to increase the number of observed events in the SRs, i. e. $\mu_s \geq 0$. The test statistic describing the discovery of such signal

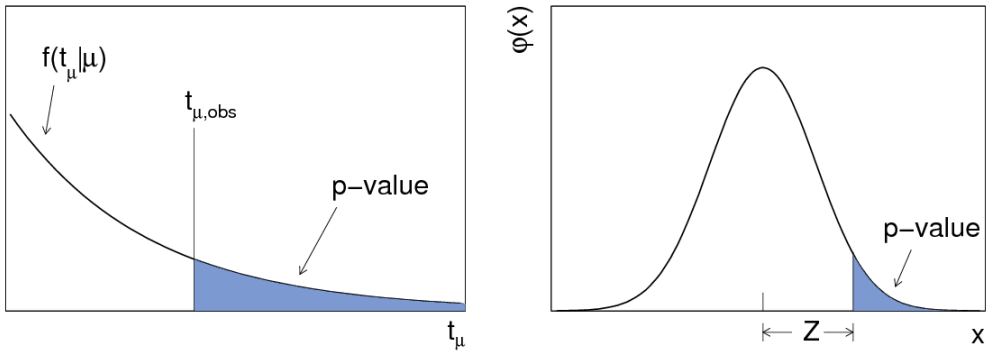

(a) (b)

Figure 5.8: Graphical representation of (a) the relation between a test statistic t and its p-value for a given signal strength μ and (b) the relation between a p-value and the significance Z. Images taken from Ref. [199]

models is:

$$q_0 = \begin{cases} -2\ln\lambda(0) & \hat{\mu_s} \geq 0 \\ 0 & \hat{\mu_s} < 0, \end{cases} \tag{5.11}$$

where $\hat{\mu_s}$ is the signal strength specific for such model. Under this assumption, an underfluctuation in the observed data would be consistent with the presence of background processes only.

If the observed data do not allow to claim for the discovery of new physical phenomena, upper limits on its production cross section are set. The test statistic used for setting upper limits is:

$$q_{\mu_s} = \begin{cases} -2\ln\lambda(\mu_s) & \hat{\mu_s} \leq \mu_s \\ 0 & \hat{\mu_s} > \mu_s. \end{cases} \tag{5.12}$$

In this case, it would not be possible to exclude signal models with observed $\hat{\mu_s} < \mu_s$. Equation 5.12 poses a problematic feature, as it might produce spurious results in some cases. If the results of the experiment is consistent with the no-signal hypothesis and large under-fluctuations compared with the expected background yield is observed, the signal plus background hypothesis would allow one to exclude signal models which predict no signal yield in that region. That would lead to the exclusion of signal models to which the experiment has no sensitivity. To cure this unwanted behaviour, the CL_s method [200] is introduced as:

$$CL_s = \frac{p_{\mu_s}}{1 - p_b}, \tag{5.13}$$

where p_{μ_s} is the p-value for the signal plus background hypothesis, while p_b is the p-value for the background-only hypothesis. Adopting this method implies that a 95% CL is reached when $CL_s < 0.05$.

Signal Region Optimisation

A good SR maximises a measure of the signal strength over the background. This measure is the significance, which is obtained from the `RooStats::NumberCountingUtils::BinomialExpZ` [177] from the ROOT Framework [178]. To optimise the SR an arbitrary 30% uncertainty is assumed. This value is chosen considering previous analysis, and it is considered as a preliminary estimation of the uncertainties for a analysis. A more accurate evaluation of the uncertainty is described in Chapter 6. Two sets of signal benchmark points, defined in Section 5.1, are used to estimate the significance, each targeting mass differences between the bottom squark and the neutralino of $\Delta m(\widetilde{b}_1, \widetilde{\chi}_1^0) = 25, 15$ GeV. The optimisation of the SR has its origin from the result from Ref. [176], where two b-tagged jets are required. Two more mutually exclusive regions are defined according to the multiplicity of b-tagged jets and TC-LVT vertices. At this stage, the significances obtained in each region are added in quadrature to have an estimate of their combined statistical power. This is an approximation which does not take into consideration any correlation between the uncertainties, or the correlations coming from the SM background normalisation. The fit procedure which takes into consideration all these correlations, already introduced earlier in this Section, is discussed in more detail in Chapter 6. As discussed in Section 5.1, the signal final state features a large $E_{\mathrm{T}}^{\mathrm{miss}}$ together with two b-hadrons. The three SRs therefore use the $E_{\mathrm{T}}^{\mathrm{miss}}$ triggers defined in Table 5.1 and the 0-lepton pre-selections introduced in Table 5.3. SRC-2b[2], which requires the presence of two b-jets, is originated by the 2b-2j-0l pre-selection, while SRC-1b1v and SRC-0b1v, requiring one or no b-jets respectively, are originated by the 1sb-2j-0l pre-selection defined in Table 5.4. The main features of these three SRs are:

- The presence of a leading high-p_T jet; this is assumed to be an ISR jet against which the sbottom pair system is recoiling. The leading jet is therefore required not to be b-tagged. This requirement creates a topology where the bottom squark pair system is boosted. The b-hadrons produced by the decay of the bottom squarks receive a small fraction of the boost, while most of it is absorbed by the neutralinos, hence the presence of large $E_{\mathrm{T}}^{\mathrm{miss}}$.

- The presence of low extra hadronic activity in the event; that is ensured by requiring low values of the $\mathrm{H}_{\mathrm{T};3}$ variable.

- Signal events feature a larger imbalance between the jets in the event, with the sub-leading jet having a much smaller p_T than the leading jet. That does not happen for the background where the sub-leading jet tends to have a p_T closer to that of the leading jet. This is exploited by requiring a high value of A. This selection is not applied to the SRC-0b1v selection since the presence of a second jet is not guaranteed.

[2] In Section 6.2 the reasons for the presence of SRC in the naming convention is clarified.

Table 5.6: Kinematic selections for the SRC.

Selection	SRC-2b	SRC-1b1v	SRC-0b1v
Is $j1$ b-tagged?	0	0	0
$\mathrm{p}_{\mathrm{T}}^{j_1}$ (GeV)	> 500	> 400	> 400
$E_{\mathrm{T}}^{\mathrm{miss}}$ (GeV)	> 500	> 400	> 400
$\mathrm{H}_{\mathrm{T};3}$	–	< 80	< 80
A	> 0.80	> 0.86	–
m_{jj} (GeV)	> 250	> 250	–
$N_{b-\mathrm{jets}}$	≥ 2	$= 1$	$= 0$
$\Delta\phi(j1, b1)$	–	> 2.2	–
N_{vtx}	≥ 0	≥ 1	≥ 1
m_{vtx} (GeV)	–	> 0.6	> 1.5
p_T^{vtx} (GeV)	–	> 3	> 5
$\Delta\phi(j1, vtx)$	–	–	> 2.2
$\lvert\eta_{vtx}\rvert$	–	< 1.2	< 1.2

– A selection on the invariant mass of the two leading jets, m_{jj}, useful to reject the $t\bar{t}$ background. This selection is not applied to the SRC-0b1v selection.

– In the SRC-1b1v and SRC-0b1v, together with the request of at least one TC-LVT vertex, a selection on p_T^{vtx} and m_{vtx} is applied. These selections effectively change the TC-LVT loose working point defined in Chapter 4: they help to suppress the identification of fake vertices, usually characterized by lower mass and momentum.

– A large angular distance between the b-jet (TC-LVT vertex) and the leading jet for the SRC-1b1v (SRC-0b1v) selection. This is due to the fact that the b-tagged jet (TC-LVT vertex) should recoil against the ISR.

The complete definition of the three SR is reported in Table 5.6.

An important tool to understand whether the cuts applied are optimised is the so called n-1 plots. These plots show the distribution of a given kinematic variable used in the definition of a SR with the full selection applied except that on the plotted variable. Figure 5.9 shows some n-1 distributions for the three SRs. A close inspection of these plots leads to the conclusion that the selections applied are highly optimised, as they suppress a large fraction of SM background processes while having a good efficiency on the benchmark signals. More n-1 distributions are reported in Appendix B.

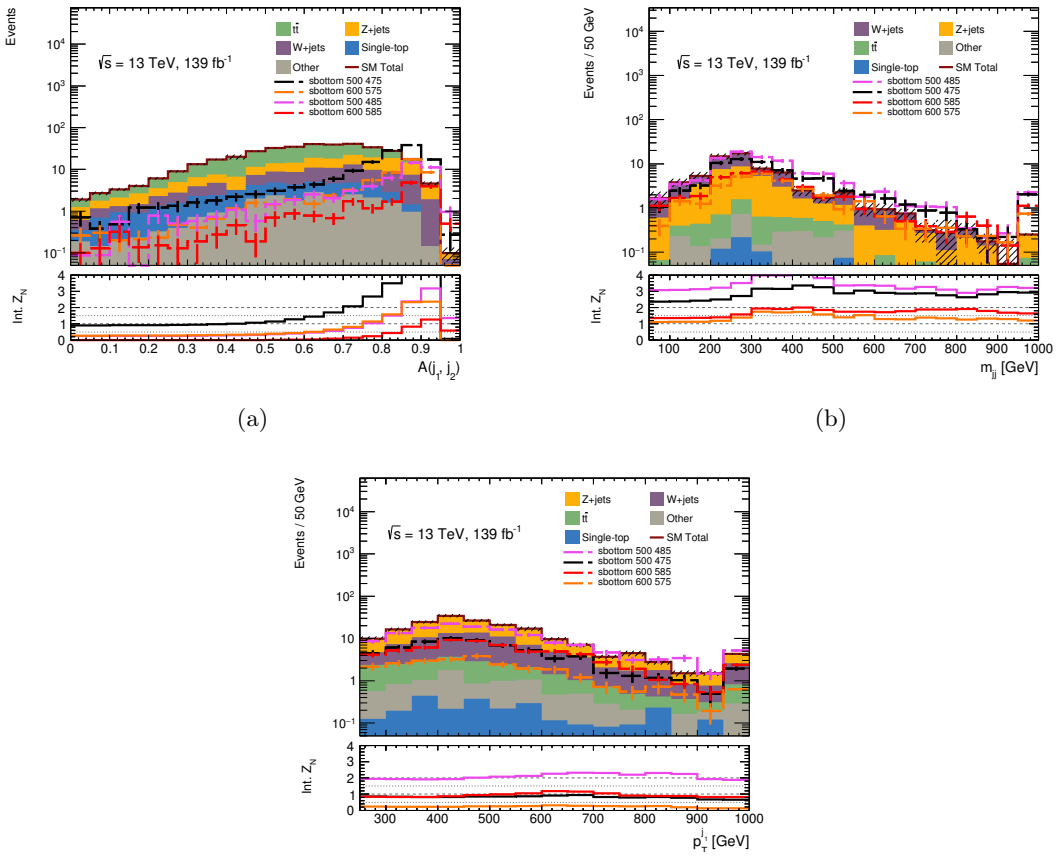

(a) (b)

(c)

Figure 5.9: N-1 distribution of signal and SM background processes for (a) A in SRC-2b, (b) m_{jj} in SRC-1b1v and (c) p_T^{j1} in SRC-0b1v. The four signal benchmark points are shown. The plots do not include the background normalisation factors derived as part of the fit procedure described in Section 5.3, and only the statistical uncertainties are considered. The plots for selections where at least one TC-LVT vertex is required do not include the TC-LVT SFs. The inset plot shows the significance distribution for each benchmark mass point calculated for a cut applied at a given vale of the variable examined.

Figure 5.10 shows the E_T^{miss} distributions for the three SRs.

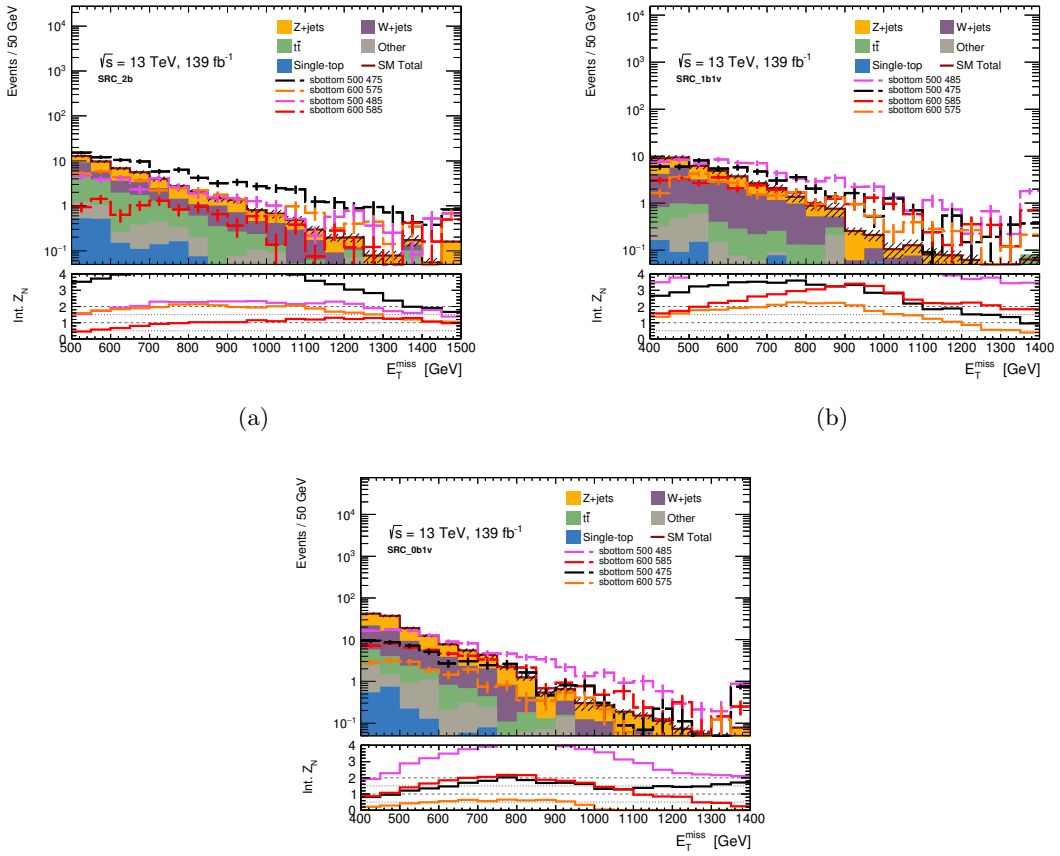

Figure 5.10: $E_{\mathrm{T}}^{\mathrm{miss}}$ distribution of signal and SM background processes for (a) SRC-2b, (b) SRC-1b1v and (c) SRC-0b1v. The four signal benchmark points are shown. The plots do not include the background normalisation factors derived as part of the fit procedure described in Section 5.3, and only the statistical uncertainties are considered. The plots for selections where at least one TC-LVT vertex is required do not include the TC-LVT SFs. The inset plot shows the significance distribution for each benchmark mass point calculated for a cut applied to a given value of the variable examined.

It is possible to see how the different SRs target different benchmark points: SRC-2b is more sensitive to mass points where $\Delta m(\widetilde{b}_1, \widetilde{\chi}_1^0)$ is larger, while SRC-1b1v and SRC-0b1v provide a higher significance for more compressed benchmark points. For each benchmark point there is a different $E_{\mathrm{T}}^{\mathrm{miss}}$ value for which the maximum sensitivity can be obtained. This behaviour is particularly evident in the inset plot of Figure 5.10(b). A $E_{\mathrm{T}}^{\mathrm{miss}}$ binning exploits this feature, as described in Chapter 6.

Table 5.7 summarises the expected yields for the SRs defined before. It shows that the main SM backgrounds populating the three SRs are Z+jets and W+jets , while the $t\bar{t}$ production is relevant only for SRC-2b. The multijet background is suppressed by the selections on $\Delta\phi(j1, b1)$ and $\Delta\phi(j1, vtx)$. All other SM background processes discussed in Section 5.1 are negligible. This background composition suggests the need for specific Z+jets , W+jets and $t\bar{t}$ control regions.

Table 5.7: Yields for SM background processes and the four benchmark signal point obtained for the three SRC regions.

SM process	SRC-2b	SRC-1b1v	SRC-0b1v
Z+jets	19.25	21.13	77.22
W+jets	13.84	24.11	51.56
$t\bar{t}$	12.33	2.63	9.73
single top	1.72	0.57	1.94
other	2.72	2.07	5.11
Total SM	49.88	50.52	145.56
Signal $(m_{\tilde{b}_1}, m_{\tilde{\chi}_1^0})$ [GeV]			
(500,475)	84.71	51.96	46.22
(500,485)	33.04	71.39	106.09
(600,575)	34.56	25.30	17.81
(600,585)	10.98	28.78	48.64

Background Control Regions

These regions are dedicated to estimate the main SM background processes populating the SR. The procedure, which is described in Section 6.2, is to provide a fit with the CR yields, which then determines the normalisation factors. Each CR targets one of the main SM backgrounds populating the SR, hence each CR should be dominated by one SM production process. The main backgrounds populating the SR are listed in Table 5.7, and are the Z+jets and W+jets . An extra control region to normalise the top production processes ($t\bar{t}$ and single top) is required by the analysis. This is needed mainly to normalise the top SM production processes in the W+jets CRs.
The main feature of the CRs are introduced:

- The CRs should reproduce the same b-tagged jet and TC-LVT vertex multiplicity. This strategy aims to compensate for the uncertainties in the simulations of $Z/W+b\bar{b}$ production. Normalising the Z/W+jets in regions reflecting the same b-tagged jet and TC-LVT vertex multiplicity reduces the final systematic uncertainties on the background estimation.

- The CRs should estimate the targeted SM background production process in a phase-space resembling the kinematic properties of the SR, but with a selection mutually exclusive to that of the SRs, and featuring small signal contamination. In this analysis this goal is achieved by defining 2-leptons and 1-lepton CRs.

- The CRs should be pure in the targeted SM background production process. This is achieved by requiring two same-flavour opposite-sign (SFOS) leptons in the CRs targeting the Z+jets SM production process, or one lepton in the CR targeting the W+jets and top SM production processes.

A set of six mutually exclusive CRs is defined: three for the Z+jets background production process, two for the W+jets background production process and one for the top background production processes.

2ℓ Control Regions

These CRs target the dominant Z+jets production background process. They are defined by requiring two SFOS leptons. These CRs make use of the single-lepton trigger menu introduced in Table 5.2. The definition of these control regions starts from the 2b-2j-2l and 1sb-2j-2l pre-selection from Table 5.3 and Table 5.4. Two requirements are crucial to ensure a high-purity Z+jets control region: a requirement on the invariant mass of the two leptons, $m_{\ell\ell} \sim m_Z$; and a small value of $E_{\mathrm{T}}^{\mathrm{miss}}$. The Z+jets CRs exploit two different definitions for the $E_{\mathrm{T}}^{\mathrm{miss}}$: the *original* $\mathbf{E}_{\mathrm{T}}^{\mathrm{miss}}$, which is the real missing transverse momentum, and it is usually very small given the $Z \to \ell^+\ell^-$ decay; and the *corrected* $\mathbf{E}_{\mathrm{T}}^{\mathrm{miss}}$, or $\mathbf{E}_{\mathrm{T},\ell\ell}^{\mathrm{miss}}$ already defined in Section 5.2, which is the missing transverse momentum to which the $\mathbf{p}_T$ of the two leptons is subtracted. The $\mathbf{E}_{\mathrm{T},\ell\ell}^{\mathrm{miss}}$ is used to mimic the dominant $Z \to \nu\bar{\nu}$ decay populating the SR in a 2-lepton region.
To reproduce a phase-space similar to the SR, selections on the $N_{b-\mathrm{jets}}$ and N_{vtx} are applied. This provides a one-to-one correspondence between CR and SR, and it makes the three Z+jets CRs mutually exclusive to each other. The full definition of the CRs, which apply a few more selections on A, m_{jj}, m_{vtx} and p_T^{vtx}, is summarised in Table 5.8.

Table 5.8: Kinematic selections for the 2-leptons control regions.

Selection	CRC-Z2b0v	CRC-Z1b1v	CRC-Z0b1v
N_{leptons}	2, SFOS		
$\mathrm{H_{T;3}}$	< 80		
$m_{\ell\ell}$ (GeV)	$76 < m_{\ell\ell} < 106$		
$E_{\mathrm{T}}^{\mathrm{miss}}$ (GeV)	< 100		
$\mathrm{p}_{\mathrm{T}}^{j_1}$ (GeV)	> 300	> 400	> 400
$E_{\mathrm{T},\ell\ell}^{\mathrm{miss}}$ (GeV)	> 250	> 400	> 400
A	> 0.5	> 0.4	–
m_{jj} (GeV)	–	> 250	–
$N_{b-\mathrm{jets}}$	≥ 2	1	0
N_{vtx}	0	≥ 1	≥ 1
m_{vtx} (GeV)	–	> 0.6	> 1.5
p_T^{vtx} (GeV)	–	> 3	> 5

Figure 5.11 displays some distributions of kinematic variables for a common pre-selection for the Z+jets CR, which is made of the common cuts from Table 5.8. This pre-selection provides the control regions with a high purity. The data/MC agreement is good. More distributions are presented in Appendix B.

Figure 5.12 shows the $E_{\mathrm{T},\ell\ell}^{\mathrm{miss}}$ distributions for the three control regions, while Table 5.9 shows the yields of the SM processes in the three control regions.

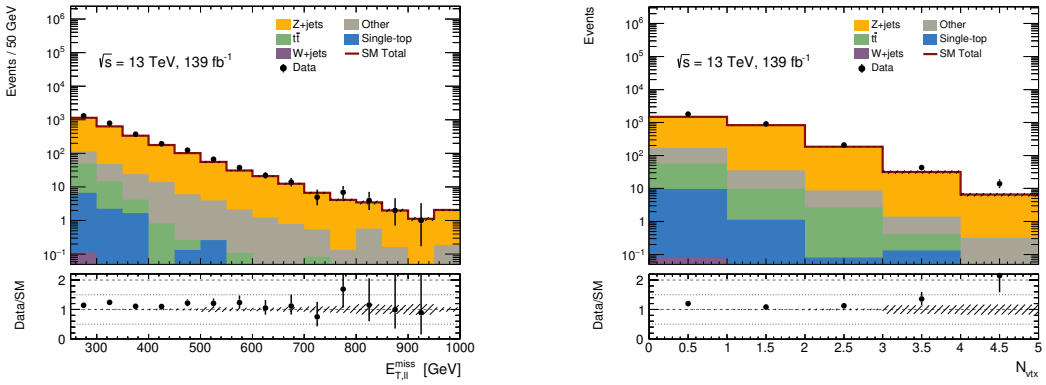

(a) (b)

Figure 5.11: Distribution of data and MC prediction for (a) $E_{\mathrm{T},\ell\ell}^{\mathrm{miss}}$ and (b) N_{vtx} for the common pre-selection for the Z+jets control regions. The plots do not include the background normalisation factors derived as part of the fit procedure described in Section 5.3, and only the statistical uncertainties are considered. The plots for selections where at least one TC-LVT vertex is required do not include the TC-LVT SFs. The inset plot shows the ratio between the data and the MC prediction.

Table 5.9: Yields for SM background processes obtained for the 2-leptons control regions.

Process	CRC-Z2b0v	CRC-Z1b1v	CRC-Z0b1v
Z+jets	88.36	109.56	72.72
$t\bar{t}$	7.09	0.11	0.00
W+jets	0.00	0.00	0.00
single top	0.49	0.00	0.00
other	9.17	3.30	2.62
SM	100.4	112.88	75.34
Data	81.00	95.00	72.00

1ℓ Control Regions

These control regions are designed to normalise the W+jets and top production backgrounds processes. These regions are defined by requiring the presence of one lepton, and they use the $E_{\mathrm{T}}^{\mathrm{miss}}$ trigger menu introduced in Table 5.1. The definition of these control regions starts from the 2b-2j-1l and 1sb-2j-1l pre-selections introduced in Table 5.3 and Table 5.4. A good purity for these regions is obtained by requiring exactly one lepton and the presence of different b-tagged jet multiplicities. The selections on the $N_{b-\mathrm{jets}}$ and N_{vtx} is relevant for two reasons: it makes the CRs mutually exclusive, as the top region requires the presence of at least two b-tagged jets and any number of TC-LVT vertices, while the W+jets control regions always require the presence of at least one TC-LVT vertex and either one or no b-tagged jets; and it reflects the selections applied in the SRs. It is difficult to define a control region for the W+jets production background process with two b-tagged jets because this region would be mainly populated by $t\bar{t}$ events. The CRC-W1b1v region is therefore used to normalise the W+jets background in both SRC-2b and SRC-1b1v. The full definition of the CRs, which apply a few more cuts on A, m_{jj}, m_{vtx} and p_T^{vtx}, is

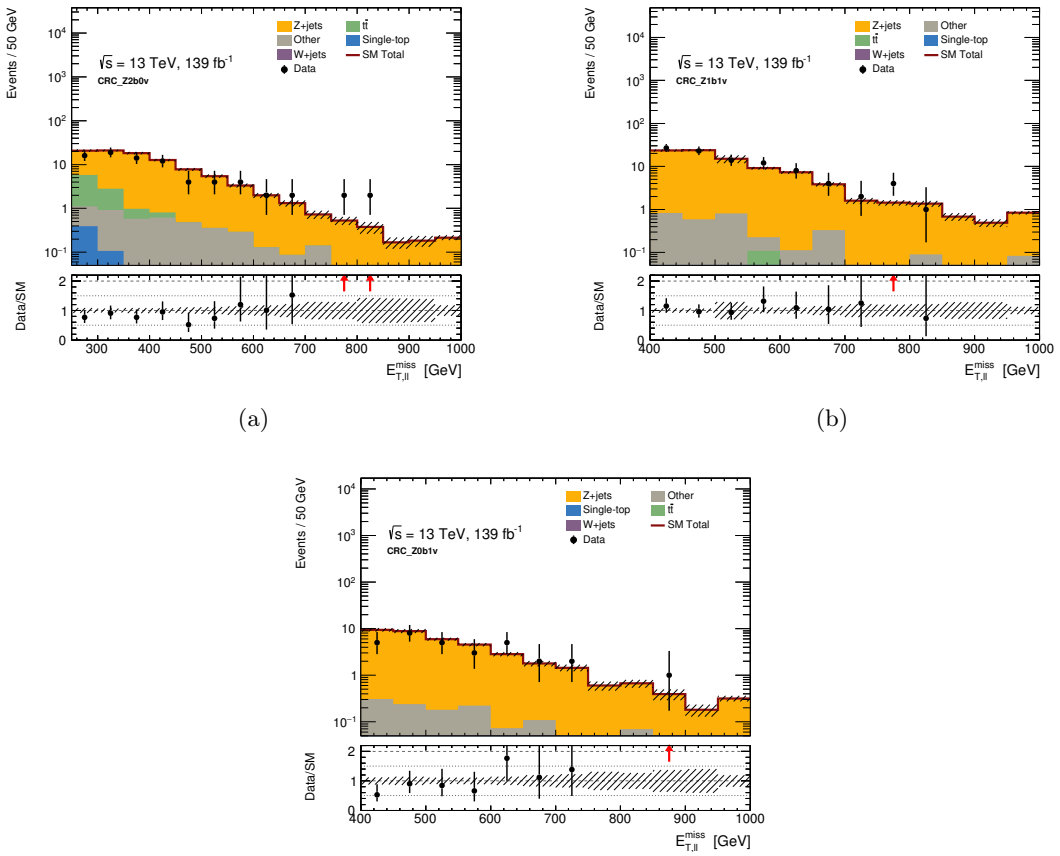

Figure 5.12: $E_{\mathrm{T},\ell\ell}^{\mathrm{miss}}$ distribution of data and MC for (a) CRC-Z2b0v, (b) CRC-Z1b1v and (c) CRC-Z0b1v. The plots do not include the background normalisation factors derived as part of the fit procedure described in Section 5.3, and only the statistical uncertainties are considered. The plots for selections where at least one TC-LVT vertex is required do not include the TC-LVT SFs. The inset plot shows the ratio between the data and the MC prediction.

summarised in Table 5.10

Table 5.10: Kinematic selections for the 1-lepton control regions.

Selection	CRC-Top	CRC-W1b1v	CRC-W0b1v
is $j1$ b-tagged?		0	
N_{leptons}		1	
$\mathrm{p_T^{j_1}}$ (GeV)		> 400	
$\mathrm{H_{T;3}}$		< 80	
m_T (GeV)		$20 < m_T < 120$	
$E_{\mathrm{T}}^{\mathrm{miss}}$ (GeV)		> 400	
A	> 0.5	> 0.8	–
m_{jj} (GeV)	> 250	> 250	–
$N_{b-\mathrm{jets}}$	≥ 2	1	0
N_{vtx}	–	≥ 1	≥ 1
m_{vtx} (GeV)	–	> 0.6	> 1.5
p_T^{vtx} (GeV)	–	> 3	> 5

Figure 5.13 presents some distributions of kinematic variables for a common pre-selection for the W+jets and top CRs, which is defined in Table 5.10. This common selection provides the control regions with a good purity in the W+jets and $t\bar{t}$ SM production processes. The MC models the data well. More distributions are presented in Appendix B.

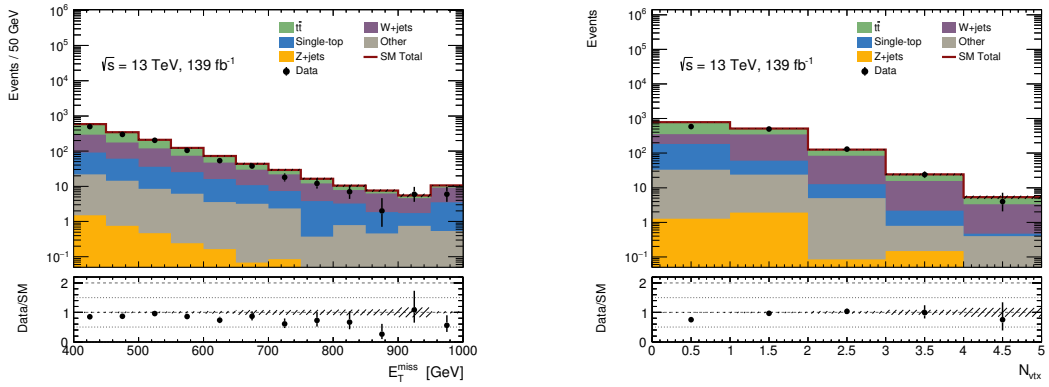

(a) (b)

Figure 5.13: Distribution of data and MC prediction for (a) $E_{\mathrm{T}}^{\mathrm{miss}}$ and (b) N_{vtx} for the common pre-selection for the W+jets and Top control regions. The plots do not include the background normalisation factors derived as part of the fit procedure described in Section 5.3, and only the statistical uncertainties are considered. The plots for channels where at least one TC-LVT vertex is required do not include the TC-LVT scale factor. The inset plot shows the ratio between the data and the MC prediction.

Figure 5.14 shows the $E_{\mathrm{T}}^{\mathrm{miss}}$ distributions for the three control regions, while Table 5.11 shows the yields of the SM processes in the three control regions defined. The top background is not dominant in any of the SR. However there is a significant top contamination in the W+jets CRs. Hence the need for a Top CR.

Table 5.11: Yields for SM background processes obtained for the 1-lepton control regions.

Process	CRC-Top	CRC-W1b1v	CRC-W0b1v
$t\bar{t}$	108.60	25.75	46.19
W+jets	48.80	84.55	215.69
single top	14.21	5.36	9.22
Z+jets	0.39	0.69	1.22
other	6.73	3.91	9.81
SM	179.58	120.48	282.13
Data	145.00	106.00	287.00

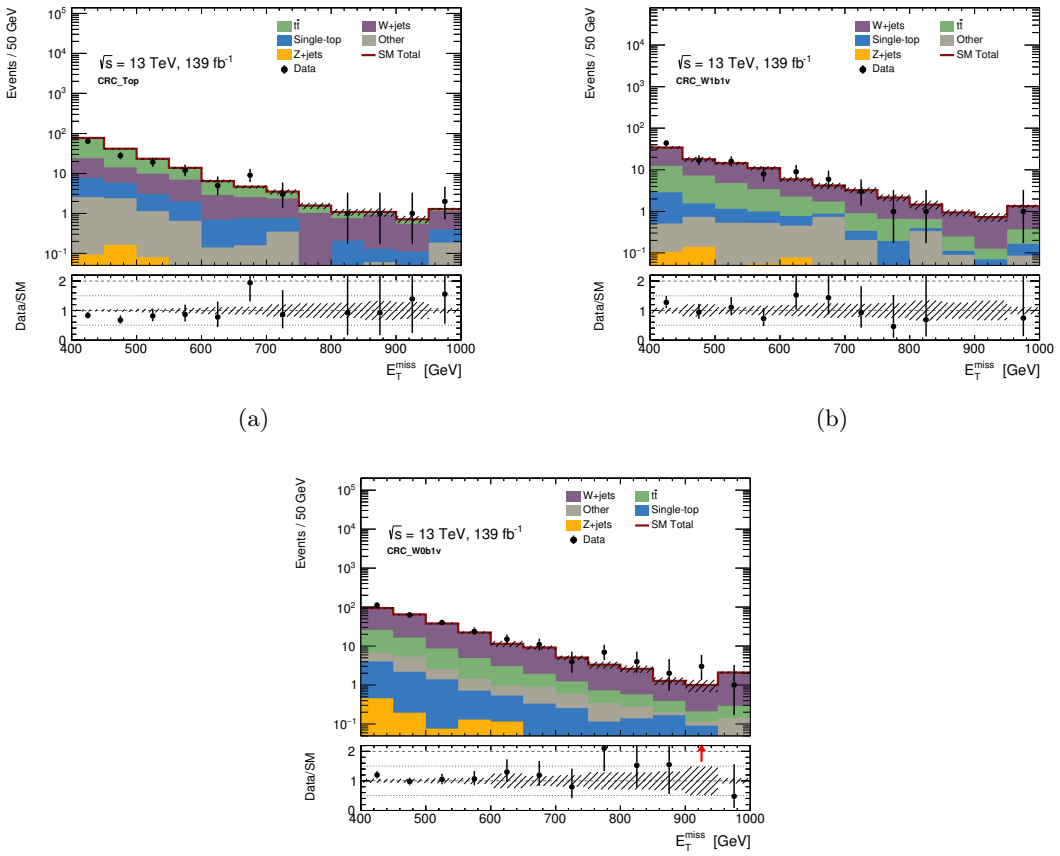

Figure 5.14: $E_{\mathrm{T}}^{\mathrm{miss}}$ distribution of data and MC for (a) CRC-Top, (b) CRC-W1b1v and (c) CRC-W0b1v. The plots do not include the background normalisation factors derived as part of the fit procedure described in Section 5.3, and only the statistical uncertainties are considered. The plots for selections where at least one TC-LVT vertex is required do not include the TC-LVT scale factor. The inset plot shows the ratio between the data and the MC prediction.

Background Validation Regions

These regions are designed to provide a phase-space similar to the signal region, but with a small signal contamination. As it is discussed in more detail in Chapter 6 , they satisfy the need to validate the background prediction to a phase-space which is as similar as possible to the SR, but with a negligible signal contribution. To be confident that this can be achieved, the VR are designed to replicate the same SM background composition of the SR. The definition of the validation regions for this analysis uses the $E_{\mathrm{T}}^{\mathrm{miss}}$ triggers defined in Table 5.1 and it starts, as for the SR, from the 2b-2jets-0l and 1sb-2jets-0l pre-selections introduced in Table 5.3 and Table 5.4. As for the signal region strategy, the validation region strategy relies on three mutually-exclusive selections, which is guaranteed by the selections on $N_{b-\mathrm{jets}}$ and N_{vtx}.

The cuts that define a phase-space mutually-exclusive to the SRs are:

Table 5.12: Kinematic selections for the validation regions.

Selection	VRC-2b0v	VRC-1b1v	VRC-0b1v
Is $j1$ b-tagged?	0	0	0
$\mathrm{p}_{\mathrm{T}}^{j_1}$ (GeV)	< 500	> 400	> 400
$E_{\mathrm{T}}^{\mathrm{miss}}$ (GeV)	< 500	> 400	> 400
$\mathrm{H}_{\mathrm{T};3}$ (GeV)	–	< 80	< 80
A	$[0.8, 0.9]$	> 0.86	> 0.5
m_{jj} (GeV)	$[150, 250]$	> 150	–
$N_{b-\mathrm{jets}}$	≥ 2	$= 1$	$= 0$
N_{vtx}	–	≥ 1	≥ 1
m_{vtx} (GeV)	–	> 0.6	> 1.5
p_T^{vtx} (GeV)	–	> 3	> 5
$\lvert\eta_{vtx}\rvert$	–	> 1.2	> 1.2
$\Delta\phi(j1, vtx)$	–	–	< 2.2
$\Delta\phi(j1, b1)$	–	< 2.2	–

– $\mathrm{p}_{\mathrm{T}}^{j_1}$ and $E_{\mathrm{T}}^{\mathrm{miss}}$ for the region with two b-tagged jets.

– $\Delta\phi(j1, b1)$ for the region with one b-tagged jet and at least one TC-LVT vertex.

– $\Delta\phi(j1, vtx)$ for the region with no b-tagged jet and at least one TC-LVT vertex.

The full selections defining the VR strategy are listed in Table 5.12

Figure 5.15 show the final $E_{\mathrm{T}}^{\mathrm{miss}}$ distribution for the three validation regions, while Table 5.13 displays the pre-fit SM yields. Although the data/MC agreement is already good, it is expected to change once the normalisation factors obtained by the fit procedure are applied. From a comparison with the results in Table 5.7 it is possible to conclude that the background composition is fairly compatible across regions.

Table 5.13: Yields for SM background processes obtained for the validation regions.

Process	VRC-2b0v	VRC-1b1v	VRC-0b1v
Z+jets	65.72	51.34	88.20
W+jets	81.20	18.21	43.74
$t\bar{t}$	22.95	1.55	4.58
single top	2.91	0.53	1.10
other	2.01	1.95	4.65
SM	142.28	73.58	174.79
Data	152	68	131

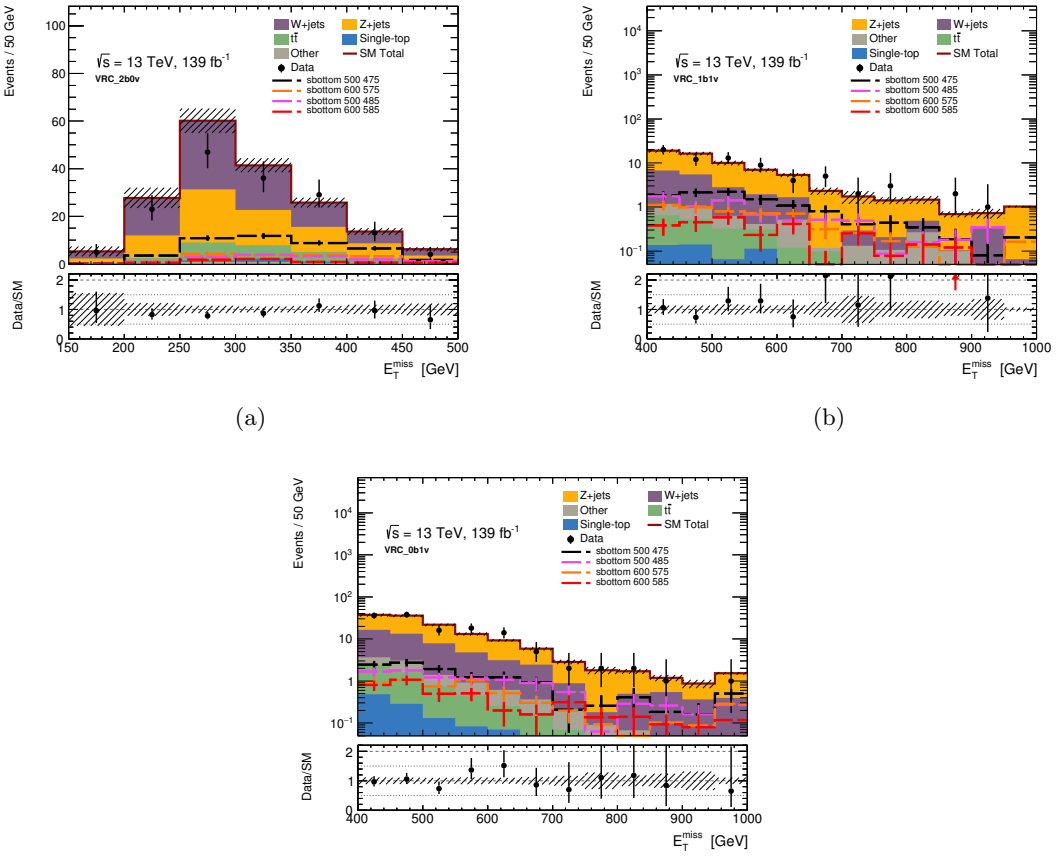

Figure 5.15: $E_{\mathrm{T}}^{\mathrm{miss}}$ distribution of data and MC for (a) VRC-2b0v, (b) VRC-1b1v and (c) VRC-0b1v. The plots do not include the background normalisation factors derived as part of the fit procedure described in Section 5.3, and only the statistical uncertainties are considered. The plots for selections where at least one TC-LVT vertex is required do not include the TC-LVT scale factor. The inset plot shows the ratio between the data and the MC prediction.

Regions Background Composition

The introduction to this Section commented about the importance of the study of the background composition when defining the analysis strategy. Two properties of the SM background are analysed. First there is the study of the relative abundance of the SM background production processes. This is important when designing the validation regions, as the background composition should resemble that of the SR. The other property is the regions' heavy flavour composition, which needs to be as similar as possible across all SR, CR and VR. This requirement allows one to reduce a potential mismodelling in the $V + b\bar{b}$ production. This property, already investigated in other analysis such as Ref. [176], is of particular interest for this analysis because the scale factors applied to the TC-LVT vertices depend on the whether the vertex originates from a b-hadron or not, as described in Chapter 4. The study on the heavy flavour compositions are based on truth information coming from the MC samples, and three categories are defined:

– *b-matched* events: the class of events with a truth b-hadron.

– *c-matched* events: the class of events with no truth b-hadron, but in which a truth c-hadron is found.

– *light* events: the class of events where neither a b-hadron nor a c-hadron is found.

The results of the background SM production processes composition for each class of selections (2b, 1b1b and 0b1v) are presented and discussed. These composition are based on pre-fit yields, and do not include TC-LVT scale factors.

2b Selections

The background and heavy flavour compositions of the regions requiring the presence of at least two b-tagged jets are discussed. The signal and validation regions are dominated by the Z+jets process, with a sizeable presence of W+jets . The background composition in the SRC-2b and VRC-2b0v is summarised in Figure 5.16. It can be seen that the

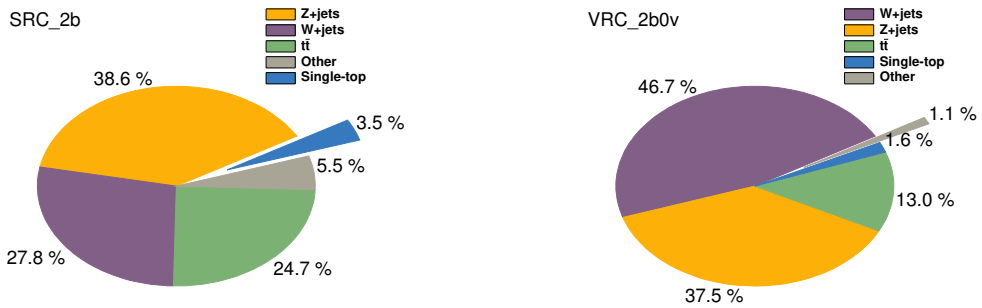

(a) (b)

Figure 5.16: Background composition for (a) SRC-2b and (b) VRC-2b0v.

background composition in the SRC-2b and VRC-2b0v are not exactly the same, as the W+jets production is the dominant SM production process in VRC-2b0v. This is due to the definition of VRC-2b0v, which inverts some kinematic cuts, such as A, which reduce the W+jets production process in SRC-2b. Having discussed the SM production processes composition, it is possible to focus on the heavy flavour composition. The presence of at least two b-tagged jets suggests that these regions are dominated by b-matched events. This expectation is confirmed by the results shown in Figure 5.17. The five regions are dominated by b-matched events, while the abundance of light events is always negligible. The only region where the light and c-matched events are comparable is the VRC-2b0v. This discrepancy does not affect the analysis strategy.

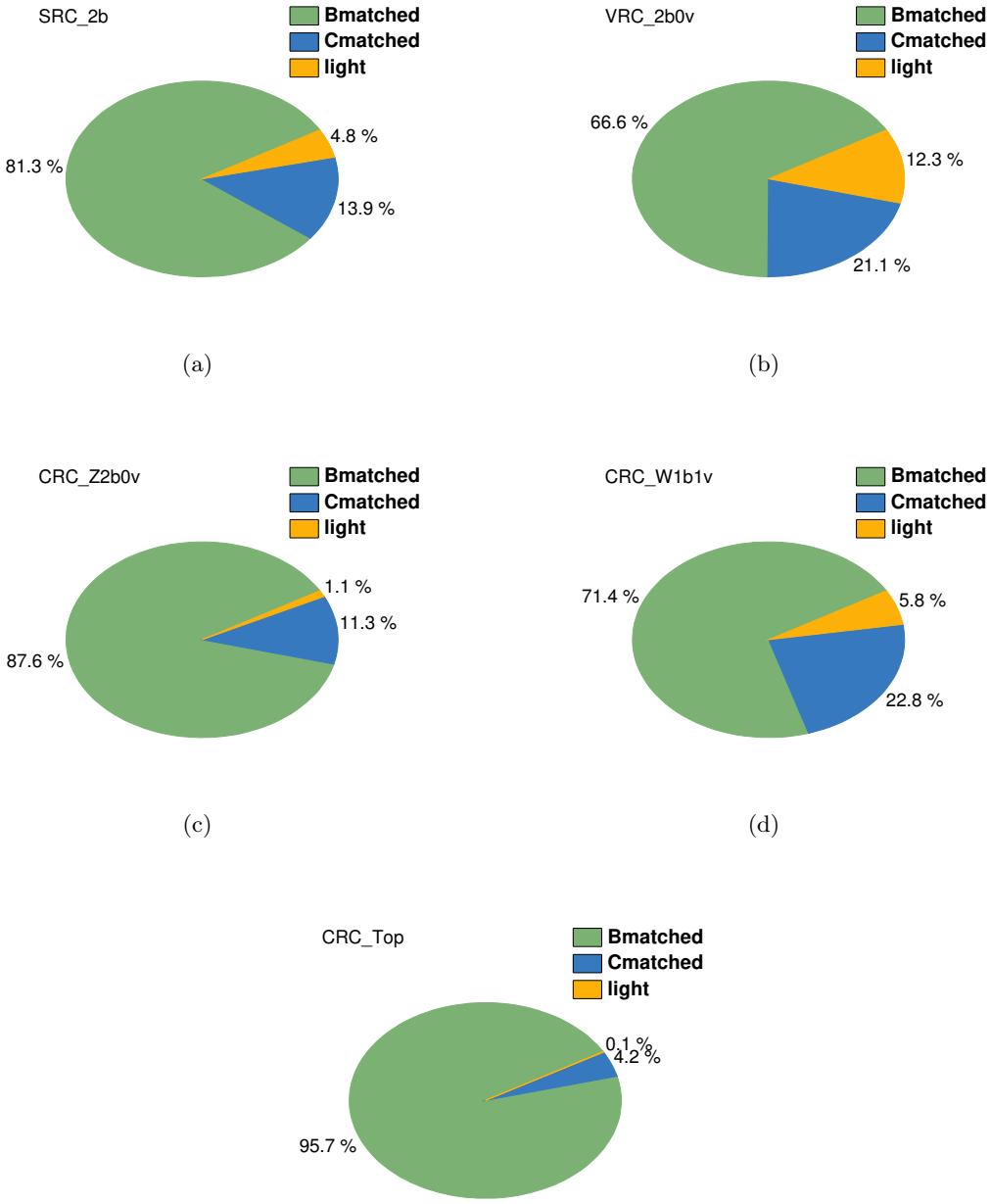

Figure 5.17: Heavy flavour composition for (a) SRC-2b, (b) VRC-2b0v, (c) CRC-Z2b0v, (d) CRC-W1b1v and (e) CRC-Top.

1b1v Selections

The background and heavy flavour compositions of the regions requiring the presence of exactly one b-tagged jet and at least one TC-LVT vertex are discussed. The signal and validation regions are dominated by the Z+jets process, with a significant presence of W+jets . The background composition in the SRC-1b1v and VRC-1b1v is summarised in Figure 5.18. The different abundances of the Z+jets and W+jets SM backgrounds are

due to the inverted kinematic cuts defining the VRC-1b1v.

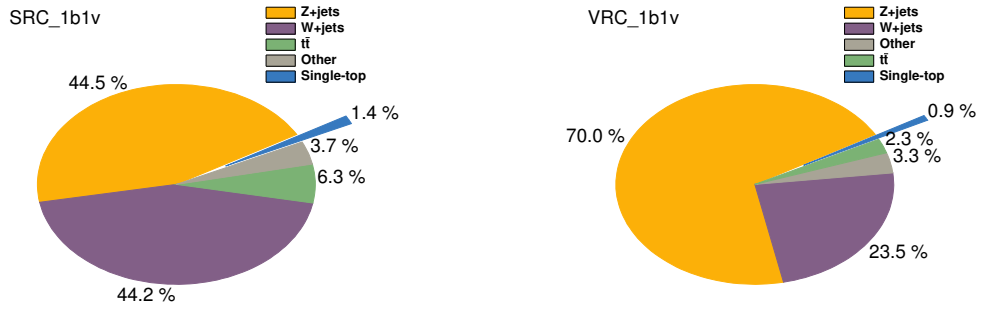

(a) (b)

Figure 5.18: Background composition for (a) SRC-1b1v and (b) VRC-1b1v.

After discussing the SM production processes composition, the focus is now on the heavy flavour composition. The presence of both one b-tagged jet and at least one TC-LVT vertex suggests that the regions are dominated by the b-matched events, because of the requirement on the presence of a b-tagged jet, but with a larger contribution of the light events introduced by the TC-LVT vertex. The heavy flavour compositions for SRC-1b1v, VRC-1b1v, CRC-Z1b1v and CRC-W1b1v are shown in Figure 5.19.

The expectations on the heavy flavour composition is confirmed for SRC-1b1v, where the b-matched events are still dominant, and the light events are nearly as abundant as the c-matched. This behaviour is not as evident in the validation and control regions, where the light events contribution is less abundant. This only main difference with the signal region here is due to the inverted (VRC-1b1v) or absent (CRC-Z1b1v, CRC-W1b1v) selection on $\Delta\phi(j1, b1)$.

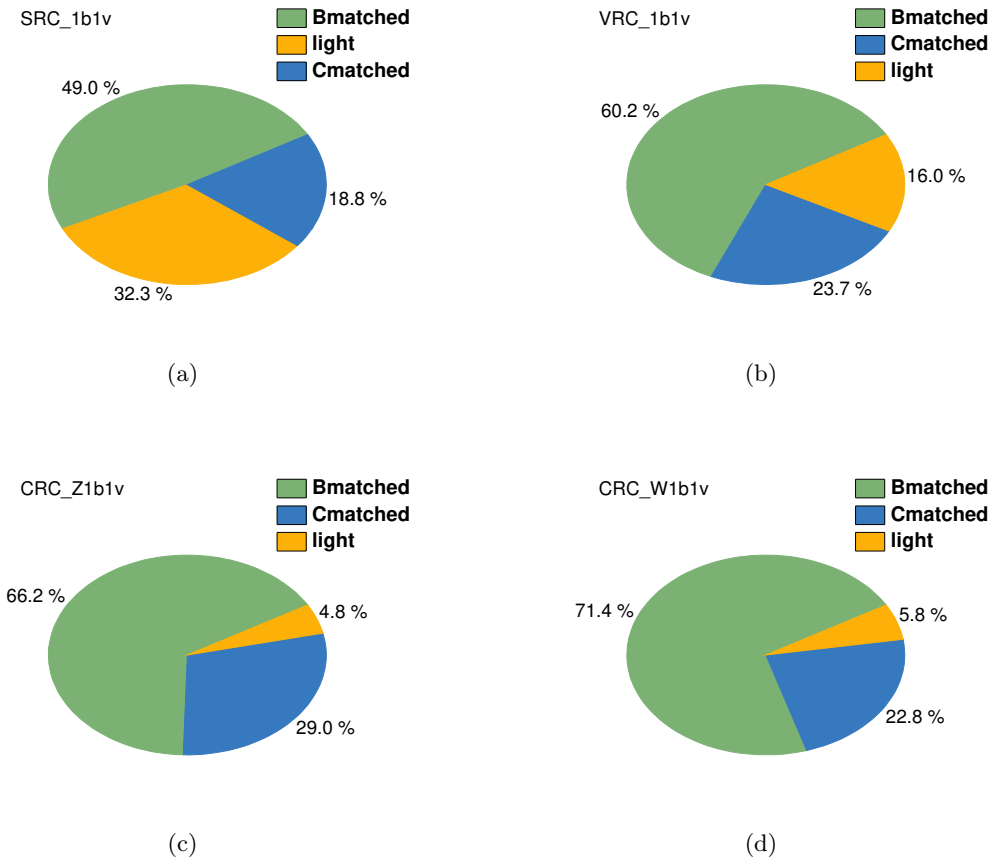

Figure 5.19: Heavy flavour composition for (a) SRC-1b1v, (b) VRC-1b1v, (c) CRC-Z1b1v, (d) CRC-W1b1v.

0b1v Selections

The background and heavy flavour compositions of the regions requiring the presence of no b-tagged jets and at least one TC-LVT vertex are discussed. The signal and validation regions are dominated by the Z+jets process, with a significant presence of W+jets .

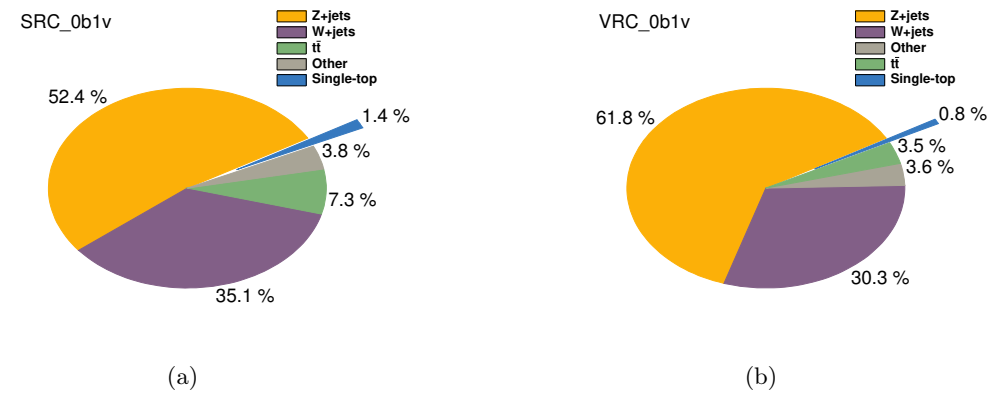

Figure 5.20: Background composition for (a) SRC-0b1v and (b) VRC-0b1v.

The background composition in the SRC-0b1v and VRC-0b1v are summarised in Figure 5.20. Regarding the heavy flavour composition, the absence of b-tagged jets in the event suggests that these regions are mainly populated by light events. This expectation is confirmed by the results shown in Figure 5.21.

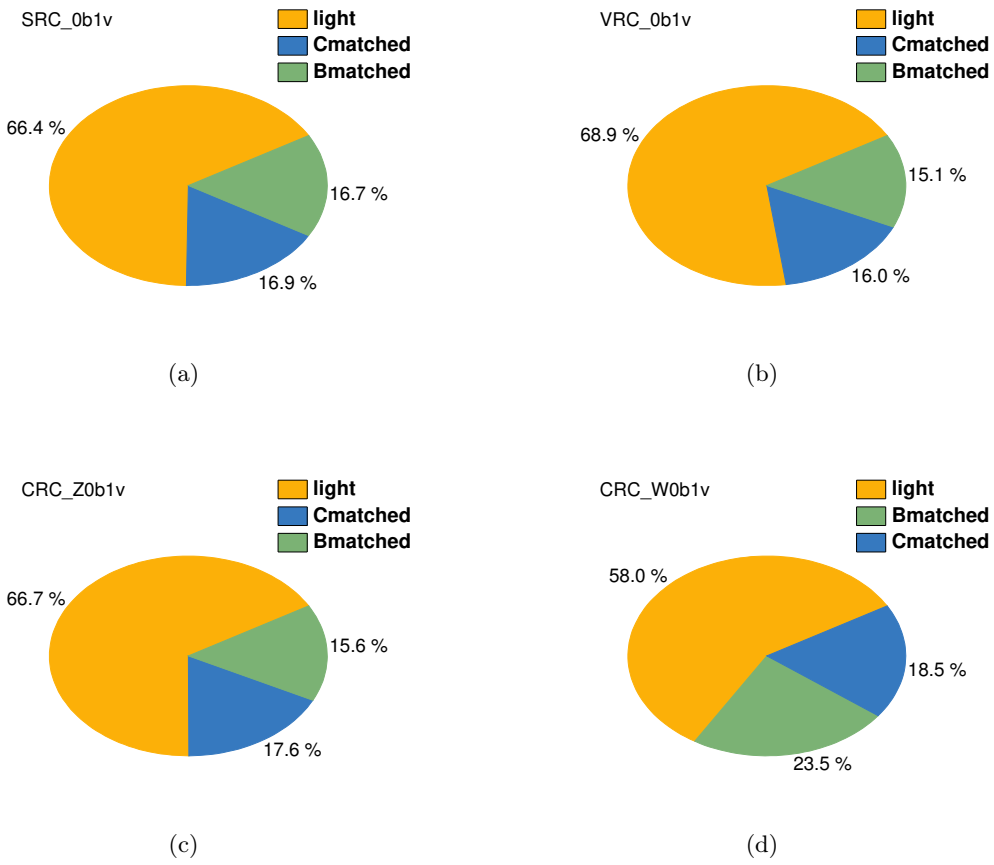

Figure 5.21: Heavy flavour composition for (a) SRC-0b1v, (b) VRC-0b1v, (c) CRC-Z0b1v, (d) CRC-W0b1v.

5.4 Summary

This Chapter has described the analysis strategy for targeting signal models with $E_{\mathrm{T}}^{\mathrm{miss}}$ and b-jets in full-hadronic final states.

Section 5.1 has provided a more detailed theoretical motivation for the such signal models already introduced in Chapter 1. Section 5.2 has commented on the event selection and introduced the relevant kinematic variables exploited by this work. Section 5.3 has described the statistical procedure adopted by this analysis. Selections to target signal-enriched regions have been designed by exploiting the novel TC-LVT algorithm described in Chapter 4. The SM background processes have been studied in dedicated control regions which have been defined by requiring the presence of leptons. It has been found that

MC predictions for the SM background model well the data. The background and flavour composition has been studied and it has been found to be consistent across all the regions.

Statistical Interpretation and Results

6

This Chapter presents the results of the searches for direct pair production of bottom squarks in final states with large $E_{\mathrm{T}}^{\mathrm{miss}}$ and b-jets.
Section 6.1 briefly introduces the main systematic variations applied to the analysis.
Section 6.2 presents the final results of the analysis according to three fit strategies, which are defined in the same Section.

6.1 Systematic Variations

This Section presents the systematic variations applied to this analysis, and are divided into two different categories.

- *Experimental systematics.* These variations arise from the reconstruction of the objects used in the analysis, i. e. electrons, muons, jets, heavy flavour jets and $E_{\mathrm{T}}^{\mathrm{miss}}$.

- *Modelling systematics.* These variations arise from the arbitrary choice of parameters when performing the MC calculations.

The impact of the systematic variations on the background and signal expectations are accounted for in Equation 5.4 by introducing the nuisance parameter (NP) θ^j whose uncertainty σ^j represents the modelling uncertainty. The variation on the signal and background expectation for the j-th systematic variation is obtained by performing the analysis varying the prediction in the way corresponding to σ^j. The variations due to the experimental systematics are treated as totally uncorrelated between them, but it is completely correlated across the different signal and background production processes. The modelling uncertainties are instead treated as completely uncorrelated across the different processes. In the following more details on the experimental and modelling systematic variations exploited by this analysis are presented.

Experimental Systematics

Jet Energy Scale (JES) These are the uncertainties related to the JES, as described in more detail in Section 3.4. The calibration process is based on about 100 JES uncertainties, which are grouped into three JES NP uncertainties [155]. This set of systematic variations is completed by considering the uncertainties related to the calibration at high values of p_T and η of the jet.

Jet Energy Resolution (JER) These are the uncertainties related to the smearing of the jet resolution, according to Ref. [201]. Seven NP arise from the choice of a reduced set of such systematic variations, and the set of systematic variations is completed by considering the uncertainties related to the jet flavour response.

Jet Vertex Tagger (JVT) These are the uncertainties related to the variations on the JVT tagger used to suppress the pileup. The systematic variation is computed by varying its scale factor within the measured error, as described in Ref. [202].

Flavour Tagging Uncertainties These are the uncertainties related to the efficiency and mis-tag rates for the b-tagging algorithm. The uncertainty is estimated by varying the scale factors obtained in dileptonic $t\bar{t}$ events for the efficiency and in generic dileptonic events for the fakes. The uncertainties are calculated as function of the jet p_T, η and flavour according to the uncertainties of their measurements, as discussed in Ref. [186].

TC-LVT Uncertainties These are the systematic uncertainties arising from the use of the TC-LVT algorithm. As it is described in Chapter 4, there are two sources of systematic uncertainties: one related to the tagging of vertices originated from the decay of a b-hadron; the other related to the tagging of fake vertices. The systematic uncertainty for the fake vertices depends on the specific selections on m_{vtx} and p_T^{vtx}.

$\mathbf{E}_{\mathrm{T}}^{\mathrm{miss}}$ Uncertainties These are the uncertainty related to the missing transverse momentum, which arises from the propagation of the variations applied to final-state physics objects. This systematic variation is completed by considering uncertainties on the scale and resolution of the soft term [167].

Lepton Uncertainties These are the uncertainties related to electron and muon reconstruction and calibration separately. Uncertainties are estimated by varying the scale factor related to each step of the reconstruction, identification and calibration of the leptons within their errors.

Pile-up Re-weighting Uncertainty This is the uncertainty related to the pile-up re-weighting. Each MC sample is weighted accordingly to the actual pile-up distribution observed in data by a scale factor $\langle\mu\rangle$. The scale factor is varied by $\pm 10\%$ according to its measured uncertainties, and the varied $\langle\mu\rangle$ profiles are used to estimate this systematic variation.

Luminosity Uncertainty The luminosity uncertainties for each year are combined together by considering the covariance matrix of the absolute luminosity uncertainties for the different years , and the final uncertainty is 1.7% [203]. This uncertainty is added as an additional systematic.

Modelling Systematics

V+jets processes These are the modelling uncertainties for Z+jets and W+jets . The magnitude of these uncertainties for the factorisation, renormalisation, resummation for the soft gluon emission and CKKW matching scale are evaluated by using 7-point variations of each scale by factor of 0.5 and 2, as discussed in Ref. [204]. The fit strategy described in Section 5.3 is designed to mitigate the uncertainties in the modelling the $V + b\bar{b}$ production. By defining a unique normalisation factor as a function of the b-jet multiplicity, the fit tends to absorb mismodelling in the b-hadron multiplicity production of the process.

Top processes These are the model uncertainties arising from $t\bar{t}$ and single top. The uncertainty originates from varying the hard-scattering generator and matching scheme, and it is obtained by comparing the nominal sample to the variated samples generated with MadGraph5_aMC@NLO. The shower starting scale is set to $\mu_q = H_T/2$, where H_T is obtained by adding the p_T of the outgoing partons. The uncertainty arising from the parton shower and hadronisation model is obtained by comparing the nominal sample with the varied samples generated with Powheg interfaced to Herwig 7 [121, 205], using H7UE set of tuned parameters [205]. The uncertainty arising from the renormalisation and factorisation scales, the initial- and final-state radiation parameters and PDF sets are considered according to Ref. [206].

Signal Uncertainties These are the signal modelling uncertainty, which is introduced by varying the signal production cross section by $\pm$ 1σ of the theoretical uncertainty. The effects due to the choice of the generators' parameters are studied and are negligible.

6.2 Results and Interpretation

This Section presents the final results of this work. The results from the previous analysis by ATLAS using 36 fb^{-1} [176] are briefly presented. This work is then put in the context of the full Run 2 analysis [3].

36.1 fb^{-1} Results

This work is based on the previous result obtained by analysing the early Run 2 data, which is based on 36 fb^{-1} of collected data at $\sqrt{s} = 13$ TeV centre-of-mass energy and it is fully described in Ref. [176]. The analysis strategy is based on the definition of three 0-lepton SRs targeting different phase-spaces of the decay of a bottom squark pair into b quarks and neutralinos. A common requirement for the three SRs is the absence of leptons in the final state and the presence of b-jets and $E_{\mathrm{T}}^{\mathrm{miss}}$. The main characteristics of the three SRs are summarized in the following.

- *b0L-SRA* is optimised for having maximum sensitivity to the models where the mass difference between the bottom squark and the neutralino is $\Delta m\left(\tilde{b}_1, \tilde{\chi}_1^0\right) > 250$ GeV. The kinematic selection requires the two leading jets to be both b-tagged, and incremental thresholds are imposed on the main discriminating variable, m_{CT}.
- *b0L-SRB* is optimised for having maximum sensitivity to the models where the mass difference between the bottom squark and the neutralino is 50 GeV $< \Delta m\left(\tilde{b}_1, \tilde{\chi}_1^0\right) <$ 250 GeV. The kinematic selection requires the presence of two b-jets, and angular variables between the (b) jets and the $E_{\mathrm{T}}^{\mathrm{miss}}$ are exploited.
- *b0L-SRC* is optimised for having maximum sensitivity to the compressed models, where the mass difference between the bottom squark and the neutralino is $\Delta m\left(\tilde{b}_1, \tilde{\chi}_1^0\right) < 50$ GeV. The kinematic selection defines a mono-jet-like phase-space, obtained by requiring a large-p_T leading jet and a high value of the $E_{\mathrm{T}}^{\mathrm{miss}}$, together with angular requirements between the leading jet p_T and the $E_{\mathrm{T}}^{\mathrm{miss}}$. The leading jet is required not to be b-tagged. At the time of this analysis, no algorithms for identifying low-p_T b-hadrons were developed, resulting in a low sensitivity to very compressed models.

The results from this analysis are reported in Figure 6.1. It can be seen that the analysis has no sensitivity to scenarios with $\Delta m(\tilde{b}_1, \tilde{\chi}_1^0) \leq 20$ GeV, since no low-p_T algorithms, such as the TC-LVT, were available.

139 fb^{-1} Analysis

The work presented in this thesis is part of a larger analysis, described in Ref. [3]. The aim of the analysis is to improve the results shown in Figure 6.1 across the whole ($\tilde{b}_1$,$\tilde{\chi}_1^0$) mass

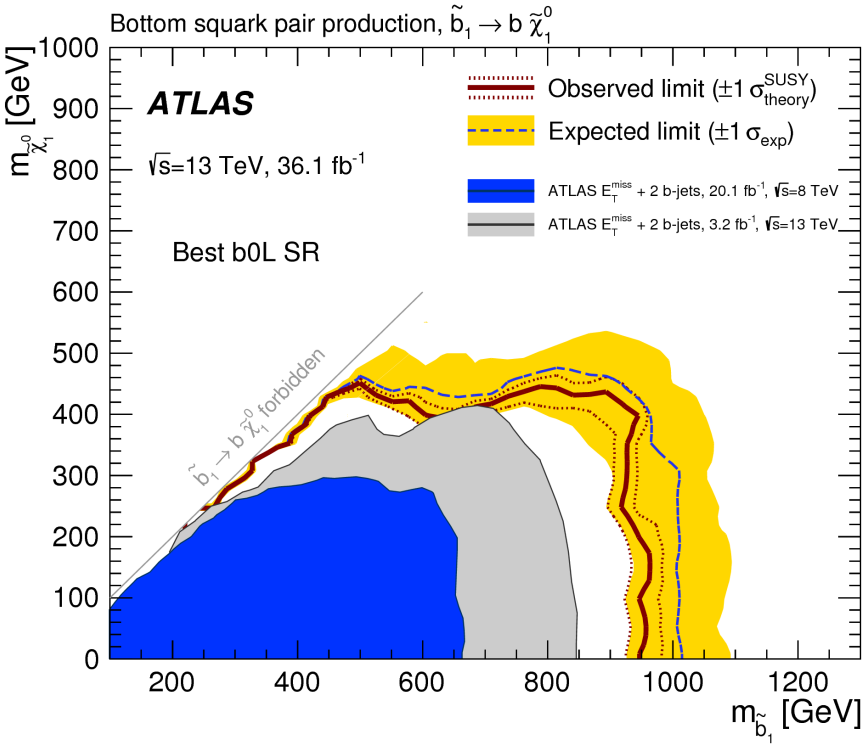

Figure 6.1: Exclusion limits on bottom squark pair production $\widetilde{b}_1$ decaying into $b\widetilde{\chi}_1^0$ with 100% BR. The result exploits 36 fb^{-1} of data and it is based on [176].

plane. Similarly to the previous analysis, three SUSY SRs are developed, each targeting a specific region of the masses plane. An additional SR is defined to investigate DM models. In detail:

- **SRA** targets the bulk region of the phase space, $\Delta m(\widetilde{b}_1, \widetilde{\chi}_1^0) > 200$ GeV. As for [176], the signal region strategy exploits a shape fit in the m_{CT} and m_{eff} variables. SRA is also used to set limits on the models where the scalar third-generation down-type lepto-quarks are produced. The decay channel $\text{LQ}_3^{\text{d}} \to b\nu_\tau$ is considered, and it shares the same final states (bottom quark and $E_{\text{T}}^{\text{miss}}$) as the main analysis.

- **SRB** targets the intermediate region of the phase space 50 GeV $\leq \Delta m(\widetilde{b}_1, \widetilde{\chi}_1^0) \leq$ 200 GeV. The signal region strategy is based on a boosted-decision tree (BDT) algorithm implemented by the XGBoost (XGB) framework [207]. It is defined so that it can be statistically combined with SRA.

- **SRC** targets the compressed region of the phase space, $\Delta m(\widetilde{b}_1, \widetilde{\chi}_1^0) < 50$ GeV. This is the analysis described here in detail.

- **SRD** targets the DM production processes. The analysis strategy targets both scalar and pseudo-scalar mediators, and it is defined according to mediator mass as low- and high-mediator mass signals. The analysis is based on BDT discriminants targeting the signal and the three most relevant background processes (Z+jets , W+jets and $t\bar{t}$). The main discriminant is the $\cos\theta^*_{bb}$ [208].

Strategy Summary

A summary of the analysis strategy for SRC defined in Section 5.3 is reported in the following:

- *Signal Regions* Three Signal Regions (SRs) defined as function of b-jets and TC-LVT vertices multiplicities.
- *Control Regions* Six Control Regions (CRs); three target the main Z+jets SM background, with a one-to-one match to each SR; two target the sub-leading W+jets SM background; one targets the top ($t\bar{t}$ and single top) SM backgrounds.
- *Validation Regions* Three Validation Regions (VRs) defined as function of b-jets and TC-LVT vertices multiplicities, they grant a one-to-one match to each SR.

The results shown in this Section are obtained by using the `HistFitter` framework [198] interfaced with the `HistFactory` [209] package. The statistical procedure is based on a frequentist approach, where the experiment is simulated a large number of times.
The `HistFitter` framework is used primarily to implement two procedures: to estimate the SM background normalisation factors; and to perform the hypothesis testing. The statistical analysis strategy is described in Section 5.3. Three main functions, or fits, are used and their main features are described in the following.

Background-only Fit This fit aims to give an estimate of the total SM background processes production in SR. To achieve this goal, the only input to this fit are the CRs predicted and measured yields, which are assumed to have no signal contamination. With reference to Equation 5.4 and Equation 5.5, μ_s is set to zero, so the fit is performed only with SM background samples as input. The background estimate is compared to the observed yields first in the VRs, then, after validation, in the SR.

Discovery Fit This fit aims to produce model-independent upper limits on the number of generic signal events populating the SRs. This fit uses both CRs and one SR at a time, and a generic signal event of arbitrary intensity is assumed in the SR. The fit sets the limits on each individual SR by taking into consideration single-bin regions. The fit exploits an asymptotic profile maximum likelihood test statistics.

Exclusion Fit This fit aims to study specific signal models. It takes into consideration both CRs and SRs. Since no excess is observed, the fit sets exclusion limits. To maximise the sensitivity to the signal model, the fit combines together the SRs, if more then one. The SRs can be binned to improve their sensitivity to the signal.

The details of each fit configuration together with their results are more extensively presented in the following.

Background Fit Results

This fit aims to estimate the yields of the SM production processes in the SRs. To achieve this goal, the fit procedure is based only on the CRs. The six control regions are statistically independent because of the mutually-exclusive cuts on the b-jet and TC-LVT multiplicities; for this reason it is possible to statistically combine them by performing one single fit.
Six unconstrained normalisation factors (NFs) normalisation factors μ are associated to the fit:

- one common NF μ_{top} is applied to the $t\bar{t}$ and single top contributions;
- one NF μ_{W_0} is applied to the W+jets MC predictions in all regions with no b-tagged jets, while an independent μ_{W_1} is applied to those regions with at least one b-tagged jet;
- three independent NFs μ_{Z_0}, μ_{Z_1}, μ_{Z_2} are applied to the Z+jets MC prediction depending on the b-tagging multiplicity.

The six NFs are treated as free parameters, and their value is obtained by the fitting procedure. The post-fit values of the six NFs are reported in Table 6.1.

Table 6.1: Normalisation factors from the background-only fit.

μ_{W_0}	1.10 ± 0.10
μ_{W_1}	1.08 ± 0.19
μ_{Z_0}	0.96 ± 0.12
μ_{Z_1}	0.95 ± 0.11
μ_{Z_2}	0.86 ± 0.11
μ_{top}	0.72 ± 0.19

The total error on an extrapolated background, $\sigma_{b,tot}$, is calculated according to:

$$\sigma_{b,tot}^2 = \sum_i^n \left(\frac{\partial b}{\partial \eta_i}\right)^2 \sigma_{\eta_i}^2 + \sum_i^n \sum_{j \neq i}^n \rho_{ij} \left(\frac{\partial b}{\partial \eta_i}\right) \left(\frac{\partial b}{\partial \eta_j}\right) \sigma_{\eta_i} \sigma_{\eta_j} \tag{6.1}$$

where:

- η_i are the fit parameters, which include the normalisation factors μ_k and the NPs θ_i.
- $\rho_{i,j}$ is the post-fit correlation coefficient between the fit parameters η_i, η_j.
- σ_{η_i} is the the standard deviation of the fit parameter η_i.

The systematic uncertainties are kept correlated across all regions. For all the CRs defined in Ref. [3], Figure 6.2 shows the pre-fit agreement between the predicted MC yields and the observed data for the single-bin CRs adopted as input for the fit, together with the values of each μ_{bkg}.

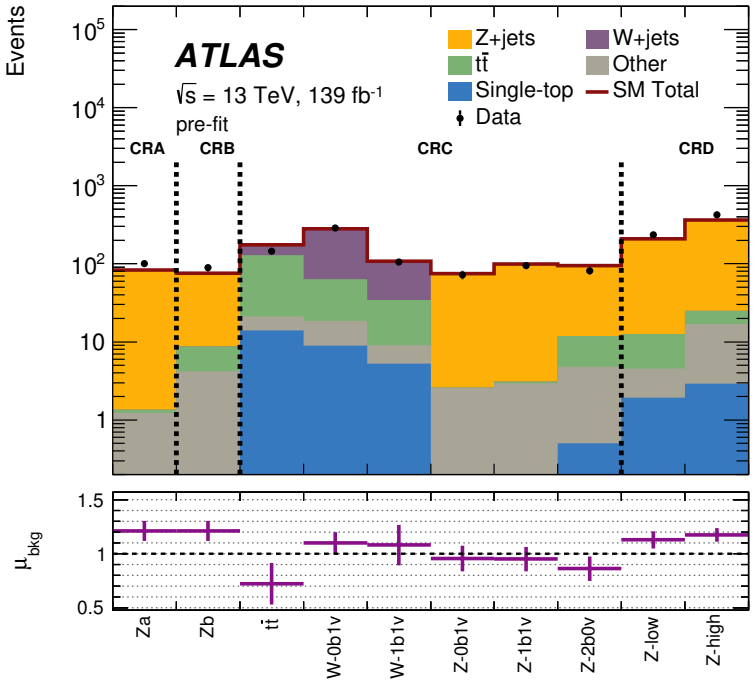

Figure 6.2: Agreement between the observed data and predicted pre-fit background yields for all the control regions from Ref. [3]. The CRs of interest for this thesis are the ones under the **CRC** labelling. The total SM prediction does not include systematic uncertainties. The inset plot shows the normalisation factor for the dominant background process in each region.

Figure 6.3 shows the post-fit correlation matrix of the NP for each systematic variation considered in this analysis. The correlation ρ_{ij} between the i-th and j-th systematic variation is crucial in correctly estimating the total uncertainty, as it is described in Equation 6.1. If $\rho_{ij} \sim 0$ then the two systematic variations are not correlated, while if $\rho_{ij} \sim \pm 1$ then the two systematics are correlated (+1) or anti-correlated (-1). As it can be seen in Figure 6.3, the majority of the systematics are not correlated. Few others are slightly anti-correlated, such as μ_{top} and μ_{W_0} which have a correlation factor $\rho = -0.49$, or slightly correlated, such as the μ_{top} and the W theory uncertainties which have a correlation factor $\rho = -0.46$. These relationship are due to the sizeable presence of top processes in the W+jets regions.

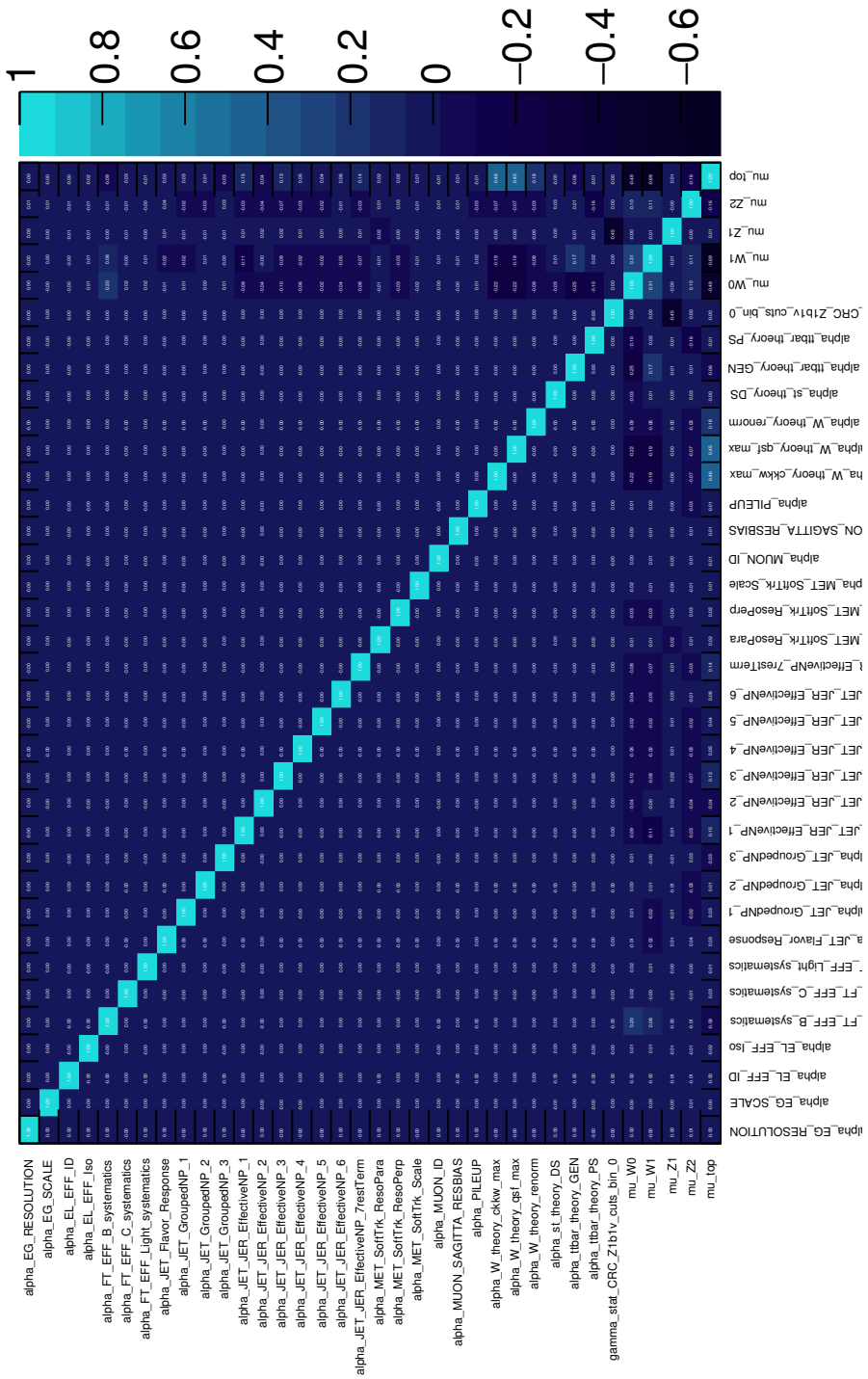

Figure 6.3: Post-fit correlation matrix of the NP for the systematic variations exploited by the analysis. Correlations <1% are removed from the plot. Values closer to 1 (-1) indicate a strong correlation (anti-correlation), while values close to 0 indicate uncorrelated systematic variations.

Once the fit is performed, it is possible to validate the fitted background predictions with the data in the validation regions. The data/MC predictions comparison before and after performing the fit is shown in Figure 6.4 in the three VRs described in this work.

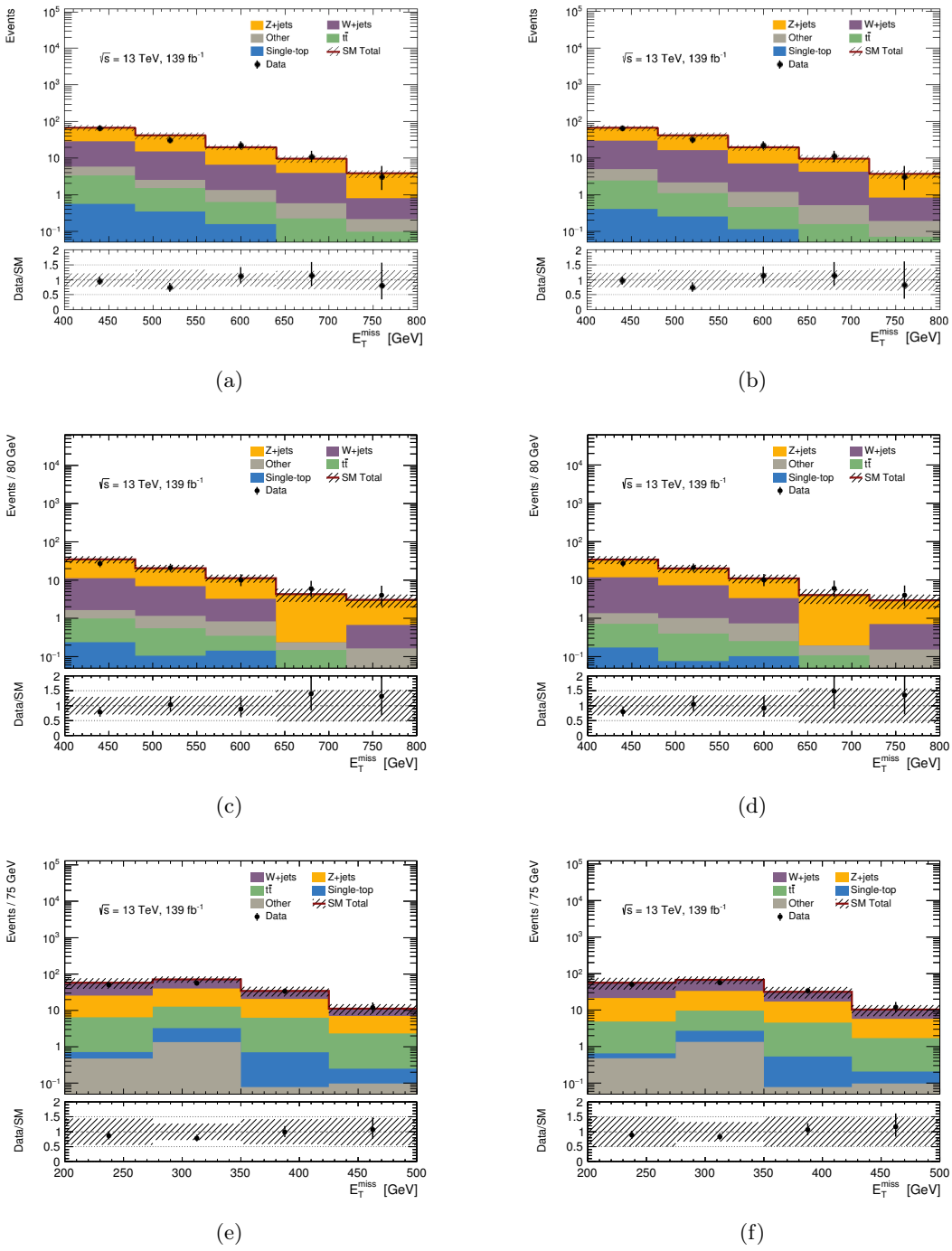

Figure 6.4: $E_{\mathrm{T}}^{\mathrm{miss}}$ distribution of data and SM prediction for (a) VRC-0b1v pre-fit and (b) VRC-0b1v post-fit, (c) VRC-1b1v pre-fit and (d) VRC-1b1v post-fit, (d) VRC-2b0v pre-fit and (e) VRC-2b0v post-fit. The inset plot shows the ratio between observed data and SM background predictions. Error bands include both systematic and statistical uncertainties.

For all the analysis strategies exploited by Ref. [3], Figure 6.5 shows the observed yields compared with the fit background predictions. The predicted yields are in agreement with the observed data.

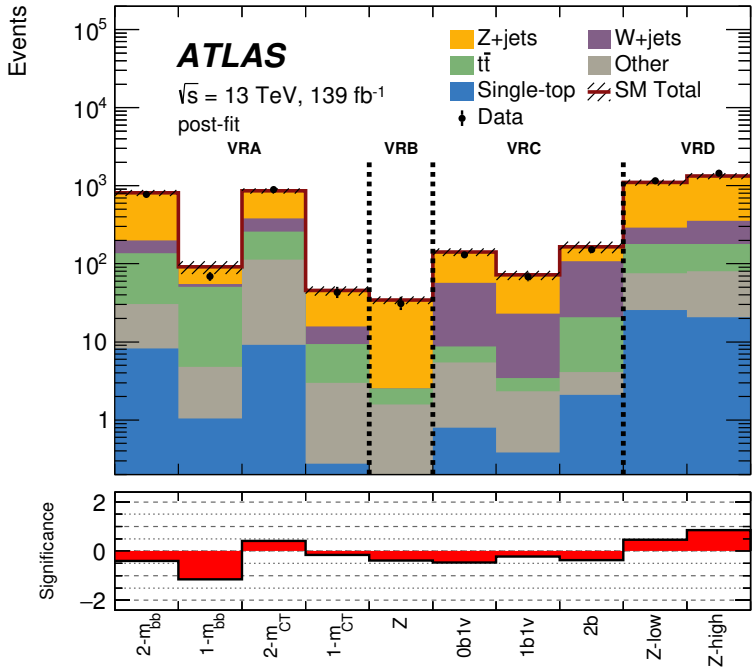

Figure 6.5: Comparison of the observed data with the predicted post-fit background yields for all the validation regions from Ref. [3]. The VRs of interest for this thesis are the ones under the **VRC** labelling. The total SM includes systematic uncertainties. The inset plot shows the significance of the discrepancy between observed and predicted values in each region.

Having validated the SM background prediction in the VRs, the SRs yields are reported in Table 6.2, while the $E_{\mathrm{T}}^{\mathrm{miss}}$ distributions with the fit background yields for the three signal regions are shown in Figure 6.6. No significant excess is in data is observed over the SM predictions.

Table 6.2: Observed data in the three signal regions. The observations are compared with the post-fit SM predictions from the background-only fit. No significant excess is observed.

	SRC-0b1v	SRC-1b1v	SRC-2b
Observed events	151	43	58
Fitted bkg events	147.92 ± 24.87	50.57 ± 10.07	44.47 ± 5.76
Fitted Z+jets events	73.87 ± 18.73	20.10 ± 5.13	16.61 ± 4.01
Fitted W+jets events	60.51 ± 11.18	26.07 ± 8.33	14.96 ± 3.68
Fitted $t\bar{t}$ events	7.04 ± 2.22	1.90 ± 0.96	8.92 ± 3.82
Fitted single top events	1.40 ± 0.48	0.42 ± 0.41	1.25 ± 0.49
Fitted Other events	5.11 ± 1.23	2.07 ± 0.30	2.73 ± 0.58
MC exp. SM events	148.99	50.52	49.88

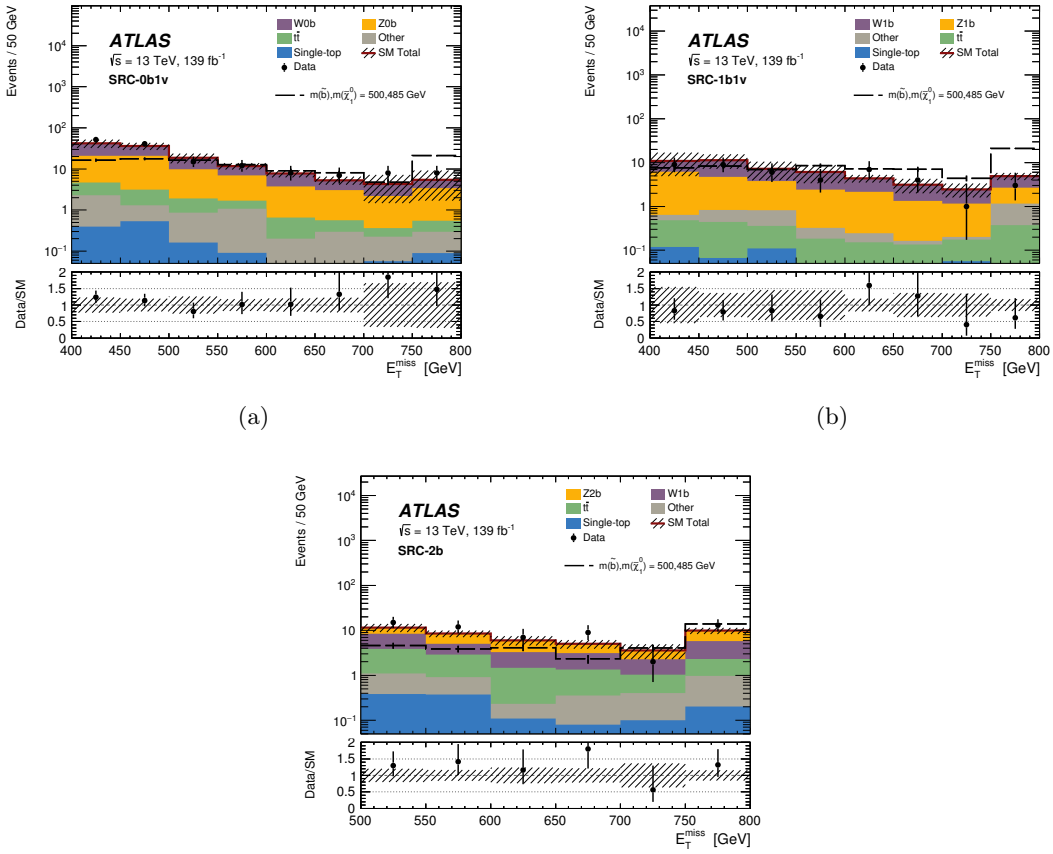

Figure 6.6: Post-fit $E_{\mathrm{T}}^{\mathrm{miss}}$ distribution of data and SM prediction for (a) SRC-0b1v, (b) SRC-1b1v and (c) SRC-2b. The distribution of one signal point $m(\widetilde{b}_1, \widetilde{\chi}_1^0) = (500, 485)$ GeV are also shown. The inset plot shows the ratio between observed data and SM background predictions. Error bands include both systematic and statistical uncertainties.

For all SRs defined for the analysis, Figure 6.7 shows the impact of the most relevant background systematic uncertainties. The most important modelling uncertainties for the analysis discussed in this thesis are the uncertainties on the Z+jets process, which dominate the SRs's uncertainties, and the W+jets process uncertainties. The most important experimental uncertainties are the ones related to the JES.

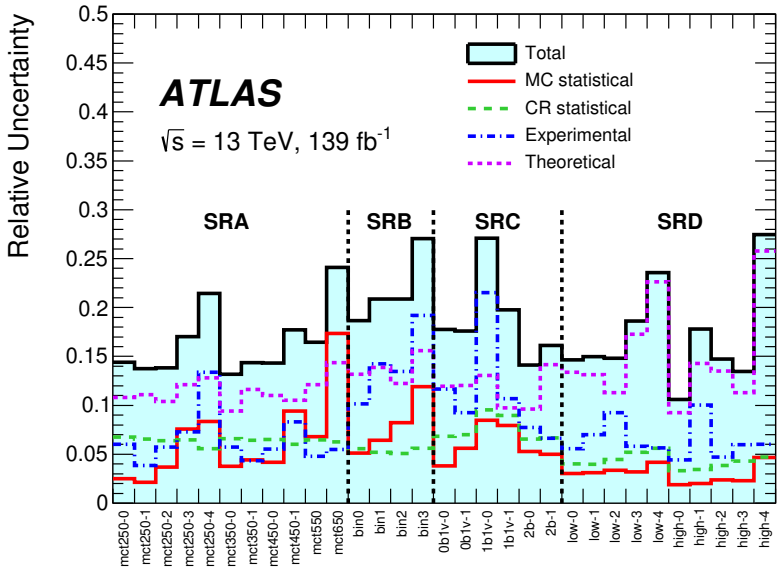

Figure 6.7: Summary of the post-fit relative systematic uncertainties of the various signal region yields split by component. The values of the systematics are obtained from the background-only fit, but are shown in the exclusion SRs. The systematic uncertainties of interest for this thesis are the ones under the **SRC** labelling.

Discovery Fit Results

This fit aims to set upper limits on the signal cross section in a model independent way. This is achieved by performing an asymptotic scan of the signal strength μ_{sig}. There are some main differences compared to the background-only fit previously introduced: the fit also includes the SRs to constrain the likelihood; three independent fits, one per each single-bin SR, are performed; the CRs are explicitly required to be signal-free. This model-independent fit exploits a profile likelihood ratio which tests the background-only hypothesis (namely, $\mu_{sig} = 0$) against the signal hypothesis $\mu_{sig} \neq 0$. An arbitrary signal yield $s = 1$ is considered in the SR. The scans for each SR are reported in Figure 6.8. In those plots, the three hypothesis CL_s, CL_b and CL_{s+b} are shown, together with the expected CL_s. The expected excluded signal strength S^{95}_{exp} is obtained when the median of the expected CL_s crosses the red line, which indicates a p-value of 0.05 (corresponding to a 95% CL), while the observed excluded signal strength S^{95}_{obs} is obtained when the observed CL_s distribution has a p-value smaller than 0.05.

The upper limit on the observed cross section is defined as $\langle \epsilon\sigma \rangle = S^{95}_{obs} / \int \mathcal{L}\, dt$, which is the 95% observed upper limit divided by the total luminosity. Table 6.3 reports the upper limits on the visible cross-section, the number of predicted and observed signal events, the observed confidence level of the background-only hypothesis, and the discovery p-value with its significance.

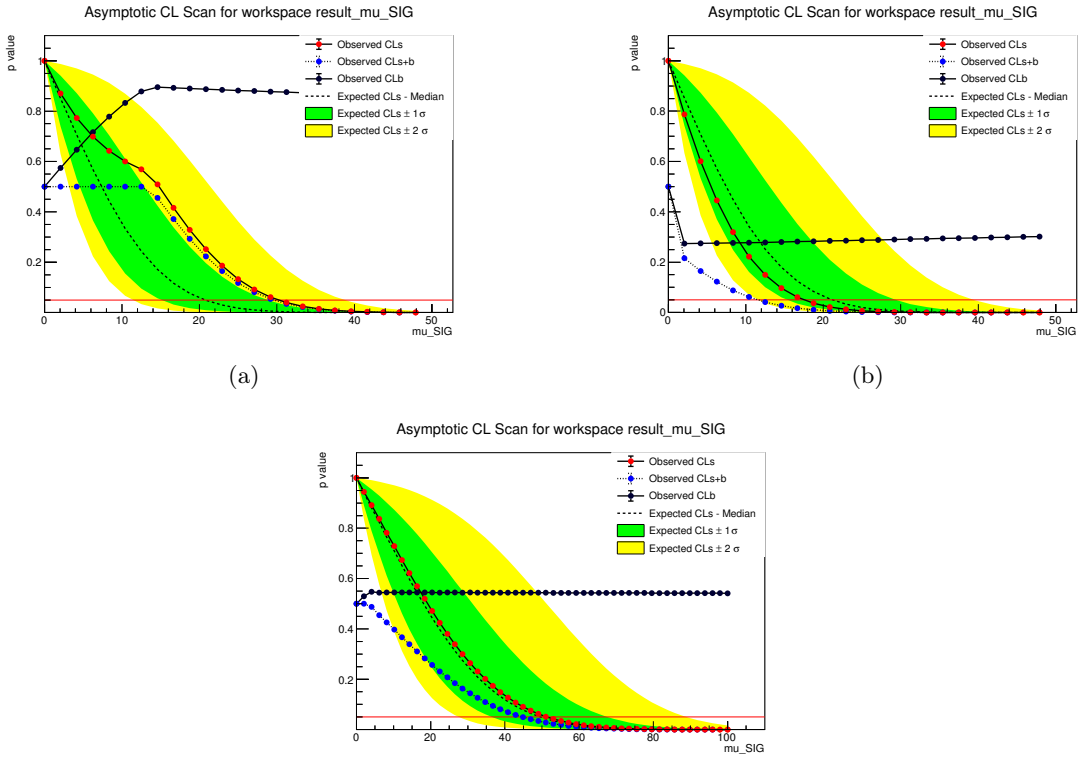

Figure 6.8: μ_s asymptotic scans for (a) SRC-2b, (b) SRC-1b1v and (c) SRC-0b1v. The broken black line represents the expected CL_s median value with its error band in green (yellow) referring to the one standard deviation (two standard deviations). Three different hypothesis are take in consideration: background only, and its observed confidence level CL_b; signal only, and its observed CL_s; and signal+background, and its observed CL_{s+b}. The horizontal red line indicates a p-value of 0.05, and the upper limit on μ_s is set when the observed CL_s crosses that threshold.

Table 6.3: Left to right: the 95% CL upper limits on the visible cross-section ($\langle\epsilon\sigma\rangle^{95}_{\text{obs}}$) ; the number of observed and predicted signal events S^{95}_{obs} and S^{95}_{exp}; the observed confidence level for the background-only hypothesis CL_b; the discovery p-value $p(s = 0)$ and the corresponding significance Z.

Signal channel	$\langle\epsilon\sigma\rangle^{95}_{\text{obs}}$[fb]	S^{95}_{obs}	S^{95}_{exp}	CL_B	$p(s=0)$ (Z)
SRC_0b1v	0.37	51	50^{+18}_{-13}	0.54	0.48 (0.2)
SRC_1b1v	0.13	17.6	$21.2^{+8.2}_{-5.8}$	0.28	0.50 (0)
SRC_2b	0.22	30.3	$20.7^{+8.1}_{-5.6}$	0.88	0.09 (1.33)

Exclusion Fit Results

This fit, also known as model-dependent fit, is used to test the validity of a specific signal model. To do so, all CRs and SRs are fitted at the same time by combining the three signal regions. To further increase the sensitivity of the analysis, a shape-fit on the $E_{\text{T}}^{\text{miss}}$ distribution is performed. This is obtained by splitting each signal region in two mutually exclusive bins, defined in Table 6.4. The exclusion fit is performed for each mass in the

$(m_{\tilde{b}}, m_{\widetilde{\chi}_1^0})$ mass plane. For each point, the signal strength which results in an exclusion at 95% CL of the signal+background hypothesis is extracted. Such a value is labelled as μ_s^{UL}. The final result from the exclusion fit is a plot in the mass plane $(m_{\tilde{b}}, m_{\widetilde{\chi}_1^0})$ for which $\mu_s^{\mathrm{UL}} = 1$ for both expected and observed limits.

Table 6.4: $E_{\mathrm{T}}^{\mathrm{miss}}$ binning for the three signal regions applied for the exclusion fit.

Signal Region	Bin0	Bin1
SRC_0b1v	$E_{\mathrm{T}}^{\mathrm{miss}} \in [400, 600)$ GeV	$E_{\mathrm{T}}^{\mathrm{miss}} \in [600, \infty)$ GeV
SRC_1b1v	$E_{\mathrm{T}}^{\mathrm{miss}} \in [400, 600)$ GeV	$E_{\mathrm{T}}^{\mathrm{miss}} \in [600, \infty)$ GeV
SRC_2b	$E_{\mathrm{T}}^{\mathrm{miss}} \in [500, 650)$ GeV	$E_{\mathrm{T}}^{\mathrm{miss}} \in [650, \infty)$ GeV

Figure 6.9 shows the observed and expected exclusion limits obtained by the model-dependent fit in the $(m_{\tilde{b}_1}, m_{\widetilde{\chi}_1^0})$ mass plane. The exclusion limits are obtained by combining all the SRs defined by the analysis as follows.

- SRA and SRB are designed in order to be statistically independent; for this reason they are combined together in a single fit, SR-AB.
- SRC_0b1v, SRC_1b1v and SRC_2b are statistically independent, hence they are combined in a single fit, SRC.
- SR-AB and SRC are not statistically independent, hence in the regions of the $(m_{\tilde{b}}, m_{\widetilde{\chi}_1^0})$ mass plane where both fits are sensitive the fit with the best sensitivity is considered.

As it can be seen, the analysis improves the previous results across the whole mass plane. A different mass plane, $(m_{\tilde{b}_1}, \Delta m(\widetilde{b}_1, \widetilde{\chi}_1^0))$, is exploited to better visualise the mass points with $\Delta m(\widetilde{b}_1, \widetilde{\chi}_1^0) < 60$ GeV, and it is shown in Figure 6.10. It can be observed that the small excess observed in the SRC-2b region is responsible for the weaker than expected limit observed in Figure 6.10 for the mass points around $m_{\tilde{b}_1} = 700$ GeV and $\Delta m(\widetilde{b}_1, \widetilde{\chi}_1^0) > 20$ GeV. The use of the new TC-LVT algorithm significantly improved the sensitivity of the analysis to signal models with small mass splitting, and it allows the exclusion of bottom squark masses up to $m_{\tilde{b}_1} = 660$ GeV for mass splitting of $\Delta m(\widetilde{b}_1, \widetilde{\chi}_1^0) = 10$ GeV. The analysis is not sensitive to mass splitting of $\Delta m(\widetilde{b}_1, \widetilde{\chi}_1^0) < 5$ GeV, which are not investigated.

Figure 6.11 shows the best expected limits arising from the combined SR-AB fit and the SRC. The plot highlights the specific contribution of SRC to the exclusion limit: it is by far the most sensitive SR for mass splitting $\Delta m(\widetilde{b}_1, \widetilde{\chi}_1^0) < 50$ GeV, which was the design target.

Finally, Figure 6.12 shows the 95% CL observed exclusion limits on the model cross section.

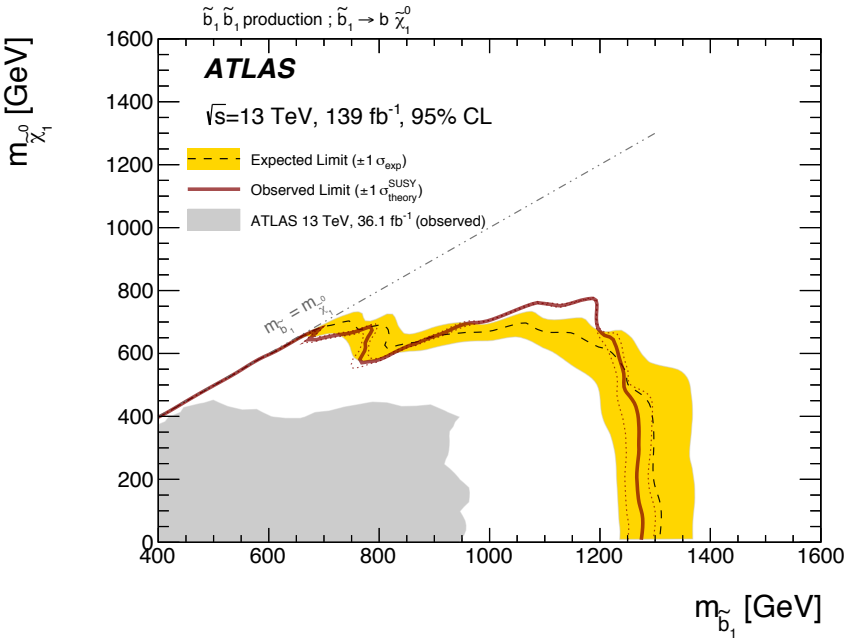

Figure 6.9: Exclusion limit at 95% CL on the masses of $\widetilde{b}_1$ and $\widetilde{\chi}_1^0$. The limit is shown in the $(m_{\widetilde{b}_1}, m_{\widetilde{\chi}_1^0})$ plane. The dashed black line corresponds to the expected exclusion, with its $\pm 1\sigma$ uncertainty band in yellow. The solid red line is the mean observed limit for the central value of the signal cross-section, with its $\pm 1\sigma$ uncertainty arising from $\pm 1\sigma$ variation of the cross-section represented by the red dotted lines. The region excluded by the previous analysis [176] is shaded in light gray.

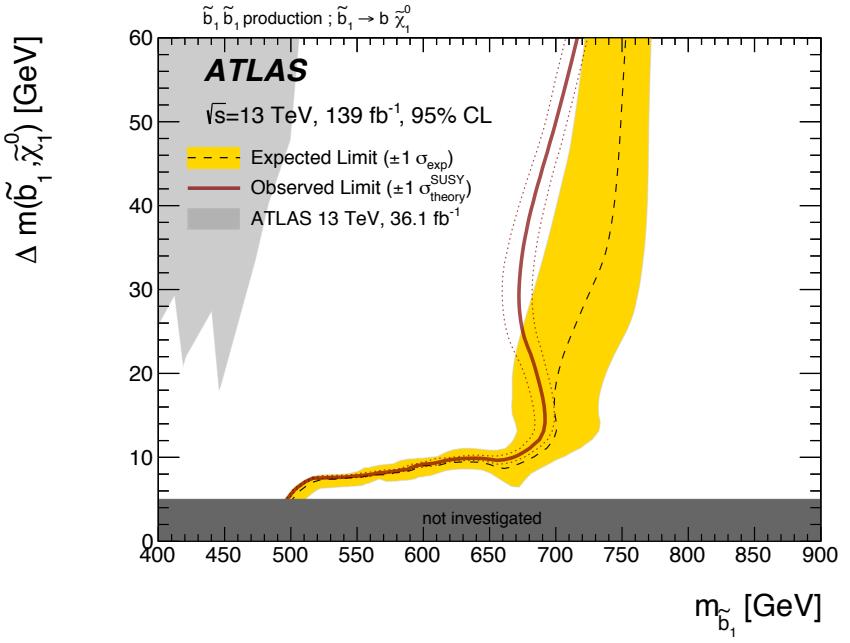

Figure 6.10: Exclusion limit at 95% CL on the masses of $\widetilde{b}_1$ and $\widetilde{\chi}_1^0$. The limit is shown in the $(m_{\widetilde{b}_1}, \Delta m(\widetilde{b}_1, \widetilde{\chi}_1^0))$ plane. The dashed black line corresponds to the expected exclusion, with its $\pm 1\sigma$ uncertainty band in yellow. The solid red line is the mean observed limit for the central value of the signal cross-section, with its $\pm 1\sigma$ uncertainty arising from $\pm 1\sigma$ variation of the cross-section represented by the red dotted lines. The region excluded by the previous analysis [176] is shaded in light gray. The region with $\Delta m(\widetilde{b}_1, \widetilde{\chi}_1^0) < 5$ GeV is not investigated by this analysis, and it is shaded in dark gray.

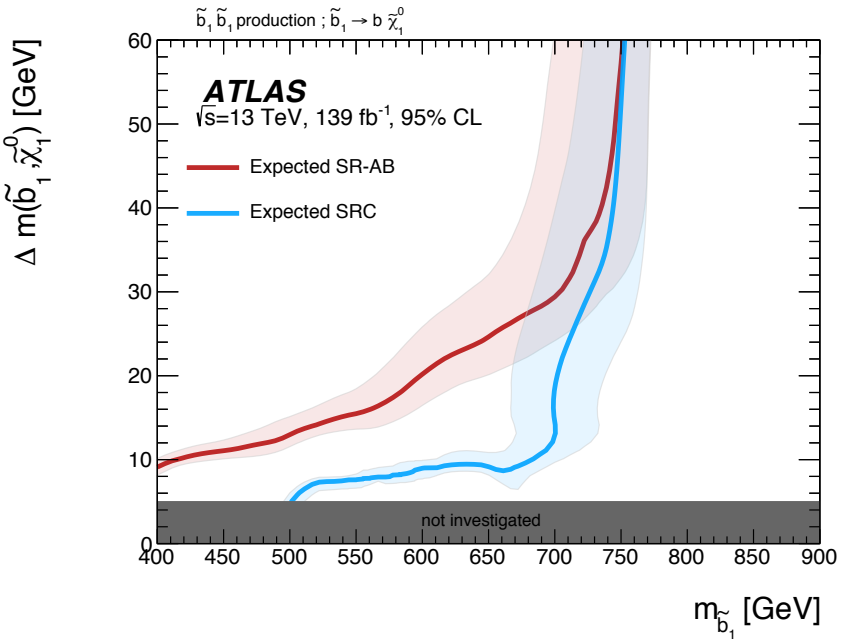

Figure 6.11: Expected exclusion limits at 95% CL on the masses of $\widetilde{b}_1$ and $\widetilde{\chi}_1^0$ for SR-AB and SRC combined fits. The limits are shown in the $(m_{\widetilde{b}_1}, \Delta m(\widetilde{b}_1, \widetilde{\chi}_1^0))$ plane. The red (blue) solid line refers to the mean expected value for SR-AB (SRC), while the band refers to the $\pm 1\sigma$ uncertainty. The region with $\Delta m(\widetilde{b}_1, \widetilde{\chi}_1^0) < 5$ GeV is not investigated by this analysis, and it is shaded in dark gray.

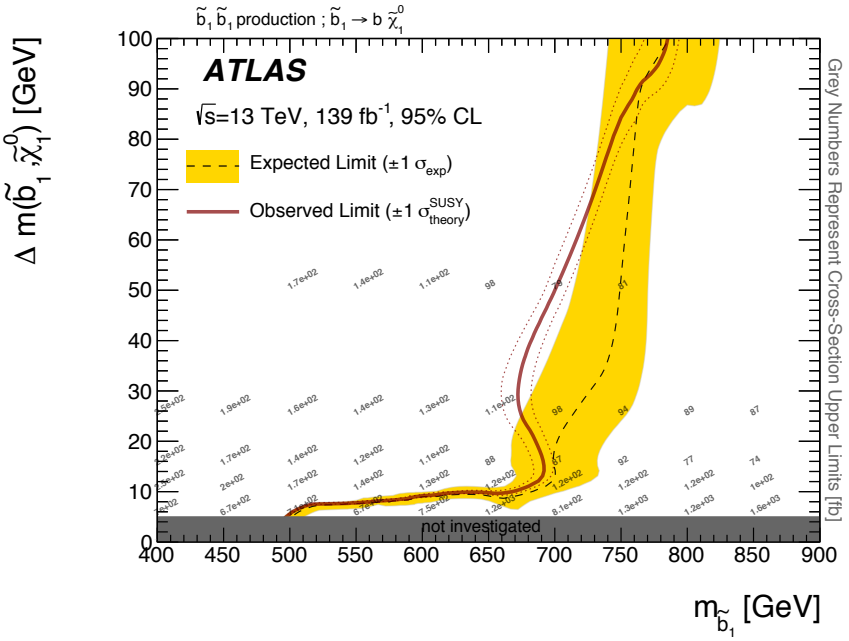

Figure 6.12: Exclusion limit at 95% CL on the masses of $\widetilde{b}_1$ and $\widetilde{\chi}_1^0$. The limit is shown in the $(m_{\widetilde{b}_1}, \Delta m(\widetilde{b}_1, \widetilde{\chi}_1^0))$ plane. The dashed black line corresponds to the expected exclusion, with its $\pm 1\sigma$ uncertainty band in yellow. The solid red line is the mean observed limit for the central value of the signal cross-section, with its $\pm 1\sigma$ uncertainty arising from $\pm 1\sigma$ variation of the cross-section represented by the red dotted lines. The region with $\Delta m(\widetilde{b}_1, \widetilde{\chi}_1^0) < 5$ GeV is not investigated by this analysis, and it is shaded in dark gray. The grey numbers report the 95% CL observed exclusion limits on the model cross-section.

6.3 Summary

This Chapter has presented the results of the searches for direct pair production of bottom squarks in final states with large $E_{\mathrm{T}}^{\mathrm{miss}}$ and b-jets. The search has been based on the regions defined in Chapter 5, and it exploits 139 fb^{-1} of pp collision at a centre-of-mass energy of $\sqrt{s} = 13$ TeV collected by the ATLAS experiment at the LHC between 2015 and 2018. The search has not observed any significant excess over the SM predictions. Limits on the visible cross-section have been placed, in a range from 0.13 fb and 0.37 fb. Stringent exclusion limits on specific BSM RPC SUSY scenarios have been set, where the bottom squark decays into a b-quark and the lightest neutralino. In particular, the analysis significantly improves the sensitivity to compressed scenarios where $\Delta m(\widetilde{b}_1, \widetilde{\chi}_1^0) \leq 25$ GeV by applying dedicated techniques to reconstruct the secondary vertices from low-p_T b-hadrons. Such techniques have allowed the exclusion of bottom masses up to 660 GeV for $\Delta m(\widetilde{b}_1, \widetilde{\chi}_1^0) = 10$ GeV.

This analysis has been able to largely improve the limits set by the previous 36.1 fb^{-1} thanks both to the increased integrated luminosity and the use of the TC-LVT algorithm.

Conclusions

The Standard Model of particle physics is the most successful theoretical framework for describing the fundamental particles and their interactions. Its success has been supported by decades of experimental confirmation, from the discovery and precise measurement of the electroweak W and Z bosons to the discovery of quarks and gluons. Neutrino physics observations, such as neutrino oscillations, can be accounted for by including the Pontecorvo-Maki-Nakagawa-Sakata [32] (PMNS) matrix in the SM. The most recent confirmation of the SM is the discovery of the Higgs boson by the ATLAS and CMS [7, 8], which is needed to explain the origin of the mass of the particles.

Despite its numerous successes, the SM is not the ultimate particle physics theory. Observations from cosmological experiments [24, 26, 27] suggest the existence of matter not accounted for by the SM. Theoretical motivations [34] also suggest that additional particles are needed to solve the naturalness problem of the SM. These issues can be addressed by defining a supersymmetric extension of the SM [23] (SUSY). If discovered, the additional particles introduced by SUSY would solve the naturalness problem and provide a good candidate for explaining the dark matter (DM).

The core of this thesis focuses on the searches for the direct pair-production of the third-generation bottom squarks, $\widetilde{b}_1$. The search is based on 139 fb^{-1} of proton-proton collisions data at a centre-of-mass energy of $\sqrt{s} = 13$ TeV delivered by the LHC and collected by the ATLAS detector. The bottom squarks are introduced in a natural SUSY model, and they decay according to a R-parity conserving model into bottom quarks and the LSP with a 100% BR. For the LSP to be the particle to describe the DM observed in the Universe, its relic density should be comparable with the observed value obtained by the Planck collaboration [27]. To constrain the LSP relic density, co-annihilation models [46] are considered. These impose that the $\widetilde{b}_1$ and the LSP are almost mass degenerate, resulting in final states with low-p_T b-hadrons.

A novel algorithm developed to detect those low-p_T b-hadrons, and its performance, is described in Chapter 4 and it is the first important result of this thesis. The b-hadrons are reconstructed by only exploiting the tracks present in the event, allowing one to extend the already excellent b-tagging performance of the ATLAS detector towards lower b-hadron p_T. The calibration studies of the algorithm demonstrate that other analyses, even outside the SUSY area, can benefit of the extended sensitivity provided by this low-p_T b-tagging algorithm.

The major results of this thesis are reported in Chapter 5, where the analysis strategy targeting the decay of bottom squarks into bottom quark and the LSP is defined, and Chapter 6, where the statistical interpretation of the measurement is presented. The analysis strategy is designed to target the compressed decay of the bottom squarks, which results in the presence of low-p_T b-hadrons; the analysis therefore benefits from the novel low-p_T b-tagging algorithm. The results for the model-dependent statistical interpretation largely improves the measurement from the previous iteration of the analysis [176], and sets the best exclusion limits in the search for direct pair-production of bottom squarks excluding up to $m_{\tilde{b}_1} = 660$ GeV for mass splitting of $\Delta m(\tilde{b}_1, \tilde{\chi}_1^0) = 10$ GeV. Upper limits on the visible cross section at 95% CL have been set and range between 0.11 fb^{-1} and 0.37 fb^{-1}, depending on the signal region [3].

The limits set by the analysis presented in this thesis are obtained by the analysis of the full Run 2 dataset recorded by the ATLAS detector between 2015 and 2018, and they will remain the best results until at least well into Run 3.

Electron Trigger Efficiency and Scale Factors

A

To gain the ATLAS authorship, the Author of this thesis significantly contributed to the ATLAS electron and photon (e/γ) trigger group. This appendix summarises the work done to measure the trigger electron efficiencies in data and Monte Carlo (MC) simulations for the Run 2 data recorded between 2015 and 2017. The efficiencies are measured for two sets of isolation operating point (OP). Scale factors (SFs) are derived to correct the electron trigger efficiency simulations to the measured efficiencies in data. The efficiency measurements performed with the e/γ trigger group were used by any ATLAS analysis using SF, and directly contributed to Ref. [1].

Electron trigger menu in Run 2

Section 3.3 presents the ATLAS trigger sequences used by the analysis presented in this thesis. This Appendix focuses on the electron triggers defined in the ATLAS trigger menu, namely the single-electron trigger, di-electron trigger and multi-lepton trigger chains used for data taking during Run 2. Accordingly to the naming convention presented in Equation 3.5, the electron trigger chains are named following this nomenclature:

- *HLT_NeX*: indicates a High-Level Trigger chain, requiring the presence of N electrons with a lower transverse energy threshold of X GeV. For the multi-lepton trigger, e may be replaced by *mu* or *tau* to indicate that a muon or tau is required in the event.
- *lhvloose, lhloose, lhmedium, lhtight*: *lh* indicates that a likelihood-based identification [133] is used. The following naming describes the cut on the *lh* discriminant, increasing from *vloose*, or very loose, to *tight*. Each tighter identification category selects a subset of events from the previous looser category.
- *nod0*: this indicates that no selection on the transverse impact parameter is applied. The 2015 triggers are the only ones with a selection on d_0.
- *ivarloose*: this indicates that track-based isolation requirements are applied to the chain.

– *Combined triggers*: High-Level Trigger (HLT) chains can be defined by joining different individual trigger legs. The combined chains are joined by a _ for a logical AND (e. g. in the multi-lepton triggers), or by a _OR to indicate a logical OR requirement between the chains (e. g. in the single electron triggers).

The single electron chain is referred to as *single electron trigger combination* in the following, unless a specific chain is used.
The time evolution from 2015 to 2018 of the unprescaled electron trigger menu is presented in Table A.1. The increasing instantaneous luminosity delivered by the LHC and the higher pileup dictated the tightening of the trigger selections to mantain the trigger rate at acceptable levels. The transverse impact parameter selections were dropped from 2016. Such requirements are kept during the offline selection, but introduced inefficiencies in the online selection due to their poor resolution. Another improvement was the introduction of track-based isolation requirements at L1 and HLT to improve background rejection and rate reduction. In 2017 a new ringer algorithm [210] was introduced to improve the fast calorimeter selection. The algorithm exploits the conic shape of an electron-induced shower by building successive rings in the calorimeter. Such rings are then used to create a vector of discriminating variables which are fed into a neural network classifier.

Electron efficiency measurements

The aim of this work is to measure the efficiency ϵ_{trig} for each electron trigger chain presented in Table A.1. The electron trigger efficiency is measured with respect to each offline identification and isolation OP. Electron triggers can be used by any SM measurement or new physics search involving the presence of electrons in the SR or CR. The determination of the electron trigger efficiency, which contributes to the total electron efficiency, plays a major role within the ATLAS experiment, as it is needed to compute the total electron efficiency according to:

$$\epsilon_{\text{total}} = \epsilon_{\text{offline}} \times \epsilon_{\text{trig}} = \left(\frac{N_{\text{offline}}}{N_{\text{all}}}\right) \times \left(\frac{N_{\text{trig}}}{N_{\text{offline}}}\right) \tag{A.1}$$

where N_{all} is the total number of produced electrons; N_{offline} is the number of isolated, identified and reconstructed offline electron candidates; and N_{trig} is the number of triggered electron candidates. The $\epsilon_{\text{offline}}$ term in Equation A.1 can be factorised as the product of the efficiencies for each step of the electron offline identification according to:

$$\epsilon_{\text{offline}} = \epsilon_{\text{EMclus}} \times \epsilon_{\text{reco}} \times \epsilon_{\text{ID}} \times \epsilon_{\text{iso}}, \tag{A.2}$$

where: ϵ_{EMclus} is the fraction of prompt electrons that produce a candidate EM cluster in the calorimeters, and it is estimated by matching clusters to electrons produced at generator level using MC information only; ϵ_{reco}, ϵ_{ID}, ϵ_{iso} are the reconstruction, identification and isolation efficiencies, respectively. The chains which do not require any isolation do not include the isolation efficiency term in Equation A.2.

Table A.1: Evolution of the electron trigger menu for data taking during Run 2.

Year	Trigger	Chain
2015	single electron	HLT_e24_lhmedium_OR_e60_lhmedium_ OR_e120_lhloose
	di-electron	HLT_2e12_lhloose
	multi-electron	HLT_e17_lhloose_2e9_lhloose
	combined	HLT_e17_lhloose_mu14 HLT_e7_lhloose_mu24 HLT_2e12_lhloose_mu10 HLT_e12_lhloose_2mu10
2016	single electron	HLT_e26_lhtight_nod0_ivarloose_OR _e60_lhmedium_nod0_OR_e140_lhloose_nod0
	di-electron	HLT_2e17_lhvloose_nod0
	multi-electron	HLT_e17_lhloose_nod0_2e9_lhloose_nod0
	combined	HLT_e17_lhloose_nod0_mu14 HLT_e24_lhmedium_nod0_mu8 HLT_2e12_lhloose_nod0_mu10 HLT_e12_lhloose_nod0_2mu10
2017	single electron	HLT_e26_lhtight_nod0_ivarloose_OR _e60_lhmedium_nod0_OR_e140_lhloose_nod0
	di-electron	HLT_2e17_lhvloose_nod0 HLT_2e24_lhvloose_nod0
	multi-electron	HLT_e24_lhvloose_nod0_2e12_lhvloose_nod0
	combined	HLT_e17_lhloose_nod0_mu14 HLT_e26_lhmedium_nod0_mu8 HLT_2e12_lhloose_nod0_mu10 HLT_e12_lhloose_nod0_2mu10 HLT_e7_lhloose_nod0_mu14
2018	single electron	HLT_e26_lhtight_nod0_ivarloose_OR _e60_lhmedium_nod0_OR_e140_lhloose_nod0
	di-electron	HLT_2e17_lhvloose_nod0 HLT_2e24_lhvloose_nod0
	multi-electron	HLT_e24_lhvloose_nod0_2e12_lhvloose_nod0
	combined	HLT_e17_lhloose_nod0_mu14 HLT_e26_lhmedium_nod0_mu14 HLT_2e12_lhloose_nod0_mu10 HLT_e12_lhloose_nod0_2mu10 HLT_e7_lhmedium_nod0_mu24 HLT_e12_lhloose_nod0_e24_lhmedium_nod0 HLT_e17_lhmedium_nod0_tau29

To measure the trigger efficiency a clean and unbiased sample of electrons needs to be first obtained in data. The data sample is selected by using the lowest unprescaled single electron trigger for each year reported in Table A.1. The clean, unbiased sample is obtained by exploiting the *tag-and-probe* method, sketched in Figure A.1, to select electrons coming from the $Z \to ee$ decay. The decay is reconstructed by requiring the presence of two

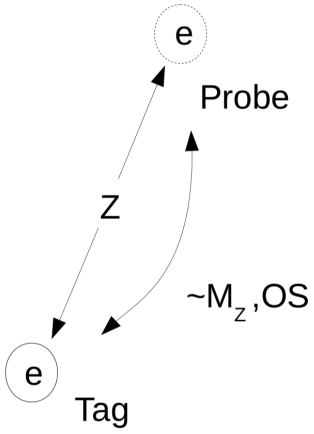

Figure A.1: Sketch of the-tag-and-probe method to identify $Z \to ee$ electrons. The two electrons are required to have opposite charge, and they are matched if their invariant mass is close to the Z boson mass, M_Z.

electrons with opposite electric charge. One of the two electrons, the *tag*, is required to satisfy the following tight selection criteria:

- *Trigger-matching*: the tag electron is required to be angularly matched to the online object which fired the single electron trigger.
- *Transverse energy*: the transverse energy of the tagged electron is required to be 1 GeV larger than the lowest transverse energy threshold of the single electron trigger. This requirement is needed to ensure a constant trigger efficiency with respect to the offline identification OP.
- *Offline identification*: the tag electron is required to satisfy offline identification criteria. Three different identification+isolation OPs are used, to compute systematic variations on the trigger efficiency: `Tight`, `Tight` with isolation and `Medium` with isolation.

Once the tag electron is identified, the second electron is classified as *probe* if the invariant mass of the di-electron system is within a mass window from the Z boson mass, M_Z. Three mass windows are considered, to evaluate the systematic uncertainties on the efficiency measurement: $M_Z \in [80, 100]$ GeV, $M_Z \in [75, 105]$ GeV and $M_Z \in [70, 110]$ GeV. The probe electron is then required to have a transverse energy larger that 4 GeV and to satisfy identification and isolation OPs. From Equation A.1, the trigger efficiency can be computed as the number of probe electrons firing the trigger chain for a given offline selection divided by the total number of probes satisfying the same offline selection, in terms of reconstruction, identification and isolation OPs.
Multi-object trigger efficiencies are obtained by measuring separately the individual efficiency of each single object. As can be seen in Table A.1, multi-object triggers tend to have lower E_T threshold as they fire the triggers at lower rates. The single-object components of the triggers need to be prescaled in order to keep the trigger rate at acceptable levels.

The data which are lost due to the trigger prescale are recovered by reprocessing offline events that were recorded by other triggers and which would have satisfied the low-E_T electron trigger requirements. The same procedure is followed to measure the electron trigger efficiency for MC simulated events.

To gain ATLAS authorship, the Author of this thesis performed the electron trigger efficiency measurements for all the trigger chains reported in Table A.1 from 2015 to 2017 on the set of isolation OP listed in Table A.2. In 2018 a new set of isolation OP was

Table A.2: Isolation OPs [146] for the 2015-2017 data taking.

Operating point	$E_{\mathrm{T,cone}}^{\mathrm{isol}}$ ($\Delta R = 0.2$)	$p_{\mathrm{T,var}}^{\mathrm{isol}}$ ($R_{\mathrm{max}} = 0.2$)	Total ϵ_{iso}
Loose (Track Only)	-	$\epsilon_{\mathrm{iso}} = 99\%$	99%
Loose	$\epsilon_{\mathrm{iso}} = 99\%$	$\epsilon_{\mathrm{iso}} = 99\%$	98%
Gradient	$\epsilon_{\mathrm{iso}} = 0.1143 \times p_{\mathrm{T}} + 92.14\%$	$\epsilon_{\mathrm{iso}} = 0.1143 \times p_{\mathrm{T}} + 92.14\%$	90(99)% at 25(60) GeV
Gradient (Loose)	$\epsilon_{\mathrm{iso}} = 0.057 \times p_{\mathrm{T}} + 95.57\%$	$\epsilon_{\mathrm{iso}} = 0.057 \times p_{\mathrm{T}} + 95.57\%$	95(99)% at 25(60) GeV
Fix (Loose)	$E_{\mathrm{T,cone}}^{\mathrm{isol}}/p_{\mathrm{T}} < 0.20$	$p_{\mathrm{T,var}}^{\mathrm{isol}}/p_{\mathrm{T}} < 0.15$	-
Fix (Tight)	$E_{\mathrm{T,cone}}^{\mathrm{isol}}/p_{\mathrm{T}} < 0.06$	$p_{\mathrm{T,var}}^{\mathrm{isol}}/p_{\mathrm{T}} < 0.06$	-
Fix (Tight, Track Only)	-	$p_{\mathrm{T,var}}^{\mathrm{isol}}/p_{\mathrm{T}} < 0.06$	-
Fix (Calo Only)	$E_{\mathrm{T,cone}}^{\mathrm{isol}} < 3.5$ GeV	-	-
Fix (Track $R_{\mathrm{max}} = 0.4$)	$E_{\mathrm{T,cone}}^{\mathrm{isol}}/p_{\mathrm{T}} < 0.11$	$p_{\mathrm{T,var}}^{\mathrm{isol}}/p_{\mathrm{T}} < 0.06$	-

reoptimized, and their definition is summarised in Table A.3. As a consequence, the Author of this thesis performed the measurement of the trigger efficiencies for the single- and di-electron triggers from 2015 to 2017 from Table A.1. Figure A.2 shows the single electron

Table A.3: Reoptimized isolation OPs [132] for the 2015-2018 data taking.

Working point	Calorimeter isolation	Track isolation
Gradient	$\epsilon = 0.1143 \times p_{\mathrm{T}} + 92.14\%$ (with $E_{\mathrm{T}}^{\mathrm{cone20}}$)	$\epsilon = 0.1143 \times p_{\mathrm{T}} + 92.14\%$ (with $p_{\mathrm{T}}^{\mathrm{varcone20}}$)
HighPtCaloOnly	$E_{\mathrm{T}}^{\mathrm{cone20}} < \max(0.015 \times p_{\mathrm{T}}, 3.5$ GeV)	-
Loose	$E_{\mathrm{T}}^{\mathrm{cone20}}/p_{\mathrm{T}} < 0.20$	$p_{\mathrm{T}}^{\mathrm{varcone20}}/p_{\mathrm{T}} < 0.15$
Tight	$E_{\mathrm{T}}^{\mathrm{cone20}}/p_{\mathrm{T}} < 0.06$	$p_{\mathrm{T}}^{\mathrm{varcone20}}/p_{\mathrm{T}} < 0.06$

trigger combination efficiency for 2016 data and MC for two isolation OP as function of the probe electron's E_T and η. The data and MC distribution are overall in good agreement, except for a few regions: in the E_T-dependent efficiency there is a bit of disagreement in the turn-on region; in the η-dependent efficiency there is a larger disagreement in the transition region, $1.37 < |\eta| < 1.5$, where a larger amount of material is present to service the detector. The transition region does not raise concern as that region is usually not investigated by analyses.

Background subtraction The background electron contribution, i. e. the prompt electrons not coming from the $Z \to ee$ decay, is estimated using the invariant mass of the tag-and-probe pair m_{ee} as discriminating variable. The background template is selected from probe electrons by inverting the identification and isolation requirement, to minimize the signal electron contribution, i. e. the prompt electrons coming from the $Z \to ee$ decay. The contribution due to the remaining signal electrons is estimated from MC simulations. The normalisation of the background template is determined by a sideband method, selecting the electrons in a band above the Z mass peak, in a range 120 GeV $< m_{ee} <$ 250

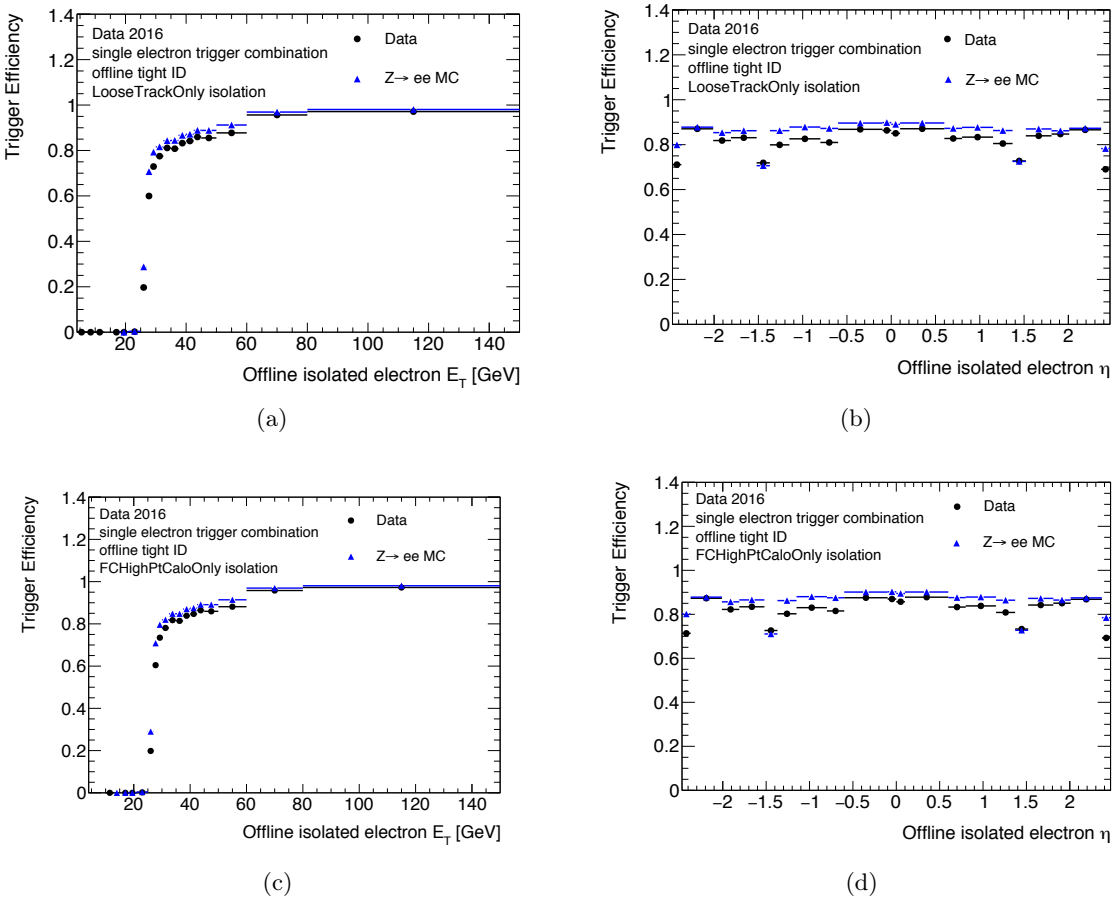

Figure A.2: Electron efficiencies in 2016 data for the single electron trigger combination from Table A.1. The top-row plots refer to the efficiencies calculated for the `LooseTrackOnly` isolation OP, while the bottom-row plots refer to the `FCHighPtCaloOnly` isolation OP. The plots on the left display the efficiency as function of E_T. The plots on the right show the efficiency as function of η, requiring E_T to be larger than the trigger threshold plus 1 GeV. No background subtraction is applied for these plots. The error bar show binomial uncertainties.

GeV. The same template is used to estimate the m_{ee} distribution in both the numerator and denominator, but the numerator, for which the signal electron contribution is more important, is defined by requiring same-sign electrons. Figure A.3 shows the invariant mass distribution in data for the probe electrons. Systematic uncertainties are determined by varying the background template. Figure A.4 shows the single electron trigger combination efficiency in data as function of the probe electron E_T for the four years of data taking after the background subtraction procedure is applied. The inefficiency observed in 2016 is due to too stringent online identification optimisation with respect to the previous offline selection criteria. The efficiency improvements in 2017-2018 are due to a better online selection, involving looser track-calorimeter matching, removal of likelihood-only calorimeter selection, with the final offline selection for Run 2.

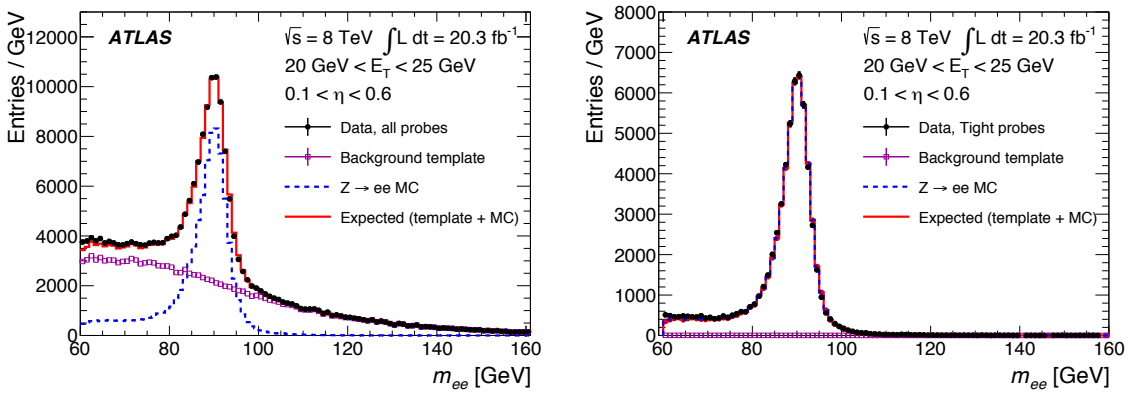

(a) (b)

Figure A.3: Invariant mass of the di-electron system in data and MC in the 20 GeV $< E_T <$ 25 GeV, $0.1 < \eta < 0.6$ bin for (a) EM clusters with matching tracks reconstructed as electron and (b) for the probe electron passing the `Tight` identification OP. The background template is normalized in the range 100 GeV $< m_{ee} <$ 250 GeV. The $Z \to ee$ MC simulation is scaled to match the estimated signal in the Z-mass window. The di-electron system is selected by using the tag-and-probe method, with the tag electron satisfying the `Medium` identification OP. Images taken from Ref. [211].

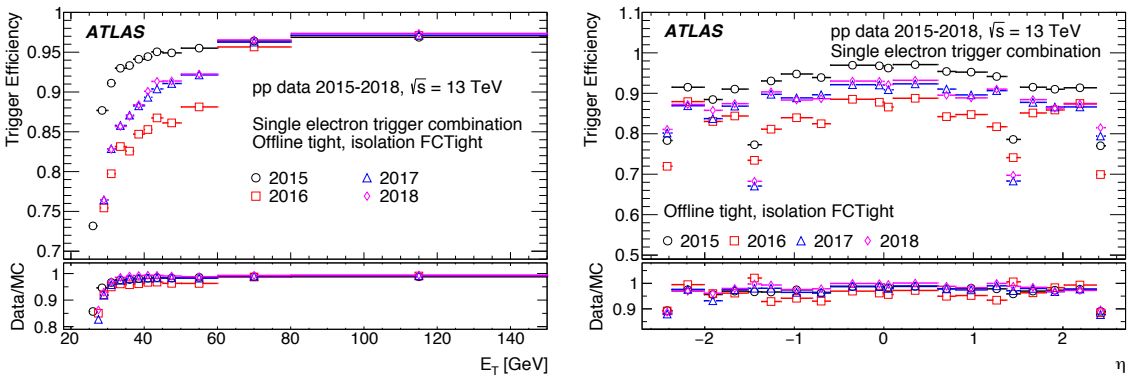

(a) (b)

Figure A.4: Evolution of the single-electron trigger combination efficiency as a function of the offline electron (a) E_T and (b) η during Run 2. The trigger chain definition for each year is reported in Table A.1. The efficiency is measured with respect to the offline tight identification and `FCTight` isolation OP. The ratios of data to MC simulation efficiencies are shown in the inset plot. The background subtraction is applied for these plots. The error bars indicate the total uncertainties. For (b), only offline electron candidates with E_T at least 1 GeV above the corresponding trigger threshold are used. Image taken from Ref. [1].

Scale Factors The ratio of efficiencies calculated for $Z \to ee$ events for both data and MC simulations, referred to as scale factor, is calculated as a 2D map and it is function of the electron E_T and η. The background subtraction procedure is applied to the efficiencies. Scale factors are used to correct the mis-modelling of the electron trigger efficiency MC simulations. For each (E_T, η) bin the scale factor mean value is calculated as the arithmetic mean of the systematic variations on the background template, tag identification OP and

Z mass window. Similarly, the statistical uncertainty for each (E_T, η) bin is calculated as the arithmetic mean of the statistical uncertainties for each variation. The systematic uncertainties on the efficiency are taken as the standard deviation of the variations with respect to the arithmetic mean. The 2D scale factor maps and their total error for the `FCHighPtCaloOnly` isolation OP from Table A.3 are shown in Figure A.5 for the single electron trigger chain measured with the 2016 data. Overall the scale factors are close to

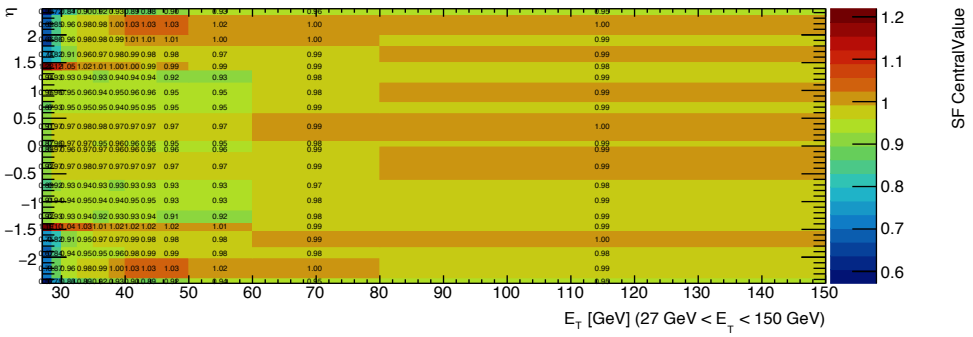

(a)

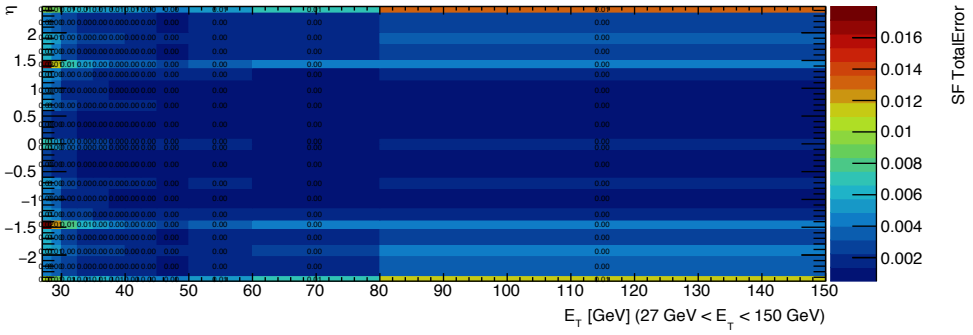

(b)

Figure A.5: 2D map showing the scale factor corrections (a) mean value and (b) total uncertainty. The maps are binned by E_T and η. The single electron trigger combination for the 2016 data is considered. The efficiencies used in the derivation of the scale factors are measured with respect to the `FCHighPtCaloOnly` isolation OP. Background subtraction is applied for these plots.

unity in the majority of the bins, with the anticipated exceptions of the transition region and the end-caps. Also the total relative uncertainty is below 1% of the measured value across most of the bins.

Summary

This Appendix summarises the work conducted by the Author of this thesis to gain the ATLAS authorship. The evolution of the ATLAS electron trigger menu during the full Run 2 data taking is summarised, and the tag-and-probe methodology for measuring the electron trigger efficiency is described. The scale factors correction obtained during this

work were distributed to the whole ATLAS collaboration, and are applied in a vast number of analyses exploiting any electron trigger. These efforts converged in the paper in Ref. [1].

Appendix - Additional Plots

B

Preliminary Plots

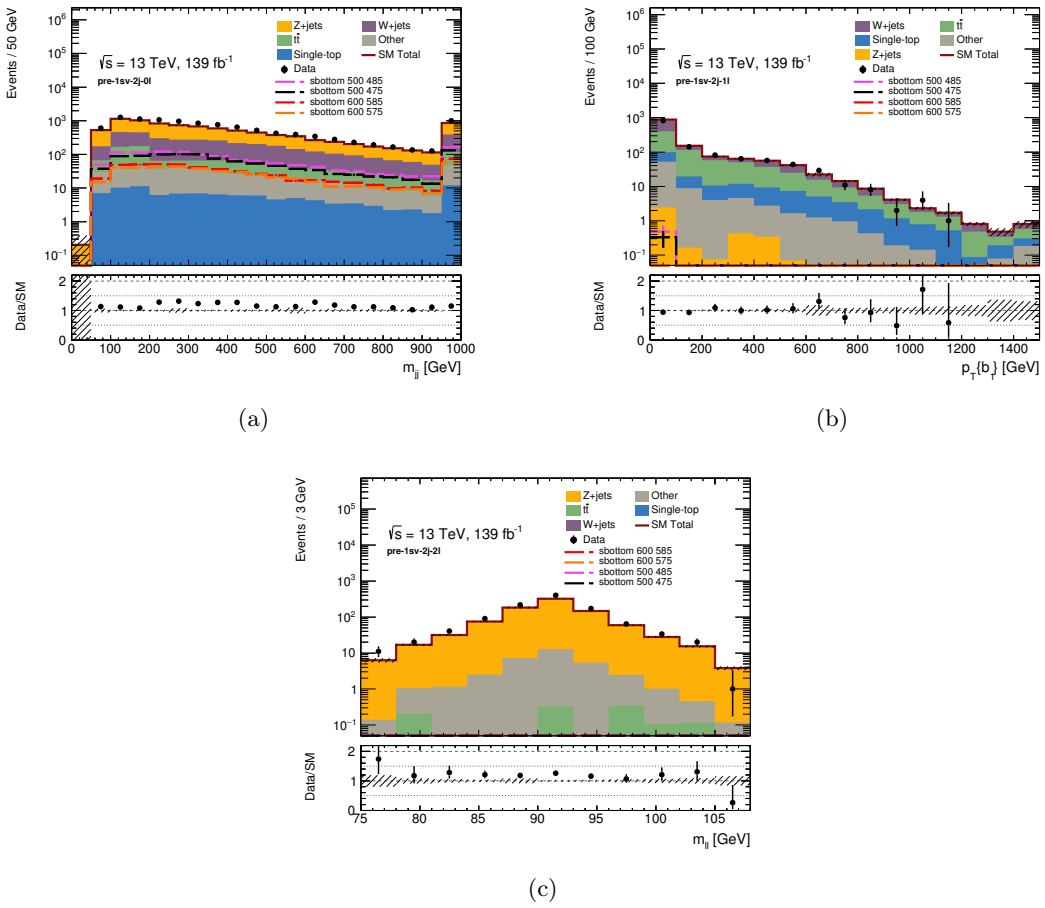

Figure B.1: Distribution of (a) m_{jj} for pre-1sb-2j-0l, (b) $\mathrm{p_T^{b_1}}$ for pre-1sb-2j-1 l, (c) $m_{\ell\ell}$ for pre-1sb-2j-2l. The four signal benchmark points are shown, and their yield in 1L and 2L regions is negligible as expected. The data yields are not shown in those bins where the expected ratio between the signal and background is larger than 10 % for any of the signal considered. The plots do not include the background normalisation factors derived as part of the fit procedure described in Section 5.3, and only the statistical uncertainties are considered. The plots of channels where at least one TC-LVT vertex is required do not include the TC-LVT scale factor. The inset plot shows the ratio between the data and the MC prediction.

N-1 Plots

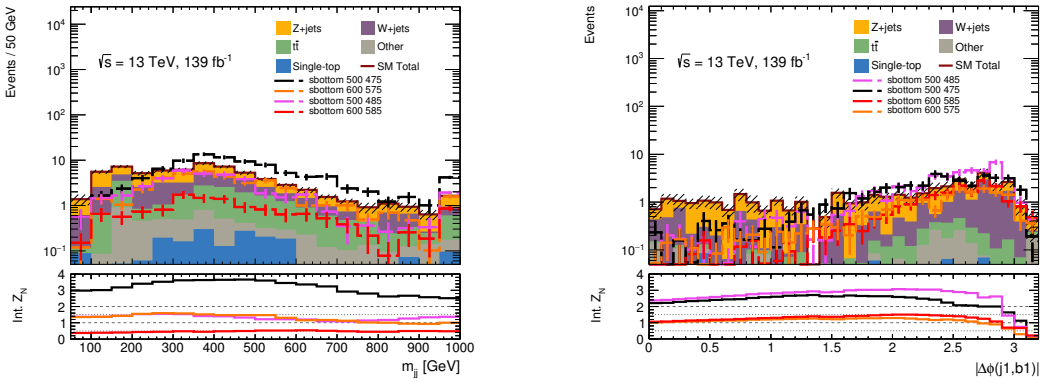

(a)

(b)

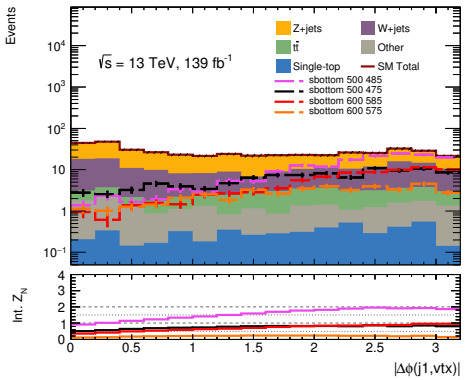

(c)

Figure B.2: N-1 distribution of signal and SM background processes for (a) m_{jj} in SRC-2b, (b) $\Delta\phi(j1, b1)$ in SRC-1b1v and (c) $\Delta\phi(j1, vtx)$ in SRC-0b1v. The four signal benchmark points are shown. The plots do not include the background normalisation factors derived as part of the fit procedure described in Section 5.3, and only the statistical uncertainties are considered. The plots of channels where at least one TC-LVT vertex is required do not include the TC-LVT scale factor. The inset plot shows the significance distribution for each benchmark mass point.

2ℓ Control Regions

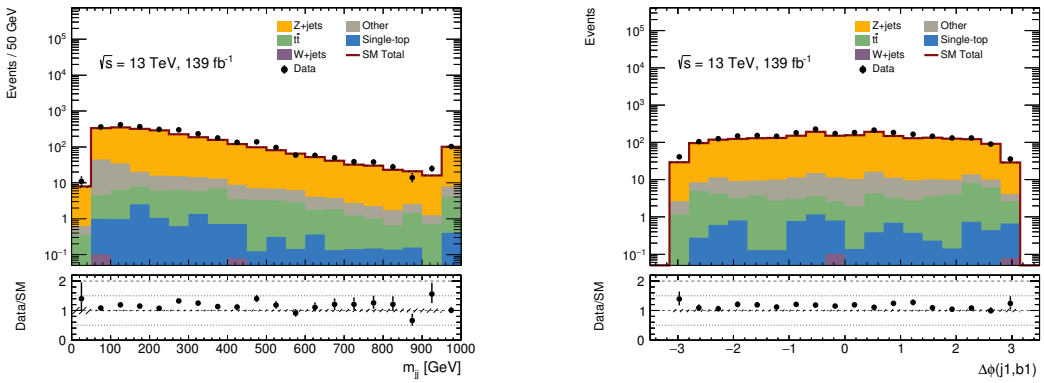

(a) (b)

Figure B.3: Distribution of data and MC prediction for (a) m_{jj}, (b) $\Delta\phi(j1, b1)$ for the common pre-selection for the Z+jets control regions. The plots do not include the background normalisation factors derived as part of the fit procedure described in Section 5.3, and only the statistical uncertainties are considered. The plots of channels where at least one TC-LVT vertex is required do not include the TC-LVT scale factor. The inset plot shows the ratio between the data and the MC prediction.

1ℓ Control Regions

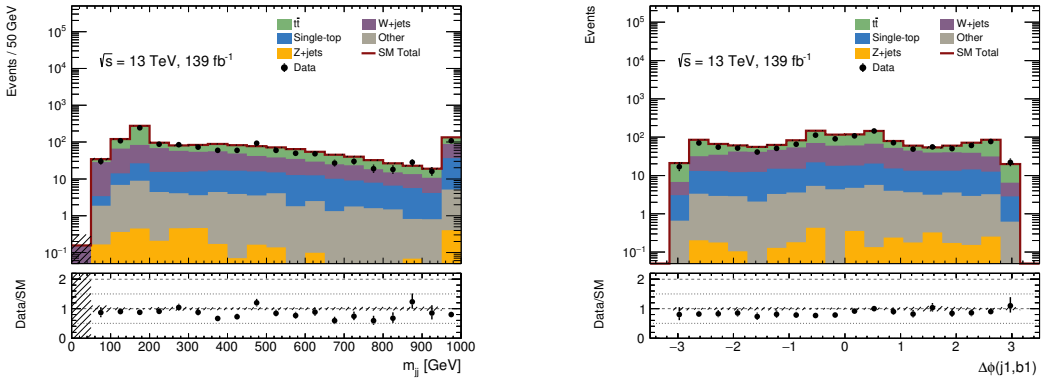

(a) (b)

Figure B.4: Distribution of data and MC prediction for (a) m_{jj} and (b) $\Delta\phi(j1, b1)$ for the common pre-selection for the W+jets and Top control regions. The plots do not include the background normalisation factors derived as part of the fit procedure described in Section 5.3, and only the statistical uncertainties are considered. The plots of channels where at least one TC-LVT vertex is required do not include the TC-LVT scale factor. The inset plot shows the ratio between the data and the MC prediction.

List of Acronyms

ALICE A Large Ion Collider Experiment

AMSB anomaly-mediated SUSY breaking

ATLAS A Toroidal LHC ApparatuS

BDT boosted decision tree

BR branching ratio

BSM beyond Standard Model

CERN European Organization for Nuclear Research

CKKW Catani-Krauss-Kuhn-Webber

CKM Cabibbo-Kobayashi-Maskawa

CL confidence level

CMB cosmic microwave background

CMS Compact Muon Solenoid

CP Charge-Parity

CP cluster processor

CPU Central Processing Unit

CR Control Region

CSC cathode strip chamber

CTP Central Trigger Processor

DGLAP Dokshitzer-Gribov-Lipatov-Altarelli-Parisi

DQ Data Quality

DL1 neural network algorithm

DM dark matter

ECAL electromagnetic calorimeter

EM electromagnetic

EW electroweak interaction

EWSB electroweak symmetry breaking

FCAL forward calorimeter

FE Front-End

FSR Final State Radiation

FTK Fast TracKer

GRL Good Run List

GSF Gaussian Sum Filter

HCAL hadronic calorimeter

HEC hadronic end-cap

HLT High-Level Trigger

IBL insertable B-layer

ID Inner Detector

IP interaction point

ISR Initial State Radiation

JEP Jet/Energy-sum processor

JER Jet Energy Resolution

JES Jet Energy Scale

JVT Jet Vertex Tagger

L1 Level-1

L1Calo L1 calorimeter

L1Muon L1 muon

L1Topo level-1 topological processor

LAr liquid argon

LH likelihood

LHC Large Hadron Collider

LHCb Large Hadron Collider beauty

LHCf Large Hadron Collider forward

Linac2 Linear Accelerator 2

LO leading-order

LSP lightest supersymmetric particle

MC Monte Carlo

MDT monitored drift tube

ME Matrix Element

MIP minimum-ionising particle

MLM Michelangelo L. Magnano *et al.*

MoEDAL Monopole & Exotics Detector At the LHC

MS muon spectrometer

MSSM minimal supersymmetric standard model

MV2 multivariate algorithm

NEWT new tracking reconstructor

NF normalisation factor

NLO next-to-leading-order

NN neural network

NNLL next-to-next-to-leading-logarithmic

NNLO next-to-next-to-leading-order

NP nuisance parameter

OP operating point

OR overlap removal

PDF parton density function

PFlow particle flow

PMNS Pontecorvo-Maki-Nakagawa-Sakata

pMSSM phenomenological MSSM

PS Parton Shower

PS Proton Synchrotron

PSB Proton Synchrotron Booster

PU Processing Unit

PV primary vertex

PV_0 hard-scattering PV

QCD quantum chromodynamics

QFT quantum field theory

ROD ReadOut Driver

ROI Region of Interest

ROS ReadOut System

RPC R-parity conserving

RPC resistive plate chamber

RPV R-parity violating

S/B signal/backround ratio

SCT semi-conductor tracker

SF scale factor

SFOS same-flavour opposite-sign

SM Standard Model

SPS Super Proton Synchrotron

SR Signal Region

SSVF single secondary vertex finder

SUSY supersymmetry

SV secondary vertex

SVF secondary vertex finder

2HDM two-Higgs-doublet model

3G third-generation

T-LVT *Track-based Low-p_T Vertex Tagger*

TC-LVT *Track-Cluster-based Low-p_T Vertex Tagger*

TDAQ trigger and data acquisition

TGC thin gap chamber

TMVA Toolkit for Multivariate Data Analysis

TOTEM TOTal cross section, Elastic scattering and diffraction dissociation Measurement at the LHC

TRT transtion radiation tracker

VEV vacuum expectation value

VR Validation Region

WIMP weakly interacting massive particle

XGB XGBoost

List of Figures

List of Tables

Bibliography

[1] ATLAS Collaboration, *Performance of electron and photon triggers in ATLAS during LHC Run 2*, Eur. Phys. J. C **80** (2019) 47. 56 p, arXiv:1909.00761. https://cds.cern.ch/record/2688248. v, 54, 152, 158, 160, 172, 180

[2] ATLAS Collaboration, *Soft b-hadron tagging for compressed SUSY scenarios*, tech. rep., CERN, Geneva, Jul, 2019. https://cds.cern.ch/record/2682131. v, 81, 86, 87, 88, 174

[3] ATLAS Collaboration, *Search for new phenomena in final states with b-jets and missing transverse momentum in* $\sqrt{s} = 13$ *TeV pp collisions with the ATLAS detector*, JHEP **2105** (2021) 093. 51 p, arXiv:2101.12527. v, 135, 138, 139, 141, 142, 151, 177, 178

[4] E. Noether, *Invariante Variationsprobleme*, Nachrichten von der Gesellschaft der Wissenschaften zu Göttingen, Mathematisch-Physikalische Klasse **1918** (1918) 235–257. http://eudml.org/doc/59024. 1

[5] S. Weinberg, *The Quantum Theory of Fields*, vol. 1. Cambridge University Press, 1995. 1, 4

[6] M. E. Peskin and D. V. Schroeder, *An Introduction to quantum field theory*. Addison-Wesley, Reading, USA, 1995. 1, 4, 5

[7] ATLAS Collaboration, *Observation of a new particle in the search for the Standard Model Higgs boson with the ATLAS detector at the LHC*, Physics Letters B **716** no. 1, (2012) 1–29. https://www.sciencedirect.com/science/article/pii/S037026931200857X. 4, 10, 16, 150

[8] CMS Collaboration, *Observation of a new boson at a mass of 125 GeV with the CMS experiment at the LHC*, Physics Letters B **716** no. 1, (2012) 30–61. https://www.sciencedirect.com/science/article/pii/S0370269312008581. 4, 10, 16, 150

[9] A. Salam and J. C. Ward, *On a gauge theory of elementary interactions*, 1961. https://doi.org/10.1007/BF02812723. 5

[10] S. L. Glashow, *Partial-symmetries of weak interactions*, Nuclear Physics **22** no. 4, (1961) 579–588. https://doi.org/10.1016/0029-5582(61)90469-2. 5

[11] D. Griffiths, *Introduction to Elementary Particles*. Wiley. 6, 7, 8, 9

[12] T. Nakano and K. Nishijima, *Charge Independence for V-particles*, Progress of Theoretical Physics **10** no. 5, (1953) 581–582. https://doi.org/10.1143/PTP.10.581. 6

[13] M. Gell-Mann, *The interpretation of the new particles as displaced charge multiplets*, Il Nuovo Cimento (1955-1965) **4** no. 2, (1956) 848–866. https://doi.org/10.1007/BF02748000. 6

[14] A. Bettini, *Introduction to Elementary Particle Physics*. Cambridge University Press. 7, 8

[15] L. Di Lella and C. Rubbia, *The Discovery of the W and Z Particles*, Adv. Ser. Direct. High Energy Phys. **23** (2015) 137–163. 8

[16] P. W. Higgs, *Spontaneous Symmetry Breakdown without Massless Bosons*, Phys. Rev. **145** (1966) 1156–1163. https://link.aps.org/doi/10.1103/PhysRev.145.1156. 8, 16

[17] T. W. B. Kibble, *Symmetry Breaking in Non-Abelian Gauge Theories*, Phys. Rev. **155** (1967) 1554–1561. https://link.aps.org/doi/10.1103/PhysRev.155.1554. 8, 16

[18] F. Englert and R. Brout, *Broken Symmetry and the Mass of Gauge Vector Mesons*, Phys. Rev. Lett. **13** (1964) 321–323. https://link.aps.org/doi/10.1103/PhysRevLett.13.321. 8, 16

[19] J. Ellis, *Higgs Physics*, arXiv:1312.5672. 9, 170

[20] Particle Data Group Collaboration, *Review of Particle Physics*, Phys. Rev. D **98** (2018) 030001. https://link.aps.org/doi/10.1103/PhysRevD.98.030001. 10, 11, 16, 20, 182

[21] M. C. Gonzalez-Garcia and Y. Nir, *Neutrino masses and mixing: evidence and implications*, Rev. Mod. Phys. **75** (2003) 345–402. https://link.aps.org/doi/10.1103/RevModPhys.75.345. 11

[22] H. Georgi et al., *Hierarchy of Interactions in Unified Gauge Theories*, Phys. Rev. Lett. **33** (1974) 451–454. https://link.aps.org/doi/10.1103/PhysRevLett.33.451. 11

[23] S. P. Martin, *A Supersymmetry Primer*, Advanced Series on Directions in High Energy Physics (1998) 1–98. http://dx.doi.org/10.1142/9789812839657_0001. 12, 19, 150

[24] D. Merritt et al., *Dark Matter: A Primer*, Advances in Astronomy **2011** (2011) 968283. https://doi.org/10.1155/2011/968283. 12, 20, 150

[25] A. Doroshkevich et al., *A solution to the problems of cusps and rotation curves in dark matter halos in the cosmological standard model*, Physics-uspekhi - PHYS-USP **55** (2012). 12, 170

[26] N. Jarosik et al., *Nine-year Wilkinson Microwave Anisotropy Probe (WMAP) observations: final maps and results*, The Astrophysical Journal Supplement Series **208** no. 2, (2013) 20. http://dx.doi.org/10.1088/0067-0049/208/2/20. 13, 150

[27] Planck Collaboration, *Planck 2018 results*, Astronomy & Astrophysics **641** (2020) A6. http://dx.doi.org/10.1051/0004-6361/201833910. 13, 20, 27, 150

[28] L. Roszkowski et al., *WIMP dark matter candidates and searches—current status and future prospects*, Reports on Progress in Physics **81** no. 6, (2018) 066201. http://dx.doi.org/10.1088/1361-6633/aab913. 13

[29] A. D. Sakharov, *Violation of CP Invariance, C asymmetry, and baryon asymmetry of the universe*, Pisma Zh. Eksp. Teor. Fiz. **5** (1967) 32–35. 13

[30] M. Kobayashi and T. Maskawa, *CP Violation in the Renormalizable Theory of Weak Interaction*, Prog. Theor. Phys. **49** (1973) 652–657. 13

[31] W. M. Alberico and S. M. Bilenky, *Neutrino oscillations, masses and mixing*, Phys. Part. Nucl. **35** (2004) 297–323, arXiv:hep-ph/0306239. 13

[32] Z. Maki et al., *Remarks on the unified model of elementary particles*, Prog. Theor. Phys. **28** (1962) 870–880. 13, 150

[33] C. Giunti et al., *Running coupling constants and grand unification models*, Mod. Phys. Lett. A **6** (1991) 1745–1755. 13

[34] L. Susskind, *Dynamics of Spontaneous Symmetry Breaking in the Weinberg-Salam Theory*, Phys. Rev. D **20** (1979) 2619–2625. 14, 150

[35] H. Weyl, *Electron and Gravitation. 1. (In German)*, Z. Phys. **56** (1929) 330–352. 14

[36] A. H. Chamseddine et al., *Locally Supersymmetric Grand Unification*, Phys. Rev. Lett. **49** (1982) 970. 15

[37] G. L. Kane et al., *Study of constrained minimal supersymmetry*, Physical Review D **49** no. 11, (1994) 6173–6210. http://dx.doi.org/10.1103/PhysRevD.49.6173. 15

[38] R. Barbieri et al., *Gauge models with spontaneously broken local supersymmetry*, Physics Letters B **119** no. 4, (1982) 343–347. https://www.sciencedirect.com/science/article/pii/0370269382906852. 15

[39] J. F. Gunion et al., *The Higgs Hunter's Guide*, vol. 80. 2000. 16

[40] G. R. Farrar and P. Fayet, *Phenomenology of the Production, Decay, and Detection of New Hadronic States Associated with Supersymmetry*, Phys. Lett. B **76** (1978) 575–579. 17

[41] K. Hidaka and A. Bartl, *Impact of bosonic decays on the search for $\tilde{t}_1$ and $\tilde{b}_1$ squarks*, Physics Letters B **501** no. 1, (2001) 78–85. https://www.sciencedirect.com/science/article/pii/S0370269301001083. 18

[42] A. Schuessler and D. Zeppenfeld, *Unitarity constraints on MSSM trilinear couplings*, pp. , 236–239. 10, 2007. arXiv:0710.5175 [hep-ph]. 19

[43] R. Barbieri and G. F. Giudice, *Upper bounds on supersymmetric particle masses*, Nucl. Phys. B **306** (1987) 63–76. 19 p. https://cds.cern.ch/record/180560. 19

[44] M. Papucci et al., *Natural SUSY endures*, Journal of High Energy Physics **2012** no. 9, (2012). http://dx.doi.org/10.1007/JHEP09(2012)035. 20, 170

[45] H. Baer et al., *Neutralino versus axion/axino cold dark matter in the 19 parameter SUGRA model*, Journal of High Energy Physics **2010** no. 10, (2010). http://dx.doi.org/10.1007/JHEP10(2010)023. 21, 170

[46] K. Griest and D. Seckel, *Three exceptions in the calculation of relic abundances*, Phys. Rev. D **43** (1991) 3191–3203. https://link.aps.org/doi/10.1103/PhysRevD.43.3191. 21, 150

[47] J. Alwall et al., *Searching for directly decaying gluinos at the Tevatron*, Physics Letters B **666** no. 1, (2008) 34–37. https://www.sciencedirect.com/science/article/pii/S0370269308007727. 22

[48] J. Alwall et al., *Simplified models for a first characterization of new physics at the LHC*, Phys. Rev. D **79** (2009) 075020. https://link.aps.org/doi/10.1103/PhysRevD.79.075020. 22

[49] D. Alves et al., *Simplified models for LHC new physics searches*, Journal of Physics G: Nuclear and Particle Physics **39** no. 10, (2012) 105005. https://doi.org/10.1088/0954-3899/39/10/105005. 22

[50] ATLAS Collaboration, *SUSY Summary Plots June 2021*, tech. rep., CERN, Geneva, Jun, 2021. http://cds.cern.ch/record/2771785. 24, 25, 26, 27, 170, 171

[51] G. Giudice and A. Romanino, *Erratum to: "Split supersymmetry" [Nucl. Phys. B 699 (2004) 65]*, Nuclear Physics B **706** no. 1-2, (2005) 487. http://dx.doi.org/10.1016/j.nuclphysb.2004.11.048. 25

[52] N. Arkani-Hamed and S. Dimopoulos, *Supersymmetric unification without low energy supersymmetry and signatures for fine-tuning at the LHC*, Journal of High Energy Physics **2005** no. 06, (2005) 073–073. http://dx.doi.org/10.1088/1126-6708/2005/06/073. 25

[53] L. Randall and R. Sundrum, *Out of this world supersymmetry breaking*, Nuclear Physics B **557** no. 1-2, (1999) 79–118. http://dx.doi.org/10.1016/S0550-3213(99)00359-4. 26

[54] G. F. Giudice et al., *Gaugino Mass without Singlets*, JHEP **12** (1998) 027. 25 p. http://cds.cern.ch/record/368799. 26

[55] C.-S. Huang et al., *The Promising process to distinguish supersymmetric models with large tan Beta from the standard model: $B \to X_s \mu^+ \mu^-$*, Phys. Rev. D **59** (1999) 011701, arXiv:hep-ph/9803460. 27

[56] M. Pospelov, *Higgs-mediated FCNC in supersymmetric models with large* $\tan\beta$, Nucl. Phys. B Proc. Suppl. **101** (2001) 385–394. 27

[57] S. Rai Choudhury and N. Gaur, *Dileptonic decay of B_s meson in SUSY models with large* $\tan\beta$, Physics Letters B **451** no. 1-2, (1999) 86–92. http://dx.doi.org/10.1016/S0370-2693(99)00203-8. 27

[58] K. S. Babu and C. F. Kolda, *Higgs mediated $B^0 \to \mu^+ \mu^-$ in minimal supersymmetry*, Phys. Rev. Lett. **84** (2000) 228–231, arXiv:hep-ph/9909476. 27

[59] S. R. Choudhury et al., *Signatures of new physics in dileptonic B-decays*, Int. J. Mod. Phys. A **21** (2006) 2617–2634, arXiv:hep-ph/0504193. 27

[60] ATLAS Collaboration, *Study of the rare decays of B_s^0 and B^0 mesons into muon pairs using data collected during 2015 and 2016 with the ATLAS detector*, JHEP **04** (2018) 098. 44 p, arXiv:1812.03017. http://cds.cern.ch/record/2650331. 27

[61] LHCb Collaboration, *Measurement of the $B_s^0 \to \mu^+ \mu^-$ Branching Fraction and Effective Lifetime and Search for $B^0 \to \mu^+ \mu^-$ Decays*, Physical Review Letters **118** no. 19, (2017). http://dx.doi.org/10.1103/PhysRevLett.118.191801. 27

[62] J. R. Ellis et al., *A phenomenological profile of the Higgs boson*, Nucl. Phys. B **106** (1976) 292–340. 64 p. https://cds.cern.ch/record/874049. 27

[63] A. Djouadi, *Squark effects on Higgs boson production and decay at the LHC*, Physics Letters B **435** no. 1-2, (1998) 101–108. http://dx.doi.org/10.1016/S0370-2693(98)00784-9. 27

[64] L. R. Evans and P. Bryant, *LHC Machine*, JINST **3** (2008) S08001. 164 p. https://cds.cern.ch/record/1129806. 29

[65] ATLAS Collaboration, *The ATLAS Experiment at the CERN Large Hadron Collider*, JINST **3** (2008) S08003. 437 p. https://cds.cern.ch/record/1129811. 29, 32, 33, 36, 40, 42, 43, 171, 172, 182

[66] CMS Collaboration, *The CMS experiment at the CERN LHC*, Journal of Instrumentation **3** no. 08, (2008) S08004–S08004. https://doi.org/10.1088/1748-0221/3/08/s08004. 29, 32

[67] ALICE Collaboration, *The ALICE experiment at the CERN LHC*, Journal of Instrumentation **3** no. 08, (2008) S08002–S08002. https://doi.org/10.1088/1748-0221/3/08/s08002. 29

[68] LHCb Collaboration, *The LHCb Detector at the LHC*, Journal of Instrumentation **3** no. 08, (2008) S08005–S08005. https://doi.org/10.1088/1748-0221/3/08/s08005. 29

[69] LHCf Collaboration, *The LHCf detector at the CERN Large Hadron Collider*, Journal of Instrumentation **3** no. 08, (2008) S08006–S08006. https://doi.org/10.1088/1748-0221/3/08/s08006. 29

[70] TOTEM Collaboration, *The TOTEM Experiment at the CERN Large Hadron Collider*, Journal of Instrumentation **3** no. 08, (2008) S08007–S08007. https://doi.org/10.1088/1748-0221/3/08/s08007. 29

[71] MoEDAL Collaboration, *Technical Design Report of the MoEDAL Experiment*, Tech. Rep. CERN-LHCC-2009-006. MoEDAL-TDR-001, Jun, 2009. https://cds.cern.ch/record/1181486. 29

[72] F. Marcastel, *CERN's Accelerator Complex. La chaîne des accélérateurs du CERN*,. https://cds.cern.ch/record/1621583. 30, 171

[73] ATLAS Collaboration, *Luminosity Public Results Run 2*,. https://twiki.cern.ch/twiki/bin/view/AtlasPublic/LuminosityPublicResultsRun2. 31, 32, 171

[74] ATLAS Collaboration, *ATLAS magnet system: Technical Design Report, 1*. Technical Design Report ATLAS. CERN, Geneva, 1997. https://cds.cern.ch/record/338080. 34, 35, 171

[75] ATLAS Collaboration, *ATLAS Insertable B-Layer Technical Design Report*, Tech. Rep. CERN-LHCC-2010-013. ATLAS-TDR-19, Sep, 2010. https://cds.cern.ch/record/1291633. 36

[76] ATLAS Collaboration, *ATLAS pixel detector electronics and sensors*, JINST **3** (2008) P07007. https://cds.cern.ch/record/1119279. 37

[77] ATLAS Collaboration, *Performance of the ATLAS track reconstruction algorithms in dense environments in LHC Run 2*, The European Physical Journal C **77** no. 10, (2017). http://dx.doi.org/10.1140/epjc/s10052-017-5225-7. 37, 172

[78] ATLAS Collaboration, *Operation of the ATLAS Trigger System in Run 2*, Tech. Rep. ATL-COM-DAQ-2019-205, CERN, Geneva, Dec, 2019. https://cds.cern.ch/record/2703235. 44, 172

[79] ATLAS Collaboration, *Operation of the ATLAS trigger system in Run 2*, Journal of Instrumentation **15** no. 10, (2020) P10004–P10004. http://dx.doi.org/10.1088/1748-0221/15/10/P10004. 43, 53

[80] ATLAS Collaboration, *The ATLAS Level-1 Topological Processor: from design to routine usage in Run-2*, Tech. Rep. ATL-DAQ-PROC-2018-044, CERN, Geneva, Dec, 2018. https://cds.cern.ch/record/2649959. 44

[81] ATLAS Collaboration, *Fast TracKer (FTK) Technical Design Report*, Tech. Rep. CERN-LHCC-2013-007. ATLAS-TDR-021, Jun, 2013. http://cds.cern.ch/record/1552953. 45

[82] ATLAS Collaboration, *ATLAS data quality operations and performance for 2015–2018 data-taking*, Journal of Instrumentation **15** no. 04, (2020) P04003–P04003. http://dx.doi.org/10.1088/1748-0221/15/04/P04003. 46, 47

[83] D. J. Gross and F. Wilczek, *Ultraviolet Behavior of Non-Abelian Gauge Theories*, Phys. Rev. Lett. **30** (1973) 1343–1346. https://link.aps.org/doi/10.1103/PhysRevLett.30.1343. 47

[84] H1 and ZEUS Collaboration, *Combination of measurements of inclusive deep inelastic $e^{\pm}p$ scattering cross sections and QCD analysis of HERA data*, Eur. Phys. J. C **75** no. 12, (2015) 580, arXiv:1506.06042 [hep-ex]. 47, 48

[85] J. M. Campbell et al., *Hard interactions of quarks and gluons: a primer for LHC physics*, Reports on Progress in Physics **70** no. 1, (2006) 89–193. http://dx.doi.org/10.1088/0034-4885/70/1/R02. 47

[86] J. C. Collins et al., *Factorization of Hard Processes in QCD*, Adv. Ser. Direct. High Energy Phys. **5** (1989) 1–91, arXiv:hep-ph/0409313. 47

[87] A. Buckley et al., *General-purpose event generators for LHC physics*, Physics Reports **504** no. 5, (2011) 145–233. http://dx.doi.org/10.1016/j.physrep.2011.03.005. 47, 49

[88] M. Dobbs and J. B. Hansen, *The HepMC C++ Monte Carlo Event Record for High Energy Physics*, tech. rep., CERN, Geneva, Jun, 2000. https://cds.cern.ch/record/684090. 48, 52, 172

[89] H1 Collaboration, *Technical proposal for the H1 detector*. DESY, Hamburg, 1986. http://cds.cern.ch/record/108544. 48

[90] ZEUS Collaboration, *THE ZEUS DETECTOR: TECHNICAL PROPOSAL*,. https://cds.cern.ch/record/1478623. 48

[91] D0 Collaboration, *The D0 Detector*, Nucl. Instrum. Meth. A **338** (1994) 185–253. 48

[92] CDF Collaboration, *The CDF Detector: An Overview*, Nucl. Instrum. Meth. A **271** (1988) 387–403. 48

[93] D0 Collaboration, *Inclusive Jet Production in $p\bar{p}$ Collisions*, Physical Review Letters **86** no. 9, (2001) 1707–1712. http://dx.doi.org/10.1103/PhysRevLett.86.1707. 48

[94] CDF Collaboration, *Charged jet evolution and the underlying event in proton-antiproton collisions at 1.8 TeV*, Phys. Rev. D **65** (2002) 092002. https://link.aps.org/doi/10.1103/PhysRevD.65.092002. 48

[95] V. N. Gribov and L. N. Lipatov, *Deep inelastic ep scattering in perturbation theory*, Sov. J. Nucl. Phys. **15** (1972) 438–450. 48

[96] G. Altarelli and G. Parisi, *Asymptotic Freedom in Parton Language*, Nucl. Phys. B **126** (1977) 298–318. 48

[97] Y. L. Dokshitzer, *Calculation of the Structure Functions for Deep Inelastic Scattering and e^+e^- Annihilation by Perturbation Theory in Quantum Chromodynamics*, Sov. Phys. JETP **46** (1977) 641–653. 48

[98] R. D. Ball et al., *Parton distributions with LHC data*, Nuclear Physics B **867** no. 2, (2013) 244–289. http://dx.doi.org/10.1016/j.nuclphysb.2012.10.003. 48

[99] T. Kinoshita, *Mass singularities of Feynman amplitudes*, J. Math. Phys. **3** (1962) 650–677. 49

[100] T. D. Lee and M. Nauenberg, *Degenerate Systems and Mass Singularities*, Phys. Rev. **133** (1964) B1549–B1562. 49

[101] V. V. Sudakov, *Vertex parts at very high-energies in quantum electrodynamics*, Sov. Phys. JETP **3** (1956) 65–71. 50

[102] S. Catani et al., *QCD Matrix Elements + Parton Showers*, Journal of High Energy Physics **2001** no. 11, (2001) 063–063. http://dx.doi.org/10.1088/1126-6708/2001/11/063. 50

[103] M. L. Mangano et al., *Matching matrix elements and shower evolution for top-pair production in hadronic collisions*, Journal of High Energy Physics **2007** no. 01, (2007) 013–013. http://dx.doi.org/10.1088/1126-6708/2007/01/013. 50

[104] S. Hoeche et al., *Matching parton showers and matrix elements,*. https://cds.cern.ch/record/926597. 50

[105] S. Catani et al., *New clustering algorithm for multi-jet cross-sections in e^+e^- annihilation*, Phys. Lett. B **269** (1991) 432–438. 50

[106] S. Catani et al., *The $k_\perp$-clustering algorithm for jets in deep inelastic scattering and hadron collisions*, Phys. Lett. B **285** (1992) 291–299. 13 p. https://cds.cern.ch/record/236610. 50

[107] S. Catani et al., *Longitudinally invariant K_t clustering algorithms for hadron hadron collisions*, Nucl. Phys. B **406** (1993) 187–224. 50

[108] B. Andersson et al., *Parton Fragmentation and String Dynamics*, Phys. Rept. **97** (1983) 31–145. 51

[109] T. Sjostrand, *Jet Fragmentation of Nearby Partons*, Nucl. Phys. B **248** (1984) 469–502. 51

[110] B. R. Webber, *A QCD Model for Jet Fragmentation Including Soft Gluon Interference*, Nucl. Phys. B **238** (1984) 492–528. 51

[111] G. Marchesini and B. R. Webber, *Monte Carlo Simulation of General Hard Processes with Coherent QCD Radiation*, Nucl. Phys. B **310** (1988) 461–526. 51

[112] D. Amati and G. Veneziano, *Preconfinement as a Property of Perturbative QCD*, Phys. Lett. B **83** (1979) 87–92. 51

[113] Y. Kulchitsky, *Measurement of the underlying-event properties with the ATLAS detector*, 2016. 51

[114] T. Sjostrand and M. van Zijl, *A Multiple Interaction Model for the Event Structure in Hadron Collisions*, Phys. Rev. D **36** (1987) 2019. 51

[115] G. Corcella et al., *HERWIG 6: an event generator for hadron emission reactions with interfering gluons (including supersymmetric processes)*, Journal of High Energy Physics **2001** no. 01, (2001) 010–010. http://dx.doi.org/10.1088/1126-6708/2001/01/010. 51

[116] J. M. Butterworth et al., *Multiparton interactions in photoproduction at HERA*, Zeitschrift für Physik C: Particles and Fields **72** no. 4, (1996) 637–646. http://dx.doi.org/10.1007/s002880050286. 51

[117] T. Gleisberg et al., *Event generation with SHERPA 1.1*, Journal of High Energy Physics **2009** no. 02, (2009) 007–007. http://dx.doi.org/10.1088/1126-6708/2009/02/007. 52, 100, 102

[118] T. Sjöstrand et al., *A brief introduction to PYTHIA 8.1*, Computer Physics Communications **178** no. 11, (2008) 852–867. http://dx.doi.org/10.1016/j.cpc.2008.01.036. 52, 97, 102

[119] T. Sjöstrand and P. Z. Skands, *Transverse-momentum-ordered showers and interleaved multiple interactions*, The European Physical Journal C **39** no. 2, (2005) 129–154. http://dx.doi.org/10.1140/epjc/s2004-02084-y. 52

[120] ATLAS Collaboration, *ATLAS Pythia 8 tunes to 7 TeV datas*, Tech. Rep. ATL-PHYS-PUB-2014-021, CERN, Geneva, Nov, 2014. https://cds.cern.ch/record/1966419. 52, 97

[121] M. Bähr et al., *Herwig++ physics and manual*, The European Physical Journal C **58** no. 4, (2008) 639–707. http://dx.doi.org/10.1140/epjc/s10052-008-0798-9. 52, 134

[122] J. Alwall et al., *The automated computation of tree-level and next-to-leading order differential cross sections, and their matching to parton shower simulations*, Journal of High Energy Physics **2014** no. 7, (2014). http://dx.doi.org/10.1007/JHEP07(2014)079. 52, 97, 102

[123] S. Alioli et al., *A general framework for implementing NLO calculations in shower Monte Carlo programs: the POWHEG BOX*, Journal of High Energy Physics **2010** no. 6, (2010). http://dx.doi.org/10.1007/JHEP06(2010)043. 52, 102, 103

[124] ATLAS Collaboration, *The ATLAS Simulation Infrastructure*, The European Physical Journal C **70** no. 3, (2010) 823–874. http://dx.doi.org/10.1140/epjc/s10052-010-1429-9. 53

[125] P. Calafiura et al., *The Athena Control Framework in Production, New Developments and Lessons Learned*,. https://cds.cern.ch/record/865624. 53

[126] S. Agostinelli et al., *Geant4: A simulation toolkit*, Nuclear Instruments and Methods in Physics Research Section A: Accelerators, Spectrometers, Detectors and Associated Equipment **506** no. 3, (2003) 250 – 303. http://www.sciencedirect.com/science/article/pii/S0168900203013688. 53, 98

[127] ATLAS Collaboration, *The simulation principle and performance of the ATLAS fast calorimeter simulation FastCaloSim*, Tech. Rep. ATL-COM-PHYS-2010-838, CERN, Geneva, Oct, 2010. https://cds.cern.ch/record/1298808. 53, 98

[128] ATLAS Collaboration, *Performance of the ATLAS trigger system in 2015*, The European Physical Journal C **77** no. 5, (2017). http://dx.doi.org/10.1140/epjc/s10052-017-4852-3. 53, 103

[129] ATLAS Collaboration, *Trigger Menu in 2016*, Tech. Rep. ATL-DAQ-PUB-2017-001, CERN, Geneva, Jan, 2017. https://cds.cern.ch/record/2242069. 53, 103

[130] ATLAS Collaboration, *Trigger Menu in 2017*, Tech. Rep. ATL-DAQ-PUB-2018-002, CERN, Geneva, Jun, 2018. https://cds.cern.ch/record/2625986. 53, 103

[131] ATLAS Collaboration, *Trigger menu in 2018*, Tech. Rep. ATL-DAQ-PUB-2019-001, CERN, Geneva, Oct, 2019. https://cds.cern.ch/record/2693402. 53, 103

[132] ATLAS Collaboration, *Electron and photon performance measurements with the ATLAS detector using the 2015–2017 LHC proton-proton collision data*, Journal of Instrumentation **14** no. 12, (2019) P12006–P12006. http://dx.doi.org/10.1088/1748-0221/14/12/P12006. 55, 156, 183

[133] A. Hoecker et al., *TMVA: Toolkit for Multivariate Data Analysis*, PoS **ACAT** (2007) 040, arXiv:physics/0703039. 55, 73, 75, 152

[134] ATLAS Collaboration, *Electron reconstruction and identification in the ATLAS experiment using the 2015 and 2016 LHC proton-proton collision data at* $\sqrt{s} = 13$ *TeV*, Eur. Phys. J. C **79** (2019) 639. 40 p, arXiv:1902.04655. http://cds.cern.ch/record/2657964. 55

[135] ATLAS Collaboration, "Public egamma trigger plots for collision data." https://twiki.cern.ch/twiki/bin/view/AtlasPublic/EgammaTriggerPublicResults. 56, 172

[136] ATLAS Collaboration, *Performance of the ATLAS muon triggers in Run 2*, Journal of Instrumentation **15** no. 09, (2020) P09015–P09015. http://dx.doi.org/10.1088/1748-0221/15/09/p09015. 56

[137] ATLAS Collaboration, "Muon trigger public results." https://twiki.cern.ch/twiki/bin/view/AtlasPublic/MuonTriggerPublicResults. 58, 172

[138] ATLAS Collaboration, *Performance of the missing transverse momentum triggers for the ATLAS detector during Run-2 data taking*, Journal of High Energy Physics **2020** no. 8, (2020). http://dx.doi.org/10.1007/JHEP08(2020)080. 57

[139] ATLAS Collaboration, "Missing energy trigger public results." https://twiki.cern.ch/twiki/bin/view/AtlasPublic/MissingEtTriggerPublicResults. 60, 172

[140] T. Cornelissen et al., *The new ATLAS track reconstruction (NEWT)*, Journal of Physics: Conference Series **119** no. 3, (2008) 032014. https://doi.org/10.1088/1742-6596/119/3/032014. 61

[141] R. Fruhwirth, *Application of Kalman filtering to track and vertex fitting*, Nucl. Instrum. Meth. A **262** (1987) 444–450. 61, 74

[142] ATLAS Collaboration, *Performance of the ATLAS track reconstruction algorithms in dense environments in LHC Run 2*, Eur. Phys. J. C 77, 673 (2017). https://doi.org/10.1140/epjc/s10052-017-5225-7. 61

[143] K. Shingo, *Search for Charginos Nearly Mass-Degenerate with the Lightest Neutralino Based on a Disappearing-Track signature in pp Collisions at* $\sqrt{s} = 8$ *TeV*, Mar, 2016. https://cds.cern.ch/record/1966691. 62, 172

[144] ATLAS Collaboration, *Reconstruction of primary vertices at the ATLAS experiment in Run 1 proton–proton collisions at the LHC*, The European Physical Journal C **77** no. 5, (2017). http://dx.doi.org/10.1140/epjc/s10052-017-4887-5. 62

[145] ATLAS Collaboration, *Secondary vertex finding for jet flavour identification with the ATLAS detector*, tech. rep., CERN, Geneva, Jun, 2017. https://cds.cern.ch/record/2270366. 63, 74, 82, 85

[146] ATLAS Collaboration, *Electron reconstruction and identification in the ATLAS experiment using the 2015 and 2016 LHC proton–proton collision data at* $\sqrt{s} = 13$ *TeV*, The European Physical Journal C **79** no. 8, (2019). http://dx.doi.org/10.1140/epjc/s10052-019-7140-6. 65, 66, 156, 173, 183

[147] ATLAS Collaboration, *Improved electron reconstruction in ATLAS using the Gaussian Sum Filter-based model for bremsstrahlung*, tech. rep., CERN, Geneva, May, 2012. http://cds.cern.ch/record/1449796. 65

[148] ATLAS Collaboration, *Muon reconstruction performance of the ATLAS detector in proton-proton collision data at* $\sqrt{s} = 13$ *TeV*, Eur. Phys. J. C **76** no. 5, (2016) 292. 65, 67, 68, 173

[149] M. Cacciari et al., *The anti-k_t jet clustering algorithm*, Journal of High Energy Physics **2008** no. 04, (2008) 063–063. http://dx.doi.org/10.1088/1126-6708/2008/04/063. 67, 69, 173

[150] ATLAS Collaboration, *Topological cell clustering in the ATLAS calorimeters and its performance in LHC Run 1*, The European Physical Journal C **77** no. 7, (2017). http://dx.doi.org/10.1140/epjc/s10052-017-5004-5. 69, 71

[151] ATLAS Collaboration, *Jet reconstruction and performance using particle flow with the ATLAS Detector*, The European Physical Journal C **77** no. 7, (2017). http://dx.doi.org/10.1140/epjc/s10052-017-5031-2. 70, 72, 173

[152] ATLAS Collaboration, *Determination of jet calibration and energy resolution in proton-proton collisions at* $\sqrt{s} = 8$ *TeV using the ATLAS detector*, Eur. Phys. J. C

80 (2019) 1104. 81 p, arXiv:1910.04482. https://cds.cern.ch/record/2693121. 71

[153] M. Cacciari et al., *The catchment area of jets*, Journal of High Energy Physics **2008** no. 04, (2008) 005–005. http://dx.doi.org/10.1088/1126-6708/2008/04/005. 71, 86

[154] M. Cacciari and G. P. Salam, *Pileup subtraction using jet areas*, Physics Letters B **659** no. 1-2, (2008) 119–126. http://dx.doi.org/10.1016/j.physletb.2007.09.077. 71, 86

[155] ATLAS Collaboration, *Jet energy scale measurements and their systematic uncertainties in proton-proton collisions at* $\sqrt{s} = 13$ *TeV with the ATLAS detector*, Phys. Rev. D **96** (2017) 072002. https://link.aps.org/doi/10.1103/PhysRevD.96.072002. 71, 133

[156] ATLAS Collaboration, *Jet energy measurement and its systematic uncertainty in proton–proton collisions at* $\sqrt{s} = 7$ *TeV with the ATLAS detector*, The European Physical Journal C **75** no. 1, (2015). http://dx.doi.org/10.1140/epjc/s10052-014-3190-y. 72

[157] ATLAS Collaboration, *Characterisation and mitigation of beam-induced backgrounds observed in the ATLAS detector during the 2011 proton-proton run*, Journal of Instrumentation **8** no. 07, (2013) P07004–P07004. http://dx.doi.org/10.1088/1748-0221/8/07/P07004. 72

[158] ATLAS Collaboration, *Performance of pile-up mitigation techniques for jets in pp collisions at* $\sqrt{s} = 8$ *TeV using the ATLAS detector*, The European Physical Journal C **76** no. 11, (2016). http://dx.doi.org/10.1140/epjc/s10052-016-4395-z. 73

[159] ATLAS Collaboration, *Performance and Calibration of the JetFitterCharm Algorithm for c-Jet Identification*, tech. rep., CERN, Geneva, Jan, 2015. http://cds.cern.ch/record/1980463. 73

[160] ATLAS Collaboration, *ATLAS b-jet identification performance and efficiency measurement with* $t\bar{t}$ *events in pp collisions at* $\sqrt{s} = 13$ *TeV*, The European Physical Journal C **79** no. 11, (2019). http://dx.doi.org/10.1140/epjc/s10052-019-7450-8. 73, 75, 76, 86, 96, 174, 182

[161] N. Bartosik, "Diagram showing the common principle of identification of jets initiated by b-hadron decays." http://bartosik.pp.ua/hep_sketches/btagging. 74, 174

[162] ATLAS Collaboration, *Optimisation of the ATLAS b-tagging performance for the 2016 LHC Run*, tech. rep., CERN, Geneva, Jun, 2016. https://cds.cern.ch/record/2160731. 74

[163] G. Piacquadio and C. Weiser, *A new inclusive secondary vertex algorithm for b-jet tagging in ATLAS*, Journal of Physics: Conference Series **119** no. 3, (2008) 032032. https://doi.org/10.1088/1742-6596/119/3/032032. 74

[164] ATLAS Collaboration, *Optimisation and performance studies of the ATLAS b-tagging algorithms for the 2017-18 LHC run*, tech. rep., CERN, Geneva, Jul, 2017. https://cds.cern.ch/record/2273281. 74

[165] ATLAS Collaboration, *Calibration of the b-tagging efficiency on charm jets using a sample of $W+c$ events with $\sqrt{s} = 13$ ATLAS data*, tech. rep., CERN, Geneva, Dec, 2018. http://cds.cern.ch/record/2652195. 76, 96

[166] ATLAS Collaboration, *Calibration of the performance of b-tagging for c and light-flavour jets in the 2012 ATLAS data*, tech. rep., CERN, Geneva, Jul, 2014. https://cds.cern.ch/record/1741020. 76

[167] ATLAS Collaboration, *Performance of missing transverse momentum reconstruction with the ATLAS detector using proton–proton collisions at $\sqrt{s} = 13$ TeV*, The European Physical Journal C **78** no. 11, (2018). http://dx.doi.org/10.1140/epjc/s10052-018-6288-9. 77, 133

[168] ATLAS Collaboration, *Search for supersymmetry in final states with charm jets and missing transverse momentum in 13 TeV pp collisions with the ATLAS detector*, Journal of High Energy Physics **2018** no. 9, (2018). http://dx.doi.org/10.1007/JHEP09(2018)050. 79

[169] ATLAS Collaboration, *Search for a scalar partner of the top quark in the jets plus missing transverse momentum final state at $\sqrt{s} = 13$ TeV with the ATLAS detector*, Journal of High Energy Physics **2017** no. 12, (2017). http://dx.doi.org/10.1007/JHEP12(2017)085. 79

[170] ATLAS Collaboration, *Search for top-squark pair production in final states with one lepton, jets, and missing transverse momentum using 36 fb^{-1} of $\sqrt{s} = 13$ TeV pp collision data with the ATLAS detector*, Journal of High Energy Physics **2018** no. 6, (2018). http://dx.doi.org/10.1007/JHEP06(2018)108. 79

[171] ATLAS Collaboration, *Search for direct top squark pair production in final states with two leptons in $\sqrt{s} = 13$ TeV pp collisions with the ATLAS detector*, The European Physical Journal C **77** no. 12, (2017). http://dx.doi.org/10.1140/epjc/s10052-017-5445-x. 79

[172] CMS Collaboration, *Search for top squarks decaying via four-body or chargino-mediated modes in single-lepton final states in proton-proton collisions at* $\sqrt{s} = 13$ *TeV*, Journal of High Energy Physics **2018** no. 9, (2018). http://dx.doi.org/10.1007/JHEP09(2018)065. 79

[173] CMS Collaboration, *Search for direct production of supersymmetric partners of the top quark in the all-jets final state in proton-proton collisions at* $\sqrt{s} = 13$ *TeV*, Journal of High Energy Physics **2017** no. 10, (2017). http://dx.doi.org/10.1007/JHEP10(2017)005. 79, 81, 174

[174] ATLAS Collaboration, *Flavor Tagging with Track Jets in Boosted Topologies with the ATLAS Detector*, tech. rep., CERN, Geneva, Aug, 2014. https://cds.cern.ch/record/1750681. 81

[175] ATLAS Collaboration, *Performance of vertex reconstruction algorithms for detection of new long-lived particle decays within the ATLAS inner detector*, tech. rep., CERN, Geneva, Mar, 2019. https://cds.cern.ch/record/2669425. 81

[176] ATLAS Collaboration, *Search for supersymmetry in events with b-tagged jets and missing transverse momentum in pp collisions at* $\sqrt{s} = 13$ *TeV with the ATLAS detector*, Journal of High Energy Physics **2017** no. 11, (2017). http://dx.doi.org/10.1007/JHEP11(2017)195. 82, 83, 100, 114, 125, 135, 136, 147, 151, 177, 178, 179

[177] L. Moneta et al., *The RooStats Project*, PoS **ACAT2010** (2010) 057, arXiv:1009.1003 [physics.data-an]. 84, 114

[178] R. Brun and F. Rademakers, *ROOT: An object oriented data analysis framework*, Nuclear Instruments and Methods in Physics Research Section A: Accelerators, Spectrometers, Detectors and Associated Equipment **389** no. 1, (1997) 81 – 86. http://www.sciencedirect.com/science/article/pii/S016890029700048X. New Computing Techniques in Physics Research V. 84, 114

[179] ATLAS Collaboration, *Measurement of the CP-violating phase* ϕ_s *in* $B_s^0 \to J/\psi\phi$ *decays in ATLAS at 13 TeV*, Eur. Phys. J. C **81** no. 4, (2021) 342, arXiv:2001.07115 [hep-ex]. 92

[180] ATLAS Collaboration, *Calibration of light-flavour b-jet mistagging rates using ATLAS proton-proton collision data at* $\sqrt{s} = 13$ *TeV*, tech. rep., CERN, Geneva, Apr, 2018. http://cds.cern.ch/record/2314418. 96

[181] S. Carrazza et al., *Parton Distributions and Event Generators*, pp. , 89–96. 2013. arXiv:1311.5887 [hep-ph]. 98

[182] L. Lönnblad and S. Prestel, *Matching tree-level matrix elements with interleaved showers*, Journal of High Energy Physics **2012** no. 3, (2012). http://dx.doi.org/10.1007/JHEP03(2012)019. 98

[183] W. Beenakker et al., *Stop production at hadron colliders*, Nucl. Phys. B **515** (1998) 3–14, arXiv:hep-ph/9710451. 98

[184] W. Beenakker et al., *Supersymmetric top and bottom squark production at hadron colliders*, Journal of High Energy Physics **2010** no. 8, (2010). http://dx.doi.org/10.1007/JHEP08(2010)098. 98

[185] W. Beenakker et al., *Squark and gluino hadron production*, International Journal of Modern Physics A **26** no. 16, (2011) 2637–2664. http://dx.doi.org/10.1142/S0217751X11053560. 98

[186] ATLAS Collaboration, *ATLAS b-jet identification performance and efficiency measurement with $t\bar{t}$ events in pp collisions at $\sqrt{s} = 13$ TeV*, The European Physical Journal C **79** no. 11, (2019). http://dx.doi.org/10.1140/epjc/s10052-019-7450-8. 99, 133

[187] S. Catani et al., *Vector Boson Production at Hadron Colliders: A Fully Exclusive QCD Calculation at Next-to-Next-to-Leading Order*, Physical Review Letters **103** no. 8, (2009). http://dx.doi.org/10.1103/PhysRevLett.103.082001. 100, 102

[188] M. Czakon et al., *Total Top-Quark Pair-Production Cross Section at Hadron Colliders Through $O(\alpha_S^4)$*, Physical Review Letters **110** no. 25, (2013). http://dx.doi.org/10.1103/PhysRevLett.110.252004. 102, 107

[189] M. Czakon and A. Mitov, *NNLO corrections to top pair production at hadron colliders: the quark-gluon reaction*, Journal of High Energy Physics **2013** no. 1, (2013). http://dx.doi.org/10.1007/JHEP01(2013)080. 102, 107

[190] M. Czakon and A. Mitov, *NNLO corrections to top-pair production at hadron colliders: the all-fermionic scattering channels*, Journal of High Energy Physics **2012** no. 12, (2012). http://dx.doi.org/10.1007/JHEP12(2012)054. 102, 107

[191] P. Bärnreuther et al., *Percent-Level-Precision Physics at the Tevatron: Next-to-Next-to-Leading Order QCD Corrections to $q\bar{q} \to t\bar{t} + X$*, Physical Review Letters **109** no. 13, (2012). http://dx.doi.org/10.1103/PhysRevLett.109.132001. 102, 107

[192] M. Cacciari et al., *Top-pair production at hadron colliders with next-to-next-to-leading logarithmic soft-gluon resummation*, Physics Letters B **710** no. 4-5, (2012) 612–622. http://dx.doi.org/10.1016/j.physletb.2012.03.013. 102, 107

[193] M. Czakon and A. Mitov, *Top++: A program for the calculation of the top-pair cross-section at hadron colliders*, Computer Physics Communications **185** no. 11, (2014) 2930–2938. http://dx.doi.org/10.1016/j.cpc.2014.06.021. 102

[194] N. Kidonakis, *Next-to-next-to-leading-order collinear and soft gluon corrections fort-channel single top quark production*, Physical Review D **83** no. 9, (2011). http://dx.doi.org/10.1103/PhysRevD.83.091503. 102

[195] N. Kidonakis, *Two-loop soft anomalous dimensions for single top quark associated production with a W^- or H^-*, Physical Review D **82** no. 5, (2010). http://dx.doi.org/10.1103/PhysRevD.82.054018. 102

[196] N. Kidonakis, *Next-to-next-to-leading logarithm resummation fors-channel single top quark production*, Physical Review D **81** no. 5, (2010). http://dx.doi.org/10.1103/PhysRevD.81.054028. 102

[197] ATLAS Collaboration, *Identification and rejection of pile-up jets at high pseudorapidity with the ATLAS detector*, The European Physical Journal C **77** no. 9, (2017). http://dx.doi.org/10.1140/epjc/s10052-017-5081-5. 104

[198] M. Baak et al., *HistFitter software framework for statistical data analysis*, The European Physical Journal C **75** no. 4, (2015). http://dx.doi.org/10.1140/epjc/s10052-015-3327-7. 110, 137

[199] G. Cowan et al., *Asymptotic formulae for likelihood-based tests of new physics*, The European Physical Journal C **71** no. 2, (2011). http://dx.doi.org/10.1140/epjc/s10052-011-1554-0. 111, 112, 113, 176

[200] A. L. Read, *Presentation of search results: the CL_s technique*, Journal of Physics G: Nuclear and Particle Physics **28** no. 10, (2002) 2693–2704. https://doi.org/10.1088/0954-3899/28/10/313. 113

[201] ATLAS Collaboration, *Jet energy resolution in proton-proton collisions at $\sqrt{s} = 7$ TeV recorded in 2010 with the ATLAS detector*, The European Physical Journal C **73** no. 3, (2013). http://dx.doi.org/10.1140/epjc/s10052-013-2306-0. 133

[202] ATLAS Collaboration, *Tagging and suppression of pileup jets with the ATLAS detector*, Tech. Rep. ATLAS-CONF-2014-018, CERN, Geneva, May, 2014. https://cds.cern.ch/record/1700870. 133

[203] ATLAS Collaboration, *Luminosity determination in pp collisions at $\sqrt{s} = 13$ TeV using the ATLAS detector at the LHC*, Tech. Rep. ATLAS-CONF-2019-021, CERN, Geneva, Jun, 2019. http://cds.cern.ch/record/2677054. 134

[204] E. Bothmann et al., *Reweighting QCD matrix-element and parton-shower calculations*, The European Physical Journal C **76** no. 11, (2016). http://dx.doi.org/10.1140/epjc/s10052-016-4430-0. 134

[205] J. Bellm et al., *Herwig 7.0/Herwig++ 3.0 release note*, The European Physical Journal C **76** no. 4, (2016). http://dx.doi.org/10.1140/epjc/s10052-016-4018-8. 134

[206] ATLAS Collaboration, *Improvements in $t\bar{t}$ modelling using NLO+PS Monte Carlo generators for Run 2*, Tech. Rep. ATL-PHYS-PUB-2018-009, CERN, Geneva, Jul, 2018. https://cds.cern.ch/record/2630327. 134

[207] T. Chen and C. Guestrin, *XGBoost: A Scalable Tree Boosting System*, in *Proceedings of the 22nd ACM SIGKDD International Conference on Knowledge Discovery and Data Mining*, pp. , 785–794. ACM, New York, NY, USA, 2016. http://doi.acm.org/10.1145/2939672.2939785. 136

[208] U. Haisch et al., *Determining the CP nature of spin-0 mediators in associated production of dark matter and $t\bar{t}$ pairs*, Journal of High Energy Physics **2017** no. 2, (2017). http://dx.doi.org/10.1007/JHEP02(2017)131. 136

[209] ROOT Collaboration, *HistFactory: A tool for creating statistical models for use with RooFit and RooStats*, Tech. Rep. CERN-OPEN-2012-016, New York U., New York, Jan, 2012. https://cds.cern.ch/record/1456844. 137

[210] ATLAS Collaboration, *Ring-shaped Calorimetry Information for a Neural Egamma Identification with ATLAS Detector*, J. Phys. Conf. Ser. **762** no. 1, (2016) 012049. 153

[211] ATLAS Collaboration, *Electron efficiency measurements with the ATLAS detector using 2012 LHC proton–proton collision data*, The European Physical Journal C **77** no. 3, (2017). http://dx.doi.org/10.1140/epjc/s10052-017-4756-2. 158, 179